

Synchronization in Delay-Coupled Laser Networks

vorgelegt von
Diplom-Physiker
Thomas Dahms
aus Rüdersdorf

von der Fakultät II – Mathematik und Naturwissenschaften –



der Technischen Universität Berlin

zur Erlangung des akademischen Grades

Doktor der Naturwissenschaften

– Dr. rer. nat. –

genehmigte Dissertation

Promotionsausschuss:

Vorsitzender: Prof. Dr. Christian Thomsen
Berichter: Prof. Dr. Eckehard Schöll, PhD
Berichter: Prof. Dr. Wolfgang Kinzel

Tag der wissenschaftlichen Aussprache: 16. Juni 2011

Berlin 2011

D 83

To Emil and Matteo

Abstract

In this work I investigate patterns of synchronization in networks of semiconductor lasers. Two main questions arise when studying synchronization phenomena in these networks: (i) What kind of synchronization patterns can exist in a given network and (ii) is the synchronization stable? The basis for this study is formed by the chaotic dynamics that lasers may exhibit when coupled via time-delayed links. The lasers are modeled by the well established Lang-Kobayashi model. The main focus lies on the characterization of network topologies and parameter regimes that generate distinct patterns of synchronization in such laser networks.

Since the stability analysis can be carried out only numerically for chaotic dynamics, I complement my investigations by another model for the local dynamics in the networks' nodes – the Stuart-Landau oscillator. These nonlinear equations represent a normal form for any periodic dynamics near a Hopf bifurcation. In this model, the question of stability of synchronization can be answered by derivations of analytic equations. Furthermore, I show how conditions for the coupling parameters can be derived that allow for the selection and control of desired synchronization states.

At the heart of the stability analysis is the *master stability function* introduced by [Pecora and Carroll](#). This formalism allows one to separate the network dynamics from the network topology, which is only used in terms of the eigenvalues of the coupling matrix. I extend this theory for networks where delay-induced dynamics becomes important and show in detail the application to such delay-coupled networks in general and to laser and oscillator networks in particular. For laser networks, I study particular network topologies – simple network motifs as well as complex random networks – for different regimes of the laser dynamics. I will also make use of a symmetry argument of the master stability function that was recently shown in the limit of large coupling delay times. In addition, multiple delay times are dealt with by an extension to multiple coupling matrices.

Isochronous synchronization is the most prominent type of synchronization, but I show that certain topologies may instead exhibit cluster synchronization depending on symmetries in the network. For a better understanding of this dynamical scenario, I extend a formalism by [Sorrentino and Ott](#) that enables a stability analysis of these patterns of synchronization. The original approach has a restriction on the allowed topologies, which I partly lift by introducing multiple coupling matrices. As an application of this theory I consider examples of simple hierarchical networks.

In networks of Stuart-Landau oscillators different cluster states may coexist depending upon the coupling parameters. I elaborate this finding by analytic results similar to the case of isochronous synchronization. Furthermore, I show in detail the derivation of a rigorous condition for the coupling phase, under which all but one of the multistable states can be suppressed and thus a desired state can be deliberately selected.

Zusammenfassung

In dieser Arbeit untersuche ich Synchronisationszustände in Netzwerken aus Halbleiterlasern. Zwei wichtige Fragen stellen sich bei der Untersuchung von Synchronisation in diesen Netzwerken: (i) Welche Arten von Synchronisation können in einem bestimmten Netzwerk existieren und (ii) Sind diese Zustände stabil? Das Fundament für diese Untersuchungen ist durch die chaotische Dynamik gegeben, die Laser mit zeitverzögerter Kopplung zeigen können. Die Laser werden hierbei durch das etablierte Lang-Kobayashi-Modell modelliert. Das Hauptaugenmerk liegt hier in der Charakterisierung der Netzwerktopologien und Parameterbereiche, die die Entstehung bestimmter Synchronisationsmuster in solchen Netzwerken aus Halbleiterlasern beeinflussen.

Für chaotische Dynamik kann die Stabilitätsanalyse nur rein numerisch erfolgen. Daher beziehe ich ein weiteres Modell für die lokale Dynamik der Netzwerkknoten in meine Untersuchungen ein – den Stuart-Landau-Oszillator. Die entsprechenden nichtlinearen Gleichungen stellen eine Normalform für jegliche periodische Dynamik in der Nähe einer Hopf-Bifurkation dar. Die Frage der Stabilität der Synchronisation kann in diesem Modell mit Hilfe analytischer Gleichungen beantwortet werden. Weiterhin zeige ich die Ableitung von Bedingungen an die Kopplungsparameter, die es erlauben, gezielt bestimmte Synchronisationszustände auszuwählen und zu kontrollieren.

Im Zentrum der Stabilitätsanalyse steht die *Master stability function*, die auf [Pecora und Carroll](#) zurück geht. Dieser Formalismus erlaubt eine Abspaltung der Dynamik von der Topologie des Netzwerks, charakterisiert durch die Eigenwerte der entsprechenden Kopplungsmatrix. Ich erweitere diese Theorie für Netzwerke, in denen die Dynamik durch die zeitverzögerte Kopplung induziert wird. Die Anwendung auf Netzwerke mit zeitverzögerter Kopplung im Allgemeinen und auf Laser-Netzwerke und Netzwerke aus Oszillatoren im Speziellen werde ich detailliert darstellen. Für Laser-Netzwerke untersuche ich die Synchronisierbarkeit in verschiedenen Netzwerktopologien, von einfachen Netzwerkmotiven bis hin zu komplexen Zufalls-Netzwerken. Dabei werde ich ein Symmetrie-Argument benutzen, dass die Form der Master stability function für große Verzögerungszeiten vorhersagt.

Isochrone Synchronisation ist die bekannteste Art der Synchronisation. Ich zeige, dass bestimmte Topologien eine weitere Art der Synchronisation zeigen – Cluster-Synchronisation. Zum Verständnis dieser dynamischen Szenarien erweitere ich einen Formalismus von [Sorrentino und Ott](#), der eine Stabilitätsanalyse für Cluster-Synchronisation erlaubt. Dieser ursprüngliche Formalismus beinhaltet eine Beschränkung für die möglichen Topologien. Durch die Einführung mehrerer Kopplungsmatrizen hebe ich diese Beschränkung teilweise auf. Als Anwendung dieser Theorie zeige ich Ergebnisse für einfache hierarchische Netzwerke.

In Netzwerken aus Stuart-Landau-Oszillatoren können je nach Wahl der Kopplungsparameter mehrere verschiedene Cluster-Zustände gleichzeitig stabil sein. Ich erkläre diese Multistabilität an Hand analytischer Gleichung ähnlich wie im Fall isochroner Synchronisation. Außerdem zeige ich die Ableitung einer strengen Bedingung für die Kopplungsparameter, mit Hilfe dieser die Multistabilität unterdrückt und gezielt ein bestimmter Synchronisationszustand eingestellt werden kann.

Publications

- CHOE, C.-U., DAHMS, T., HÖVEL, P., AND SCHÖLL, E. (2010). *Controlling synchrony by delay coupling in networks: from in-phase to splay and cluster states*. Phys. Rev. E **81**, 025205(R).
- CHOE, C.-U., DAHMS, T., HÖVEL, P., AND SCHÖLL, E. (2011). *Control of synchrony by delay coupling in complex networks*. In *Proceedings of the Eighth AIMS International Conference on Dynamical Systems, Differential Equations and Applications*. In print.
- DAHMS, T., FLUNKERT, V., HENNEBERGER, F., HÖVEL, P., SCHIKORA, S., SCHÖLL, E., AND WÜNSCHE, H. J. (2010). *Noninvasive optical control of complex semiconductor laser dynamics*. Eur. Phys. J. ST **191**, 71.
- DAHMS, T., HÖVEL, P., AND SCHÖLL, E. (2007). *Control of unstable steady states by extended time-delayed feedback*. Phys. Rev. E **76**, 056201.
- DAHMS, T., HÖVEL, P., AND SCHÖLL, E. (2008). *Stabilizing continuous-wave output in semiconductor lasers by time-delayed feedback*. Phys. Rev. E **78**, 056213.
- DAHMS, T., LEHNERT, J., AND SCHÖLL, E. (2011). *Cluster and group synchronization in delay-coupled laser networks*. In preparation.
- FLUNKERT, V., YANCHUK, S., DAHMS, T., AND SCHÖLL, E. (2010). *Synchronizing distant nodes: a universal classification of networks*. Phys. Rev. Lett. **105**, 254101.
- HEINRICH, M., DAHMS, T., FLUNKERT, V., TEITSWORTH, S. W., AND SCHÖLL, E. (2010). *Symmetry breaking transitions in networks of nonlinear circuit elements*. New J. Phys. **12**, 113030.
- HÖVEL, P., DAHLEM, M. A., DAHMS, T., HILLER, G., AND SCHÖLL, E. (2009). *Time-delayed feedback control of delay-coupled neurosystems and lasers*. In *Preprints of the Second IFAC meeting related to analysis and control of chaotic systems (CHAOS09)*. World Scientific. (arXiv:0912.3395).
- LEHNERT, J., DAHMS, T., HÖVEL, P., AND SCHÖLL, E. (2011). *Loss of synchronization in complex neural networks with delay*. Submitted.

Contents

Abstract	5
Zusammenfassung	7
Publications	9
1. Introduction	25
I. Isochronous synchronization	33
2. Laser dynamics in networks	35
2.1. Dynamics in networks	36
2.1.1. Direct and pseudo-diffusive coupling	37
2.1.2. Coupling matrix and adjacency matrix	38
2.1.3. Self-feedback in the coupling matrix	39
2.1.4. Origin and role of coupling delays	40
2.1.5. Patterns of synchronization	41
2.1.6. Isochronous synchronization	41
2.1.7. The isochronous synchronization manifold	42
2.2. Semiconductor laser dynamics	43
2.2.1. Dynamical scenarios of a single laser subject to optical feedback	46
2.3. Quantifying the degree of chaos	50
2.3.1. Lyapunov exponents	51
2.3.2. Dimension of the chaotic attractor	54
2.4. Networks of lasers	54
2.4.1. Synchronous dynamics of lasers	56
2.5. Conclusion	57
3. Stability of synchronization in laser networks	59
3.1. Master stability function	59
3.2. Master stability function for delay-coupled networks	61
3.3. Master stability function for laser networks	66
3.3.1. The dependence on the delay time	68

3.4. Conclusion	70
4. Network motifs and regular networks	73
4.1. Weighted motifs with feedback	74
4.2. Two-node motifs	75
4.2.1. Example: motif no. 5	78
4.3. Three-node motifs	84
4.4. Where the master stability function fails	84
4.5. Regular networks	88
4.5.1. Unidirectionally coupled rings	88
4.5.2. Bidirectionally coupled rings	90
4.5.3. All-to-all coupling	93
4.5.4. Circulant matrices	96
4.5.5. Bidirectional linear chain	97
4.6. Conclusion	98
5. Complex networks	101
5.1. Erdős-Rényi random networks	101
5.1.1. A directed random graph	102
5.1.2. Meeting the unity row-sum condition	102
5.2. Network quantities	103
5.3. Subgraphs and the percolation threshold	106
5.4. The eigenvalue spectrum of random networks	108
5.5. Results for laser networks	111
5.6. The relation to motifs	112
5.7. Conclusion	113
6. Multiple coupling matrices	115
6.1. Multiple coupling contributions	115
6.2. Finding the eigenvalue pairs	117
6.3. Matrices that commute	118
6.4. Nearest and next-nearest neighbors	119
6.5. Master stability function for different delay times	119
6.6. The influence of the delay times	119
6.7. Conclusion	121
7. Control of synchronization in oscillator networks	123
7.1. The Stuart-Landau oscillator	123

7.2. Oscillator networks	125
7.2.1. Synchronous oscillator dynamics	126
7.3. Stability of in-phase synchronization	128
7.3.1. Obtaining the master stability function	129
7.3.2. Control of in-phase synchronization	136
7.3.3. Gerschgorin's circle theorem	139
7.3.4. Control of desynchronization	140
7.4. Robustness against parameter mismatch	141
7.5. Conclusion	142
 II. Cluster and group synchronization	 143
 8. Stability of cluster and group synchronization	 145
8.1. The network dynamics	145
8.2. Stability of the synchronous state for group synchronization	148
8.3. Allowed topologies	151
8.3.1. Groups coupled in a unidirectional ring structure	152
8.3.2. The ring is generic	153
8.3.3. Two groups having the same input	155
8.4. The spectrum of the coupling matrix	156
8.5. The symmetry of the master stability function	158
8.6. Cluster synchronization in laser networks	158
8.7. The relation of the number of clusters and the delay time	160
8.8. Application: two-cluster states in laser networks	161
8.8.1. Stability of the 2-cluster state	162
8.9. Bipartite random networks	165
8.10. Conclusion	168
 9. Beyond the one-block restriction	 169
9.1. The master stability function	169
9.2. A minimal example for groups	170
9.2.1. Cluster states in an all-to-all network?	173
9.2.2. A sufficient condition for the existence of a cluster state	174
9.3. Towards hierarchical networks	175
9.4. More than two clusters	180
9.5. Conclusion	181

10. Controlling cluster synchronization: an analytic approach	183
10.1. Cluster and splay states	185
10.1.1. Synchronous states	185
10.1.2. The unidirectionally coupled ring	188
10.2. Controlling and selecting cluster and splay states	191
10.3. Topologies allowing for cluster states	193
10.4. A generalized order parameter for cluster states	197
10.4.1. The Kuramoto order parameter	197
10.4.2. Identifying a two-cluster state	198
10.4.3. Higher-order cluster states	200
10.4.4. Example: Ring of 4 oscillators	201
10.5. Outlook: Nonidentical oscillators	206
10.6. Conclusion	209
11. Conclusion	211
11.1. Summary	211
11.2. Outlook	212
A. Invariance of eigenvalues in matrix products	215
A.1. Implications	215
Bibliography	217
Acknowledgments	235
Index	237

List of Figures

- 2.1. Schematic diagram of a semiconductor laser subject to optical feedback by an external cavity. τ denotes the traveling time of the light in the external cavity and K is the coupling strength, tuned by a neutral density filter. The phase differences φ and ϕ are introduced by the traveling time of the light between the external cavity and the laser diode and inside the external cavity, respectively. R denotes the reflectivity of the cavity mirrors. 45
- 2.2. (a) Bifurcation diagram of intensity maxima in dependence on the coupling (or feedback) strength σ for a semiconductor laser subject to optical feedback according to Eq. (2.12). Parameters: $p = 0.1$, $\alpha = 4$, $T = 200$, and $\tau = 1000$. The vertical dashed line at $\sigma = 0.12$ corresponds to the LFF regime according to Tab. 2.2. (b) Blow-up. 47
- 2.3. (a) Bifurcation diagram of intensity maxima in dependence on the coupling (or feedback) strength σ for a semiconductor laser subject to optical feedback according to Eq. (2.12). Parameters: $p = 1$, $\alpha = 4$, $T = 200$, and $\tau = 1000$. The vertical dashed line at $\sigma = 0.12$ corresponds to the CC regime according to Tab. 2.2. (b) Blow-up. 48
- 2.4. (a) Bifurcation diagram of intensity maxima in dependence on the delay time τ for a semiconductor laser subject to optical feedback according to Eq. (2.12). Parameters: $p = 0.1$, $\alpha = 4$, $T = 200$, and $\sigma = 0.12$. The vertical dashed line at $\tau = 1000$ corresponds to the LFF regime according to Tab. 2.2. (b) Blow-up. 50
- 2.5. (a) Bifurcation diagram of intensity maxima in dependence on the delay time τ for a semiconductor laser subject to optical feedback according to Eq. (2.12). Parameters: $p = 1$, $\alpha = 4$, $T = 200$, and $\sigma = 0.12$. The vertical dashed line at $\tau = 1000$ corresponds to the CC regime according to Tab. 2.2. (b) Blow-up. 51
- 2.6. Time series of a semiconductor laser according to Eq. (2.12). (a) Intensity $I = |E|^2$, (b) carrier inversion n . Parameters: $p = 0.1$, $\alpha = 4$, $T = 200$, $\tau = 1000$, and $\sigma = 0.12$ corresponding to the LFF regime. 52

2.7. Time series of a semiconductor laser according to Eq. (2.12). (a) Intensity $I = E ^2$, (b) carrier inversion n . Parameters: $p = 1$, $\alpha = 4$, $T = 200$, $\tau = 1000$, and $\sigma = 0.12$ corresponding to the CC regime.	53
2.8. Kaplan-Yorke dimension D_{KY} calculated from the Lyapunov spectrum of a single laser with delayed feedback according to Eq. (2.12) in dependence of the time delay τ . Blue: LFF regime ($p = 0.1$), green: CC regime ($p = 1$), red: $p = 10$. Other parameters as in Tab. 2.2.	55
3.1. Master stability function in the complex γ plane for a network of delay-coupled lasers according to Eq. (2.7). Parameters: (a) $p = 0.1$, $\sigma = 0.12$; (b) $p = 1$, $\sigma = 0.12$; (c) $p = 10$, $\sigma = 0.12$; (d) $p = 0.1$, $\sigma = 0.4$; (e) $p = 1$, $\sigma = 0.4$; (f) $p = 10$, $\sigma = 0.4$; other parameters as in Tab. 2.2. . . .	65
3.2. Master stability function Λ in dependence on the parameter $\text{Re } \gamma$. Blue: LFF regime ($p = 0.1$). Green: CC regime ($p = 1$) with other parameters given by Tab. 2.2. The vertical lines correspond to the location of the zero crossing.	67
3.3. Master stability function in the $(\text{Re } \gamma, \tau)$ plane for a network of delay-coupled lasers according to Eq. (2.7) with fixed $\text{Im } \gamma = 0$. Parameters as in Fig. 3.1.	69
3.4. Master stability function in the $(\text{Re } \gamma, \tau)$ plane for a network of delay-coupled lasers according to Eq. (2.7) with fixed $\text{Im } \gamma = 0$. Parameters: (a) $p = 0.1$, $\sigma = 0.12$; (b) $p = 1$, $\sigma = 0.12$; other parameters as as in Tab. 2.2.	70
3.5. Master stability function in the complex γ plane for a network of delay-coupled lasers according to Eq. (2.7). Parameters: (a) $p = 0.1$, $\tau = 1$; (b) $p = 0.11$, $\tau = 5$; (c) $p = 0.1$, $\tau = 20$; (d) $p = 1$, $\tau = 1$; (e) $p = 1$, $\tau = 5$; (f) $p = 1$, $\tau = 20$; other parameters as in Tab. 2.2.	71
4.1. Network motifs: all possible three-node connected subgraphs [reproduced from Milo et al., 2002].	74
4.2. Master stability function for a laser network operating in the LFF regime according to Tab. 2.2, see Fig. 3.1(a). Red dot: longitudinal eigenvalue $\gamma_1 = 1$, blue dot: transverse eigenvalue corresponding to motif no. 5 from Tab. 4.1 with $a = 0.83$	79
4.3. Synchronization diagrams from simulations of the network motif (4.1) with (a) $a = 0.95$, (b) $a = 0.83$, and (c) $a = 0.5$. Laser and coupling parameters chosen in the LFF regime according to Tab. 2.2.	80

4.4. Synchronization diagrams from simulations of the network motif (4.1) with (a) $a = 0.95$, (b) $a = 0.55$, and (c) $a = 0.5$. Laser and coupling parameters chosen in the CC regime according to Tab. 2.2.	81
4.5. Correlation of the intensities I_1 and I_2 of the two lasers in a simulation of motif no. 5, see Tab. 4.1 and Eq. (4.1).	83
4.6. Example motif in which synchronization cannot be described by the master stability function.	86
4.7. Synchronization diagrams I_1 vs. I_2 and I_2 vs. I_3 from numerical simulations of the network motif (4.9) with the laser model. Parameters chosen in the LFF regime according to Tab. 2.2.	87
4.8. Schematic view of 7 nodes coupled in a unidirectional ring structure without (left) and with feedback loops (right).	89
4.9. Master stability function for a laser network operating in the LFF regime according to Tab. 2.2, see Fig. 3.1(a). Red dot: longitudinal eigenvalue $\gamma_1 = 1$, green circle: location of transverse eigenvalues for unidirectional rings according to Eq. (4.12), green dots: transverse eigenvalues for a unidirectional ring with $N = 5$, blue circle: location of transverse eigenvalues for unidirectional rings with feedback according to Eq. (4.14), blue dots: transverse eigenvalues for a unidirectional ring with feedback with $N = 5$	90
4.10. Schematic view of 7 nodes coupled in a bidirectional ring structure without (left) and with feedback loops (right).	91
4.11. Master stability function for a laser network operating in the LFF regime according to Tab. 2.2, see Fig. 3.1(a). Red dot: longitudinal eigenvalue $\gamma_1 = 1$, green dots: transverse eigenvalues for a bidirectional ring according to Eq. (4.16) with $N = 5$, blue dots: transverse eigenvalues for a bidirectional ring with feedback according to Eq. (4.17) with $N = 5$	92
4.12. Synchronization diagrams for the bidirectionally ring of $N = 4$ coupled lasers. (a-f): Intensities I_1 vs. I_2 , I_2 vs. I_3 , I_3 vs. I_4 , I_1 vs. I_3 , I_2 vs. I_4 , and I_1 vs. I_4 , respectively. Parameters according to the LFF regime in Tab. 2.2.	93
4.13. Cross correlation in an all-to-all network corresponding to Eq. (4.20) in dependence on the number of nodes N . Blue and green dots correspond to the LFF and the CC regime according to Tab. 2.2. The vertical lines indicate the threshold to synchronization predicted by Eq. (4.22).	95
4.14. Schematic view of 7 nodes coupled in a bidirectional chain structure without (top) and with feedback loops (bottom).	97

- 4.15. Master stability function for a laser network operating in the LFF regime according to Tab. 2.2, see Fig. 3.1(a). Red dot: longitudinal eigenvalue $\gamma_1 = 1$, green dots: transverse eigenvalues for a bidirectional chain according to Eq. (4.28) with $N = 5$, blue dots: transverse eigenvalues for a bidirectional chain with feedback according to Eq. (4.30) with $N = 5$. Note that a green dot is covered by a blue one at $\gamma = 0$ 99
- 5.1. Scheme of a simple network with 5 nodes and 5 links for illustration of the network quantities [reproduced from Newman, 2003]. 103
- 5.2. Emergence of subgraphs in random graphs depending on the parameter z , which combines the link probability p and the number of nodes N as $p \sim N^z$. The values correspond to the threshold above which the respective subgraphs begin to emerge. [reproduced from Albert and Barabási, 2002]. 107
- 5.3. Master stability function in the γ plane for a network of delay-coupled lasers according to Eq. (2.7). (a-c) LFF regime, (d-f) CC regime according to Tab. 2.2. The blue dots show the eigenvalue spectra from a single realization of a directed random graph with link probabilities (a) $p = 0.2$, (b) $p = 0.5$, (c) $p = 0.95$, (d) $p = 0.2$, (e) $p = 0.5$, and (f) $p = 0.95$ 110
- 5.4. Mean cross correlation in a directed random network of $N = 30$ lasers in dependence on the link probability p . Blue: LFF regime; green: CC regime, according to Tab. 2.2. The blue and green lines correspond to the threshold of stability according to Eq. (5.16) for the LFF and the CC regime, respectively. 111
- 6.1. Master stability function in dependence on the parameters $\text{Re } \gamma^{(1)}$ and $\text{Re } \gamma^{(2)}$ of two coupling matrices for different values of the delay time $\tau^{(1)}$ and fixed $\text{Im } \gamma^{(1)} = \text{Im } \gamma^{(2)} = 0$. (a-f): $\tau^{(1)} = 250, 500, 750, 1000, 1500$, and 2000 , respectively. $\sigma^{(1)} = \sigma^{(2)} = \sigma/2$ with $\sigma = 0.12$, $\tau^{(2)} = 1000$ and other parameters in the LFF regime in Tab. 2.2. Red dot: longitudinal eigenvalue pair (1,1), red line: general location of eigenvalue pairs of matrices (6.4) and (6.5), green and blue dots: transversal eigenvalue pairs of matrices (6.4) and (6.5) for $N = 2$ and $N = 5$, respectively. . . . 120
- 7.1. (a) Subcritical and (b) supercritical Hopf bifurcation: Radius of oscillations and stability in dependence on the bifurcation parameter λ . Solid and dashed lines denote stable and unstable states, respectively. 125

7.2.	Schematic view of (a) in-phase, (b) two-cluster, and (c)-(d) splay states in a network with 4 oscillators. The phase differences are $\Delta\phi_0 = 0$, $\Delta\phi_2 = \pi$, $\Delta\phi_1 = \pi/2$, and $\Delta\phi_3 = 3\pi/2$ in panels (a), (b), (c), and (d), respectively, according to Eqs. (7.8) and (7.9).	128
7.3.	(a) Collective frequency Ω and (b) squared amplitude r_0^2 of in-phase oscillation vs. time delay τ for coupling strength $K = 0.3$ and phase $\beta = 0$. Blue and red curves correspond to physical and unphysical solutions, i.e., $r_0^2 \geq 0$ and < 0 , respectively. Parameters: $\lambda = 0.1$, $\omega = 1$, $\gamma = 0$	130
7.4.	(a) Collective frequency Ω and (b) squared amplitude r_0^2 of in-phase oscillation vs. time delay τ for coupling strength $K = 0.7$ and phase $\beta = 0$. Blue and red curves correspond to physical and unphysical solutions, i.e., $r_0^2 \geq 0$ and < 0 , respectively. Parameters: $\lambda = 0.1$, $\omega = 1$, $\gamma = 0$	131
7.5.	Master stability function for in-phase synchronization of Stuart-Landau oscillators in the $(\text{Re } \nu, \text{Im } \nu)$ -plane for $\beta = 0$ and different coupling strengths K and delay times τ . The color code corresponds to the largest real part of the Floquet exponents for a given value of the parameter ν . All eigenvalues of the coupling matrix \mathbf{G} of a unidirectional ring lie on the black circle. Parameters: (a) $K = 0.08$, $\tau = 3\pi/2$, (b) $K = 0.3$, $\tau = 3\pi/2$, (c) $K = 0.7$, $\tau = 3\pi/2$, (d) $K = 0.08$, $\tau = 2\pi$, (e) $K = 0.3$, $\tau = 2\pi$, (f) $K = 0.7$, $\tau = 2\pi$; others as in Fig. 7.3.	134
7.6.	Master stability function for in-phase synchronization of Stuart-Landau oscillators in the $(\text{Re } \nu, K)$ plane for fixed $\text{Im } \nu = 0$. (a) $\tau = 3\pi/2$, (b) $\tau = 2\pi$. Other parameters as in Fig. 7.5.	136
7.7.	Master stability function for in-phase synchronization of Stuart-Landau oscillators in the $(\text{Re } \nu, \beta)$ plane for fixed $\text{Im } \nu = 0$. Other parameters as in the respective panels of Fig. 7.5.	137
7.8.	(a) Collective frequency Ω and (b) squared amplitude r_0^2 of in-phase oscillation vs. time delay τ for coupling strength $K = 0.7$ and phase $\beta = \Omega\tau$. Parameters: $\lambda = 0.1$, $\omega = 1$, $\gamma = 0$	138
7.9.	Distribution of the relative phases $\theta = \varphi_i - \Theta$ around the order parameter (7.32) for 200 slightly nonidentical elements with different standard deviations σ_ω of the frequencies ω for $\beta = \Omega\tau$. Dotted (black) curve: $\beta = \Omega\tau + \pi$ (desynchronization). Other coupling parameters $\tau = 0.52\pi$, $K = 0.08$	141
8.1.	Bidirectionally coupled ring of 4 lasers in 2 groups, where the elements of group (1) and (2) are colored in blue and green, respectively. $\sigma^{(1)}$ and $\sigma^{(2)}$ and $\tau^{(1)}$ and $\tau^{(2)}$ denote the coupling strengths and the time delays for couplings from group (2) to (1) and (1) to (2), respectively.	150

8.2. Master stability function in terms of the largest Lyapunov exponent Λ from Eq. (8.26) for $M = 1, 2, 3$, and 4 groups of delay-coupled lasers (2.17) in panels (a,e), (b,f), (c,g), and (d,h), respectively. Black stars mark the position of longitudinal eigenvalues. (a-d): $\tau^{(k)} = \tau = 1$, (e-h): $\tau^{(k)} = \tau = 1000$. $\sigma^{(k)} = \sigma = 0.12$. Other parameters chosen in the LFF regime according to Tab. 2.2.	159
8.3. Master stability function evaluated at $\gamma = 0$, which corresponds to stability of cluster synchronization in the bidirectionally coupled ring with $N = 4$, in dependence of the coupling strength $\sigma^{(1)}$ and coupling delay $\tau^{(1)}$. Other parameters are chosen in the LFF regime according to Tab. 2.2.	163
8.4. Cross correlations in a bidirectionally coupled ring of 4 nodes in dependence on the coupling strength $\sigma^{(1)}$ for fixed $\tau^{(1)} = 1000$. Blue: correlation in cluster (1), green: correlation in cluster (2), red: correlation of the whole network. Other parameters are chosen in the LFF regime according to Tab. 2.2.	164
8.5. Scheme of the partial synchronization that arises in the bidirectional ring of 4 lasers for low correlation inside group (1) according to Fig. 8.4. Elements of group (1) are colored in blue and red, elements of group (2) are green. $\sigma^{(1)}$ and $\sigma^{(2)}$ and $\tau^{(1)}$ and $\tau^{(2)}$ denote the coupling strengths and the time delays for couplings from group (2) to (1) and (1) to (2), respectively.	165
8.6. Master stability function in terms of largest Lyapunov exponent Λ from Eq. (8.26) for $M = 2$ groups of delay-coupled lasers (2.17). Parameters: $\tau^{(k)} = \tau = 1000$, $\sigma^{(k)} = \sigma = 0.12$, $T = 200$, $p = 1$, $\alpha = 4$, according to the CC regime in Tab. 2.2. Blue dots indicate the location of the eigenvalues of a directed bipartite random graph of $N = 30$ nodes with link probability $p = 0.4$, red dots show the longitudinal values $\gamma = \pm 1$	166
8.7. Mean cross correlations in a bipartite random network of $N = 30$ lasers in dependence on the link probability p . Blue: correlation inside the clusters, green: correlation in the whole network. Parameters are chosen in the CC regime according to Tab. 2.2.	167
9.1. Master stability function for two coupling matrices using the structures \mathbf{Q}_1 as in Eq. (9.4) and \mathbf{Q}_2 as in Eq. (9.5) with coupling strengths $\sigma_1^{(1)} = \sigma_2^{(1)} = \sigma_1^{(2)} = \sigma_2^{(2)} = \sigma/2$. Parameters chosen in the LFF regime according to Tab. 2.2. The pairs $(\text{Re } \gamma^{(1)}, \text{Re } \gamma^{(2)})$ plotted as blue dots correspond to eigenvalues of the matrices (9.4) and (9.5) using Eq. (9.11), i.e., an all-to-all network.	172

9.2. Scheme of a hierarchical structure [reproduced from Barabási and Oltvai, 2004].	176
9.3. Schematic view of a simple hierarchical network structure according to Eqs. (9.15) and (9.16) with 30 nodes. The two topological clusters are separated for illustration. Blue and red arrows correspond to links inside and between the clusters, respectively.	177
9.4. Master stability function for two commuting matrices with the structures \mathbf{Q}_1 as in Eq. (9.4) and \mathbf{Q}_2 as in Eq. (9.5) with coupling strengths $\sigma_1 = 0.05\sigma$ and $\sigma_2 = 0.95\sigma$. The pairs $(\text{Re } \gamma^{(1)}, \text{Re } \gamma^{(2)})$ plotted as blue dots correspond to eigenvalues of the hierarchical example with matrices (9.15) and (9.16) using a link probability $p = 0.5$ in the Erdős-Rényi graph (9.16).	178
9.5. Master stability function for two commuting matrices with the structures \mathbf{Q}_1 as in Eq. (9.4) and \mathbf{Q}_2 as in Eq. (9.5) in the $(\text{Re } \gamma^{(2)}, \sigma_1/\sigma)$ plane. The parameter $\text{Re } \gamma^{(2)}$ is fixed as unity and the coupling strength σ_2 arises as $\sigma - \sigma_1$. The dashed blue lines form the boundary of the parameter range where no 2-cluster exists. Parameters chosen in the LFF regime according to Tab. 2.2.	179
10.1. Schematic view of (a) in-phase, (b) two-cluster, and (c)-(d) splay states in a network with 4 oscillators. The phase differences are $\Delta\phi_0 = 0$, $\Delta\phi_2 = \pi$, $\Delta\phi_1 = \pi/2$, and $\Delta\phi_3 = 3\pi/2$ in panels (a), (b), (c), and (d), respectively, according to Eqs. (7.8) and (7.9).	184
10.2. Stability diagram of a unidirectional ring of $N = 4$ oscillators in the (K, τ) -plane ($\beta = 0$). Panels (a), (b), (c), and (d) show the domain of stability for in-phase ($m = 0$), splay state ($m = 1$), 2-cluster state ($m = 2$), and splay state ($m = 3$), respectively. White regions denote instability of the corresponding state.	190

10.3. (a) Stability diagram of a unidirectional ring of $N = 4$ oscillators in the (K, τ) -plane ($\beta = 0$). Solid, dash-dotted, dashed, and dotted boundaries correspond to a stability change of in-phase ($m = 0$), 2-cluster ($m = 2$), splay states with $m = 1$, and $m = 3$, respectively. The blue, red, green, and yellow regions denote multistability of one, two, three, and four of the above states. (b)-(e) Time series of the phase differences for a unidirectional ring of four slightly nonidentical oscillators: (b) $\beta = \Omega_0 \tau$, (c) $\Omega_1 \tau - \pi/2$, (d) $\Omega_2 \tau - \pi$, (e) $\Omega_3 \tau - 3\pi/2$, with $\Omega_0 = 1$, $\Omega_1 = 0.83903$, $\Omega_2 = 1$, and $\Omega_3 = 1.16097$. Black (blue), dark gray (red), and light gray (green) lines denote the differences $\varphi_2 - \varphi_1$, $\varphi_3 - \varphi_1$, and $\varphi_4 - \varphi_1$, respectively (in (b),(d) black (blue) is hidden behind light gray (green)). Parameters: $\lambda = 0.1$, $\gamma = 0$, $K = 3$, $\tau = 3\pi$, $\omega_1 = 0.99757$, $\omega_2 = 0.99098$, $\omega_3 = 1.01518$ and $\omega_4 = 0.99496$ [Choe et al., 2010].	192
10.4. Snapshot of the dynamics of two oscillators with different phase differences in between them. (a) $\varphi_2 - \varphi_1 = 0$, (b) $\varphi_2 - \varphi_1 = \pi/2$, and (c) $\varphi_2 - \varphi_1 = \pi$	199
10.5. Order parameters R (blue), R_2 (green), and r_2 (red) in dependence of the phase difference $\varphi_2 - \varphi_1$ for two oscillators. Dashed lines correspond to phase differences of 0 , $\pi/2$, and π , corresponding to Fig. 10.4(a), (b), and (c), respectively.	200
10.6. Order parameters R , r_2 , and r_4 for the unidirectionally coupled ring of 4 Stuart-Landau oscillators. Initial conditions are chosen as $r_k = \sqrt{\lambda}$, $\varphi_{k+1 \bmod 4} - \varphi_k = 0$, $k = 1, \dots, 4$, i.e., in an in-phase state.	202
10.7. Order parameters R , r_2 , and r_4 for the unidirectionally coupled ring of 4 Stuart-Landau oscillators. Initial conditions are chosen as $r_k = \sqrt{\lambda}$, $\varphi_{k+1 \bmod 4} - \varphi_k = 2\pi/2$, $k = 1, \dots, 4$, i.e., in the 2-cluster state.	203
10.8. Order parameters R , r_2 , and r_4 for the unidirectionally coupled ring of 4 Stuart-Landau oscillators. Initial conditions are chosen as $r_k = \sqrt{\lambda}$, $\varphi_{k+1 \bmod 4} - \varphi_k = 2\pi/4$, $k = 1, \dots, 4$, i.e., in a splay state.	204
10.9. Order parameters R , r_2 , and r_4 for the unidirectionally coupled ring of 4 Stuart-Landau oscillators. Initial conditions are chosen as $r_k = \sqrt{\lambda}$, $\varphi_{k+1 \bmod 4} - \varphi_k = -2\pi/4$, $k = 1, \dots, 4$, i.e., in a splay state.	205
10.10. Order parameters R , r_2 , and r_4 for a unidirectionally coupled ring of 4 Stuart-Landau oscillators with a coupling phase $\beta = \Omega\tau$. Initial conditions are chosen as $r_k = \sqrt{\lambda}$, $\varphi_{k+1 \bmod 4} - \varphi_k = 0$, $k = 1, \dots, 4$, i.e., in an in-phase state.	207

List of Tables

1.1. Structure of the thesis.	29
2.1. Relation of the variables, parameters and time scale in the dimensionless Lang-Kobayashi model to their dimensional counterparts.	44
2.2. Set of parameters used for the networks of semiconductor lasers unless explicitly noted different.	49
4.1. Two-node motifs allowing for an isochronous synchronization manifold. .	76
4.2. Two-node motifs: Stability conditions for the LFF and the CC regime according to Tab. 2.2.	77
4.3. Normalized coupling matrices and non-unity eigenvalues of selected mo- tifs depicted in Fig. 4.1.	85

1. Introduction

The scientific field of synchronization in coupled systems has evolved rapidly in the last decades [Strogatz and Stewart, 1993; Rosenblum et al., 1996; Brown and Rulkov, 1997; Pikovsky et al., 2001; Boccaletti et al., 2002; Mosekilde et al., 2002; Balanov et al., 2009]. Complete synchronization of coupled chaotic units [Pecora and Carroll, 1990; Kocarev and Parlitz, 1995; Pecora et al., 1997] as well as of oscillatory systems has been extensively studied [Earl and Strogatz, 2003; D’Huys et al., 2008; Sethia et al., 2008].

In parallel, the research on complex networks has evolved into a rapidly expanding field [Albert and Barabási, 2002; Barabási, 2002; Newman, 2003; Newman et al., 2006; Boccaletti et al., 2006]. The models of random graphs [Erdős and Rényi, 1959, 1960], scale-free networks [Barabási and Bonabeau, 2003] and small-world networks [Watts and Strogatz, 1998] have been found to reproduce many of the properties of real network structures. On one hand, short paths in very large networks – while locally well-connected clusters still persist – are modeled in a reasonable way by the Watts and Strogatz small-world model, for example. On the other hand, the scale-free model by Barabási and Bonabeau [2003], which exhibits a power-law node-degree distribution, resembles the hub-like structures occurring in technological, structural networks, but also in networks of scientific collaborations [Newman, 2001a,b].

There have been attempts to merge the efforts in both areas of research. Synchronization has not only been studied in systems of a few coupled nodes, but also in complex networks [Pecora and Barahona, 2006], in particular in the Watts and Strogatz small-world network and in modifications of this network model [Barahona and Pecora, 2002; Lehnert et al., 2011]. While most work focused on time-independent topologies, Sorrentino and Ott [2008] studied synchronization in evolving complex networks. Network structure is usually characterized by nodes and links, where only the existence of links is considered, but not their strength. For the stability of synchronization it is, however, crucial to include the strength of the links in the analysis [Hwang et al., 2005; Chavez et al., 2005, 2006]. This is an important point that I will elaborate in this thesis.

Even more important than the weight of the links are delays in the couplings. Such delay times due to the physical length of the links and the corresponding signal propagating times have a significant impact on the dynamics in the network, but also on the stability of synchronization of this dynamics. Both periodic [D’Huys et al., 2008, 2011] and chaotic synchronization [Murphy et al., 2009, 2010] of small network motifs with delayed couplings have been studied. Again, applications to both coupled lasers [Flunkert et al., 2009] and neuronal systems [Vicente et al., 2009; Lehnert et al., 2011] have been made.

The ground-breaking work by Pecora and Carroll [1998]; Pecora [1998], in which they introduced the *master stability function*, opened up the field of complex networks for a simple analysis of stability of synchronization in these networks. The master stability function allows to separate the network dynamics from the network topology, where the latter is only needed in terms of the eigenvalue spectrum of the coupling matrix. It is worth noting that a similar theory was already developed by Fujisaka and Yamada in a series of papers [Fujisaka and Yamada, 1983; Yamada and Fujisaka, 1983, 1984; Fujisaka and Yamada, 1986], which did not result in a comparable impact in the community at that time. There has been an alternative approach by Restrepo et al. [2006], who used an order parameter to determine the threshold from desynchronization to synchronization. For globally coupled oscillatory systems with a large number of nodes, the Antonsen-Ott method has recently had much impact [Ott and Antonsen, 2008]. For the problem of synchronization, this method allows the reduction of the network dynamics to the evolution of a single order parameter.

Concerning possible applications, being able to securely transmit messages is a necessity in the age of digital and electronic communication. In the light of secure communication, the isochronous synchronization of coupled chaotic lasers has gained much interest in the last years [Fischer et al., 2000b; Heil et al., 2001; Peil et al., 2002; Heil et al., 2002; Mulet et al., 2004; Yang, 2004; Erzgräber et al., 2005; Argyris et al., 2005; Wünsche et al., 2005; Gross et al., 2006; Klein et al., 2006b; Vicente et al., 2007; Kinzel and Kanter, 2008; Kinzel et al., 2009, 2010; Englert et al., 2011]. An attacker would be unable to decode a message which is modulated on top of the chaotic signal that two mutually coupled lasers exchange. The degree of security that this scheme can potentially offer is still hard to quantify. An alternative public-channel scheme using filters has been introduced, which overcomes some of these uncertainties [Klein et al., 2005, 2006a; Kinzel and Kanter, 2008; Kanter et al., 2008b,a]. Also, multiple delays have been shown to increase the chaotic dimension and thus the degree of security [Zigzag et al., 2008, 2009; Englert et al., 2010, 2011].

Starting with few coupled lasers, identifying possible topologies of laser networks that

can show stable isochronous synchronization has been the subject of several researchers. Two lasers, for example, will only synchronize without a time lag when they are coupled via a relay or with additional feedback loops [Fischer et al., 2006; Vicente et al., 2008; Flunkert et al., 2009; D’Huys et al., 2011]. Even for stable synchronization and depending upon the dynamical regime in which the coupled lasers operate, the stability of synchronization may be disturbed by on-off intermittency or bubbling [Venkataramani et al., 1996a,b; Flunkert et al., 2009].

Regardless of the specific implementation or setup, the dynamics of the coupled lasers needs to be chaotic in order to allow applications in the area of secure communications. In semiconductor lasers, which emit continuous-wave constant intensity when they are uncoupled, this chaotic dynamics is induced by the delayed coupling between multiple lasers. In fact, the dynamics of coupled lasers resemble those of a single laser subject to delayed feedback, as I will also show in this thesis.

The dynamics of semiconductor lasers with feedback from an external mirror or an external cavity have been widely studied [Fischer et al., 1994; Heil et al., 1998; Krauskopf et al., 2000; Heil et al., 2000, 2003; Rottschäfer and Krauskopf, 2005; Radziunas et al., 2006; Tronciu et al., 2006; Rottschäfer and Krauskopf, 2007; Otto et al., 2010, 2012]. The effect of additional filters in the feedback loop was considered as well [Mandre et al., 2003; Green and Krauskopf, 2006; Erzgräber et al., 2006, 2007a,b; Erzgräber and Krauskopf, 2007]. Most of that work focused on the feedback-induced dynamical scenarios and bifurcation scenarios leading to complex dynamics. External feedback is also able to stabilize unstable dynamics in lasers [Schikora et al., 2006; Wünsche et al., 2008; Dahms et al., 2008; Schikora et al., 2008; Dahms et al., 2010; Schikora et al., 2011]. The theoretical basis for those studies has been founded by Pyragas [1992]. This *time-delay autosynchronization* (TDAS) has since then not only been used to control laser dynamics; for reviews see Schöll and Schuster [2008]; Just et al. [2010]; Schöll et al. [2010]; Hövel [2010]. It was believed to be impossible to stabilize a certain type of periodic orbits – odd-number orbits – by this control scheme, according to an alleged “theorem” proposed by Nakajima and Ueda [1998]. This so-called odd-number theorem has been refuted [Fiedler et al., 2007]. An experimental setup to stabilize odd-number orbits in laser dynamics has been proposed [Flunkert and Schöll, 2011b; Flunkert, 2010, 2011] and was realized experimentally [Schikora et al., 2011].

Experimental realization of laser networks with more than two lasers is still hard to set up. The reason is that the lengths of the optical pathways have to be tuned with meticulous precision such that the optical phases match at each laser. The influence of parameter mismatches and sub-wavelength phase dependency has been studied in detail by Hicke et al. [2011] and Flunkert and Schöll [2011a], respectively. In a very

recent work, [Reidler and Kanter \[2011\]](#) have found a setup which shows isochronous synchronization independently of this sub-wavelength tuning. A similar setup was already used by [Peil et al. in 2007](#). Another alternative approach originates from [Amann et al. \[2008\]](#), who exploit globally coupled multi-mode lasers to realize complex networks. In this setup, the modes in the lasers act as the nodes of the network, while the lasers themselves act as the links [[Osborne et al., 2009](#)]. Being optically globally coupled by one mirror, such a mode-coupled network of many lasers can resemble a variety of complex networks.

Isochronous synchronization is the most prominent type of synchronization in applications to coupled lasers. Other types of synchronizations include, for example, phase synchronization [[Aviad et al., 2008](#)] and generalized synchronization. In phase synchronization, only the suitably defined phases of the coupled systems but not their amplitudes are synchronized. This is particularly interesting in neural applications, where only the times when neurons spike are important but not the exact amplitudes. In generalized synchronization, coupled systems obey some – potentially nonlinear – functional dependence. This functional dependence is generally not easily disclosed by just looking at the dynamics of the nodes and by standard time-series analysis.

As yet another type of synchronization, I will study cluster synchronization in the second part of this thesis. In cluster synchronization, several clusters exist in the network, where all nodes in one cluster are synchronized while there is no synchronization between the different clusters. As a generalization, group synchronization can take place in networks where the local dynamics in different clusters or the coupling between clusters is non-identical [[Sorrentino and Ott, 2007](#)]. [Kestler et al. \[2007, 2008\]](#) have found rules for the topological structure of networks that allows for the existence of cluster – or sublattice – synchronization. Recently, an argument based on the greatest common divisor of the length of closed loops in networks has been shown to predict the existence of cluster states in chaotic [[Kanter et al., 2011b](#)] and neuronal networks [[Kanter et al., 2011a](#)].

As an extension of the work by [Pecora and Carroll \[1998\]](#), [Sorrentino and Ott \[2007\]](#) have introduced a method which allows for the calculation of a master stability function for cluster and group synchronization. I will use and extend this method in the second part of the thesis to study stability of cluster synchronization in laser networks.

This thesis will pick up a variety of the above mentioned topics of ongoing research. It will focus on dynamics in networks and stability of synchronization in these network using two different models. The major parts will deal with chaotic dynamics in networks of coupled semiconductor lasers modeled by the Lang-Kobayashi model [[Lang](#)

	<i>networks of semiconductor lasers</i>	<i>networks of Stuart-Landau oscillators</i>
Part I: Isochronous synchronization		
<i>Dynamical scenarios</i>	Chapter 2: Laser dynamics in networks	Chapter 7: Control of synchronization in oscillator networks
<i>Stability of isochronous synchronization</i>	Chapter 3: Stability of synchronization in laser networks	
<i>Examples</i>	Chapter 4: Network motifs and regular networks Chapter 5: Complex networks	
<i>Multiple coupling matrices</i>	Chapter 6: Multiple coupling matrices	–
Part II: Cluster and group synchronization		
<i>Stability of cluster and group states</i>	Chapter 8: Stability of cluster and group synchronization	Chapter 10: Controlling cluster synchronization: an analytic approach
<i>Control of cluster states</i>	–	
<i>Multiple coupling matrices</i>	Chapter 9: Beyond the one-block restriction	–

Table 1.1.: Structure of the thesis.

and Kobayashi, 1980]. The methods that I will use and develop – based on the master stability function – are valid for dynamics on networks with any kind of local dynamics. Considering periodic instead of chaotic dynamics, analytic results can be obtained based on Floquet theory. As other type of node dynamics I will therefore use periodic dynamics modeled by the Stuart-Landau oscillator, which arises as a generic normal form near any Hopf bifurcation. In addition to the plain study of stability of synchronization, I will show that the introduction of a phase in the coupling allows for selection and control of the desired state of synchronization.

This thesis is organized in two parts according to the patterns of synchronization that occur. See Tab. 1.1 for a schematic overview. Part I focuses on isochronous synchronization, which is also known as complete, zero-lag, or in-phase synchronization. Cluster and group synchronization will be the topic of Part II.

In Part I, Chapter 2 will introduce the dynamics in laser networks. I will demonstrate that lasers connected in a network with delayed coupling show the same dynamical scenarios as a single laser subject to feedback from an external cavity. In Chapter 3, I will introduce the *master stability function* with which the transverse stability of synchronization can be treated in an elegant way. The mathematical technique of this Chapter will be applied to small network motifs of lasers in Chapter 4 and to more complex networks in Chapter 5. The formalism will be extended to multiple coupling matrices and multiple delays in Chapter 6.

In Chapter 7 I will investigate networks of nodes exhibiting periodic dynamics using the Stuart-Landau model. With this model, the calculation of the master stability function is simplified to the solution of analytic equations. I will also show the effect of a coupling parameter – namely a coupling phase – on synchronization. Rigorous conditions for an optimal coupling phase can be derived under which synchronization can be achieved.

In Part II the concepts and methods of Part I will be used and extended to describe cluster synchronization in networks of both lasers and Stuart-Landau oscillators. In Chapter 8, I will derive a master stability function for cluster states, which is a generalization of the isochronous master stability function treated in Chapter 3. Examples of simple network motifs and more complex topologies showing cluster synchronization will be used to illustrate the results in this Chapter. In order to apply the master stability approach, a restriction to the coupling matrices is necessary. This restriction is partly overcome in Chapter 9, which introduces multiple coupling matrices for cluster synchronization and is as such the continuation of Chapter 6. Again, the results for Stuart-Landau oscillators can be obtained in an analytic fashion, which I will show in Chap-

ter 10. The role of the coupling phase gains additional importance here, as it will allow to deliberately select any one of several multistable cluster states.

I will conclude with a summary and review of all results in Chapter 11, which also includes an outlook on possible continuations of this work.

Part I.

Isochronous synchronization

2. Laser dynamics in networks

In this Chapter I will first introduce the dynamics on networks in a general form. According to the terminology of networks [Albert and Barabási, 2002; Newman, 2003; Boccaletti et al., 2006], a network is usually constructed of nodes – or vertices – on which in my case the dynamics takes place. These nodes are coupled via links – or edges – along which information is transmitted between nodes.

In order to study dynamics on networks, each node is described by a differential equation including coupling terms, which account for input from other nodes. Using this notion, I will discuss the different kinds of synchronization that may occur, including in-phase, time-lag, and group synchronization. Introducing a model for semiconductor laser dynamics, I will describe the dynamical scenarios that arise in the optically coupled laser network.

In general, models for the local dynamics of each node can be classified depending on the type of dynamics:

Chaotic dynamics is in this thesis achieved using the *Lang-Kobayashi* semiconductor laser model [Lang and Kobayashi, 1980]. While the isolated lasers emit continuous-wave (cw) output, coupling in the network may drive the dynamics into the chaotic regime similar to a laser with self-feedback. Chaotic dynamics are in general also given by, e.g., the Rössler or the Lorenz model [Rössler, 1976; Lorenz, 1963], but the focus in this thesis lies on chaotic dynamics that is induced only by the coupling. In this scope, the Lang-Kobayashi model is the paradigmatic choice.

Periodic dynamics is treated using the *Stuart-Landau* oscillator, i.e., the normal form of an oscillator near a Hopf bifurcation [Choe et al., 2010, 2011].

Excitable nodes which rest in a stable fixed point and are only showing spikes or oscillations when excited can be modeled by *FitzHugh-Nagumo* neurons [FitzHugh, 1961; Nagumo et al., 1962], *Hindmarsh-Rose* neurons [Hindmarsh and Rose,

1982; Dhamala et al., 2004], or the normal form of the *saddle-node infinite period bifurcation* (SNIPER) [Hu et al., 1993; Ditzinger et al., 1994; Hizanidis et al., 2008; Aust et al., 2010].

These respective models are of course only examples for the different kinds of dynamics. They are, however, the most generic and paradigmatic ones for each type. In this thesis I focus on chaotic and periodic dynamics using the Lang-Kobayashi and the Stuart-Landau model, respectively. In this Chapter I will introduce the dynamics on laser networks, while the periodic dynamics will be the topic of Chapter 7.

Although only induced by the coupling in the network, periodic dynamics will also occur in networks of excitatory nodes modeled by the FitzHugh-Nagumo system or the SNIPER normal form. Hence the results for periodic dynamics are valid for excitable nodes – to some degree – as well. Consequently, some of the results in this thesis allow insight into the dynamics of neural networks consisting of excitable nodes [Lehnert et al., 2011].

In the following Sec. 2.1, I will introduce the general notation of local dynamics, coupling matrices, and coupling schemes that forms the basis of the equations for dynamics on networks. I will show that the synchronized dynamics is similar to that of an isolated node with self-feedback. In Sec. 2.2 I will show the dynamical scenarios that arise in a single laser with self-feedback and proceed to laser dynamics on networks in Sec. 2.4.

2.1. Dynamics in networks

Consider a network of dynamical systems, where each of these follows a differential equation

$$\dot{\mathbf{x}}_i = \mathbf{F}_i[\mathbf{x}_i(t)], \quad (2.1)$$

where $\mathbf{x}_i \in \mathbb{R}^n$ is the state vector of each system and $\mathbf{F}_i[\mathbf{x}_i(t)]$ describes the local dynamical behavior of the node i , depending on the type of node used, i.e., on the model. Note that the local dynamics does not necessarily have to be identical for all nodes. However, for the most common types of synchronization it has to be identical.

The dynamics on an N -dimensional network is then described by

$$\dot{\mathbf{x}}_i = \mathbf{F}_i[\mathbf{x}_i(t)] + \sigma \sum_{j=1}^N G_{ij} \mathbf{H}_{ij} \mathbf{x}_j(t - \tau_{ij}), \quad i = 1, \dots, N. \quad (2.2)$$

Here, the $N \times N$ matrix \mathbf{G} describes the coupling topology in the network. If an entry G_{ij} is nonzero, then there is a link from node j to node i with strength G_{ij} . In the literature such a matrix is called *adjacency matrix* [Barabási, 2002; Newman et al., 2006; Newman, 2003; Boccaletti et al., 2006; Albert and Barabási, 2002], but only if the entries are either 0 or 1. However, I will generalize this notation and introduce \mathbf{G} as *coupling matrix* with elements $G_{ij} \in \mathbb{R}$. See Section 2.1.2 for a detailed explanation why weighted links are important for synchronization phenomena in networks.

The overall coupling strength in the network can be further scaled by the parameter σ . The $n \times n$ matrix \mathbf{H}_{ij} describes how the variables in two connected nodes interact. I will refer to this matrix as *coupling scheme* in the following. For instance, in a laser model with all-optical coupling, \mathbf{H}_{ij} will couple the electric field variables from one node to the same variables in the other node, possibly with a phase rotation. In an electro-optical coupling scheme, the electric field variables would couple into the carrier equations of the other node. In neural applications, \mathbf{H}_{ij} describes the interaction of inhibitor and activator variables, e.g., in the FitzHugh-Nagumo model. Especially in coupled neurons, the choice of this coupling schemes can influence synchronization [Hövel et al., 2009; Hövel, 2010]. As \mathbf{H}_{ij} may differ for each link in the network, different coupling schemes can be present at the same time. Note that a nonlinear function may be chosen instead of a matrix [Pecora and Carroll, 1998], but all examples shown in this thesis use a linear coupling function, which can be represented by a matrix. Finally, the time delay – denoted by τ_{ij} – accounts for delays due to the couplings and may as well be different for each link in the network. Before briefly summarizing why time delays are crucial in a majority of applications, I will cover the different coupling terms that may be used.

2.1.1. Direct and pseudo-diffusive coupling

In the network dynamics described by Eq. (2.2), the coupling happens in a “direct” way, i.e., the delayed variable $\mathbf{x}_j(t - \tau_{ij})$ of the j th node is added directly – after being weighted by $\sigma G_{ij} \mathbf{H}_{ij}$ – to the dynamics of the node i . This coupling scheme is motivated by the dynamics, e.g., of semiconductor lasers, as I will show in Sec. 2.2.

Another form of the coupling arises when looking at neuronal nodes in a network. Here, the effect that input from a node j has on node i is determined by a comparison of both variables. For example, a neuron i that has a membrane potential V_i and gets input V_j from another neuron will only see an effective input $V_j - V_i$, i.e., the voltage difference between the two nodes. In a spatio-temporal reaction-diffusion system, this corresponds to diffusive coupling. Without delay, the differences arise as discretization

of the Laplace operator. Translating this to network dynamics with discrete nodes, one ends up with network dynamics of the form

$$\dot{\mathbf{x}}_i = \mathbf{F}_i[\mathbf{x}_i(t)] + \sigma \sum_{j=1}^N G_{ij} \mathbf{H}_{ij} [\mathbf{x}_j(t - \tau_{ij}) - \mathbf{x}_i(t)], \quad i = 1, \dots, N, \quad (2.3)$$

where the delay is included in the contribution from the incoming nodes only, but not the node i itself, which is intuitively reasonable. This is also the form that I will use when studying networks of normal form oscillators in Chapters 7 and 10. For the application to neural networks with excitatory nodes see [Lehnert, 2010; Lehnert et al., 2011].

Introducing transformed local dynamics as

$$\tilde{\mathbf{F}}_i[\mathbf{x}_i(t)] = \mathbf{F}_i[\mathbf{x}_i(t)] - \sigma \sum_{j=1}^N G_{ij} \mathbf{H}_{ij} \mathbf{x}_i(t), \quad (2.4)$$

it becomes clear that Eq. (2.3) is equivalent to Eq. (2.2) using $\tilde{\mathbf{F}}_i$ as local dynamics in Eq. (2.2). In practice, I will use the form (2.3), e.g., in Chapters 7 and 10 dealing with networks of Stuart-Landau oscillators, but with this equivalence it is clear that the formulation of the master stability function that I will introduce in Chapter 3 is valid for both forms of network dynamics.

2.1.2. Coupling matrix and adjacency matrix

In the literature on complex networks [Barabási, 2002; Newman et al., 2006; Newman, 2003; Boccaletti et al., 2006; Albert and Barabási, 2002], the structure of a network is usually determined in terms of the existence of links only. In particular, there is no interest in the weights of the links. Network measures like betweenness, degree distribution, or clustering coefficient, do not use any information on the weight of individual links. For many applications, it is sufficient to describe the topology by an adjacency matrix \mathbf{A} whose entries are either zero or one. If a certain link $i \rightarrow j$ exists, the entry A_{ji} of the matrix is one, otherwise it is zero.

Unlike the papers and books cited above, the interest in this thesis lies on the dynamics on networks and synchronization of these dynamics. As can already be seen from Eq. (2.2), the dynamics in a network does depend on the individual entries in the coupling matrix \mathbf{G} . Its entries act like a coupling strength for each individual link. Reducing

this to the use of an adjacency matrix would only allow to treat networks where each link has the same strength.

However, from a coupling matrix \mathbf{G} , the corresponding adjacency matrix can be obtained by

$$A_{ij} = \Theta_0(G_{ij}) + \Theta_0(-G_{ij}), \quad (2.5)$$

where Θ_0 denotes the Heaviside function with $\Theta_0(0) = 0$. Conversely, for a network described by an adjacency matrix \mathbf{A} , the coupling matrix can be obtained by using an $N \times N$ weight matrix \mathbf{W} :

$$\mathbf{G} = \mathbf{W} \circ \mathbf{A}, \quad (2.6)$$

where \circ denotes the Hadamard product, which is also known as entrywise or Schur product and defined as $(\mathbf{A} \circ \mathbf{B})_{ij} = A_{ij}B_{ij}$ [Horn and Johnson, 1985]. Of course, if $A_{ij} = \Theta_0(W_{ij}) + \Theta_0(-W_{ij})$, the identity $\mathbf{W} = \mathbf{G}$ holds, but \mathbf{W} may for convenience contain more non-zero entries than \mathbf{A} and \mathbf{G} . Consider, for example, a power grid: Each transmission line connecting two nodes i and j gets a weight W_{ij} according to its possible transmission capacity. Cutting links from the network, \mathbf{W} stays intact, while the adjacency matrix \mathbf{A} and – following Eq. (2.6) – the coupling matrix \mathbf{G} is changed accounting for the missing link.

Several other notations of weighted coupling matrices exist, which are equivalent to the one shown here. See, for example, the work by Chavez et al. [2005, 2006], who used the load of the individual links – a property very similar to the link betweenness that I will introduce in Chapter 5 – to obtain a weight for each link.

In Chapter 5, where topology measures like the betweenness and degree distribution mentioned above will be introduced, I will mostly use Eq. (2.5) to derive an adjacency matrix from which these quantities are then calculated.

2.1.3. Self-feedback in the coupling matrix

In the definition of an adjacency matrix, the diagonal elements A_{ii} are usually zero, which is sufficient for topological properties. Feedback loops, i.e., $A_{ii} = 1$, would substantially complicate the calculation of network quantities. As an example consider the clustering coefficient, which uses the node degree and the number of neighbors of links. Should a node i be considered a neighbor of itself when $A_{ii} = 1$? Should A_{ii} contribute to the node degree of node i itself?

For the evolution of dynamics on networks, feedback loops play an important role for the stability of synchronization and cannot be neglected as I will show in Chapter 4. Consequently, concerning dynamics and stability of synchronization, I will therefore assume that adjacency matrices can contain diagonal elements. This leaves relations (2.5) and (2.6) intact.

2.1.4. Origin and role of coupling delays

Delays may arise naturally or may be introduced artificially in a variety of applications: In optical applications the finite light speed introduces a natural delay depending on the distance. Already in single lasers with feedback, delay plays a crucial role [Lang and Kobayashi, 1980]. The effect of time-delayed feedback on semiconductor lasers was investigated within Lang-Kobayashi (LK) type models [Simmendinger and Hess, 1996; Liu and Ohtsubo, 1997; Tronciu et al., 2006; Flunkert and Schöll, 2007; Fiedler et al., 2008; Dahms et al., 2008, 2010; Flunkert and Schöll, 2011b], as well as within more elaborate device models [Rogister et al., 1999; Simmendinger et al., 1999; Fischer et al., 2000a; Bauer et al., 2004; Ushakov et al., 2004; Ahlborn and Parlitz, 2006; Schikora et al., 2006; Otto et al., 2010, 2012] for various configurations, including Michelson interferometers providing a realization of *time-delay autosynchronization* (TDAS). TDAS is a simple and widely used feedback scheme introduced in 1992 by Pyragas. In particular, feedback-induced stationary external cavity modes and their bifurcations in a LK model for a laser subject to resonant feedback from a Fabry-Perot resonator were treated within the TDAS approximation [Tronciu et al., 2006].

In neural applications delays may arise naturally for three reasons:

- (i) Propagation delays due to finite distances between coupled neurons or regions of the cortex.
- (ii) Processing lags of neural activity.
- (iii) Neurovascular coupling.

While (ii) may lead to similar delays for all neurons considered, (i) and (iii) may introduce several nonidentical delays depending on the distance of any pair of neurons or regions of the cortex. Time delay may also come into account when controlling neural activity by external stimulation, as has been proposed to alleviate or cure neurological diseases such as Parkinson or migraine [Popovych et al., 2005b,a, 2006; Dahlem et al., 2008; Schneider et al., 2009].

Other systems in which delays may play an important role include electric circuits [Illing and Gauthier, 2006], electro-optical applications [Callan et al., 2010; Murphy et al., 2009], but also mechanical systems [Sieber et al., 2008; Blyuss et al., 2008; Kyrychko et al., 2009] or population dynamics [Haderler, 2008]. For a review see Just et al. [2010]. Also the area of chaos control has employed delay times in the scope of time-delayed feedback control [Schöll and Schuster, 2008].

In the following, conditions will be derived that lead to a synchronization manifold, i.e. synchronous solutions, of different types. These types include isochronous, time-lag, group, and generalized synchronization. This theoretical treatment is very similar regardless of the model used.

2.1.5. Patterns of synchronization

In a network described by the general Eq. (2.2), several types of synchronization may occur:

- (i) Isochronous or zero-lag synchronization
- (ii) Time-lag synchronization
- (iii) Group or cluster synchronization
- (iv) Generalized synchronization

In this first Part of the thesis I focus on case (i), where all nodes are completely synchronized. In Part II I will extend the theory to cluster synchronization (case (iii)). Time-lag synchronization (case (ii)) can occur as a special case of cluster synchronization.

2.1.6. Isochronous synchronization

For isochronous synchronization, both local dynamics and coupling contributions have to be identical for every node in the network in order for an invariant synchronization manifold to exist. This leads to several restrictions:

Identical local dynamics: $\mathbf{F}_i \equiv \mathbf{F}$ for $i = 1, \dots, N$. There have been studies on synchronization with parameter mismatch [Hicke et al., 2011], but the stability analysis using the master stability approach is only valid for identical local dynamics.

Identical time delays: $\tau_{ij} \equiv \tau$ for $i, j = 1, \dots, N$. Note that isochronous synchronization may also be present for different time delays, which will be investigated in Chapter 6, but the stability analysis shown in Chapter 3 relies on identical delays.

Constant row sum in the coupling matrix: $\sum_{j=1}^N G_{ij} = \text{const.}$ independently of $i = 1, \dots, N$. Since the overall coupling strength can be tuned using the parameter σ (see Eq. (2.2)), I will assume $\sum_{j=1}^N G_{ij} = 1$ without any loss of generality in the following. If the constant – or unity – row sum condition is not fulfilled, different nodes will be subject to different coupling signals even when synchronized. The synchronization manifold cannot be invariant in this case.

Identical coupling schemes: $H_{ij} \equiv H$ for $i, j = 1, \dots, N$. In the case of the phase rotation coupling scheme (2.21) that I will introduce for networks of lasers in Sec. 2.4, this implies that all phase differences are equal: $\phi_{ij} \equiv \phi$. Throughout this work I will use $\phi = 0$. This together with identical time delays and the constant row sum ensures that in a synchronized case all nodes get the same input.

Applying these restrictions to Eq. (2.2) yields the following equation governing the dynamics of the network's nodes:

$$\dot{\mathbf{x}}_i = \mathbf{F}[\mathbf{x}_i(t)] + \sigma \sum_{j=1}^N G_{ij} \mathbf{H} \mathbf{x}_j(t - \tau), \quad i = 1, \dots, N. \quad (2.7)$$

2.1.7. The isochronous synchronization manifold

The dynamics in the synchronization manifold can be found by setting $\mathbf{x}_i = \mathbf{x}_j \equiv \mathbf{x}_s$ for $i, j = 1, \dots, N$. In this case, Equation (2.7) becomes

$$\dot{\mathbf{x}}_s = \mathbf{F}[\mathbf{x}_s(t)] + \sigma \mathbf{H} \mathbf{x}_s(t - \tau). \quad (2.8)$$

Comparing this to Eq. (2.7), it is obvious that Eq. (2.8) is identical to the equation of a single node with a delayed feedback term.

In the following, I will illustrate this notion of network dynamics by introducing the model used for semiconductor laser networks. Before doing this, I make use of the fact that the dynamics on the synchronization manifold is identical to the dynamics of a single laser subject to delayed feedback and describe the scenarios that show up in such setups.

2.2. Semiconductor laser dynamics

In this Section I will review the Lang-Kobayashi model [Lang and Kobayashi, 1980], which describes a semiconductor laser subject to self-feedback, and discuss the dynamical scenarios of this system. In a network of lasers the synchronized dynamics is equivalent to this system, as discussed above.

Several models exist to describe laser dynamics, differentiating on one hand the different kinds of lasers, i.e., gas lasers, solid-state lasers, dye lasers, or semiconductor lasers. On the other hand, both the regime of operation and the required level of sophistication narrow the choice of an appropriate model. For a review see Lüdge [2011].

For semiconductor lasers subject to optical feedback, the model introduced by Lang and Kobayashi [1980] has become a de-facto standard model. This model, which is referred to as the *Lang-Kobayashi* model, is based on a rate equation model and includes as variables the carrier inversion n and the complex electric field E , which describes the slowly varying envelope of the field $\mathcal{E} = Ee^{i\omega_0 t}$.

The Lang-Kobayashi model in its dimensionless form [Alsing et al., 1996; Tronciu et al., 2006] reads

$$\begin{aligned} T \dot{n}(t) &= p - n(t) - [1 + n(t)] |E(t)|^2, \\ \dot{E}(t) &= \frac{1}{2}(1 + i\alpha)n(t)E(t) + E_b(t), \end{aligned} \quad (2.9)$$

where α denotes the linewidth enhancement factor, T is the time-scale ratio of the carrier lifetime and the photon lifetime, p is the reduced excess injection current, and $E_b(t)$ denotes the delayed feedback term, which will include a time delay τ due the light propagation time in the external cavity.

In this thesis I will not cover in detail the procedure that leads to this dimensionless form of the Lang-Kobayashi equations. Table 2.1 lists the laser properties that influence the parameters in the Lang-Kobayashi model and the corresponding relations. Note that the pump rate J is already normalized to be a rate per unit volume, i.e., it is the current density divided by the electronic charge and the thickness of the active layer and normalized to a unit volume [Lang and Kobayashi, 1980]. I refer the reader to the literature for a detailed survey of the derivation of the dimensionless model [Flunkert, 2007, 2010, 2011].

<i>laser property</i>	<i>symbol</i>	<i>typical magnitude</i>
carrier lifetime	τ_c	10^{-9} s
photon lifetime in the internal cavity	τ_p	10^{-11} s
threshold carrier density	N_{th}	10^7
threshold pump rate	$J_{th} = \frac{N_{th}}{\tau_c}$	10^{16} s^{-1}
pump rate (current density)	J	$1J_{th}, \dots, 100J_{th}$
differential gain	$G_N = \frac{\partial G}{\partial N}$	10^4 s^{-1}
<i>dimensionless parameter</i>	<i>definition</i>	
time-scale separation	$T = \frac{\tau_c}{\tau_p}$	
pump current	$p = \tau_p G_N N_{th} \left(\frac{J}{J_{th}} - 1 \right)$	
<i>dimensional dynamical variable</i>	<i>dimensionless variable</i>	
time scale s	$t = \frac{s}{\tau_p}$	
electric field $\mathcal{E}(s)$	$E(t) = \sqrt{\tau_c G_N} \mathcal{E}(s)$	
carrier inversion $N(s)$	$n(t) = \tau_p G_N [N(s) - N_{th}]$	

Table 2.1.: Relation of the variables, parameters and time scale in the dimensionless Lang-Kobayashi model to their dimensional counterparts.

While the Lang-Kobayashi model is well suited for a wide range of application, it has some limitations that arise as trade-offs for its simplicity:

- (i) As the model omits any spatial resolution of the laser device, it is restricted to situations where the external cavity is long in comparison to the length of the laser resonator. This is also needed to stay within the validity of the single-mode approximation with optical feedback [Tager and Elenkrig, 1993].
- (ii) The model assumes that the slowly varying envelope of the electric field in the laser does not change significantly during the traveling time in the external cavity. This is only valid for small feedback strength. Generalized models have been proposed to overcome this restriction [Kane and Shore, 2005].
- (iii) The model further assumes that the gain in the laser is not changed by the feedback. However, using strong feedback, which corresponds to strong injection, does not fulfill this condition. Again, small feedback strength is needed to stay within the validity of the model.

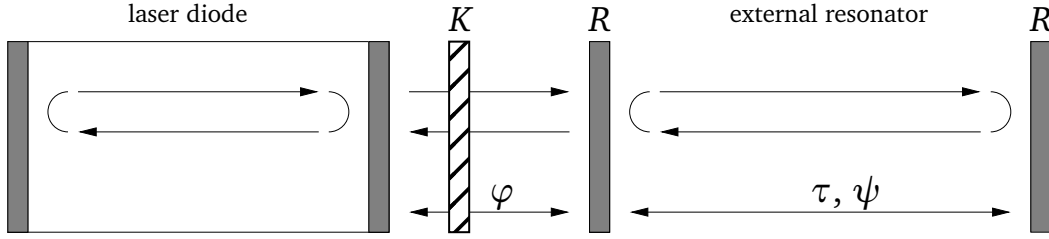


Figure 2.1.: Schematic diagram of a semiconductor laser subject to optical feedback by an external cavity. τ denotes the traveling time of the light in the external cavity and K is the coupling strength, tuned by a neutral density filter. The phase differences φ and ψ are introduced by the traveling time of the light between the external cavity and the laser diode and inside the external cavity, respectively. R denotes the reflectivity of the cavity mirrors.

As shown in Sec. 2.1.7, lasers that are coupled in a network may exhibit similar dynamics as a laser with self-feedback. In what follows, I will therefore introduce some dynamical scenarios that are known to occur in semiconductor lasers with an external cavity.

Figure 2.1 depicts schematically a laser diode with an external cavity. The delay time τ arises as the traveling time of the light in the external cavity. The influence of the reflectivity of the mirrors of the external cavity, the attenuator, and the distance between diode and external cavity are described by the parameters R , K , and φ , respectively. The latter is a phase difference that arises between the electric field of the light coming from the external cavity and the light in the laser. Phase differences in the external cavity itself can also be accounted for by an additional phase ψ . Using this scheme, the feedback term E_b in Eqs. (2.9) can be written as

$$E_b(t) = K e^{-i\varphi} \sum_{n=0}^{\infty} (R e^{i\psi})^n [e^{i\psi} E(t_{n+1}) - E(t_n)], \quad t_n = t - \tau - n\tau. \quad (2.10)$$

Let us assume that the phases φ and ψ can be considered zero. This can be achieved experimentally by tuning the positions of the mirrors very carefully [Dahms et al., 2010]. Let us further neglect multiple reflections in the external cavity, I consider only the contribution of the first round-trip in the cavity and neglect back reflections from the first mirror, which then corresponds to feedback from a single mirror only. These assumptions are valid in a wide range of applications [Tronciu et al., 2006] and lead to a simplified form of Eq. (2.10):

$$E_b(t) = \sigma E(t - \tau). \quad (2.11)$$

Here, the new feedback strength σ (corresponding to the coupling strength in networks) accounts for all contributions of the external cavity, namely a possible attenuator K and the reflectivity R . Given that there can be no gain in the external cavity, the coupling strength is bounded by $\sigma \in [0, 1]$.

2.2.1. Dynamical scenarios of a single laser subject to optical feedback

A semiconductor laser subject to optical feedback can exhibit different kinds of dynamics. Assuming that the solitary laser emits continuous-wave (cw), the following scenarios are possible when an external cavity is present:

Continuous-wave (cw): For small feedback strength the behavior will be unchanged and the laser still emits cw output. Increasing the coupling strength, the regime of external cavity modes (ECM) is reached. There, the laser still emits cw with constant intensity $I = |E|^2$, but the phase of the complex electric field is continuously rotating.

Periodic behavior: By increasing the feedback strength further, the laser may eventually undergo a bifurcation and exhibit a stable limit cycle, which corresponds to intensity pulsations.

Chaotic behavior: Going through a series of period doubling bifurcations [Hohl and Gavrielides, 1999] or by other mechanisms, the laser finally operates in a chaotic regime.

The type of dynamics I am interested in in this thesis is chaotic behavior. Recently, chaotic laser dynamics has gained much interest in the field of secure communication with chaos synchronization [Fischer et al., 2000b; Rogister et al., 2001; Heil et al., 2002; Yang, 2004; Argyris et al., 2005; Vicente et al., 2007; Kinzel and Kanter, 2008; Kinzel et al., 2010]. Different regimes of chaotic dynamics occur in semiconductor lasers; the most prominent are the *low-frequency fluctuations* (LFF) and the *coherence collapse* (CC) [van Tartwijk and Agrawal, 1998] regime. Depending on the parameters of the laser, e.g., the pump current p and the feedback parameters, namely feedback strength and delay time, the laser may be driven into one of these regimes. I will use the pump current p as a bifurcation parameter to distinguish the two regimes.

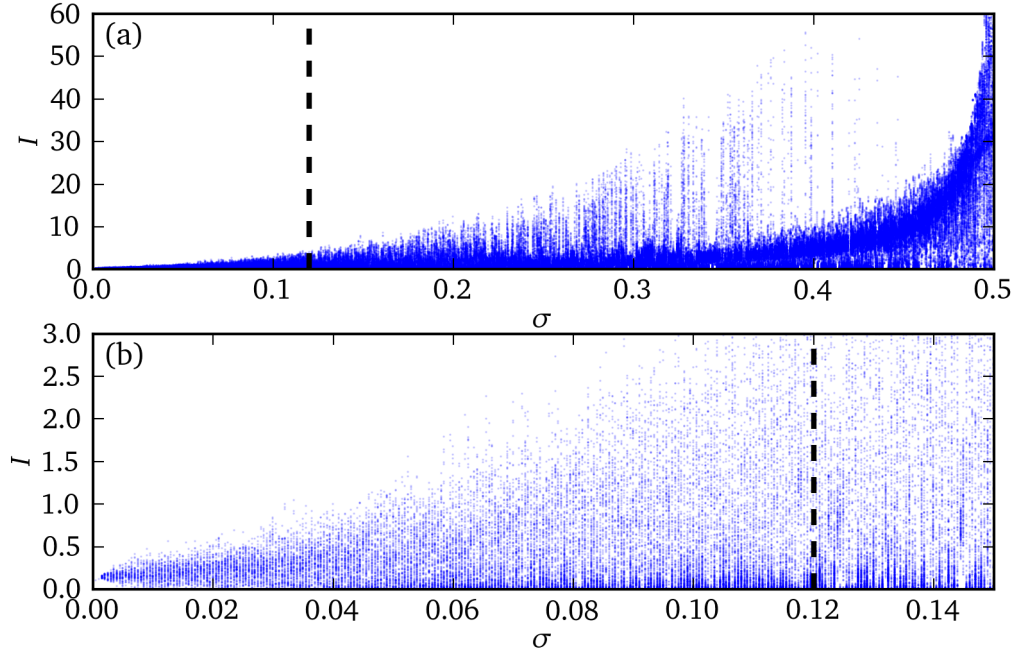


Figure 2.2.: (a) Bifurcation diagram of intensity maxima in dependence on the coupling (or feedback) strength σ for a semiconductor laser subject to optical feedback according to Eq. (2.12). Parameters: $p = 0.1$, $\alpha = 4$, $T = 200$, and $\tau = 1000$. The vertical dashed line at $\sigma = 0.12$ corresponds to the LFF regime according to Tab. 2.2. (b) Blow-up.

Adding an external cavity as above to one laser, the dynamical equations (2.9) become

$$\begin{aligned} T \dot{n}(t) &= p - n(t) - [1 + n(t)]|E(t)|^2, \\ \dot{E}(t) &= \frac{1}{2}(1 + i\alpha)n(t)E(t) + \sigma E(t - \tau). \end{aligned} \quad (2.12)$$

Figures 2.2 and 2.3 show the maxima of the intensity $I = |E|^2$ of a single laser governed by these equations for injection current $p = 0.1$ and $p = 1$, respectively. The other laser and coupling parameters are chosen as in Tab. 2.2. Panel (b) is a blow-up for small coupling strengths in both Figures. Overall, it can be seen that even for small coupling (or feedback) strength σ the laser departs from its fixed point at $I = p$ which corresponds to cw emission. For small values of the coupling strength, the intensity is

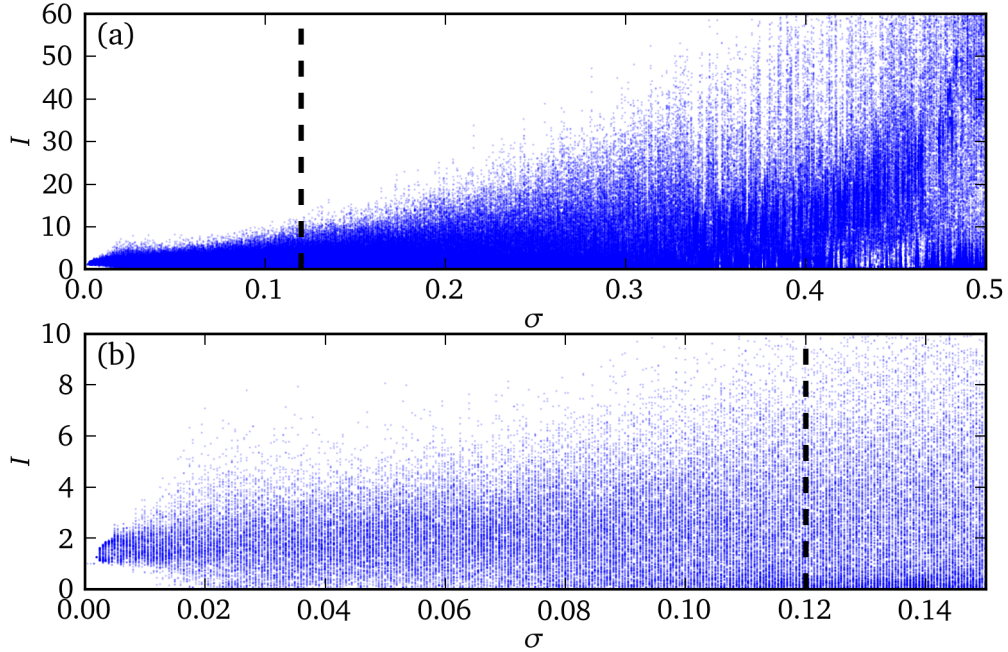


Figure 2.3.: (a) Bifurcation diagram of intensity maxima in dependence on the coupling (or feedback) strength σ for a semiconductor laser subject to optical feedback according to Eq. (2.12). Parameters: $p = 1$, $\alpha = 4$, $T = 200$, and $\tau = 1000$. The vertical dashed line at $\sigma = 0.12$ corresponds to the CC regime according to Tab. 2.2. (b) Blow-up.

comparatively higher for the higher injection current $p = 1$ in comparison to $p = 0.1$. The higher pump current leads to a larger degree of chaos for any of σ , which I will quantify using the Kaplan-Yorke dimension in Sec. 2.3.2. I will also show time series (Figs. 2.6 and 2.7) that reveal that the laser is operating in different regimes for these two injection currents $p = 0.1$ and $p = 1$. Note the explosion of the intensity for $\sigma \approx 0.5$ in Fig. 2.2. In this parameter range, the Lang-Kobayashi model loses its validity, because the input from the external cavity is no longer small in comparison to the field in the laser cavity. The explosion of the intensity can to some extent be limited by the introduction of a gain saturation term in the Lang-Kobayashi model [Agrawal, 1988]. Keeping the coupling strength at lower values, such extensions are not necessary in the scope of this thesis.

Figures 2.2 and 2.3 used a fixed time delay $\tau = 1000$. The chaos in the laser is only generated in the presence of delay, which is illustrated in Figs. 2.4 and 2.5 in bifurcation

<i>parameter</i>	<i>symbol</i>	<i>LFF regime</i>	<i>CC regime</i>
time-scale separation	T	200	200
linewidth enhancement factor	α	4	4
injection current	p	0.1	1
coupling strength	σ	0.12	0.12
coupling delay time	τ	1000	1000

Table 2.2.: Set of parameters used for the networks of semiconductor lasers unless explicitly noted different.

diagrams in dependence on the time delay τ for a fixed value of $\sigma = 0.12$. The injection current is again chosen as $p = 0.1$ and $p = 1$ in Fig. 2.4 and Fig. 2.5, respectively. Panel (b) is a blow-up for small delay times in both Figures. For vanishing time delay, i.e., $\tau = 0$, the laser rests in its fixed point in both cases. Increasing the time delay, a series of Hopf bifurcations take place, which leads to periodic dynamics first and then to chaotic dynamics through a cascade of period doublings [Hohl and Gavrielides, 1999]. The chaotic dynamics is interrupted by periodic windows which do no longer occur for large delay. For the higher pump current of $p = 1$ there is an abrupt change and the dynamics is qualitatively uniform from $\tau = 100$ onwards, while the periodic windows change in a more monotonous way for the lower pump current of $p = 0.1$.

To further illustrate the differences in dynamics depending on the injection current, Figs. 2.6 and 2.7 show time series of a laser according to Eq. (2.12) for fixed coupling strength $\sigma = 0.12$, delay time $\tau = 1000$, and injection current $p = 0.1$ and 1, respectively. These parameter choices are also marked by a dashed line in Figs. 2.2 and 2.4 for $p = 0.1$ and in Figs. 2.3 and 2.5 for $p = 1$. For the lower injection current of $p = 0.1$ the laser operates in the LFF regime, whereas the higher current of $p = 1$ leads to the CC regime. The time series for the LFF regime shows significant power drop-outs with a frequency that is much lower than the time scale of the dynamics, hence the name low-frequency fluctuation regime. In contrast to that, no such low-frequency features are present in the dynamics of the CC regime.

These time series represent the dynamics that I will use for the study of the stability of synchronization in laser networks. I will refer to these two types as LFF and CC regime, respectively.

As I will show in Chapter 3, the stability of synchronization in laser networks does – qualitatively – not depend on the choice of the parameters T , α , and σ . The pump

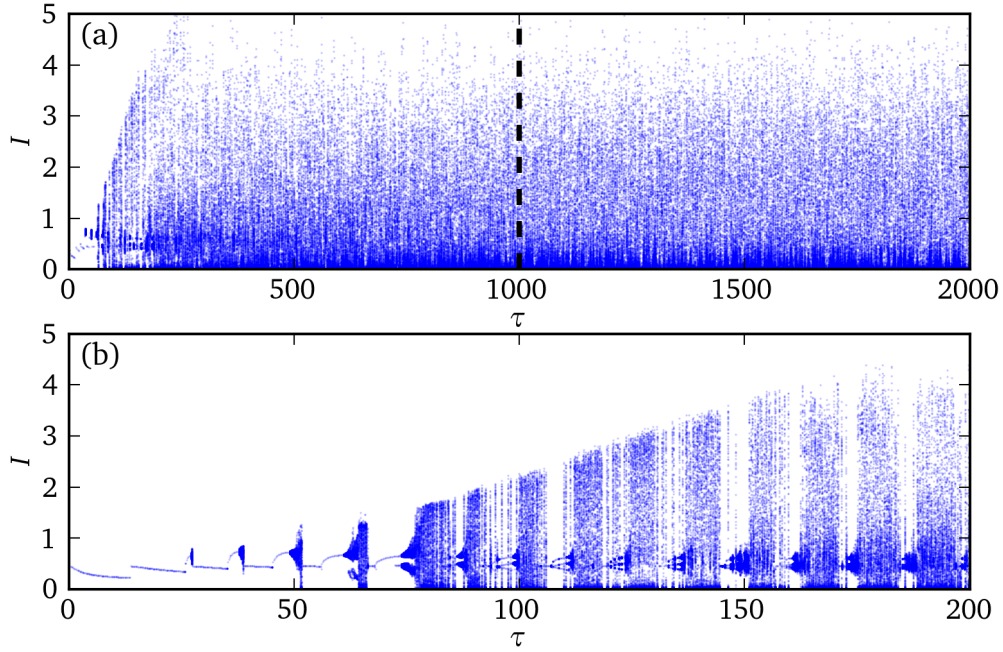


Figure 2.4.: (a) Bifurcation diagram of intensity maxima in dependence on the delay time τ for a semiconductor laser subject to optical feedback according to Eq. (2.12). Parameters: $p = 0.1$, $\alpha = 4$, $T = 200$, and $\sigma = 0.12$. The vertical dashed line at $\tau = 1000$ corresponds to the LFF regime according to Tab. 2.2. (b) Blow-up.

current influencing the regime of operation is the only crucial parameter. I will therefore choose the two sets of parameters given in Tab. 2.2.

2.3. Quantifying the degree of chaos

From the bifurcation diagrams and time series shown in the previous section, it becomes clear that a laser shows chaotic dynamics under the influence of delayed feedback or coupling. The degree of this chaos can be quantified by the largest Lyapunov exponent, which I will introduce in the following Section 2.3.1. This largest Lyapunov exponent will also be important for the analysis of stability of synchronization in networks of lasers, which will be carried out in Chapter 3. Regarding the degree of chaos, the largest Lyapunov exponent alone is of limited relevance and I will introduce the Kaplan-Yorke dimension, which is a measure for the dimension of the chaotic dynamics, in

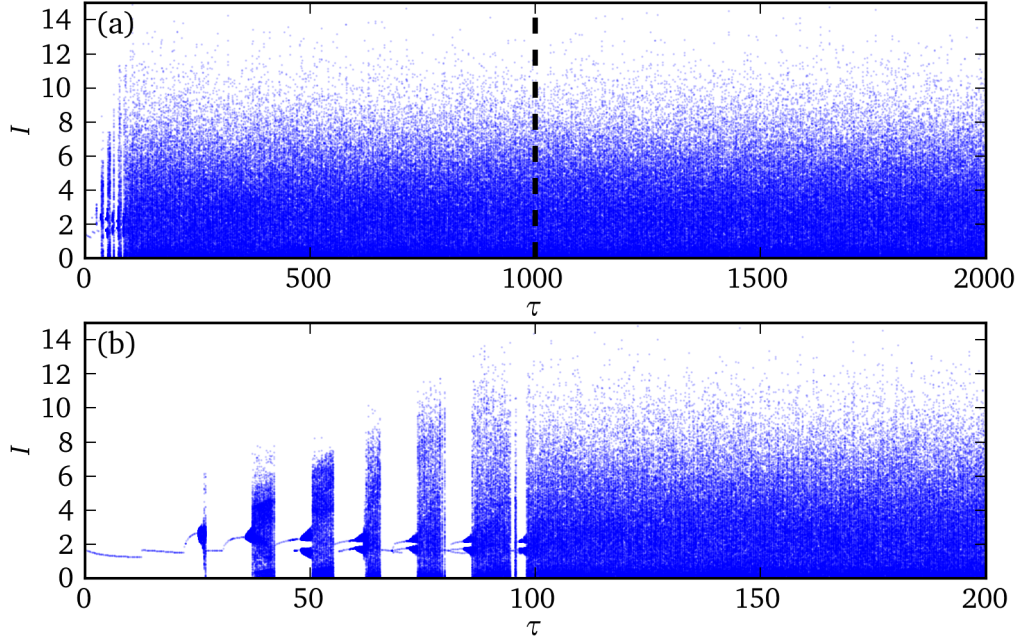


Figure 2.5.: (a) Bifurcation diagram of intensity maxima in dependence on the delay time τ for a semiconductor laser subject to optical feedback according to Eq. (2.12). Parameters: $p = 1$, $\alpha = 4$, $T = 200$, and $\sigma = 0.12$. The vertical dashed line at $\tau = 1000$ corresponds to the CC regime according to Tab. 2.2. (b) Blow-up.

Section 2.3.2. The Kaplan-Yorke dimension is based on the whole spectrum of Lyapunov exponents.

2.3.1. Lyapunov exponents

To determine if a trajectory is chaotic, the framework of Lyapunov exponents is widely used. A Lyapunov exponent characterizes the rate of separation between infinitesimally close trajectories. Instead of two trajectories, one usually considers the evolution of a variational equation, i.e., the dynamics of the linearized equation.

Let $\mathbf{x}_0(t)$ describe the trajectory of a dynamical system ($\mathbf{x}_0 \in \mathbb{R}^m$). A close-by trajectory $\mathbf{x}(t)$ is introduced by using a small variation $\delta\mathbf{x}(t)$:

$$\mathbf{x}(t) = \mathbf{x}_0(t) + \delta\mathbf{x}(t) \quad (2.13)$$

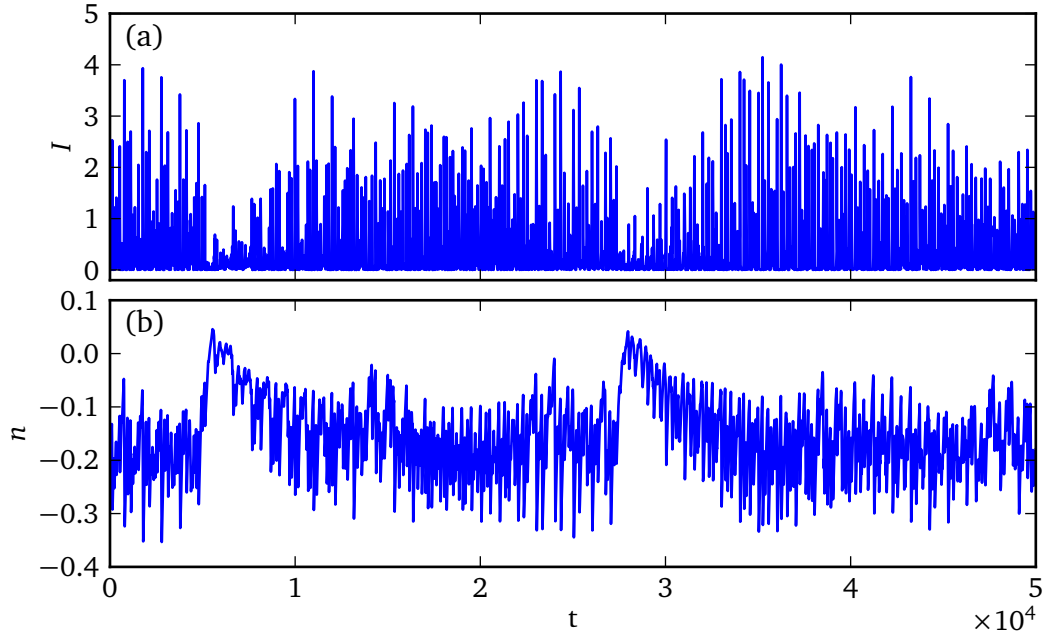


Figure 2.6.: Time series of a semiconductor laser according to Eq. (2.12). (a) Intensity $I = |E|^2$, (b) carrier inversion n . Parameters: $p = 0.1$, $\alpha = 4$, $T = 200$, $\tau = 1000$, and $\sigma = 0.12$ corresponding to the LFF regime.

with an initial separation $\delta \mathbf{x}_0$. To measure the divergence or convergence of both trajectories, it suffices to follow the variation $\delta \mathbf{x}(t)$. The largest Lyapunov exponent Λ is then defined as

$$\Lambda = \lim_{t \rightarrow \infty} \frac{1}{t} \ln \frac{|\delta \mathbf{x}(t)|}{|\delta \mathbf{x}_0|}, \quad (2.14)$$

which uses the idea that in a linear regime the separation of two trajectories takes place exponentially:

$$|\delta \mathbf{x}(t)| = e^{\Lambda t} |\delta \mathbf{x}_0|. \quad (2.15)$$

Calculating the full Lyapunov spectrum, which consists of m exponents for an m -dimensional dynamical system, is a comparatively more complex task, which involves not only following a single separation vector but a set of m linearly independent vectors. These vectors evolve and the magnitudes yield the Lyapunov exponents. The procedure includes periodic orthogonalizations of the set of variational vectors.

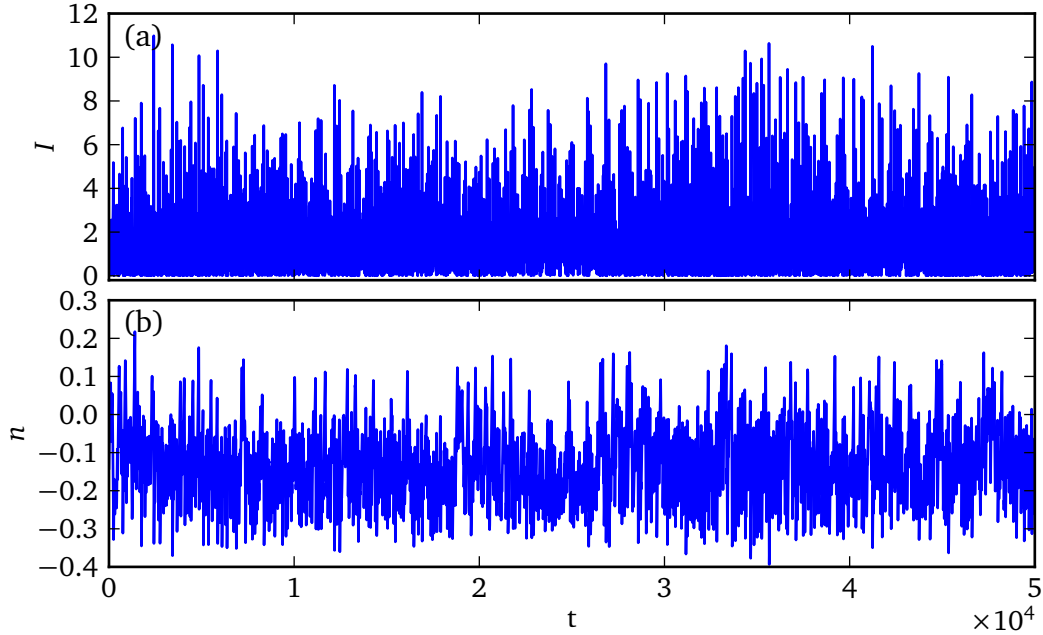


Figure 2.7.: Time series of a semiconductor laser according to Eq. (2.12). (a) Intensity $I = |E|^2$, (b) carrier inversion n . Parameters: $p = 1$, $\alpha = 4$, $T = 200$, $\tau = 1000$, and $\sigma = 0.12$ corresponding to the CC regime.

For delay-differential equations the phase space has dimension infinity, because the solution of such an equation is only uniquely determined by an initial condition covering an interval $(-\tau, 0]$. Then the Lyapunov spectrum theoretically consists of infinitely many exponents. For numerical applications, e.g., calculating the Kaplan-Yorke dimension as described in the following Section, it is sufficient to consider a subset of this spectrum.

The numerical procedure I use to calculate the spectrum follows the work by Farmer [1982] and involves a Gram-Schmidt orthonormalization scheme.

While the Lyapunov exponents as introduced here are a measure for the divergence of trajectories, they will also be used in Chapter 3 to determine the stability of synchronization. There, the concept of transverse Lyapunov exponents is used, where the reference trajectory evolves on the synchronization manifold and only directions transverse to this manifold are taken into account in the variational equations.

2.3.2. Dimension of the chaotic attractor

In the literature, several quantities exist that measure the degree of chaos. One of these is the Kaplan-Yorke dimension introduced by [Kaplan and Yorke \[1979\]](#), which will be used here as an exemplary measure. Given the ordered set of n Lyapunov exponents $\lambda_1 \geq \dots \geq \lambda_n$ of an n -dimensional dynamical system, the Kaplan-Yorke dimension is defined as

$$D_{KY} = k + \frac{\sum_{i=1}^k \lambda_i}{|\lambda_{k+1}|}, \quad (2.16)$$

where k is the largest natural number for which the sum $\sum_{i=1}^k \lambda_i$ is positive.

Note that for the calculation of the Kaplan-Yorke dimension, only the largest Lyapunov exponents $\lambda_1, \dots, \lambda_{k+1}$ are needed. As time-delayed systems have infinitely many Lyapunov exponents, it is crucial that a finite number of them is sufficient to calculate the chaotic dimension.

Numerically calculating the Kaplan-Yorke dimension involves calculating the spectrum of Lyapunov exponents following a technique by [Farmer \[1982\]](#). This numerical outcome for the Kaplan-Yorke dimension is an upper bound for the actual dimension of the chaotic attractor [[Grassberger and Procaccia, 1984](#)].

Figure 2.8 shows numerical results for the Kaplan-Yorke dimension in dependence on the delay time τ for different values of the injection current p : The blue, green, and red lines correspond to $p = 0.1, 1$, and 10 , respectively. The Kaplan-Yorke dimension increases linearly with the time delay, where the slope is steeper for higher values of the pump current p . As explained above, the numerical calculation of D_{KY} is only an upper bound for the dimension of the chaotic attractor, but it is obvious that the dimension can be orders of magnitude above the dimension of chaotic systems without delay, i.e., Lorenz or Rössler oscillators [[Lorenz, 1963](#); [Rössler, 1976](#)]. The typical dimension of the chaotic attractor in the Lorenz model has been found to be $D_{KY} = 2.0584 \pm 0.0007$ with the standard parameters $R = 28$, $\sigma = 10$, and $b = 8/3$ [[Grassberger and Procaccia, 1984](#)]. For the Rössler model it is $D_{KY} = 2.0132$ with the common parameters $a = b = 0.2$ and $c = 5.7$ [[Sprott, 2003](#)].

2.4. Networks of lasers

As opposed to a single laser subject to optical feedback, the optical injection is realized by delayed coupling in a network of lasers. Thus, in order to write the dynamics of a

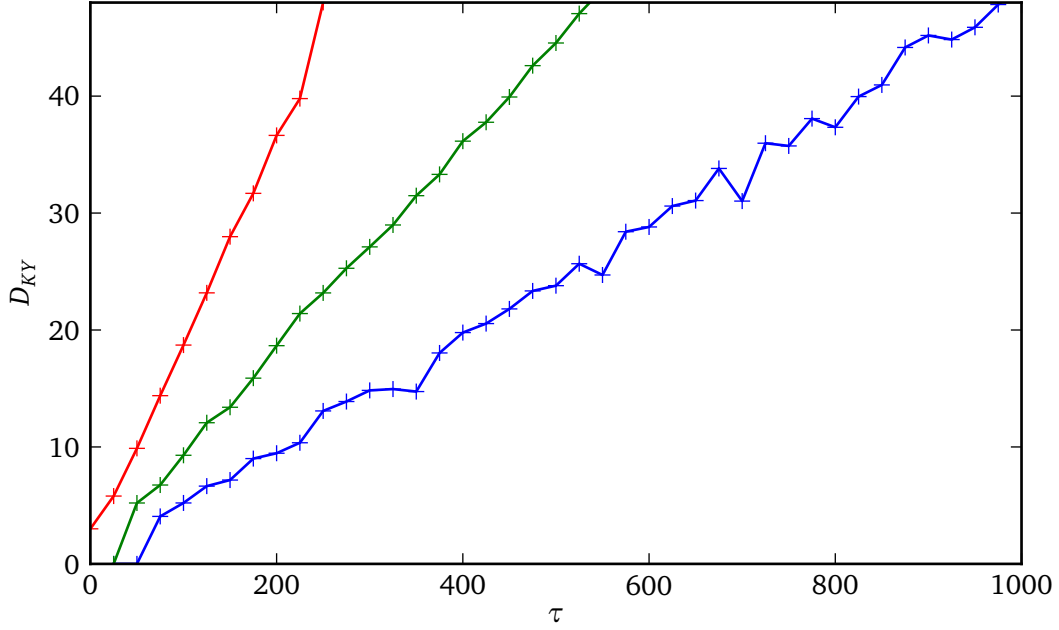


Figure 2.8.: Kaplan-Yorke dimension D_{KY} calculated from the Lyapunov spectrum of a single laser with delayed feedback according to Eq. (2.12) in dependence of the time delay τ . Blue: LFF regime ($p = 0.1$), green: CC regime ($p = 1$), red: $p = 10$. Other parameters as in Tab. 2.2.

laser network in the form of Eq. (2.2), two steps are needed:

- (i) Rewrite the Lang-Kobayashi model (2.9) in vector form.
- (ii) Account for coupling instead of feedback by removing the feedback term from the local dynamics and specify the coupling scheme \mathbf{H} to reflect all-optical coupling. The self-feedback is given by the diagonal elements of the coupling matrix \mathbf{G} .

With $\mathbf{x} = (n, x, y)^T$ and $E = x + iy$, the Lang-Kobayashi model (2.9) in vector form reads

$$\mathbf{F}(\mathbf{x}) = \begin{pmatrix} \frac{1}{T} \left[p - n - (1+n)(x^2 + y^2) \right] \\ \frac{n}{2}(x - \alpha y) \\ \frac{n}{2}(\alpha x + y) \end{pmatrix}. \quad (2.17)$$

Then the dynamics of a single laser – without any feedback or coupling – is described by

$$\dot{\mathbf{x}} = \mathbf{F}[\mathbf{x}(t)]. \quad (2.18)$$

The dynamics in a network consisting of N such systems and including coupling by a coupling matrix \mathbf{G} according to Eq. (2.7) is governed by

$$\dot{\mathbf{x}}_i = \mathbf{F}[\mathbf{x}_i(t)] + \sigma \sum_j G_{ij} \mathbf{H} \mathbf{x}_j(t - \tau). \quad (2.19)$$

The 3×3 matrix \mathbf{H} (coupling scheme) determines which channels are involved in the coupling. In its simplest form, where the light from laser j enters laser i without any phase difference, the coupling scheme reads

$$\mathbf{H} = \begin{pmatrix} 0 & 0 & 0 \\ 0 & 1 & 0 \\ 0 & 0 & 1 \end{pmatrix}. \quad (2.20)$$

Recall that the state vector describing the node dynamics reads $\mathbf{x} = (n, x, y)^T$. For the laser model, only the electric field variables x and y are involved in the coupling, resulting in the above \mathbf{H} for zero phase difference. A useful extension is the introduction of a phase rotation ϕ due to the coupling delay:

$$\mathbf{H} = \begin{pmatrix} 0 & 0 & 0 \\ 0 & \cos \phi & \sin \phi \\ 0 & -\sin \phi & \cos \phi \end{pmatrix}. \quad (2.21)$$

Note that here the same coupling phase is assumed for every coupling in the network. In general, the introduction of different phases prevents the existence of an isochronous synchronization manifold; see Sec. 2.1.6. However, under certain conditions, different phases may still lead to an invariant manifold, as has been shown for two coupled lasers by [Flunkert and Schöll \[2011a\]](#). Throughout this thesis, however, I will not consider phase shifts.

2.4.1. Synchronous dynamics of lasers

Using the model introduced above, networks of lasers can be described by Eq. (2.7).

The unity row sum condition stated in Sec. 2.1.6 can be narrowed down further for laser networks: If one does not allow for phase shifts introduced by the coupling matrix, the entries in the coupling matrix may not be negative. Such a matrix – having unity row sum and only non-negative entries – is known as *stochastic matrix* in the literature [Berman and Plemmons, 1979; Kirkland, 2005]. One particular property of stochastic matrices is the restriction that the eigenvalue spectrum is bound by the unit circle $S(0, 1)$ in the complex plane. This property is connected to Gerschgorin’s circle theorem [Gerschgorin, 1931], which allows for an estimate of a matrix’ eigenvalues and becomes important later in this thesis. See Sec. 7.3.3 on page 139 for a detailed explanation of Gerschgorin’s circle theorem.

2.5. Conclusion

Using the notion of local dynamics, coupling matrices and coupling schemes, I have shown that the dynamics of isochronously synchronized lasers is identical to the dynamics of a single laser subject to optical feedback. Concerning chaotic dynamics, the regimes of low-frequency fluctuations (LFF) and coherence collapse (CC) are most distinguishing and will be used in the following Chapters.

Opposed to a single laser, not only can the dynamics of the lasers change when varying the parameters of the laser and of the coupling, but also the transversal stability of their synchronization. I will describe how to calculate this transverse stability of synchronization in the next Chapter.

3. Stability of synchronization in laser networks

In the previous Chapter I found that dynamics on a network given by Eq. (2.7) can exhibit an invariant isochronous synchronization manifold under certain conditions, the most important of them being the constant – or, without loss of generality, unity – row sum of the coupling matrix: $\sum_{j=1}^N G_{ij} = 1$. The synchronous dynamics then follows Eq. (2.8):

$$\dot{\mathbf{x}}_s = \mathbf{F}[\mathbf{x}_s(t)] + \sigma \mathbf{H} \mathbf{x}_s(t - \tau), \quad (3.1)$$

with $\mathbf{x}_i = \mathbf{x}_j \equiv \mathbf{x}_s$ for $i, j = 1, \dots, N$.

3.1. Master stability function

In a straight forward manner, stability analysis of this synchronization manifold would be carried out by considering all possible variations perpendicular to the synchronization manifold given by Eq. (3.1) [Pecora et al., 1997; Flunkert et al., 2009]. In the space of the network – not accounting for the local dynamics of each node – there is a total of $N - 1$ linearly independent directions that are transversal to the synchronization manifold and one direction parallel to the synchronization manifold. If small perturbations in all of those $N - 1$ transversal directions die out – a property that can be expressed by Lyapunov exponents as we will see later – the synchronization manifold is transversely stable, i.e., the synchronous dynamics is stable. The behavior of perturbations inside the synchronization manifold does, on the other hand, characterize the type of synchronized dynamics, as I will show later.

This straight-forward scheme has some drawbacks:

- The directions transversal to the synchronization manifold do in general not coincide with the directions of the individual nodes. The set of perturbation vectors has to be found before the stability analysis.

- The set of perturbation vectors does depend on the coupling matrix \mathbf{G} . It has to be determined for each choice of a network topology.

In 1998, Pecora and Carroll introduced a formalism that works around both of these drawbacks. What they call *master stability function* is calculated as a continuous function $\Lambda(\alpha, \beta)$. The characteristics of the function is only determined by the local dynamics (cf. $\mathbf{F}(\mathbf{x})$ in Eq. (2.7)), while a given topology with a coupling matrix \mathbf{G} determines – through its eigenvalues γ_k ($k = 1, \dots, N$) – the values of α and β ($\alpha + i\beta = \sigma\gamma_k$) at which the master stability function needs to be evaluated. If the master stability function is negative at all of these eigenvalues, the synchronous dynamics is stable. In conclusion, the master stability function separates the local dynamics of the nodes from the topology of the network.

After briefly reviewing the original results by Pecora and Carroll, I present the extension that allows for the treatment of the dynamics considered in this thesis.

Pecora and Carroll considered instantaneous coupling, but otherwise identical network dynamics to Eq. (2.7):

$$\dot{\mathbf{x}}_i = \mathbf{F}[\mathbf{x}_i(t)] + \sigma \sum_{j=1}^N G_{ij} \mathbf{H} \mathbf{x}_j(t), \quad i = 1, \dots, N. \quad (3.2)$$

Further, they assumed the row sum of the coupling matrix \mathbf{G} to vanish: $\sum_{j=1}^N G_{ij} = 0$, corresponding to a synchronous dynamics

$$\dot{\mathbf{x}}_s = \mathbf{F}[\mathbf{x}_s(t)] \quad (3.3)$$

that is identical to the dynamics of an uncoupled node of the network. In other words, a coupling matrix with zero row sum does not alter the dynamics of the individual nodes when synchronized. In order to perform a stability analysis, perturbations $\delta \mathbf{x}_i(t)$ ($i = 1, \dots, N$) are introduced using the relation $\mathbf{x}_i(t) = \mathbf{x}_s(t) + \delta \mathbf{x}_i(t)$. Using these perturbations, variational equations can be obtained as

$$\delta \dot{\mathbf{x}}_i = D\mathbf{F}|_{\mathbf{x}_s(t)} \delta \mathbf{x}_i(t) + \sigma \sum_{j=1}^N G_{ij} \mathbf{H} \delta \mathbf{x}_j(t), \quad i = 1, \dots, N. \quad (3.4)$$

In their work they went on and showed that the set (3.4) of N equations can be diagonalized in the N -dimensional space of the network topology while leaving the local dynamics untouched, which results in another – now uncoupled – set of N equations:

$$\delta \dot{\tilde{\mathbf{x}}}_k = D\mathbf{F}|_{\mathbf{x}_s(t)} \delta \tilde{\mathbf{x}}_k(t) + \sigma \gamma_k \mathbf{H} \delta \tilde{\mathbf{x}}_k(t), \quad k = 1, \dots, N. \quad (3.5)$$

Here, $\{\gamma_k\}_{k=1,\dots,N}$ denotes the set of eigenvalues of the coupling matrix \mathbf{G} . The set of the $\delta\tilde{\mathbf{x}}_k$ is transformed from the set of $\delta\mathbf{x}_i$ according to the diagonalization of \mathbf{G} . Since these $\delta\tilde{\mathbf{x}}_k$ in Eq. (3.5) are uncoupled, they can be looked at separately, leading to the *master stability equation*

$$\delta\dot{\tilde{\mathbf{x}}} = D\mathbf{F}|_{\mathbf{x}_s(t)}\delta\tilde{\mathbf{x}}(t) + (\alpha + i\beta)\mathbf{H}\delta\tilde{\mathbf{x}}(t). \quad (3.6)$$

The master stability function $\Lambda(\alpha, \beta)$ is now given as the largest Lyapunov exponent determined by this equation in dependence on the parameters α and β . Other measures of trajectory divergence may be considered instead of the Lyapunov exponents; see, for example, Chapters 7 and 10 where I used Floquet exponents to determine stability of synchronization in networks of generic normal-form periodic oscillators.

One major condition for the coupling matrix \mathbf{G} arises by the diagonalization of Eq. (3.4): The matrix has to be diagonalizable. If, however, \mathbf{G} is not diagonalizable, Eq. (3.5) does not yield N linearly independent vectors for $k = 1, \dots, N$. An example will be shown in Sec. 4.4.

There have been other approaches to characterize stability of synchronization in networks, one of them is a method by Restrepo et al. [2006]. This method uses an order parameter to describe synchronous behavior in a network. This order parameter depends on the coupling matrix' entries as well as on the structure of the coupling term. A major drawback of this method is that it only works reliably for densely connected networks, i.e., high number of links for each node. As this condition is not met in most parts of this thesis, I will not make use of this method and focus on the master stability function.

In the following I will derive the master stability equation and master stability function for networks as used in this thesis. That is, networks with delay-coupling and non-zero – but still constant – row sum of the coupling matrix.

3.2. Master stability function for delay-coupled networks

Let us start with the network dynamics as in Eq. (2.7),

$$\dot{\mathbf{x}}_i = \mathbf{F}[\mathbf{x}_i(t)] + \sigma \sum_{j=1}^N G_{ij} \mathbf{H} \mathbf{x}_j(t - \tau), \quad i = 1, \dots, N, \quad (3.7)$$

which yields a synchronization manifold as Eq. (2.8):

$$\dot{\mathbf{x}}_s = \mathbf{F}[\mathbf{x}_s(t)] + \sigma \mathbf{H} \mathbf{x}_s(t - \tau). \quad (3.8)$$

Introducing $\mathbf{X} = [\mathbf{x}_1, \mathbf{x}_2, \dots, \mathbf{x}_N]$ and $\hat{\mathbf{F}}(\mathbf{X}) = [\mathbf{F}(\mathbf{x}_1), \mathbf{F}(\mathbf{x}_2), \dots, \mathbf{F}(\mathbf{x}_N)]$, Eq. (3.7) can be rewritten as

$$\dot{\mathbf{X}} = \hat{\mathbf{F}}[\mathbf{X}(t)] + \sigma [\mathbf{G} \otimes \mathbf{H}] \mathbf{X}(t - \tau), \quad (3.9)$$

where \otimes denotes the Kronecker product. In this notation, perturbations $\delta \mathbf{X}$ from the synchronous state can be expressed using $\mathbf{X} = \mathbf{X}_s + \delta \mathbf{X}$, where $\mathbf{X}_s = [\mathbf{x}_s, \mathbf{x}_s, \dots, \mathbf{x}_s]$. The perturbations then evolve according to

$$\delta \dot{\mathbf{X}} = D\hat{\mathbf{F}}|_{\mathbf{X}_s(t)} \delta \mathbf{X}(t) + \sigma (\mathbf{G} \otimes \mathbf{H}) \delta \mathbf{X}(t - \tau). \quad (3.10)$$

Note that in the original work by Pecora and Carroll, the coupling scheme \mathbf{H} was a general – potentially nonlinear – function. In that notation, the Jacobian $D\mathbf{H}$ of this function has to be used in the variational equation. Here, on the other hand, I use linear coupling schemes only, which can be expressed as a matrix \mathbf{H} . Consequently, the Jacobian of this linear function is identical to the matrix itself.

Now, in Eq. (3.10), it is clear that $D\hat{\mathbf{F}} = (\mathbf{1}_N \otimes D\mathbf{F})$ and thus

$$\delta \dot{\mathbf{X}} = (\mathbf{1}_N \otimes D\mathbf{F})|_{\mathbf{X}_s(t)} \delta \mathbf{X}(t) + \sigma (\mathbf{G} \otimes \mathbf{H}) \delta \mathbf{X}(t - \tau). \quad (3.11)$$

In order to arrive at a diagonalized form similar to Eq. (3.5), I assume there is a transformation \mathbf{S} such that $\text{diag } \mathbf{G} = \mathbf{S}^{-1} \mathbf{G} \mathbf{S}$, where $\text{diag } \mathbf{G}$ denotes the matrix that contains the eigenvalues of \mathbf{G} along its diagonal. Such a transformation does certainly exist if \mathbf{G} is diagonalizable. Multiplying Eq. (3.11) by $(\mathbf{S}^{-1} \otimes \mathbf{1}_m)$ from the left yields

$$(\mathbf{S}^{-1} \otimes \mathbf{1}_m) \delta \dot{\mathbf{X}} = (\mathbf{S}^{-1} \otimes \mathbf{1}_m) (\mathbf{1}_N \otimes D\mathbf{F})|_{\mathbf{X}_s(t)} \delta \mathbf{X}(t) + \sigma (\mathbf{S}^{-1} \otimes \mathbf{1}_m) (\mathbf{G} \otimes \mathbf{H}) \delta \mathbf{X}(t - \tau). \quad (3.12)$$

Using $(\mathbf{A} \otimes \mathbf{B})(\mathbf{C} \otimes \mathbf{D}) = \mathbf{AC} \otimes \mathbf{BD}$ with \mathbf{A} and \mathbf{C} and \mathbf{B} and \mathbf{D} having the same dimensions, respectively, and the fact that the identity matrices commute with all other matrices, this simplifies to

$$(\mathbf{S}^{-1} \otimes \mathbf{1}_m) \delta \dot{\mathbf{X}} = (\mathbf{1}_N \otimes D\mathbf{F})|_{\mathbf{X}_s(t)} (\mathbf{S}^{-1} \otimes \mathbf{1}_m) \delta \mathbf{X}(t) + \sigma (\mathbf{S}^{-1} \mathbf{G} \otimes \mathbf{H}) \delta \mathbf{X}(t - \tau). \quad (3.13)$$

One can always insert a unity; here I insert $\mathbf{S} \mathbf{S}^{-1}$:

$$(\mathbf{S}^{-1} \otimes \mathbf{1}_m) \delta \dot{\mathbf{X}} = (\mathbf{1}_N \otimes D\mathbf{F})|_{\mathbf{X}_s(t)} (\mathbf{S}^{-1} \otimes \mathbf{1}_m) \delta \mathbf{X}(t) + \sigma (\mathbf{S}^{-1} \mathbf{G} \mathbf{S} \mathbf{S}^{-1} \otimes \mathbf{H}) \delta \mathbf{X}(t - \tau), \quad (3.14)$$

which is – using $\mathbf{H} = \mathbf{H}\mathbf{1}_m$ – equivalent to

$$(\mathbf{S}^{-1} \otimes \mathbf{1}_m) \delta \dot{\mathbf{X}} = (\mathbf{1}_N \otimes D\mathbf{F})|_{\mathbf{x}_s(t)} (\mathbf{S}^{-1} \otimes \mathbf{1}_m) \delta \mathbf{X}(t) + \sigma (\mathbf{S}^{-1} \mathbf{G} \mathbf{S} \otimes \mathbf{H}) (\mathbf{S}^{-1} \otimes \mathbf{1}_m) \delta \mathbf{X}(t - \tau). \quad (3.15)$$

Using $\text{diag } \mathbf{G} = \mathbf{S}^{-1} \mathbf{G} \mathbf{S}$ and introducing the transformed vector as $\delta \bar{\mathbf{X}} = (\mathbf{S}^{-1} \otimes \mathbf{1}_m) \delta \mathbf{X}$, we end up with a block-diagonal variational equation

$$\delta \dot{\bar{\mathbf{X}}} = (\mathbf{1}_N \otimes D\mathbf{F})|_{\mathbf{x}_s(t)} \delta \bar{\mathbf{X}}(t) + \sigma (\text{diag } \mathbf{G} \otimes \mathbf{H}) \delta \bar{\mathbf{X}}(t - \tau). \quad (3.16)$$

Block-diagonal here means that the equation is diagonal in the N -dimensional space of the network and the m -dimensional space of each node dynamics is unchanged.

Now, splitting $\delta \bar{\mathbf{X}}$ into $\delta \bar{\mathbf{X}} = [\delta \bar{\mathbf{x}}_1, \delta \bar{\mathbf{x}}_2, \dots, \delta \bar{\mathbf{x}}_N]$ this becomes

$$\delta \dot{\bar{\mathbf{x}}}_k = D\mathbf{F}|_{\mathbf{x}_s(t)} \delta \bar{\mathbf{x}}_k(t) + \sigma \gamma_k \mathbf{H} \delta \bar{\mathbf{x}}_k(t - \tau), \quad k = 1, \dots, N, \quad (3.17)$$

where $\{\gamma_k\}_{k=1, \dots, N}$ denotes the eigenvalue spectrum of the coupling matrix \mathbf{G} , i.e., the entries of $\text{diag } \mathbf{G}$. These N equations differ only by these eigenvalues; for any network topology considered, a set of N equations arises.

With this in mind, Equation (3.17) can also be rewritten as

$$\delta \dot{\bar{\mathbf{x}}} = D\mathbf{F}|_{\mathbf{x}_s(t)} \delta \bar{\mathbf{x}}(t) + \sigma \gamma \mathbf{H} \delta \bar{\mathbf{x}}(t - \tau). \quad (3.18)$$

This is of course only equivalent to Eq. (3.17) if evaluated at the N different values of the complex parameter $\gamma = \gamma_k$, $k = 1, \dots, N$. Note that I use a notation that is different from Eq. (3.6), where $\alpha + i\beta = \sigma \gamma_k$ is introduced. As I will show in the following, for non-zero row sums, the master stability function depends on the coupling strength σ itself and it is therefore not needed to introduce a parameter that includes and effectively hides this coupling strength. It will turn out that a parameter $\gamma = \gamma_k$ is more convenient for the understanding of the effect different topologies have on stability of synchronization.

Equation (3.18) is generally referred to as the *master stability equation* [Pecora and Carroll, 1998]. The function $\Lambda(\gamma)$ of the largest Lyapunov exponents arising from Eq. (3.18) in dependence on the complex parameter γ is then called *master stability function*.

At this point the differences between the original master stability function developed by Pecora and Carroll and the one here become evident: From Eq. (3.18) it can already be seen that the time delay τ will also influence the master stability function. Additionally,

the coupling strength σ plays a subtle role. To see this, remember that DF is evaluated on the synchronous manifold \mathbf{x}_s . The synchronous dynamics \mathbf{x}_s was independent of the coupling parameters in the original paper by Pecora and Carroll due to the zero row sum of the coupling matrix (cf. Eq. (3.3)). Now, with a non-zero row sum, the synchronous dynamics does depend on the coupling parameters σ and τ (cf. Eq. (3.8)). In conclusion, the coupling strength has an implicit influence on the master stability function via the synchronous dynamics. Thus, the master stability function is a function of γ and the coupling parameters:

$$\Lambda = \Lambda(\gamma, \sigma, \tau). \quad (3.19)$$

One condition for the existence of the synchronization manifold was the constant row sum of the coupling matrix, which can be assumed to be unity without loss of generality. This condition $\sum_{j=1}^N G_{ij} = 1 \ \forall i = 1, \dots, N$ implies the existence of an eigenvalue $\gamma_1 = 1$ of \mathbf{G} with the corresponding eigenvector $\mathbf{v}_1 = (1, 1, \dots, 1)$. This can be easily seen by calculating $\gamma_1 \mathbf{v}_1 = \mathbf{G} \mathbf{v}_1$ which is obviously true for any matrix \mathbf{G} with unity row sum.

The structure of this eigenvector \mathbf{v}_1 reveals that it points into the direction of the dynamics of all nodes inside the synchronization manifold. Therefore, the eigenvalue γ_1 is not to be considered for the stability of synchronization, because the corresponding eigenvector is not transverse to the synchronization manifold. The master stability function evaluated at this eigenvalue, $\Lambda(\gamma_1)$, does, however, yield information about the type of dynamics on in the synchronized network. In fact, the master stability function yields the usual Lyapunov exponent according to Sec. 2.3.1:

$\Lambda(\gamma_1) < 0$: The synchronized nodes rest in a fixed point.

$\Lambda(\gamma_1) = 0$: The synchronized dynamics takes place on a periodic orbit.

$\Lambda(\gamma_1) > 0$: The synchronized dynamics is chaotic.

In the following I calculate the master stability function for networks of lasers. That is, I use Eqs. (2.17) as local dynamics and discuss the dependence of the master stability function on the parameters in the low-frequency fluctuation (LFF) and the coherence collapse (CC) regime according to Tab. 2.2, respectively.

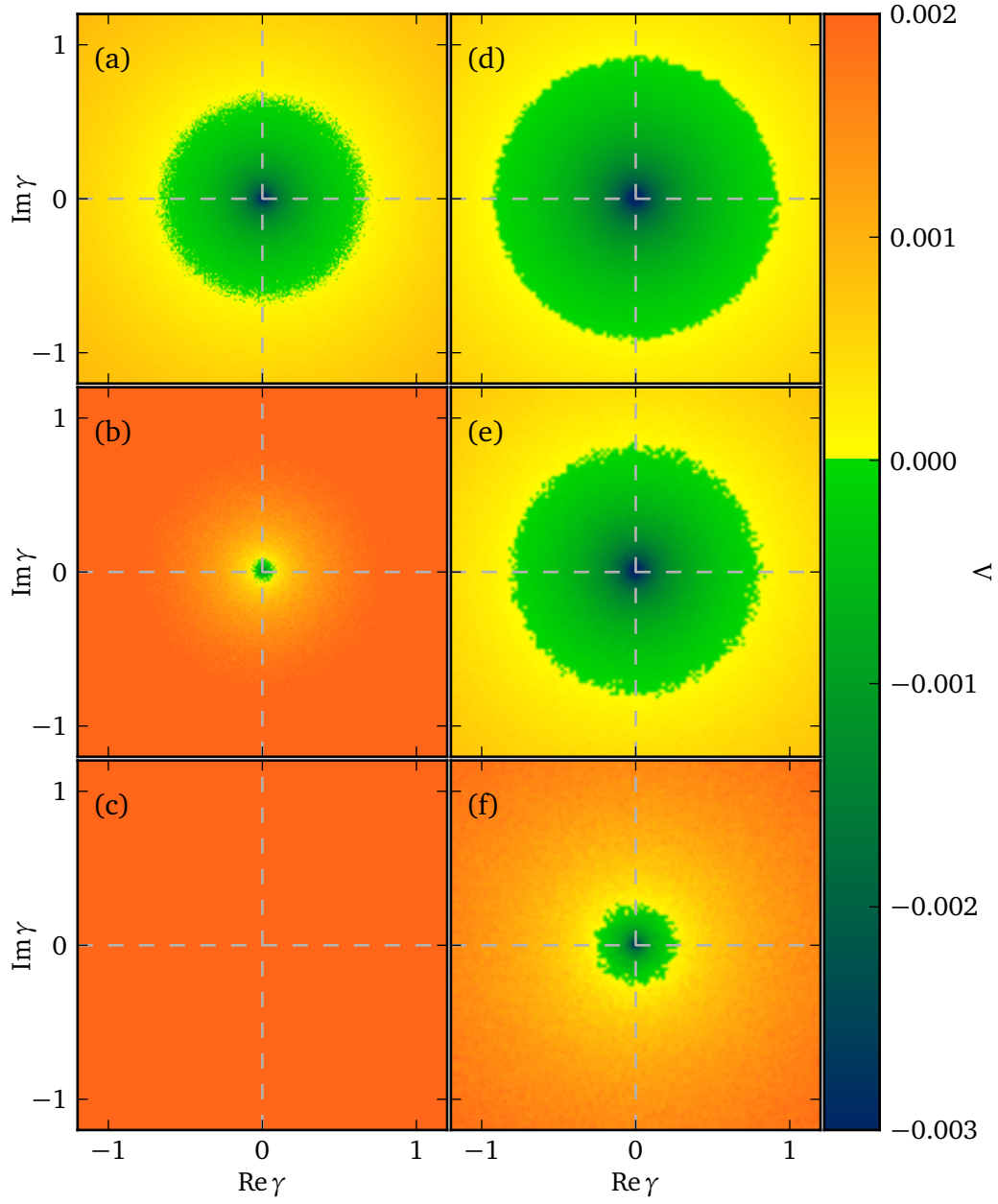


Figure 3.1.: Master stability function in the complex γ plane for a network of delay-coupled lasers according to Eq. (2.7). Parameters: (a) $p = 0.1$, $\sigma = 0.12$; (b) $p = 1$, $\sigma = 0.12$; (c) $p = 10$, $\sigma = 0.12$; (d) $p = 0.1$, $\sigma = 0.4$; (e) $p = 1$, $\sigma = 0.4$; (f) $p = 10$, $\sigma = 0.4$; other parameters as in Tab. 2.2.

3.3. Master stability function for laser networks

Figure 3.1 shows the master stability function in terms of the largest Lyapunov exponent Λ in dependence on the parameter γ for different choices of the injection current p and the coupling strength σ . In Figs. 3.1(a-c) the coupling strength is chosen as $\sigma = 0.12$, while it is $\sigma = 0.4$ in panels (d-f). The injection current is chosen as $p = 0.1$ in Fig. 3.1(a), where the laser operates in the LFF regime. In Fig. 3.1(b), on the other hand, the laser operates in the CC regime at $p = 1$. Figures 3.1(c) uses an even higher value of $p = 10$. Figs. 3.1(d-f) using the higher coupling strength $\sigma = 0.4$ also correspond to $p = 0.1, 1$, and 10 , respectively. The delay time is chosen as $\tau = 1000$.

One thing that becomes obvious is the circular shape of the master stability function in all panels of Fig. 3.1. This is a general feature for large delay, which we have proven recently [Flunkert et al., 2010]. The proof is valid only in the limit of $\tau \rightarrow \infty$, but the delay time of $\tau = 1000$ is already sufficiently large in comparison to the intrinsic system time scale to result in a circular shape: In the semiconductor the intrinsic time scale is given by the relaxation oscillations' period T_{RO} . This period is calculated as the imaginary part of the eigenvalue of the lasing fixed point in the uncoupled laser

$$T_{\text{RO}} = \frac{4\pi T}{\sqrt{p(4T - 2 - p) - 1}}. \quad (3.20)$$

For the LFF and CC regime, which use $p = 0.1$ and $p = 1$, respectively, I obtain $T_{\text{RO}} = 283.1$ and 89.1 , respectively. The value of $\tau = 1000$ used here is a factor 3 and 11 above this intrinsic time scale in the LFF and the CC regime, respectively.

In this limit of large delay, if the master stability function is negative in the origin ($\Lambda(\gamma = 0) < 0$), it increases monotonically with $|\gamma|$; see Fig. 3.1(a,b,d-f). Recently, it has been shown that this monotonic behavior follows a simple analytic equation [Englert et al., 2011] that allows to calculate the boundary of the stable region of the master stability function from the longitudinal Lyapunov exponent $\Lambda(\gamma = 1)$:

$$\gamma_b = e^{-\Lambda(\gamma=1)\tau}, \quad (3.21)$$

where γ_b denotes the boundary of the stable region such that stability is obtained for $|\gamma| < \gamma_b$. In the work by Englert et al., that analytic formula has been proven to be exact for the Bernoulli map, but works reasonably well also for networks of lasers modeled by the Lang-Kobayashi model.

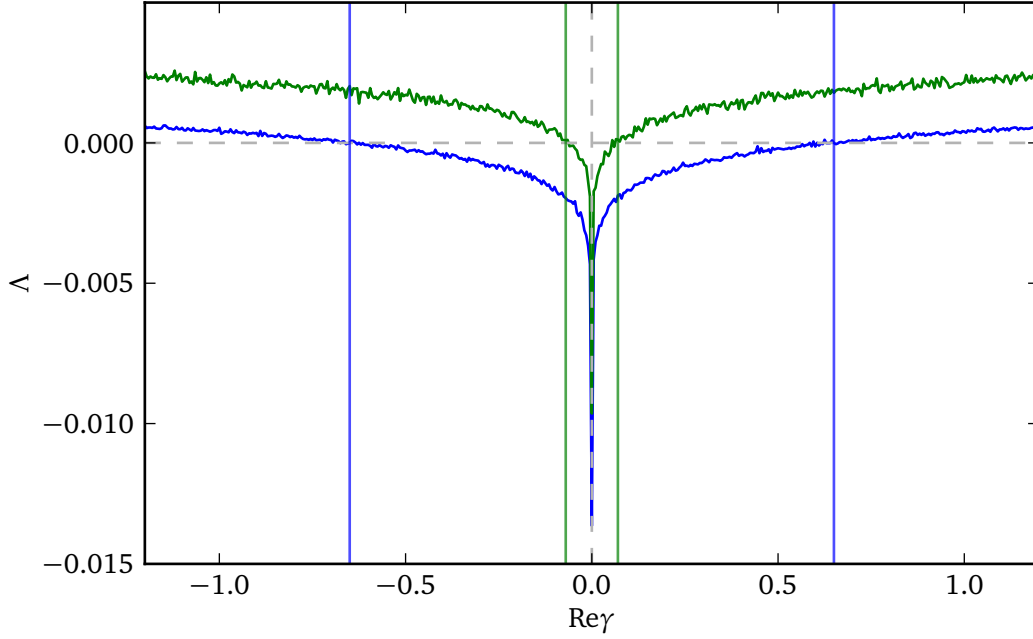


Figure 3.2.: Master stability function Λ in dependence on the parameter $\text{Re } \gamma$. Blue: LFF regime ($p = 0.1$). Green: CC regime ($p = 1$) with other parameters given by Tab. 2.2. The vertical lines correspond to the location of the zero crossing.

In conclusion, for large delay it is sufficient to consider the master stability function as a function of the absolute value $|\gamma|$ instead of γ itself.

Figure 3.2 shows a cross-section of Fig. 3.1 at $\text{Im } \gamma = 0$ for the parameters in the LFF and the CC regime according to Tab. 2.2 in blue and green colors, respectively. This corresponds to horizontal cuts in Figs. 3.1(a) and (b). Both curves are approximately identical with an offset. This is in line with the results by Englert et al.. As a result, the range of stability is much smaller for the CC regime compared to the LFF regime. The values of $\text{Re } \gamma$ where the master stability function changes sign are indicated by vertical blue and green lines for the LFF and the CC regime, respectively. For the LFF regime these are at $\text{Re } \gamma = \pm 0.65$ and at $\text{Re } \gamma = \pm 0.07$ for the CC regime.

Another outcome of the work by Flunkert et al. [2010] explains Fig. 3.1(c): If the master stability function is positive in the origin ($\Lambda(\gamma = 0) > 0$), it remains constant for any value of γ . This corresponds to the uniform color code in this figure and is related to the notion of weak and strong chaos, which is still a topic of ongoing research

[Heiligenthal et al., 2011].

3.3.1. The dependence on the delay time

Using small delays is not relevant in the context of fiber-coupled lasers or open-space setups. It is, however, relevant in integrated structures; see, for example, [Argyris et al. \[2008\]](#). From a theoretical point of view, it is worth to investigate what changes for smaller delay times. Figure 3.3 shows master stability functions in dependence on $\text{Re } \gamma$ and the delay time τ for fixed $\text{Im } \gamma = 0$. The injection current p and the coupling strength σ correspond to the respective panels of Fig. 3.1.

For all parameter sets, the stable part of the master stability function is narrowed down with increasing delay time τ . Panel (c) shows stability only for very small values of the delay time. Finally, in panels (a) and (b) the deviation from the rotational symmetry discussed above can be observed for small values of τ . The master stability function has an irregular shape here.

Figures 3.4(a) and (b) show enlargements of Figs. 3.3(a) and (b) for the interval $\tau \in [0, 200]$. Note that whenever the boundary between green and yellow color is located at $\text{Re } \gamma = 1$, the dynamics inside the synchronization manifold are periodic or of fixed point type, because this is equivalent to $\Lambda(\gamma = 1) = 0$. Comparing these figures to Figs. 2.4 and 2.5, the alternating occurrence of periodic and chaotic dynamics is reproduced here. As seen before in Sec. 2.2.1, the higher pump current $p = 1$ leads to more robust chaotic dynamics – and therefore a symmetry in the master stability function – already at smaller values of the delay time. Note that in between the periodic windows, the shape of the master stability function is nearly rotationally symmetric, while this behavior is lost for slightly larger delay times. This suggests that not the period of the relaxation oscillation is the relevant time scale in the system, but another one that is induced by the delay and is changed in these alternating windows of periodic and chaotic dynamics.

Figure 3.5 shows cross sections in the full $(\text{Re } \gamma, \text{Im } \gamma)$ plane for different values of small delay times. Figures 3.5(a-c) and (d-f) use a pump current of $p = 0.1$ and 1 respectively. Panels (a,d), (d,e), and (c,f) correspond to delay times $\tau = 1, 5$, and 20, respectively. Again, it can be seen that the shape is irregular for very small delay, where it can change its shape drastically. But already for $\tau = 20$ one can observe the transition to the circular shape that is reached for large delay times.

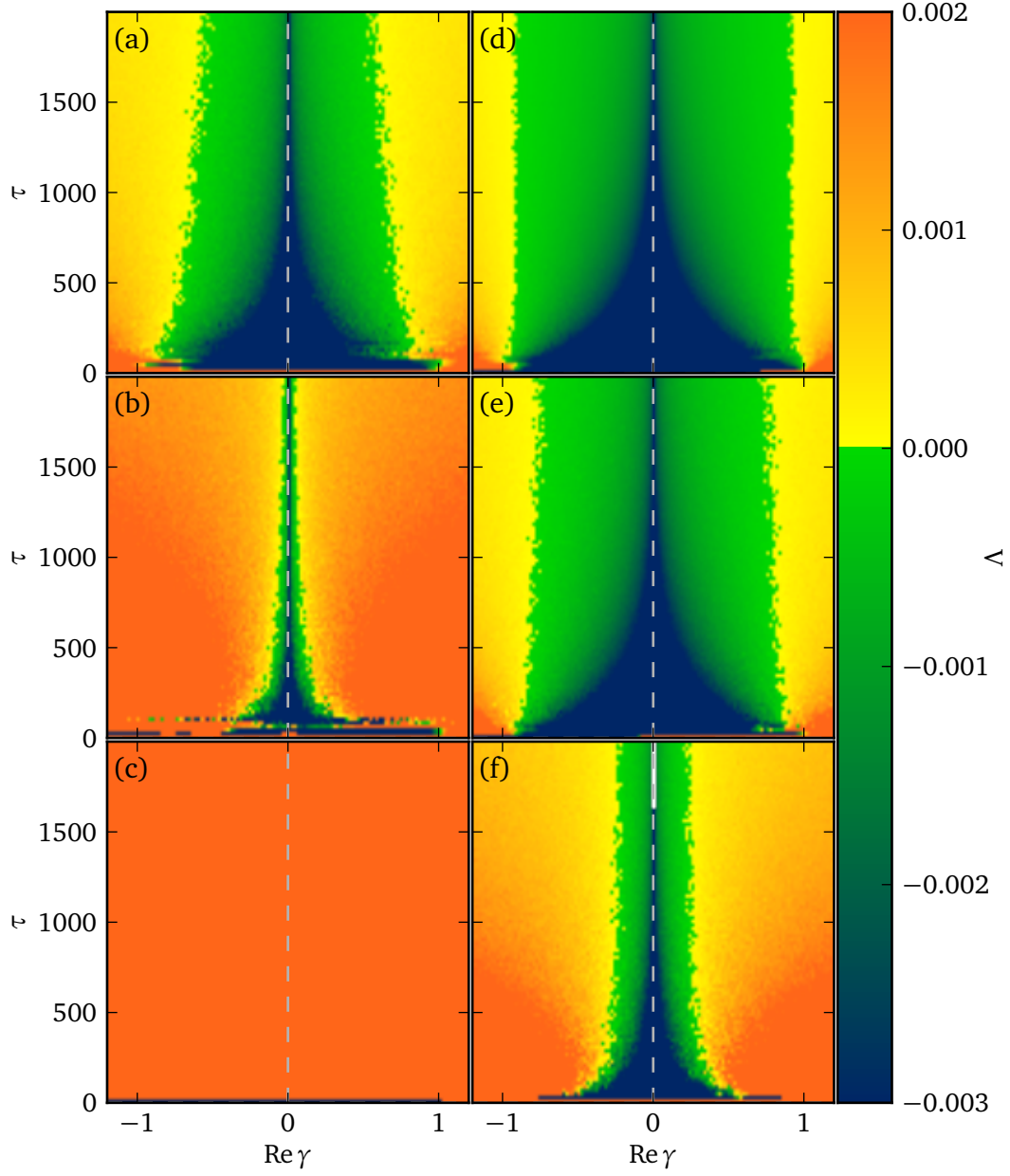


Figure 3.3.: Master stability function in the $(\text{Re } \gamma, \tau)$ plane for a network of delay-coupled lasers according to Eq. (2.7) with fixed $\text{Im } \gamma = 0$. Parameters as in Fig. 3.1.

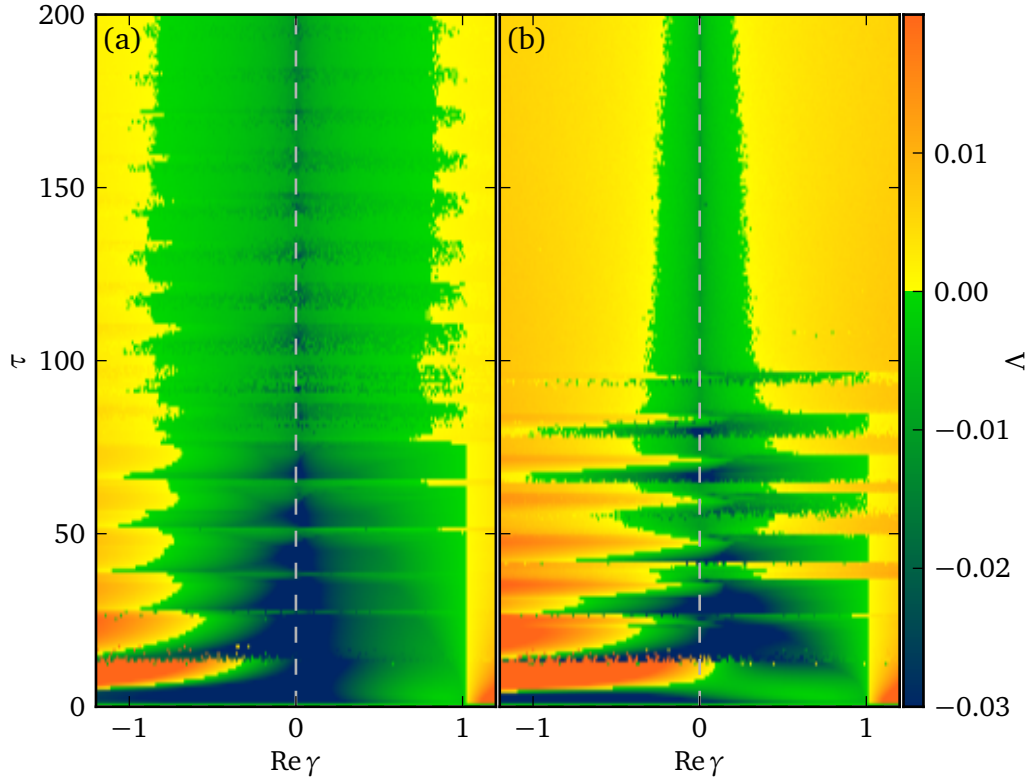


Figure 3.4.: Master stability function in the $(\text{Re } \gamma, \tau)$ plane for a network of delay-coupled lasers according to Eq. (2.7) with fixed $\text{Im } \gamma = 0$. Parameters: (a) $p = 0.1$, $\sigma = 0.12$; (b) $p = 1$, $\sigma = 0.12$; other parameters as as in Tab. 2.2.

3.4. Conclusion

I have shown results of the master stability function for delay-coupled laser networks where the nodes' dynamics is modeled using the Lang-Kobayashi rate equations. Using these results, I am able to characterize the stability of synchronization in these networks. Using a non-vanishing constant row sum instead of a zero row sum as used in the original work by Pecora and Carroll [1998], the generality of the master stability function is narrowed down, since the master stability now depends on the coupling strength which affects the synchronized dynamics.

Also the time delay has a crucial influence on the outcome of the master stability function. While for large time delays the master stability has a rotationally symmetric shape,

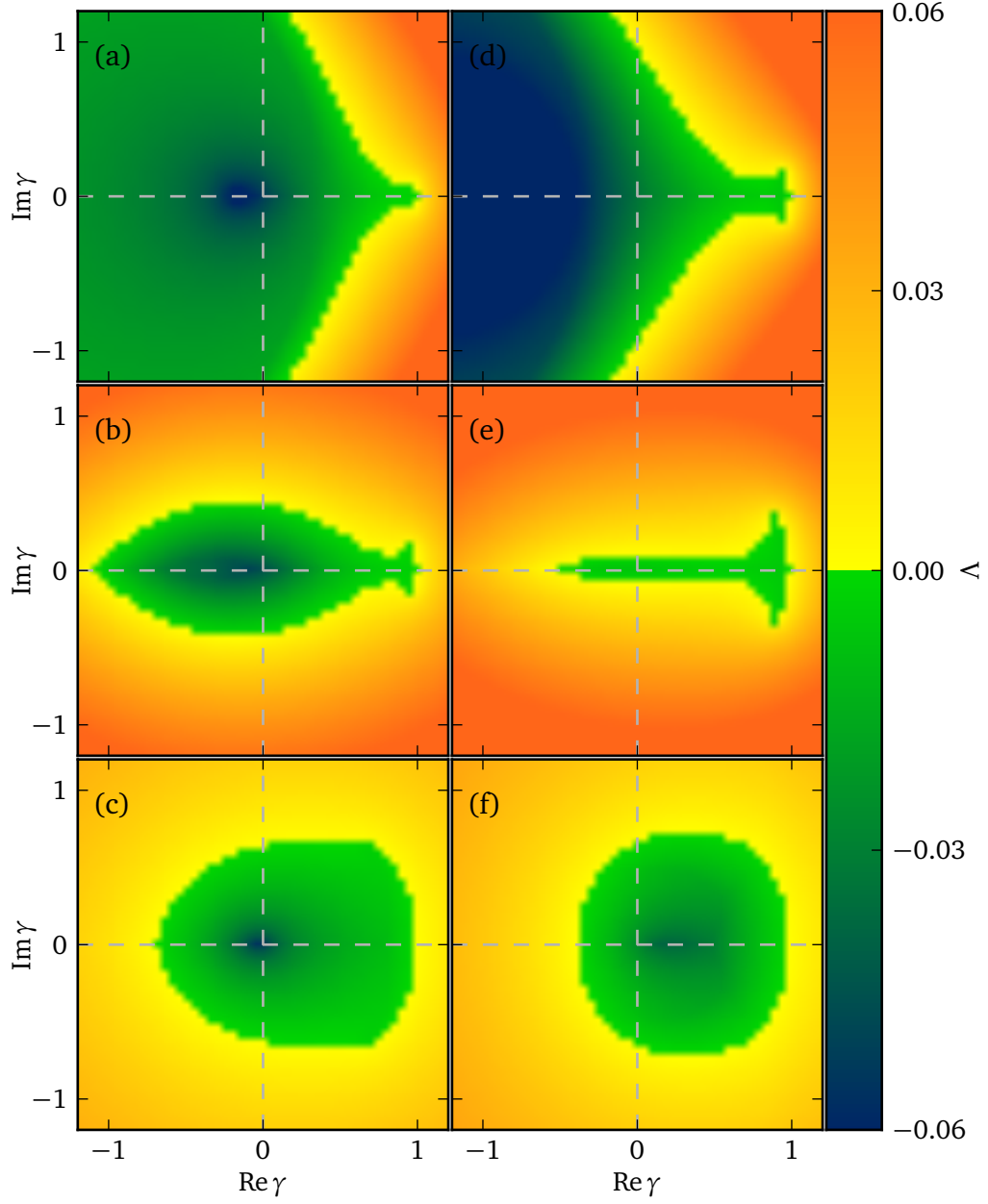


Figure 3.5.: Master stability function in the complex γ plane for a network of delay-coupled lasers according to Eq. (2.7). Parameters: (a) $p = 0.1$, $\tau = 1$; (b) $p = 0.11$, $\tau = 5$; (c) $p = 0.1$, $\tau = 20$; (d) $p = 1$, $\tau = 1$; (e) $p = 1$, $\tau = 5$; (f) $p = 1$, $\tau = 20$; other parameters as in Tab. 2.2.

large deviations from this shape occur for smaller values of the delay time.

I will use these results to study stability of synchronization in particular network topologies. These will be network motifs and regular networks in Chapter 4 and complex networks in Chapter 5.

4. Network motifs and regular networks

The idea of network motifs is two-fold. On one hand, in the study of synchronization, the effects observed in motifs may allow for predictions on the dynamics in much larger networks. On the other hand, complex networks can be seen as composed by building-blocks of a few nodes, i.e., motifs. Synchronization in isolated motifs may describe the effects that take place in a large network on the level of these building blocks. Determining synchronization in a large network can thus be split into two questions: (i) Is synchronization stable in the underlying network motifs? (ii) Is synchronization stable in the graph composed by these motifs? This Chapter focuses on the first question, while the second question is answered partly in Chapter 5 on complex networks.

In 2002, Milo et al. found that motifs characterize universal classes of networks. In particular, depending on the nature and function of a particular network, the amount of different motifs differs substantially. Milo et al. considered connected subgraphs with different number of nodes as motifs. Figure 4.1, for example, shows all 13 possible connected subgraphs with three nodes. I will focus on two- and three-node motifs in this chapter. Note that the existence of self-feedback loops, which are usually neglected in the literature on complex networks, leads to more than 13 possible connected subgraphs for the three-node motifs. I will go into detail with regard to these generalized motifs in Section 4.1.

Regular networks include unidirectionally and bidirectionally coupled rings, as well as lattices in various dimensions. Regular networks can be seen as an upscaled version of network motifs. A unidirectionally coupled ring of three nodes can, for example, be generalized to a ring with any number of nodes. As I will show, the eigenvalue spectra of many regular topologies follow simple rules, which makes them an ideal playground for my results in the master stability framework.

I will first introduce the concept of weighted motifs that also allows for self-feedback in Sec. 4.1. In Secs. 4.2 and 4.3 I will then discuss stability of synchronization in two- and three-node motifs, respectively. Section 4.4 shows an example where the master

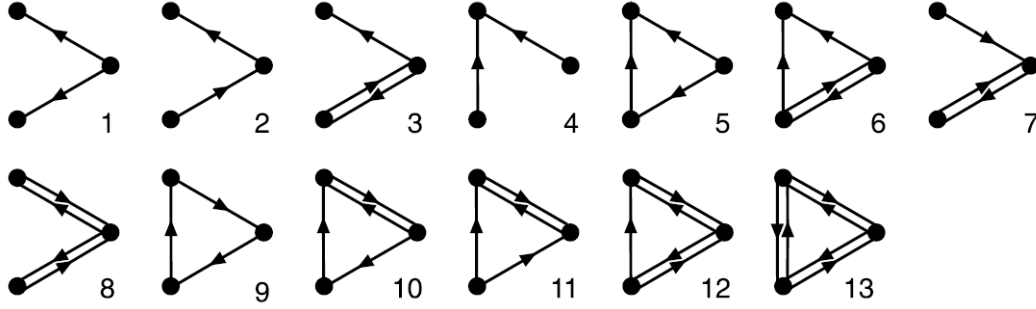


Figure 4.1.: Network motifs: all possible three-node connected subgraphs [reproduced from Milo et al., 2002].

stability function is not able to predict the stability of synchronization due to a non-diagonalizable coupling matrix. Regular networks and a discussion of synchronization in these will be the topic of Sec. 4.5.

4.1. Weighted motifs with feedback

As pointed out in Section 2.1.2 on page 38, an adjacency matrix \mathbf{A} is well sufficient to examine topological properties of a network, while a coupling matrix \mathbf{G} including individual weights for each link is needed for the investigation of dynamics on a network. I will therefore expand the concept of network motifs to what I call weighted motifs. That is, for example, in a particular motif in Fig. 4.1, different realizations may exist for varying weights of the different links. Furthermore, I will allow feedback loops, i.e., diagonal elements $A_{ii} = 1$. This increases the number of possible motifs for a given number of nodes, because each motif in Fig. 4.1 can be modified by independently adding feedback loops to the three nodes.

Since I consider isochronous synchronization in this first part of the thesis, the constant row sum condition has to be fulfilled in order to gain a synchronization manifold. As a consequence, not all combinations of link weights are possible. I will illustrate this first for two-node motifs in the following Section and later extend to three-node motifs.

4.2. Two-node motifs

As discussed above, a network only exhibits an isochronous synchronization manifold – stable or not – if the coupling matrix \mathbf{G} has a constant row sum. Without introducing compensating links or changing signs of links this can in general only be achieved in the following two cases:

- (i) For a given network, each row has the same positive row sum $g \equiv g_i = \sum_j G_{ij}$. Note that the row sum may in general also be negative, but for laser networks I consider only positive links as discussed in Sec. 2.4. The matrix is then normalized to unity row sum by dividing each entry by g .
- (ii) For a given network, each row has a positive row sum $g_i = \sum_j G_{ij}$. Normalization to unity row sum is achieved by dividing all elements in the i th row by its row sum g_i .

In real-life networks case (i) is rare, but not impossible. Constant row sums occur in regular network like rings (see Sections 4.5.1 and 4.5.2), globally coupled networks (Section 4.5.3), but also in the Erdős-Rényi model for random networks [Erdős and Rényi, 1959, 1960], although only in the thermodynamic limit of $N \rightarrow \infty$. Case (ii), where each row of a coupling matrix has an individual positive row sum, is more common, because it is less restrictive on the possible topologies due to additional degrees of freedom.

Table 4.1 shows the five possible connected two-node motifs that allow for the existence of an isochronous synchronization manifold. For each of these motifs, there is of course a unique adjacency matrix, e.g., $\mathbf{A} = \begin{pmatrix} 0 & 1 \\ 1 & 0 \end{pmatrix}$ for motif no. 1. In motifs no. 1 and 2, the weights of the links cannot be changed individually, because this would lead to a non-constant row sum. In motifs no. 3, 4 and 5, however, the weights can be changed by introducing one or two parameters a and b , respectively.

The question of synchronizability in a certain motif is thus not restricted to the schematic view or adjacency matrix of a motif but does depend on parameters describing the individual link strengths.

Using the results of the master stability function from Chapter 3, Tab. 4.2 shows the conditions to the matrix parameters a and b under which the motifs shown in Tab. 4.1 synchronize. I chose the low frequency fluctuation (LFF) and the coherence collapse (CC) regime with laser and coupling parameters according to Tab. 2.2. The master stability function depicted in Fig. 3.2 shows stability for $-0.65 < \gamma < 0.65$ and $-0.07 < \gamma < 0.07$ for the LFF and the CC regime, respectively. With the a - and b -dependent

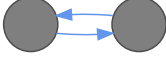
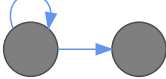
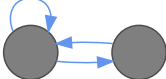
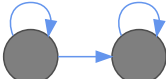
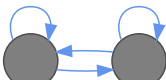
no.	scheme	coupling matrix	non-unity eigenvalue
1		$\begin{pmatrix} 0 & 1 \\ 1 & 0 \end{pmatrix}$	$\gamma_2 = -1$
2		$\begin{pmatrix} 1 & 0 \\ 1 & 0 \end{pmatrix}$	$\gamma_2 = 0$
3		$\begin{pmatrix} 1-a & a \\ 1 & 0 \end{pmatrix}$	$\gamma_2 = -a$
4		$\begin{pmatrix} 1 & 0 \\ a & 1-a \end{pmatrix}$	$\gamma_2 = 1-a$
5		$\begin{pmatrix} 1-a & a \\ b & 1-b \end{pmatrix}$	$\gamma_2 = 1-a-b$

Table 4.1.: Two-node motifs allowing for an isochronous synchronization manifold.

transversal eigenvalue γ_2 corresponding to each motif in Tab. 4.1 a condition for a and b can be derived under which a particular motif exhibits stable synchronization.

These conditions are valid only in the limit of large delay as discussed in Chapter 3, but the value of $\tau = 1000$ does already qualify as large enough; see Fig. 3.1. In this limit of large delay the master stability function is rotationally symmetric in the complex γ plane, as shown in Sec. 3.3.

In particular, the identity $\Lambda(\gamma = 1) = \Lambda(\gamma = -1)$ holds. This infers instability of synchronization for motif no. 1, because $\Lambda(\gamma = 1)$ is positive for chaotic dynamics in the synchronization manifold and the master stability function evaluated at the transversal eigenvalue $\gamma = -1$ yields the same positive value.

Motif no. 2, on the other hand, does synchronize regardless of operation of the laser nodes in the LFF or CC regime. As soon as the master stability function is negative at the origin ($\Lambda(\gamma = 0) < 0$), synchronization in this motif is stable. There are of course parameter sets for which even $\Lambda(\gamma = 0)$ is positive – see for example Fig. 3.1 – and for which no network can show stable synchronization.

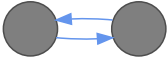
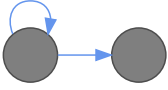
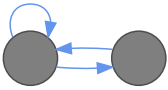
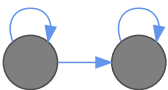
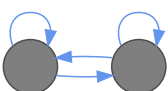
no.	scheme	LFF stable	CC stable
1		no	no
2		yes	yes
3		$ a < 0.65$	$ a < 0.07$
4		$0.35 < a < 1.65$	$0.93 < a < 1.07$
5		$0.35 < a + b < 1.65$	$0.93 < a + b < 1.07$

Table 4.2.: Two-node motifs: Stability conditions for the LFF and the CC regime according to Tab. 2.2.

The fact that motif no. 2 does synchronize while no. 1 does not can be understood in an intuitive way: In motif no. 2, perturbations to the first node will influence the dynamics of both nodes at the same time, because both nodes receive delayed input from node 1. Affecting both nodes simultaneously, these perturbations are therefore longitudinal to the synchronization manifold. In motif no. 1, on the other hand, perturbations to node 1 will travel to node 2 and arrive at node 1 after only two times this traveling time. Hence, this perturbation is transversal to the synchronization manifold as it does not affect both nodes simultaneously.

In motifs no. 3, 4, and 5, the parameters a and b determine the interplay of feedback and cross coupling. $a = 1$ corresponds to no feedback, while $a = 0$ puts all weight into a feedback link and in turn eliminates another link. The same applies to b in motif no. 5.

Differences appear for the LFF and the CC regime. In motif no. 3, the feedback links can be much stronger in comparison to the cross links while still retaining stability in the LFF regime than in the CC regime.

The same applies to motifs no. 4 and 5; in the LFF regime a much broader range is allowed for the parameter a (and the sum $a + b$ in motif no. 5, respectively) while being in the range of stable synchronization. Note that a choice of $a > 1$ or $b > 1$ would introduce negative weights for some links. While this is not forbidden, it would correspond to a phase shift π in the electric field (cf. the coupling scheme (2.20)).

Note that motif no. 5 includes the other four as special cases for particular choices of the parameters a and b . I will illustrate the results from this Section further using motif no. 5 in the following Section. This will also include direct numerical simulations of the motif to verify the predictions of the master stability function.

4.2.1. Example: motif no. 5

Note that the condition for synchronizability of motif no. 5 depends only on the sum $a + b$, but not on the individual choice of a and b . I will therefore consider a simplified version of network motif no. 5 from Tab. 4.1. A restriction to $a \equiv b$ simplifies the discussion largely but still explains the interplay of coupling and feedback. With this restriction, the motif has the coupling matrix

$$\mathbf{G} = \begin{pmatrix} 1-a & a \\ a & 1-a \end{pmatrix}, \quad (4.1)$$

with eigenvalues

$$\gamma_1 = 1, \quad (4.2)$$

$$\gamma_2(a) = 1 - 2a, \quad (4.3)$$

where γ_1 corresponds to dynamics longitudinal to the synchronization manifold.

The parameter a can in principal take on any value in \mathbb{R} . Since I allow for positive entries only in the coupling matrix for laser networks to avoid effective phase changes, $a \in [0, 1]$ is necessary. The values $a = 1$ and $a = 0$ correspond to coupling without feedback and feedback without coupling, respectively. This can be easily seen from the matrix (4.1). For a value of $a = 1/2$, feedback and coupling is equally represented.

From the master stability function depicted in Fig. 3.2, it can be seen that stability is obtained for $\gamma \in [-0.65, 0.65]$ and $\gamma \in [-0.07, 0.07]$ for the LFF and the CC regime

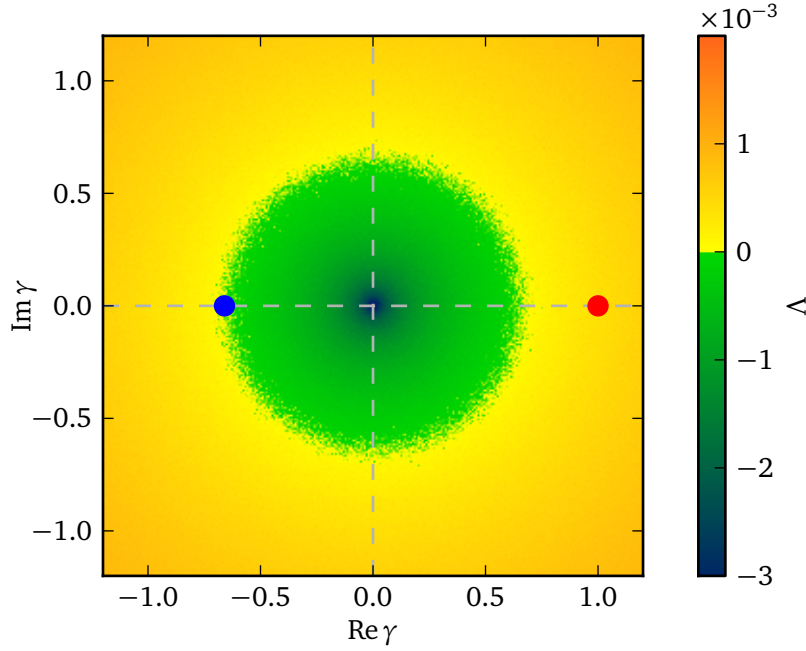


Figure 4.2.: Master stability function for a laser network operating in the LFF regime according to Tab. 2.2, see Fig. 3.1(a). Red dot: longitudinal eigenvalue $\gamma_1 = 1$, blue dot: transverse eigenvalue corresponding to motif no. 5 from Tab. 4.1 with $a = 0.83$.

according to parameters in Tab. 2.2. For the parameter a of the above network motif, this translates to stability for $a \in [0.175, 0.825]$ and $a \in [0.465, 0.535]$. Figure 4.2 shows the eigenvalues of the motif for an example value of $a = 0.83$, which is just above the threshold of stable synchronization.

Figure 4.3 displays synchronization diagrams of the intensities I_1 and I_2 of the first and second laser, respectively, from numerical simulations of the network motif for different values of the parameter a and other parameters chosen in the LFF regime according to Tab. 2.2. Figure 4.3(a) shows the synchronization diagram for $a = 0.95$. Here, no pattern of synchronization can be seen. This agrees with the prediction from the master stability function, where the transversal eigenvalue $\gamma_2(a = 0.95) = -0.9$ is located in a region with positive Lyapunov exponent. Figure 4.3(b) uses $a = 0.83$ which is just below the threshold of synchronization. Its transversal eigenvalue $\gamma_2(a = 0.83) = -0.66$ is located just outside the green region in Fig. 4.2 and thus still in a region with slightly positive Lyapunov exponent. The dynamics rests from time to time on the bisecting line of I_1 - and I_2 -axis – corresponding to isochronous synchronization – but it deviates from

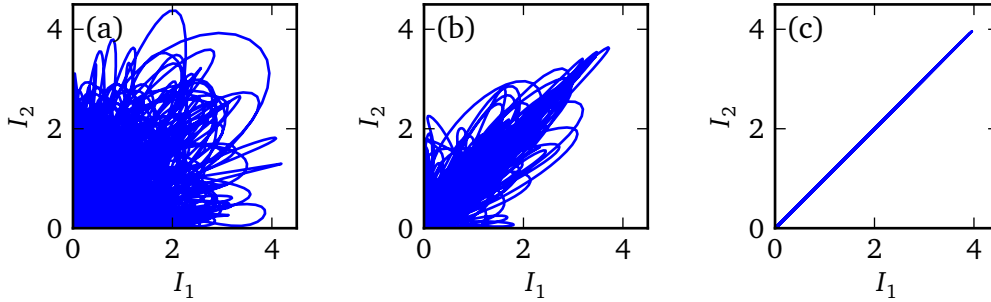


Figure 4.3.: Synchronization diagrams from simulations of the network motif (4.1) with (a) $a = 0.95$, (b) $a = 0.83$, and (c) $a = 0.5$. Laser and coupling parameters chosen in the LFF regime according to Tab. 2.2.

this line frequently. This behavior is also known as on-off intermittency [Flunkert et al., 2009]. The value $a = 0.5$, as used in Fig. 4.3(c) corresponds to equal contributions of coupling and feedback in the coupling matrix (4.1) and yields $\gamma_2(0.5) = 0$, which is at the minimum of the master stability function. The synchronization diagram shows that the dynamics takes place on the bisecting line of the I_1 - and I_2 -axis, which corresponds to perfect isochronous synchronization.

Similar results are obtained for the CC regime, which are shown in Fig. 4.4. Here, panels (a), (b), and (c) use parameters $a = 0.95$, 0.55 , and 0.5 , respectively. Compared to the LFF regime, the narrower range of possible a results in a loss of stability already at $a = 0.55$, shown in Fig. 4.4(b).

In order to quantify the amount of synchronization between two lasers, I use the cross correlation, which is defined as

$$C_{ij} = \frac{\langle I_i I_j \rangle - \langle I_i \rangle \langle I_j \rangle}{\sqrt{\langle I_i^2 \rangle - \langle I_i \rangle^2} \sqrt{\langle I_j^2 \rangle - \langle I_j \rangle^2}}. \quad (4.4)$$

The symbol $\langle \cdot \rangle$ denotes a time average. The numerical simulations to verify the predictions of the master stability function used a total time of 320,000 time units where the time average is taken over the last 1,000 time units. This way, possible transient effects are not taken into account. Starting with initial conditions on the synchronization manifold, small noise of the magnitude 10^{-9} was added to the electric field variables of each node to perturb the dynamics from the invariant synchronized state. The results

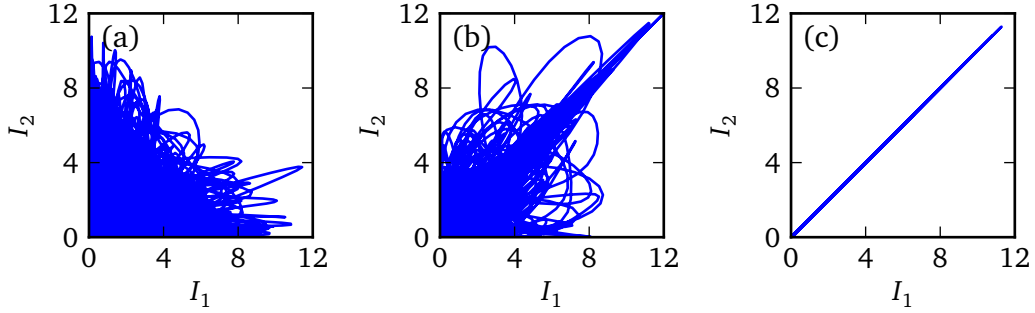


Figure 4.4.: Synchronization diagrams from simulations of the network motif (4.1) with (a) $a = 0.95$, (b) $a = 0.55$, and (c) $a = 0.5$. Laser and coupling parameters chosen in the CC regime according to Tab. 2.2.

are robust against changes in the noise strength up to 10^{-5} and against changes of the variables the noise is applied to.

In both the LFF and the CC regime, bursts of desynchronization occur even when the master stability function predicts stability of synchronization. This phenomenon is known as bubbling and has already been observed for two delay-coupled lasers [Flunkert et al., 2009]. Still, there is a difference to desynchronization; in the latter the system does not re-synchronize after perturbations from the synchronization manifold.

For the LFF regime, it is still possible to quantify the difference between a synchronized and a desynchronized state, since bubbling occurs as short bursts only. I calculated the cross correlation omitting these short bursts of desynchronization. This is realized by splitting the relevant time interval into 10 sub-intervals, calculating the cross correlation for each of the windows separately, and taking the maximum of the 10 calculated values for C_{ij} .

In the CC regime, bubbling is not restricted to short bursts, but intervals of desynchronization can reach the length of synchronized windows in between. Carefully using the above procedure of interval splitting and using the maximum obtained C_{ij} , effects of bubbling can be minimized but not fully eliminated from the results; it may happen that the obtained cross correlation is still below unity for cases the master stability function predicts stability for.

Another possible synchronization measure useful for quantifying the coherence in dy-

namics on networks is the mean synchronization error defined as

$$E_{ij} = \frac{2\langle I_i - I_j \rangle}{\langle I_i + I_j \rangle}. \quad (4.5)$$

This measure is a time average of the differences between the two nodes i and j . I do not use it in this thesis, but it is worth mentioning that for a large number of nodes where one takes the average $E = \frac{2}{N(N-1)} \sum_{i < j} E_{ij}$ this is computationally less expensive than calculating and averaging the cross correlation $C = \frac{2}{N(N-1)} \sum_{i < j} C_{ij}$. The calculation of one C_{ij} needs more time averages.

Other synchronization measures exist that characterize the synchronization of phases in coupled systems, for instance, the phase-synchronization index and the phase-synchronization interval distribution [Rosenblum et al., 2001; Hauschildt et al., 2006; Hövel et al., 2010]. These measures do not include the amplitude of the dynamics and need a definition of a phase. For spiky dynamics – as observed in excitable systems – such a phase can be defined, for instance, as

$$\varphi(t) = 2\pi \frac{t - t_{k-1}}{t_k - t_{k-1}} + 2\pi(k-1), \quad (4.6)$$

where t_k is the time of the k th spike. Intuitively, the phase between two spikes should be 2π . Considering only in-phase synchronization, a phase difference can be defined as

$$\Delta\varphi_{ij}(t) = |\varphi_i(t) - \varphi_j(t)|, \quad (4.7)$$

where φ_i and φ_j denote the phases of the i th and j th node, respectively. Using this phase difference, the phase-synchronization index is defined as

$$\Gamma_{ij} = \sqrt{\langle \cos \Delta\varphi_{ij}(t) \rangle^2 + \langle \sin \Delta\varphi_{ij}(t) \rangle^2} \quad (4.8)$$

This index varies between zero for no synchronization and unity for perfect in-phase synchronization. Considering a large network, the average $\frac{2}{N(N-1)} \sum_{i < j} \Gamma_{ij}$ could be calculated to characterize the amount of phase synchronization in the network.

If not perfectly synchronized, the phase difference $\Delta\varphi_{ij}$ may show sudden jumps, because one system may spike twice during the inter-spike interval of another system. It has been shown that the average length of the intervals of synchronization, i.e., intervals where the phase difference is zero, is a more sensitive measure than the phase-synchronization index Γ_{ij} [Hövel et al., 2010].

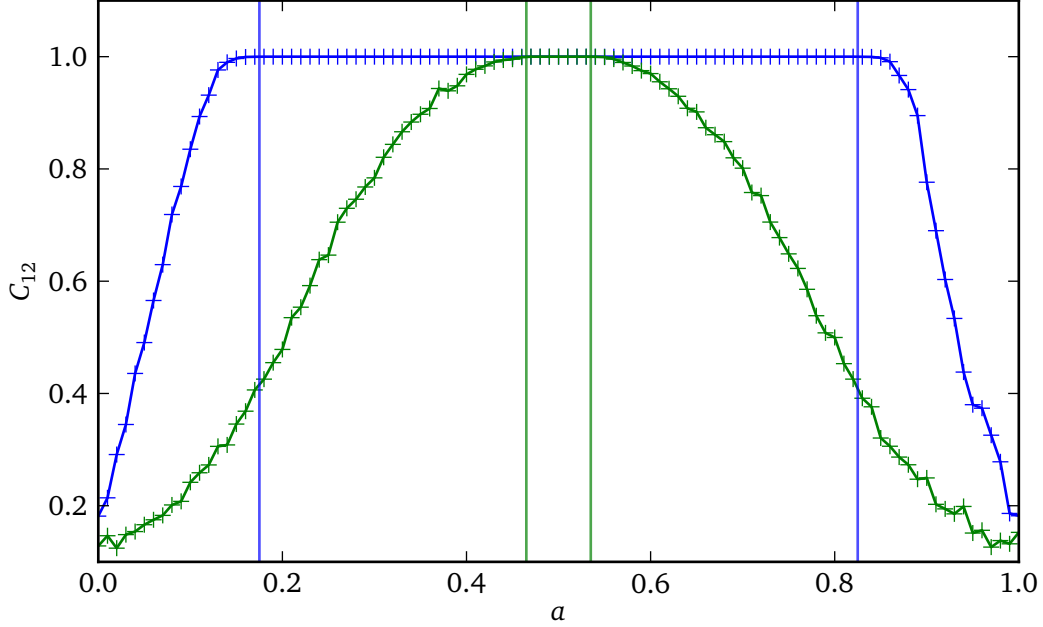


Figure 4.5.: Correlation of the intensities I_1 and I_2 of the two lasers in a simulation of motif no. 5, see Tab. 4.1 and Eq. (4.1).

Despite being very useful for investigations in neural networks, these phase synchronization measures are not appropriate to characterize the amount of synchronization in the scope of coupled lasers for two reasons: Firstly, for non-spiky dynamics the definition of a phase in analogy to Eq. (4.6) is not straight-forward. Secondly, the amplitude of the electric field varies over time to a large extent, most pronounced in the LFF regime. The differences between amplitudes of the different nodes can therefore not be neglected as done when considering only phase synchronization. For these reasons, I will stick to the cross correlation as measure for synchronization in this work.

Figure 4.5 shows the cross correlation C_{12} according to Eq. (4.4) of the two nodes in motif no. 5. The values were obtained using the above method of splitting the time series. Additionally I averaged over 50 runs with different noise realizations. The blue curve corresponds to the LFF regime, while the green curve shows the outcome for the CC regime according to the parameters in Tab. 2.2. The vertical lines show the value of a for which the master stability function predicts a change of stability; $[0.175 < a < 0.825]$ for the LFF regime (blue) and $[0.465 < a < 0.535]$ for the

CC regime (green). In conclusion, the predictions of the master stability function are perfectly valid.

4.3. Three-node motifs

From the motifs in Fig. 4.1, some cannot be normalized in the way described in Section 4.2, i.e., they do not allow for the existence of a synchronization manifold. In motifs no. 1, 2, 4, 5, 7, and 11, one or more nodes do not receive input from other nodes at all. In the coupling matrix, this leads to one or more rows without non-zero entries. But as shown above, the coexistence of rows with zero and non-zero sums cannot lead to a common normalization with equal row sums.

The normalized coupling matrices for the remaining motifs, i.e., those that allow for a synchronous solution, are shown in Tab. 4.3. Again, I have included whether stability of synchronization is stable in these motifs. The CC regime does not show stable synchronization at all, while at least two out of seven motifs do synchronize in the LFF regime. This is due to the larger stability region in the master stability function of the LFF regime compared the CC regime. Those motifs that synchronize have a higher number of links – i.e, have a denser matrix – than those that do not. In Chapter 5 on complex networks I will show that this is a general feature. Networks with a high link density tend to have an eigenvalue spectrum concentrated in a vicinity of zero, which is also the location of the minimum of the master stability function in laser networks.

In contrast to the case of two-node motifs, I do not introduce motifs with feedback links here, as the number of possible motifs would exceed a reasonable limit and would not yield an additional insight. Neither do I introduce parameters for weighted links. This can of course be done in a manner similar to Sec. 4.2 on two-node motifs. Feedback, however, does become important for synchronizability. Already for the two-node motifs, those that included feedback links would lead to stable synchronization earlier than those without as shown in Sec. 4.2. For three-node motifs this plays an important role, too. Section 4.5 on regular networks will show these results in a more general scope for even higher number of nodes.

4.4. Where the master stability function fails

One condition that has to be fulfilled in order to apply the master stability function is that the coupling matrix of a given network has to be diagonalizable. Here I will show

<i>no.</i>	<i>coupling matrix</i>	<i>non-unity eigenvalues</i>	<i>LFF stable</i>	<i>CC stable</i>
3	$\begin{pmatrix} 0 & 1 & 0 \\ 0 & 0 & 1 \\ 0 & 1 & 0 \end{pmatrix}$	$\gamma_2 = -1, \gamma_3 = 0$	no	no
6	$\begin{pmatrix} 0 & 0.5 & 0.5 \\ 0 & 0 & 1 \\ 0 & 1 & 0 \end{pmatrix}$	$\gamma_2 = -1, \gamma_3 = 0$	no	no
8	$\begin{pmatrix} 0 & 1 & 0 \\ 0.5 & 0 & 0.5 \\ 0 & 1 & 0 \end{pmatrix}$	$\gamma_2 = -1, \gamma_3 = 0$	no	no
9	$\begin{pmatrix} 0 & 0 & 1 \\ 1 & 0 & 0 \\ 0 & 1 & 0 \end{pmatrix}$	$\gamma_2 = -(-1)^{1/3}, \gamma_3 = (-1)^{2/3}$	no	no
10	$\begin{pmatrix} 0 & 0.5 & 0.5 \\ 1 & 0 & 0 \\ 0 & 1 & 0 \end{pmatrix}$	$\gamma_2 = (-1 - i)/2, \gamma_3 = (-1 + i)/2$	no	no
12	$\begin{pmatrix} 0 & 0.5 & 0.5 \\ 0.5 & 0 & 0.5 \\ 0 & 1 & 0 \end{pmatrix}$	$\gamma_2 = \gamma_3 = -1/2$	yes	no
13	$\begin{pmatrix} 0 & 0.5 & 0.5 \\ 0.5 & 0 & 0.5 \\ 0.5 & 0.5 & 0 \end{pmatrix}$	$\gamma_2 = \gamma_3 = -1/2$	yes	no

Table 4.3.: Normalized coupling matrices and non-unity eigenvalues of selected motifs depicted in Fig. 4.1.

an example of a graph where this condition is not fulfilled, but which still synchronizes. Consider the network motif depicted in Fig. 4.6.

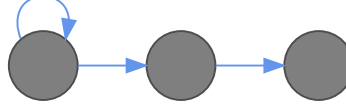


Figure 4.6.: Example motif in which synchronization cannot be described by the master stability function.

The coupling matrix for this motif reads

$$\mathbf{G} = \begin{pmatrix} 1 & 0 & 0 \\ 1 & 0 & 0 \\ 0 & 1 & 0 \end{pmatrix}, \quad (4.9)$$

where no weights for the links can be introduced since every row has only one entry. The eigenvalues of this matrix are

$$\begin{aligned} \gamma_1 &= 1 \\ \gamma_2 = \gamma_3 &= 0 \end{aligned} \quad (4.10)$$

Considering the master stability function for the laser model, e.g., Fig. 3.1(a) and (b) for the LFF and CC regimes, respectively, synchronization should be stable in this network motif.

The algebraic multiplicity of the eigenvalue $\gamma_2 = \gamma_3 = 0$ is 2, while its geometric multiplicity is only 1. This can be seen by calculating the matrix \mathbf{S} that should diagonalize \mathbf{G} as $\mathbf{S}^{-1}\mathbf{G}\mathbf{S} = \text{diag } \mathbf{G}$:

$$\mathbf{S} = \begin{pmatrix} 1 & 0 & 0 \\ 1 & 0 & 0 \\ 1 & 1 & 0 \end{pmatrix}. \quad (4.11)$$

It is obvious that the column vectors in this matrix can only span a 2-dimensional space, but not the 3-dimensional eigenspace, hence the 1-fold geometric multiplicity of the zero eigenvalue.

Indeed, this network motif does show stable isochronous synchronization. Figure 4.7 shows synchronization diagrams for this network from numerical simulations. Plotted

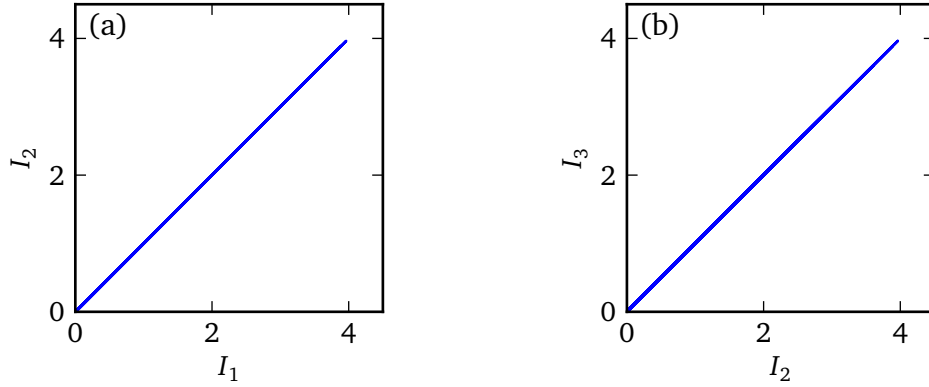


Figure 4.7.: Synchronization diagrams I_1 vs. I_2 and I_2 vs. I_3 from numerical simulations of the network motif (4.9) with the laser model. Parameters chosen in the LFF regime according to Tab. 2.2.

are the intensities I_1 vs. I_2 and I_2 vs. I_3 of the three lasers. It can be clearly seen that all three lasers synchronize.

The subgraph consisting of nodes 1 and 2 is identical to the 2-node motif no. 2 in Tab. 4.2, which shows stable synchronization in both the LFF and the CC regimes. Node 3 is driven by node 2 and does synchronize to the others as well, but this is not covered by the master stability outcome.

Attempts have been made to overcome the condition of a diagonalizable coupling matrix [Nishikawa and Motter, 2006]. In that work, a framework similar to the master stability function is derived for general matrices using the Jordan normal form of the coupling matrix. With that it is possible to characterize stability of synchronization in a motif as in Fig. 4.6, but only without time delay, i.e., instantaneous coupling. It is unclear to which extent the results can be generalized to delayed couplings, as the explanation is based on instantaneous driving of other nodes.

In conclusion, one may get the impression that the master stability function correctly predicts synchronizability in this motif. It is, however, still unclear, if a generalization similar to that by Nishikawa and Motter can be employed for delayed coupling.

4.5. Regular networks

Regular networks are in some sense a generalization of network motifs. They do occur in real systems and still retain an eigenvalue spectrum that, as we will see, is described by analytic equations. The following Sections will show results for unidirectionally and bidirectionally coupled rings, topologies described by circulant matrices in general, linear chains, and globally coupled all-to-all networks. For all these types of regular networks, I will investigate the influence of feedback links, i.e., diagonal elements in the coupling matrix, on the stability of synchronization.

4.5.1. Unidirectionally coupled rings

Consider a unidirectional ring of coupled lasers without self-feedback as illustrated in Fig. 4.8. The coupling matrix of such a topology reads

$$\mathbf{G} = \begin{pmatrix} 0 & 1 & 0 & 0 & \cdots & 0 \\ 0 & 0 & 1 & 0 & \cdots & 0 \\ 0 & 0 & 0 & 1 & \cdots & 0 \\ \vdots & \vdots & \vdots & \vdots & \ddots & \vdots \\ 0 & 0 & 0 & 0 & \cdots & 1 \\ 1 & 0 & 0 & 0 & \cdots & 0 \end{pmatrix}. \quad (4.12)$$

The eigenvalues of this matrix are given by

$$\gamma_k = e^{2\pi i(k-1)/N}, \quad k = 1, \dots, N. \quad (4.13)$$

Figure 4.9 shows the master stability function in the LFF regime as color code and additionally the location of the eigenvalues of unidirectional ring matrices following Eq. (4.13) as a green curve. Eigenvalues for any number of nodes will be located on this circle. As an example, the four longitudinal eigenvalues for $N = 5$ are shown as green dots, while the longitudinal eigenvalue $\gamma_1 = 1$ is shown in red. It is obvious that no unidirectional ring can show stable synchronization, because the eigenvalues of any such ring will be located on the green circle.

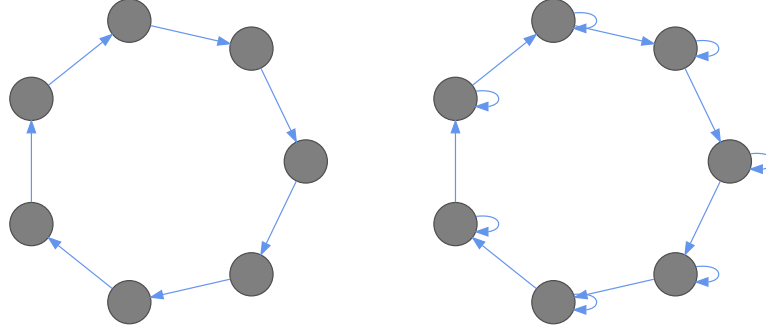


Figure 4.8.: Schematic view of 7 nodes coupled in a unidirectional ring structure without (left) and with feedback loops (right).

The matrix is very similar in the case of additional self-feedback added to Eq. (4.12) and rescaled to unity row sum:

$$\mathbf{G} = \frac{1}{2} \begin{pmatrix} 1 & 1 & 0 & 0 & \cdots & 0 \\ 0 & 1 & 1 & 0 & \cdots & 0 \\ 0 & 0 & 1 & 1 & \cdots & 0 \\ \vdots & \vdots & \vdots & \vdots & \ddots & \vdots \\ 0 & 0 & 0 & 1 & \cdots & 1 \\ 1 & 0 & 0 & 0 & \cdots & 1 \end{pmatrix}. \quad (4.14)$$

A schematic view is shown in Fig. 4.8.

The unidirectionally coupled ring with feedback has eigenvalues

$$\gamma_k = \frac{1}{2} \left(1 + e^{2\pi i(k-1)/N} \right), \quad k = 1, \dots, N, \quad (4.15)$$

whose general location is plotted as a blue circle in Fig. 4.9. Since this circle lies partially inside the green region of stability, synchronization may be stable for certain number of nodes. Using Eq. (4.15), I can show that synchronization is stable for $N = 2$ and 3, while it becomes unstable for any higher value of N . Note that in the CC regime, only the case $N = 2$ is stable, because the stable region is much smaller; see Fig. 3.1(b). Note that the case $N = 2$ resembles motif no. 5 from Sec. 4.2.1 with $a = 1/2$.

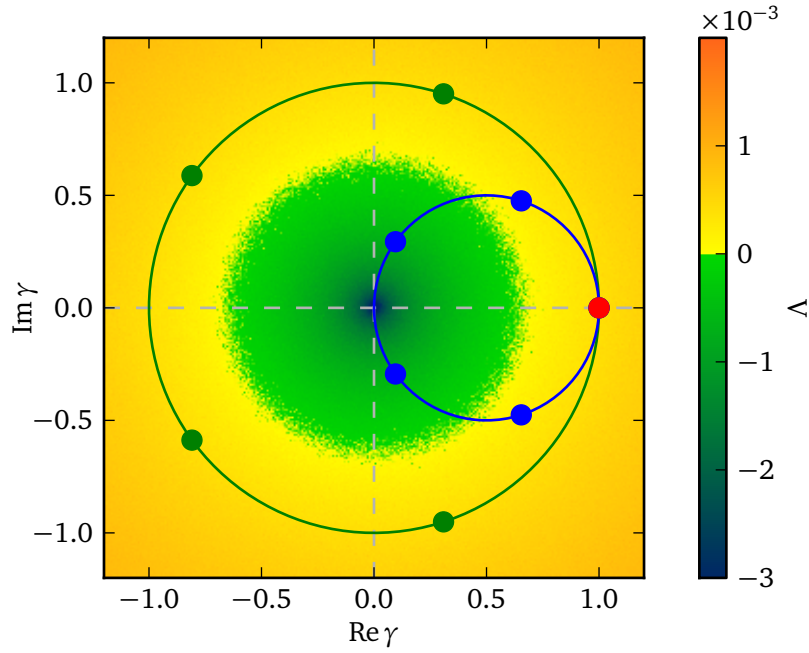


Figure 4.9.: Master stability function for a laser network operating in the LFF regime according to Tab. 2.2, see Fig. 3.1(a). Red dot: longitudinal eigenvalue $\gamma_1 = 1$, green circle: location of transverse eigenvalues for unidirectional rings according to Eq. (4.12), green dots: transverse eigenvalues for a unidirectional ring with $N = 5$, blue circle: location of transverse eigenvalues for unidirectional rings with feedback according to Eq. (4.14), blue dots: transverse eigenvalues for a unidirectional ring with feedback with $N = 5$.

4.5.2. Bidirectionally coupled rings

Similar results apply to the bidirectional ring – schematically depicted in Fig. 4.10 – where the connectivity matrix without self-feedback reads

$$\mathbf{G} = \frac{1}{2} \begin{pmatrix} 0 & 1 & 0 & 0 & \cdots & 1 \\ 1 & 0 & 1 & 0 & \cdots & 0 \\ 0 & 1 & 0 & 1 & \cdots & 0 \\ \vdots & \vdots & \vdots & \vdots & \ddots & \vdots \\ 0 & 0 & 0 & 0 & \cdots & 1 \\ 1 & 0 & 0 & 0 & \cdots & 0 \end{pmatrix}, \quad (4.16)$$

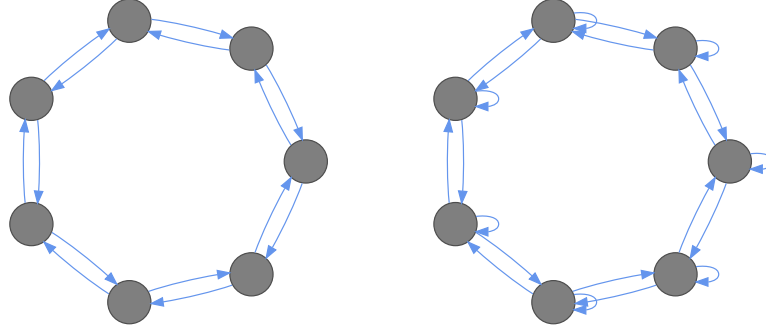


Figure 4.10.: Schematic view of 7 nodes coupled in a bidirectional ring structure without (left) and with feedback loops (right).

while the one with self-feedback is given by

$$\mathbf{G} = \frac{1}{3} \begin{pmatrix} 1 & 1 & 0 & 0 & \cdots & 1 \\ 1 & 1 & 1 & 0 & \cdots & 0 \\ 0 & 1 & 1 & 1 & \cdots & 0 \\ \vdots & \vdots & \vdots & \vdots & \ddots & \vdots \\ 0 & 0 & 0 & 0 & \cdots & 1 \\ 1 & 0 & 0 & 0 & \cdots & 1 \end{pmatrix}. \quad (4.17)$$

The eigenvalues of the matrix (4.16) are

$$\gamma_k = \cos \frac{2\pi(k-1)}{N}, \quad k = 1, \dots, N, \quad (4.18)$$

and those of the matrix (4.17) are

$$\gamma_k = \frac{1}{2} \left(1 + \cos \frac{2\pi(k-1)}{N} \right), \quad k = 1, \dots, N. \quad (4.19)$$

These are real-valued because both matrices are symmetric. The location of these eigenvalues is plotted in Fig. 4.11 for the example of $N = 5$ as green and blue dots without and with feedback, respectively.

Using Eq. (4.18), I find that $N = 3$ yields stable synchronization, the cases $N = 2$ and $N = 4$ are both unstable because they have an eigenvalue at $\gamma = -1$. Higher numbers

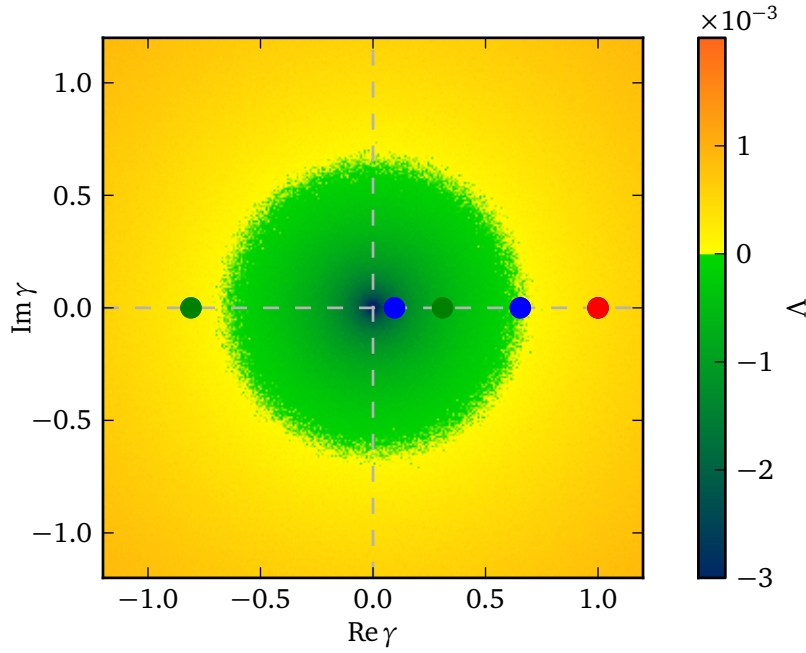


Figure 4.11.: Master stability function for a laser network operating in the LFF regime according to Tab. 2.2, see Fig. 3.1(a). Red dot: longitudinal eigenvalue $\gamma_1 = 1$, green dots: transverse eigenvalues for a bidirectional ring according to Eq. (4.16) with $N = 5$, blue dots: transverse eigenvalues for a bidirectional ring with feedback according to Eq. (4.17) with $N = 5$.

of N also do not synchronize, as some eigenvalues will always lie outside the stable region.

For the case with additional feedback, I find networks with $N = 2$ and $N = 4$ to show stable synchronization, while $N = 3$ does not synchronize. Also networks with $N \geq 5$ do not synchronize in a stable manner.

All results are backed up by numerical simulations of the corresponding networks. In Fig 4.12 I show synchronization diagrams from a simulation of 4 lasers coupled in a bidirectional ring without feedback. Two things can be observed in this figure: Firstly, isochronous synchronization is indeed unstable because some of the synchronization diagrams differ from bisecting lines corresponding to synchronization. But secondly, some of the synchronization diagrams show synchronization; namely I_1 and I_3 are synchronized, and also I_2 and I_4 . What we see is a state of cluster synchronization, where

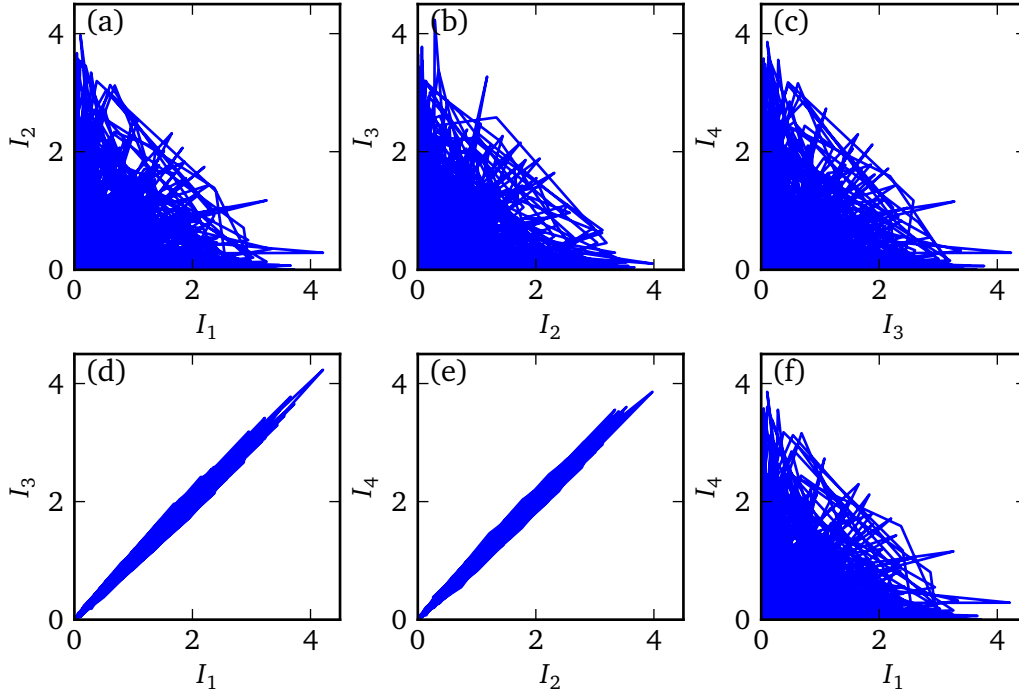


Figure 4.12.: Synchronization diagrams for the bidirectionally ring of $N = 4$ coupled lasers. (a-f): Intensities I_1 vs. I_2 , I_2 vs. I_3 , I_3 vs. I_4 , I_1 vs. I_3 , I_2 vs. I_4 , and I_1 vs. I_4 , respectively. Parameters according to the LFF regime in Tab. 2.2.

nodes 1 and 3 form a cluster and nodes 2 and 4 form another one. Stability of such states will be dealt with in Chapter 8, where I show that this two-cluster state in the bidirectional ring of 4 lasers is a stable state.

4.5.3. All-to-all coupling

All-to-all coupling, also known as global coupling or mean-field coupling, means that all nodes are pairwise connected by a link. This corresponds to a coupling matrix \mathbf{G} with entries

$$G_{ij} = \begin{cases} \frac{1}{N-1}, & i \neq j \\ 0, & i = j. \end{cases} \quad (4.20)$$

The renormalization by $N - 1$ results from the $N - 1$ entries in each row of \mathbf{G} . The eigenvalues of this coupling matrix are

$$\begin{aligned}\gamma_1 &= 1, \\ \gamma_2 = \dots = \gamma_N &= -\frac{1}{N-1}.\end{aligned}\tag{4.21}$$

For $N = 2$ this resembles motif no. 1 from Tab. 4.1, which does not show stable synchronization. In the limit of $N \rightarrow \infty$, on the other hand the $N - 1$ -times degenerate eigenvalue $\gamma_2 = \dots = \gamma_N = -\frac{1}{N-1}$ approaches zero, for which synchronization is stable in both the LFF and the CC regime according to the master stability function in Fig. 3.2.

For a given master stability function, the stability of synchronization in an all-to-all network depends on the number of nodes N . Assuming that the radius of the stable part of the master stability function is given by $|\gamma| = \gamma_c$, the threshold of synchronizability can be obtained by the equality

$$\gamma_c = \frac{1}{N-1}.\tag{4.22}$$

Since I obtained $\gamma_c = 0.65$ for the LFF regime and $\gamma_c = 0.07$ for the CC regime from Fig. 3.2, this yields stable synchronization for $N \geq 3$ and $N \geq 16$ for the LFF and the CC regime, respectively. Note that for $N = 3$ the all-to-all network is identical to a bidirectional with feedback, which does indeed synchronize in the LFF regime as I have elaborated in Sec. 4.5.2.

Figure 4.13 illustrates this result by showing the cross correlation in all-to-all networks in dependence on the number of nodes N . The blue and green dots correspond to parameters in the LFF and the CC regime according to Tab. 2.2. For the LFF regime, there is a sudden jump to high correlation already for small N , while the correlation increases only slowly for the CC regime. The blue and green lines show the values of $N = 3$ and $N = 16$ for which the master stability function predicts the threshold to synchronization according to Eq. (4.22). The numerical results are obtained for 50 different noise realizations and show very good agreement with the master stability function.

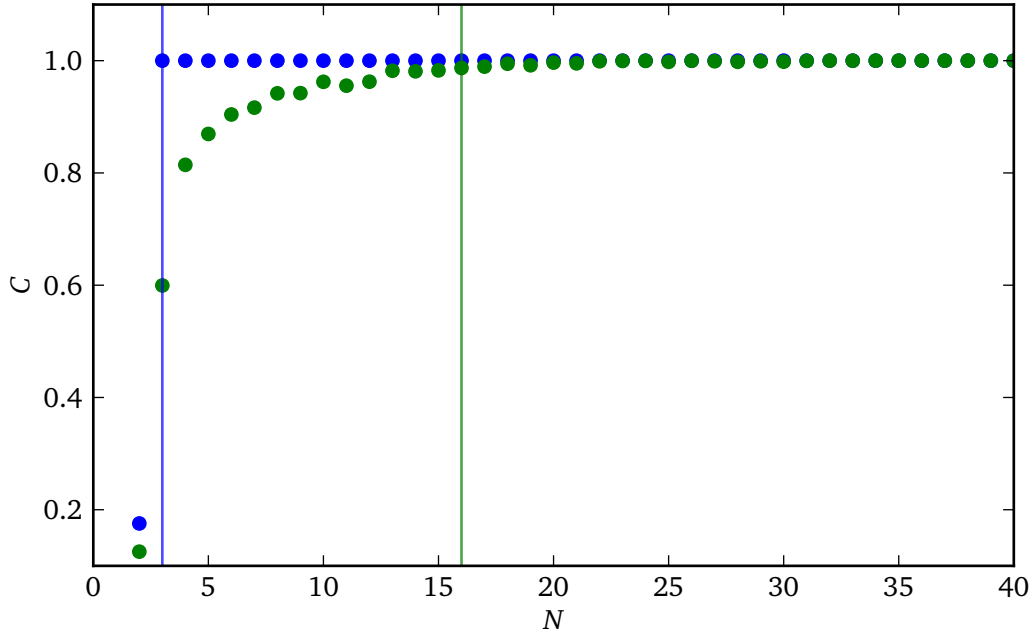


Figure 4.13.: Cross correlation in an all-to-all network corresponding to Eq. (4.20) in dependence on the number of nodes N . Blue and green dots correspond to the LFF and the CC regime according to Tab. 2.2. The vertical lines indicate the threshold to synchronization predicted by Eq. (4.22).

Additional feedback links

With additional feedback links the coupling matrix \mathbf{G} has entries

$$G_{ij} = 1/N, \quad i, j = 1, \dots, N. \quad (4.23)$$

The eigenvalues are obtained as

$$\begin{aligned} \gamma_1 &= 1, \\ \gamma_2 = \dots = \gamma_N &= 0. \end{aligned} \quad (4.24)$$

This network does synchronize stably for both the LFF and the CC regime and any number of nodes N , because $\Lambda(0)$ is negative in both regimes.

4.5.4. Circulant matrices

The coupling matrices of unidirectional and bidirectional rings are special cases of an important class of networks, the circulant matrices [Gray, 2006]. In Chapter 10, where I study cluster synchronization in oscillator networks, I will show that any circulant matrix allows for the existence of such cluster states. But already in the context of isochronous synchronization, circulant matrices play an important role, as they include several regular motifs as special cases, while the eigenvalue spectrum of the whole class of networks follows a simple law [Gray, 2006].

An $N \times N$ circulant matrix is of the form

$$\mathbf{C} = \begin{pmatrix} c_1 & c_N & \cdots & c_3 & c_2 \\ c_2 & c_1 & c_N & & c_3 \\ \vdots & c_2 & c_1 & \ddots & \vdots \\ c_{N-1} & & \ddots & \ddots & c_N \\ c_N & c_{N-1} & \cdots & c_2 & c_1 \end{pmatrix}. \quad (4.25)$$

The eigenvalues of this general form follow

$$\begin{aligned} \gamma_k &= c_1 + c_N \omega_k + c_{N-1} \omega_k^2 + \dots + c_2 \omega_k^{N-1} \\ &= \sum_{m=1}^N c_m \omega_k^{(1-m)+N \bmod N}, \quad k = 1, \dots, N, \end{aligned} \quad (4.26)$$

with $\omega_k = \exp(2\pi i k / N)$. The eigenvectors \mathbf{v}_k , on the other hand, follow

$$\mathbf{v}_k = (1, \omega_k, \omega_k^2, \dots, \omega_k^{N-1}). \quad (4.27)$$

The N different ω_k can alternatively be seen as the N th complex roots of unity, i.e., which satisfy $\omega_k^N = 1$.

Let me draw the connection to the examples considered before. Both the unidirectional and the bidirectional ring are special cases of circulant matrices. The unidirectional ring, for example, is obtained for $c_m = \delta_{N,m}$. Using this in Eq. (4.26), the eigenvalue equation of the unidirectional ring – Eq. (4.13) is recovered. Similarly, the eigenvalue equations for the bidirectionally coupled ring and the all-to-all coupled network are obtained, and also the equations for the corresponding cases with feedback.

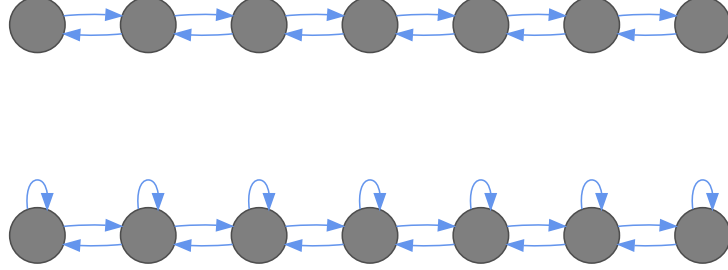


Figure 4.14.: Schematic view of 7 nodes coupled in a bidirectional chain structure without (top) and with feedback loops (bottom).

Circulant matrices in general will become important in Chapter 6 on multiple coupling matrices. When using multiple coupling matrices, for instance to use different coupling parameters, these matrices have to diagonalize simultaneously. I will show that all circulant matrices fulfill this condition.

4.5.5. Bidirectional linear chain

Circulant matrices include a number of regular networks. All of these have one property in common: spatial periodicity. One example of a regular network that does not belong to the class of circulant matrices is the bidirectional linear chain. Figure 4.14 schematically shows a bidirectional linear chain of 7 nodes with and without feedback.

The coupling matrix for the bidirectional chain without self-feedback reads

$$\mathbf{G} = \frac{1}{2} \begin{pmatrix} 0 & 2 & 0 & 0 & \cdots & 0 & 0 & 0 \\ 1 & 0 & 1 & 0 & \cdots & 0 & 0 & 0 \\ 0 & 1 & 0 & 1 & \cdots & 0 & 0 & 0 \\ \vdots & \vdots & \vdots & \vdots & \ddots & \vdots & \vdots & \vdots \\ 0 & 0 & 0 & 0 & \cdots & 0 & 1 & 0 \\ 0 & 0 & 0 & 0 & \cdots & 1 & 0 & 1 \\ 0 & 0 & 0 & 0 & \cdots & 0 & 2 & 0 \end{pmatrix}, \quad (4.28)$$

with the corresponding eigenvalues

$$\gamma_k = \cos \frac{\pi(k-1)}{N-1}, \quad k = 1, \dots, N. \quad (4.29)$$

Adding feedback yields the coupling matrix

$$\mathbf{G} = \frac{1}{3} \begin{pmatrix} 1 & 2 & 0 & 0 & \cdots & 0 & 0 & 0 \\ 1 & 1 & 1 & 0 & \cdots & 0 & 0 & 0 \\ 0 & 1 & 1 & 1 & \cdots & 0 & 0 & 0 \\ \vdots & \vdots & \vdots & \vdots & \ddots & \vdots & \vdots & \vdots \\ 0 & 0 & 0 & 0 & \cdots & 1 & 1 & 0 \\ 0 & 0 & 0 & 0 & \cdots & 1 & 1 & 1 \\ 0 & 0 & 0 & 0 & \cdots & 0 & 2 & 1 \end{pmatrix} \quad (4.30)$$

with eigenvalues

$$\gamma_k = \frac{1}{2} \left(1 + \cos \frac{\pi(k-1)}{N-1} \right), \quad k = 1, \dots, N. \quad (4.31)$$

Figure 4.15 shows the eigenvalues for the example of 5 nodes against to master stability function in the LFF regime according to Tab. 2.2. The eigenspectrum of the chain without feedback always include one eigenvalue -1 , which prevents stability of synchronization for any number of nodes.

With feedback, this eigenvalue moves to zero and is no longer the crucial part of the eigenspectrum. I find stable synchronization for $N = 2$ and 3 in the chain with feedback, but synchronization is unstable for any $N > 3$.

4.6. Conclusion

I have presented a survey of two- and three-node motifs, where the weight of the links has a crucial influence on the stability of synchronization. Also the introduction of feedback links to network motifs is important when characterizing possible synchronization in these motifs.

Going from motifs to regular networks, the regularity of the eigenvalue spectra can be used to determine stability based on the number of nodes, which yields mixed results depending on the topology used. In general, the introduction of feedback links

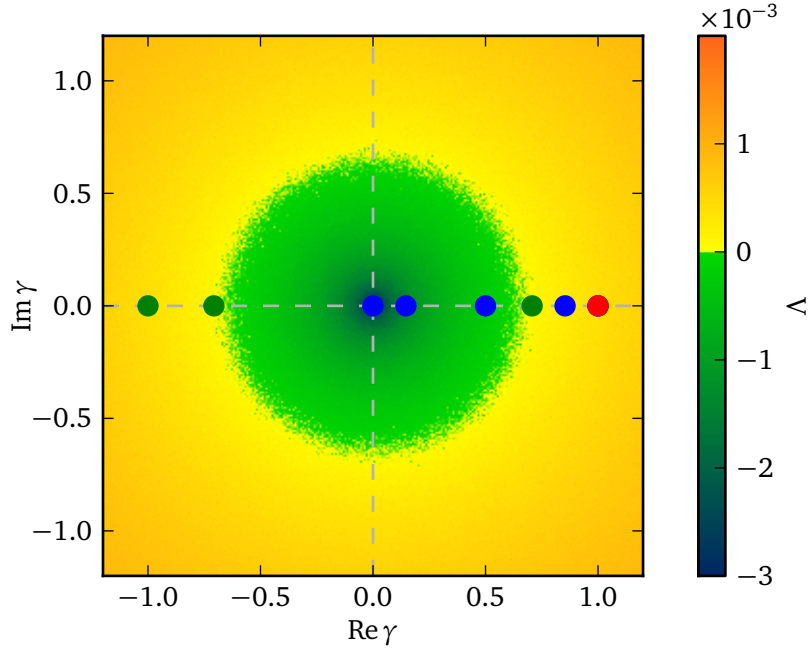


Figure 4.15.: Master stability function for a laser network operating in the LFF regime according to Tab. 2.2, see Fig. 3.1(a). Red dot: longitudinal eigenvalue $\gamma_1 = 1$, green dots: transverse eigenvalues for a bidirectional chain according to Eq. (4.28) with $N = 5$, blue dots: transverse eigenvalues for a bidirectional chain with feedback according to Eq. (4.30) with $N = 5$. Note that a green dot is covered by a blue one at $\gamma = 0$.

enhances stability of synchronization. I stress that the results are obtained for the LFF regime. In the CC regime, where the stable region of the master stability function is comparatively smaller, the picture might change substantially.

In the studies of regular network, the feedback links are introduced with the same weight as the existing links in the regular networks. In order to tune a particular network to stable synchronization, using weighted links may show better results.

5. Complex networks

Several models are known that describe complex networks, where each has some advantages in describing certain properties of real-world networks depending on the particular application [Albert and Barabási, 2002; Newman, 2003; Boccaletti et al., 2006]. The most prominent models are the Erdős-Rényi random network [Erdős and Rényi, 1959, 1960], scale-free models by Barabási and Bonabeau [2003], and the small-world model by Watts and Strogatz [1998].

In this thesis and in particular in this Chapter I will focus on the Erdős-Rényi random model for exemplary results. This has several reasons: On one hand, this model is well-established and its properties have been studied in detail [Albert and Barabási, 2002]. Most interestingly, the eigenvalue spectrum obeys an analytic law in certain limits, which combines well with the master stability function that uses only the eigenvalues of a topology's coupling matrix to characterize stability of synchronization. On the other hand, since synchronization depends only on the eigenvalue spectra, unexpected results are not likely to show up using other complex network models. The methods shown here can be applied in a straight forward manner to other models. In fact, we used the master stability function in a small-world like network of a neural model in Lehnert et al. [2011].

In the introduction of Chapter 4 I already stated the question whether network motifs that appear in a complex network can be used to characterize the stability of synchronization in such a larger network. Indeed, I will show a qualitative argument to explain the differences in synchronizability for the regimes of low-frequency fluctuations (LFF) and coherence collapse (CC). This will be based on the knowledge of network motifs or subgraphs that emerge in a random graph.

5.1. Erdős-Rényi random networks

The model proposed by Erdős and Rényi in 1959 was one of the first to describe complex networks. In this first work, they defined a random graph as constructed of N nodes

being connected by a fixed number of n links. These n links are chosen randomly from the $N(N - 1)/2$ links that are possible when considering an undirected graph where no feedback links are allowed.

Later, another slightly different definition was given as follows [Erdős and Rényi, 1960]: Start with N nodes. Then every pair of nodes is connected with a probability p . The final total number of links in the network is subject to fluctuations based on the particular realization, but the expectation value $E(n)$ follows the one obtained for the other model: $E(n) = pN(N - 1)/2$. In the thermodynamic limit $N \rightarrow \infty$ both models are equivalent.

5.1.1. A directed random graph

A directed random graph, in which I also allow for feedback links, can be obtained by a very similar adaptation: Instead of the possible $N(N - 1)/2$ links in the graph above, in a directed graph with possible feedback N^2 links may exist. Following the second approach above, each of these N^2 links is connected with a probability p . The expectation value of the final number of links is of course obtained as $E(n) = pN^2$.

In the following, I will refer to the original setup with undirected links and no feedback as *undirected random network* and I will call the adaption with directed and feedback links *directed random network*.

5.1.2. Meeting the unity row-sum condition

In the above construction rules, nothing is implied for the strength of each link. In applications that are interested only in topological properties of complex networks, e.g., connectedness of an infrastructural network, the actual strength of a link is only of secondary interest and the description by an adjacency matrix is sufficient (see Sec. 2.1.2 on the relation of adjacency and coupling matrices).

However, for the investigation of synchronization in a random network, the weight of a particular link is very important, as I have already shown for small network motifs in Chapter 4. In order to yield an invariant synchronization manifold, any network topology has to obey the unity row sum condition as shown in Chapter 2. This is achieved here in the following way: During the construction of the Erdős-Rényi random network, assign each link the weight 1. Then, when the construction of the network is

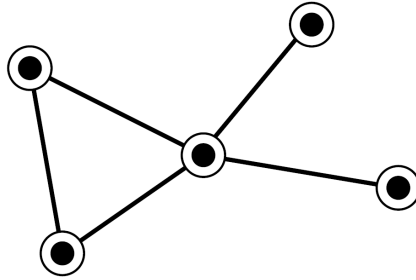


Figure 5.1.: Scheme of a simple network with 5 nodes and 5 links for illustration of the network quantities [reproduced from [Newman, 2003](#)].

finished, divide every row in the obtained random network by the sum over its entries.

This procedure of renormalization may not be possible in cases where one node is not connected to others at all. The row corresponding to this node has then only zero entries and cannot be normalized to a finite row sum. It is quite intuitive that this happens only for low link probabilities p and is related to the problem of the percolation threshold. Before discussing this threshold in Sec. 5.3, I will briefly introduce several quantities that are used to characterize the topological properties of complex networks in general. These will then be useful to understand the particular properties of the Erdős-Rényi random network.

5.2. Network quantities

Any network can be characterized by an adjacency matrix \mathbf{A} (with entries a_{ij}), describing the links between nodes. \mathbf{A} only contains zeros or ones, i.e., its entries denote only the existence of links, but not particular strengths. Most of the literature uses this adjacency matrix instead of a coupling matrix to obtain the following network quantities [[Albert and Barabási, 2002](#); [Newman, 2003](#)]. Extensions using the weights encoded in a coupling matrix do exist, but are not important for most topological problems.

I will illustrate most the quantities that I introduce using the simple network shown in Fig. 5.1. Note that this is an undirected network, where each link is present in both directions.

Node degree. The node degree k_i of a given node i is defined as its number of links. One distinguishes in-degree and out-degree, where the in-degree counts the incoming links:

$$k_i^{\text{in}} = \sum_j a_{ij} \quad (5.1)$$

and the out-degree counts the outgoing links of the i th node:

$$k_i^{\text{out}} = \sum_j a_{ji}. \quad (5.2)$$

The node degree can then be defined as either the sum of or the arithmetic mean over the in- and out-degree. I use the latter definition:

$$k_i = \frac{1}{2} (k_i^{\text{in}} + k_i^{\text{out}}). \quad (5.3)$$

Note that for undirected graphs, all three quantities will be identical for a given node: $k_i^{\text{in}} = k_i^{\text{out}} = k_i$. The node degree of, for example, the central node in Fig. 5.1 is $k = 4$.

Degree distribution. The degree distribution $P(k)$ is the probability that an arbitrary node has k links. Note that this degree distribution can be obtained for the in-, out-, or arithmetic mean degree.

Average degree. The average degree $\langle k \rangle$ is given by the first moment of the degree distribution $P(k)$. For the example shown in Fig. 5.1 the average degree is $\langle k \rangle = 2$.

Characteristic path length (mean geodesic distance). The characteristic path length ℓ is the mean distance between pairs of nodes. Here, distance refers to the minimum number of links needed to get from one node to the other.

$$\ell = \frac{1}{N(N-1)} \sum_{i,j} d_{ij}, \quad (5.4)$$

where d_{ij} is the distance between the i th and the j th node and N is the number of nodes. This definition does not include self-couplings, hence the normalization by $N(N-1)$.

In a network that consists of more than one component, i.e., where there is at least one pair of nodes without a path between, the above definition is problematic as it goes to infinity. An alternative definition that uses the reciprocal values may be used:

$$\ell^{-1} = \frac{1}{N(N-1)} \sum_{i,j} d_{ij}^{-1}. \quad (5.5)$$

For the example in Fig. 5.1 I obtain $\ell = 1.5$ from the first definition and $\ell = 4/3$ from the second definition.

Diameter. The diameter ℓ_{max} of a network is the maximum of the distances between all pairs of nodes:

$$\ell_{max} = \max\{d_{ij} : i, j = 1, \dots, N\} \quad (5.6)$$

The diameter of the example in Fig. 5.1 is $\ell_{max} = 2$.

Closeness. The closeness μ_i of a node i is defined as the inverse mean distance from all other nodes of the network:

$$\mu_i = \frac{N-1}{\sum_{j \neq i} d_{ij}} \quad (5.7)$$

In the example of Fig. 5.1, let me denote the central node by the index 1 and the top node by the index 2. I then obtain $\mu_1 = 1$ and $\mu_2 = 4/7$.

Betweenness. The betweenness of a node i is obtained as follows. Let n_{jk} be the number of shortest paths connecting the nodes j and k . Further, let $n_{jk}(i)$ be the number of these paths that go through the node i . Then the betweenness of node i is defined as

$$b_i = \sum_{\substack{j,k \\ i \neq j \neq k}} \frac{n_{jk}(i)}{n_{jk}}. \quad (5.8)$$

The betweenness of i will be higher the more paths go through i . In the example of Fig. 5.1, I obtain $b_1 = 4$ for the central node and $b_2 = 0$ for the top node.

Both the closeness and the betweenness are measures for the centrality of a certain node. Equivalent definitions can be found for the centrality of links.

Clustering coefficient The clustering coefficient measures the connectedness of neighbors of a given link. This is, for instance, useful to determine cliquishness in social networks.

The clustering coefficient of the i th node is obtained as follows. Let the node i have k_i links to other nodes. If these k_i neighbors were completely connected with each other, there would be $k_i(k_i - 1)/2$ links between them. Let E_i be the number of links that really exist between the neighbors. Then the clustering coefficient is the ratio of the existent and the possible of those links:

$$C_i = \frac{2E_i}{k_i(k_i - 1)}. \quad (5.9)$$

An equivalent definition is given by the ratio of the triangles that contain the node i and the number of triples centered at node i . The mean clustering coefficient is obtained as the average over the clustering coefficients of all nodes:

$$C = \frac{1}{N} \sum_{i=1}^N C_i. \quad (5.10)$$

To characterize clustering at a global level, there is an alternative definition also known as transitivity T :

$$T = \frac{3 \times \text{number of triangles in the network}}{\text{number of connected triples of nodes}}. \quad (5.11)$$

Newman [2003] has shown that the results from both quantities can differ substantially depending on the network under consideration. For the example shown in Fig. 5.1 I obtain $C_1 = 1/6$ for the central node and $C_2 = 0$ for the top node. The average clustering coefficient and the transitivity are obtained as $C = 13/30$ and $T = 1/3$, respectively.

Concerning the question of synchronizability in the Erdős-Rényi random graph in dependence on the link probability p and the number of nodes N , the node degree is the most important network quantity.

5.3. Subgraphs and the percolation threshold

As discussed above, the Erdős-Rényi random graph shows a threshold in dependence on p and N below which the network is decomposed into several components that are not

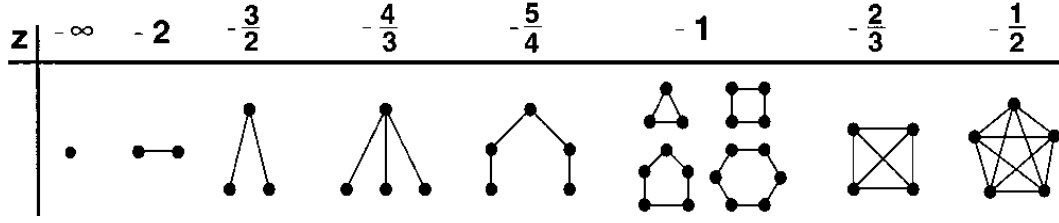


Figure 5.2.: Emergence of subgraphs in random graphs depending on the parameter z , which combines the link probability p and the number of nodes N as $p \sim N^z$. The values correspond to the threshold above which the respective subgraphs begin to emerge. [reproduced from [Albert and Barabási, 2002](#)].

connected to each other. [Bollobás \[2001\]](#) has shown that there are thresholds in the link probability p for certain subgraphs to appear until finally a fully connected network emerges.

Figure 5.2 shows the types of subgraphs that appear in a random network with increasing link probability p . The existence of these subgraphs can be characterized as follows [[Albert and Barabási, 2002](#)]: Assume that the link probability $p(N)$ in dependence on N scales as N^z , where z can take any value from $-\infty$ to 0. The occurrence of the subgraphs depicted in Fig. 5.2 can then be derived from the scaling parameter z . This parameter exhibits thresholds, above which certain subgraphs begin to appear. Because trees do not show stable synchronization (see Chapter 4), the completely connected subgraphs, i.e., all-to-all connected subgraphs, are the most interesting ones in the light of synchronization. As a generalization of the completely connected examples depicted in Fig. 5.2, the critical probability of having a completely connected subgraph with k nodes is given by $p \sim N^{-2/(k-1)}$. In particular, if z approaches zero, completely connected subgraphs of all sizes appear.

Going further, the size of the largest connected component can be characterized by deriving thresholds in dependence on the link probability [[Chung and Lu, 2001](#)]. Using the result that the average degree in a random graph is given by $\langle k \rangle = pN$, these thresholds are given as follows:

- $pN < 1$: Only isolated subgraphs exist.
- $pN > 1$: A giant component emerges. The diameter of this component is proportional to $\ln(N)/\ln(pN)$.
- $pN \geq \ln(N)$: Almost all realizations of networks are fully connected, i.e., there is a path between any two nodes.

5.4. The eigenvalue spectrum of random networks

For an undirected random network, the eigenvalue spectrum, which is crucial for the analysis of stability of synchronization using the master stability function, is known to follow a simple law under certain conditions.

If $z < 1$ in $p \sim N^{-z}$, there is a giant component (also referred to as infinite cluster) [Albert and Barabási, 2002]. Additionally, in the limit of $N \rightarrow \infty$ the probability that every node belongs to this component is converging to unity. In this case of a fully connected graph, the eigenvalue spectrum of the adjacency matrix follows a semicircular distribution according to

$$\rho(\gamma) = \begin{cases} \frac{\sqrt{4Np(1-p) - \gamma^2}}{2\pi Np(1-p)} & \text{if } |\gamma| < 2\sqrt{Np(1-p)} \\ 0 & \text{otherwise.} \end{cases} \quad (5.12)$$

One eigenvalue is separated from this distribution and is located at $\gamma = pN$ according to Albert and Barabási [2002]. In fact, in a network without feedback, where only the $N - 1$ off-diagonal entries in each row can be filled, this is rather $\gamma = p(N - 1)$, but Albert and Barabási approximated $N - 1 \approx N$. As we will see, this is the eigenvalue corresponding to the dynamics inside the synchronization manifold.

What I am interested in is not the eigenspectrum of the adjacency matrix, but that of the coupling matrix, thus Eq. (5.12) has to be transformed accordingly. As we have seen, in an undirected random graph each possible link in the network exists with a probability p . This is equivalent to the statement that in each row of the adjacency matrix, from the possible $N - 1$ off-diagonal entries, $p(N - 1)$ are present, i.e., have a value of 1. In the thermodynamic limit of $N \rightarrow \infty$ this expectation value is approached in all rows. Using the renormalization technique described in Sec. 5.1.2, each row has then to be divided by the sum over its entries, which is $p(N - 1)$ in this limit. In conclusion, if every row is divided by the same number, the whole matrix is divided by this number $p(N - 1)$. Hence, the eigenvalues of the coupling matrix that has unity row sum are given by those of the adjacency matrix times a factor $1/[p(N - 1)]$. As a consequence, the semicircular law for the coupling matrix reads

$$\rho(\gamma) = \begin{cases} \frac{\sqrt{4Np(1-p) - [\frac{\gamma}{p(N-1)}]^2}}{2\pi Np(1-p)} & \text{if } |\gamma| < \frac{2\sqrt{Np(1-p)}}{p(N-1)} \\ 0 & \text{otherwise.} \end{cases} \quad (5.13)$$

The eigenvalue that is separated from this distribution becomes transformed to $\gamma = 1$ which is exactly the row sum of this coupling matrix. Thus, this eigenvalue is the one describing stability inside the synchronization manifold.

For the characterization of the stability of synchronization, only the size of this distribution is important, but not its particular shape. In fact, it is sufficient for the network to desynchronize, if only one of the transversal eigenvalues from this distribution is outside of the stable region of the master stability function.

In the limit of large delay, the master stability function shows a rotational symmetry that was already discussed in Chapter 3. In the application to the random networks studied here, synchronization will be stable if the distribution (5.13) of eigenvalue is completely contained in the stable region of the master stability function. That is, the sharp boundary of the distribution, which is given by

$$|\gamma_b| = \frac{2\sqrt{Np(1-p)}}{p(N-1)} \quad (5.14)$$

according to Eq. (5.13) has to be inside the stable region. Let us assume the master stability function changes sign at $|\gamma_c|$, i.e., $\Lambda(\gamma) < 0$ for $|\gamma| < |\gamma_c|$. Then a random network will synchronize if

$$\gamma_b < \gamma_c. \quad (5.15)$$

In other words, given that the boundary of the stable region of the master stability function is located at a given value of $|\gamma_c|$, the critical link probability, above which synchronization is stable, is obtained by solving Eq. (5.14) for p :

$$p_{\text{crit}} = \frac{4N}{\gamma_c^2(N-1)^2 + 4N}. \quad (5.16)$$

For directed random networks I find the law (5.13) to describe the eigenvalue distribution equally well. Applying Eq. (5.13) to the absolute value of the then complex-valued spectrum $\{\gamma_i\}$ of a directed random graph matches the outcome of averaging over a number of realizations very well. Thus, Eq. (5.15) can also be used to characterize synchronization in a directed random network. I will show results for directed random networks of lasers in the following.

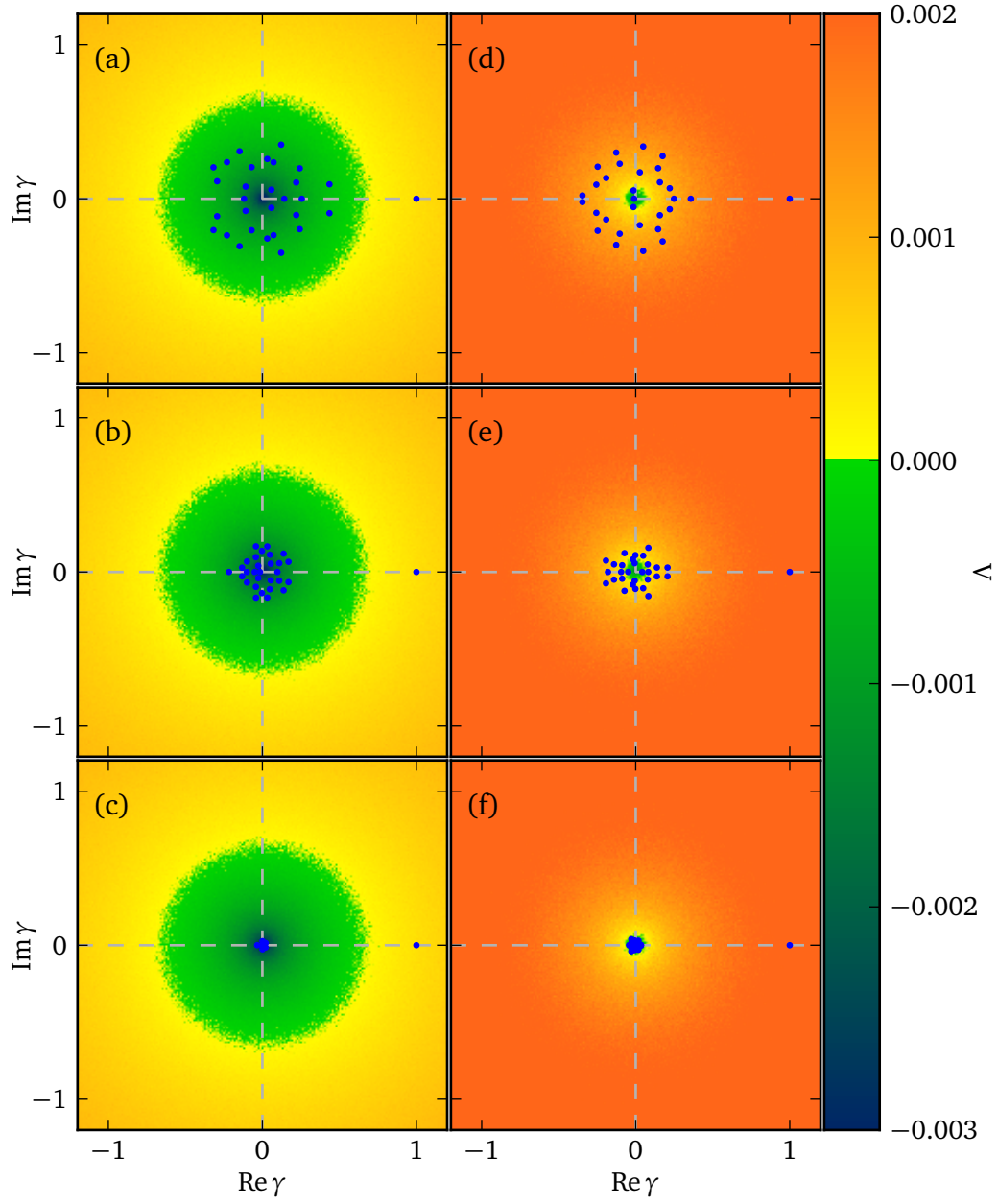


Figure 5.3.: Master stability function in the γ plane for a network of delay-coupled lasers according to Eq. (2.7). (a-c) LFF regime, (d-f) CC regime according to Tab. 2.2. The blue dots show the eigenvalue spectra from a single realization of a directed random graph with link probabilities (a) $p = 0.2$, (b) $p = 0.5$, (c) $p = 0.95$, (d) $p = 0.2$, (e) $p = 0.5$, and (f) $p = 0.95$.

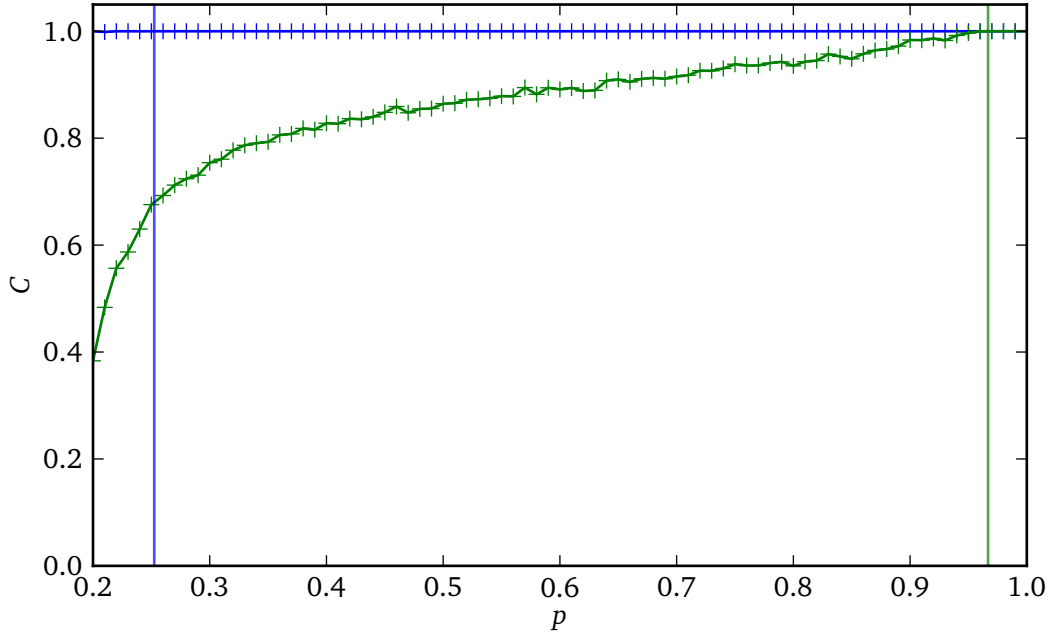


Figure 5.4.: Mean cross correlation in a directed random network of $N = 30$ lasers in dependence on the link probability p . Blue: LFF regime; green: CC regime, according to Tab. 2.2. The blue and green lines correspond to the threshold of stability according to Eq. (5.16) for the LFF and the CC regime, respectively.

5.5. Results for laser networks

Figure 5.3 shows the master stability function in the regimes of low-frequency fluctuations (LFF) and coherence collapse (CC) (see Sec. 2.2.1). Panels (a-c) correspond to the LFF regime, while panels (d-f) show results for the CC regime. In each panel I inserted the eigenvalues from one realization of a directed random graph with $N = 30$ nodes. In panels (a,d), (b,e), and (c,f), the link probability is chosen as $p = 0.2, 0.5$, and 0.95 , respectively. One eigenvalue is always located at $\gamma = 1$, which corresponds to perturbations longitudinal to the synchronization manifold as shown in Chapter 3. The other eigenvalues correspond to transversal directions and determine the stability of synchronization. It is clearly seen that in the LFF regime, any of these link probabilities lead to stable synchronization in the corresponding network, while in the CC regime only the very large value of $p = 0.95$ leads to synchronization.

To verify these predictions from the master stability function, I performed numerical simulations using $N = 30$ lasers in the corresponding random networks and calculated the mean cross correlation in order to characterize the degree of synchronization. The results are shown in Fig. 5.4 in dependence on the link probability p . The blue and green curves result from parameters in the LFF and in the CC regime, respectively. In order to obtain a smooth result, each data point is retrieved from averaging over 50 realizations of a random network with the corresponding link probability.

These results confirm the predictions from the master stability very well. For the LFF regime, synchronization is possible for any link probability in the range considered here. Note that I did not use link probabilities below $p = 0.2$, because this would cause interference with the percolation threshold under which the network is topologically separated into many components and synchronization is not possible for this structural reason alone.

For the CC regime, synchronization is only possible for very large link probabilities above $p \approx 0.95$. This could already be seen in Fig. 5.3.

The blue and green lines shown in Fig. 5.4 show the theoretical threshold of synchronization according to Eq. (5.16). These theoretical values do, however, not match the numerical results. While in the CC regime the threshold is only slightly off which could be caused by numerical fluctuations, no desynchronization can be seen for the LFF in the numerics near the analytic value of the threshold.

This discrepancy is most likely explained by the finite and relatively small number of nodes I used in the simulations. Remember that the semicircular law (5.12) from which I derived the analytic value for the threshold of synchronization is only valid in the limit of $N \rightarrow \infty$. It would be necessary to run numerical simulations for a significantly larger number of nodes, but since the numerical cost of such a simulation scales with the number of links in the network, which is $\sim \mathcal{O}(N^2)$ for fixed link probability p , this could not be done in the scope of this thesis.

5.6. The relation to motifs

At the beginning of Chapter 4 I introduced network motifs as the building blocks of larger complex networks. This was shown again in Sec. 5.3 where I have summarized the subgraphs that appear in a random graph with increasing link probability. One may argue that if the network motifs or subgraphs that are present in the graph do

not synchronize for given parameters, than a larger network constructed from these subgraphs cannot synchronize either.

Although different kinds of subgraphs occur in a random graph as shown in Sec. 5.3, I will focus on the completely connected subgraphs. Note that these completely connected subgraphs of order k are equivalent to all-to-all networks without feedback as introduced in Sec. 4.5.3. In that Section I showed that the minimum size of an all-to-all network that can synchronize is very different in the LFF and the CC regime. In the LFF regime, all-to-all networks with $N \geq 3$ could synchronize, while $N \geq 16$ is needed in the CC regime.

Now, in Sec. 5.3 I have shown that the size of the completely connected subgraphs increases with the link probability p . Subgraphs of order 3 are present even for very small link probabilities, leading to stable synchronization in the LFF regime already for these small probabilities. Completely connected subgraphs of order 16 – needed for synchronization in the CC regime – appear only at much higher values of the link probability. Keeping in mind that the number of node of the networks considered was $N = 30$, an almost unity link probability is needed to achieve all-to-all networks of size 16 in the network. This explains the differences in the critical link probabilities for the LFF and the CC regime in a qualitative but intuitive way.

5.7. Conclusion

Using the example of Erdős-Rényi random graphs, I have shown how the master stability function can be used to characterize stability of synchronization in large complex networks. With an analytic expression for the boundary of the eigenvalue spectrum, I demonstrated that the question of synchronizability may be reduced to the relation between this boundary and the boundary of the master stability function. In particular in the case of large delay, where the master stability function is rotationally symmetric in the complex plane, a single equation remains. The outcome of this equation does, however, not completely match the results from numerical simulation, which is likely caused by a finite-size effect.

I also drew the connection between synchronizability in complex networks and the occurrence of subgraphs or network motifs inside of these. This allows for an intuitive explanation of the differences between the LFF and the CC regime with regard to stability of synchronization in complex networks.

6. Multiple coupling matrices

Following the idea by [Flunkert \[2010, 2011\]](#) and [Englert et al. \[2011\]](#), stability of isochronous synchronization in a network with multiple coupling matrices can be determined by a master stability function if these multiple coupling matrices commute with each other. This is particularly interesting in the light of multiple delays in a network. These multiple delays may, for instance, arise due to differences in the physical length of links, as I will show using an example.

I will review the dynamical equations with multiple coupling contributions and introduce an example topology with two coupling matrices in Sec. 6.1. In Sections 6.2 and 6.3 I will show what matrices can be used in general and what problems arise for the calculation of the eigenvalue spectrum. Results for the example of a ring with coupling to the nearest and next-nearest neighbors will be presented in Sections 6.4, 6.5 and 6.6.

6.1. Multiple coupling contributions

Initially aiming at the ability to have multiple time delays in a network, [Flunkert \[2010, Sec. 10.7\]](#) looked at node differential equations of the form¹

$$\dot{\mathbf{x}}_i = \mathbf{F}(\mathbf{x}_i) + \sigma^{(1)} \sum_{j=1}^N G_{ij}^{(1)} \mathbf{H}^{(1)} \mathbf{x}_j(t - \tau^{(1)}) + \sigma^{(2)} \sum_{j=1}^N G_{ij}^{(2)} \mathbf{H}^{(2)} \mathbf{x}_j(t - \tau^{(2)}) \quad (6.1)$$

Note that, in order to operate in the same output regime of the laser, the sum of the coupling strengths $\sigma^{(1)}$ and $\sigma^{(2)}$ has to yield the overall coupling strength σ used with one coupling matrix as in Chapter 2: $\sigma^{(1)} + \sigma^{(2)} = \sigma$.

If the matrices $\mathbf{G}^{(1)}$ and $\mathbf{G}^{(2)}$ commute, i.e., $[\mathbf{G}^{(1)}, \mathbf{G}^{(2)}] = \mathbf{G}^{(1)}\mathbf{G}^{(2)} - \mathbf{G}^{(2)}\mathbf{G}^{(1)} = 0$, they diagonalize with the same set of eigenvectors. Then, a master stability function Λ can

¹In fact, the notation was slightly different, I use the notation of this thesis for convenience.

be calculated as a function of the eigenvalue spectra $\gamma^{(1)}$ and $\gamma^{(2)}$ of both $\mathbf{G}^{(1)}$ and $\mathbf{G}^{(2)}$, respectively:

$$\Lambda = \Lambda(\sigma^{(1)}\gamma^{(1)}, \sigma^{(2)}\gamma^{(2)}). \quad (6.2)$$

From Eq. (6.1) it can be seen that different coupling schemes \mathbf{H} and time delays τ can be used for each coupling term. Let me give an example of matrices that do commute. Consider a network coupled in a generalized bidirectional ring where every node is coupled to its nearest and next-nearest neighbors. This is described by the coupling matrix

$$\mathbf{G} = \frac{1}{2} \begin{pmatrix} 0 & 1 & 1 & 0 & 0 & 0 & \cdots & 0 & 1 & 1 \\ 1 & 0 & 1 & 1 & 0 & 0 & \cdots & 0 & 0 & 1 \\ 1 & 1 & 0 & 1 & 1 & 0 & \cdots & 0 & 0 & 0 \\ 0 & 1 & 1 & 0 & 1 & 1 & \cdots & 0 & 0 & 0 \\ & & & \ddots & & & & & & \end{pmatrix}. \quad (6.3)$$

The network can be split up using two coupling matrices: $\mathbf{G}^{(1)}$ for the nearest-neighbor couplings and $\mathbf{G}^{(2)}$ for the next-nearest neighbors:

$$\mathbf{G}^{(1)} = \begin{pmatrix} 0 & 1 & 0 & 0 & 0 & 0 & \cdots & 0 & 0 & 1 \\ 1 & 0 & 1 & 0 & 0 & 0 & \cdots & 0 & 0 & 0 \\ 0 & 1 & 0 & 1 & 0 & 0 & \cdots & 0 & 0 & 0 \\ 0 & 0 & 1 & 0 & 1 & 0 & \cdots & 0 & 0 & 0 \\ & & & \ddots & & & & & & \end{pmatrix}, \quad (6.4)$$

$$\mathbf{G}^{(2)} = \begin{pmatrix} 0 & 0 & 1 & 0 & 0 & 0 & \cdots & 0 & 1 & 0 \\ 0 & 0 & 0 & 1 & 0 & 0 & \cdots & 0 & 0 & 1 \\ 1 & 0 & 0 & 0 & 1 & 0 & \cdots & 0 & 0 & 0 \\ 0 & 1 & 0 & 0 & 0 & 1 & \cdots & 0 & 0 & 0 \\ & & & \ddots & & & & & & \end{pmatrix}. \quad (6.5)$$

These matrices do commute, which can easily be seen by calculating the products $\mathbf{G}^{(1)}\mathbf{G}^{(2)}$ and $\mathbf{G}^{(2)}\mathbf{G}^{(1)}$, and have eigenvalues

$$\gamma_m^{(1)} = \cos\left(\frac{2\pi m}{N}\right), \quad m = 1, \dots, N \quad (6.6)$$

and

$$\gamma_m^{(2)} = \cos\left(\frac{4\pi m}{N}\right), \quad m = 1, \dots, N, \quad (6.7)$$

respectively. These eigenvalues are purely real, allowing to omit the imaginary parts of the master stability function, which is then dependent purely on the real parts of $\gamma^{(1)}$ and $\gamma^{(2)}$:

$$\Lambda = \Lambda(\text{Re } \gamma^{(1)}, \text{Re } \gamma^{(2)}). \quad (6.8)$$

Note that the eigenvalues of both matrices corresponding to the same eigenvector have to be used simultaneously, which leads to pairs of $(\gamma_k^{(1)}, \gamma_k^{(2)})$ for $k = 1, \dots, N$ at which the master stability function has to be evaluated.

The formalism can be extended to an arbitrary number of matrices M , which is especially interesting for the use of many different coupling delays. The condition of commutativity must be fulfilled for every pair of these matrices.

6.2. Finding the eigenvalue pairs

In order to evaluate the master stability function for two coupling matrices, the pairs of eigenvalues $(\gamma_k^{(1)}, \gamma_k^{(2)})$, $k = 1, \dots, N$, have to be considered. That is, $\gamma_k^{(1)}$ and $\gamma_k^{(2)}$ have to correspond to the same eigenvector.

For regular matrices based on ring structures, this task is easy, since the pairs can be calculated following a simple rule. Ring structures are special cases of circulant matrices, which share an identical set of eigenvectors. This way, for pairs of circulant matrices, the pairs of eigenvalues are given explicitly, as I will show in Sec. 6.3. Equations (6.6) and (6.7) were obtained in this way.

In networks that do not fall into this class, but still commute, this task is comparatively more complicated. For larger matrices, joint diagonalization algorithms have been developed that can be easily implemented numerically. Notable work has been done by [Cardoso and Souloumiac \[1996\]](#), as well as by [Ziehe et al. \[2004\]](#). The former approach works even for only approximately jointly diagonalizable matrices, which may potentially be useful for multiple complex coupling matrices that do not commute exactly. However, in the example used in this Chapter the application of these algorithms is not needed because they fall into the class of circulant matrices.

6.3. Matrices that commute

In general, matrices that describe real-world complex networks or those that are constructed from random matrix models, e.g., Erdős-Rényi [Erdős and Rényi, 1959, 1960], Price, Barabási-Albert [Barabási and Bonabeau, 2003], or Watts-Strogatz [Watts and Strogatz, 1998] do not commute, as randomly distributed links do not tend to cancel in the commutator $[\mathbf{G}^{(1)}, \mathbf{G}^{(2)}] = \mathbf{G}^{(1)}\mathbf{G}^{(2)} - \mathbf{G}^{(2)}\mathbf{G}^{(1)}$. Certain insular realizations of such networks may of course commute as a special case.

Regular networks, on the other hand, may show structures that lead to a cancellation of both contributions in the commutator. By performing the calculation of $[\mathbf{G}^{(1)}, \mathbf{G}^{(2)}]$ it is, for example easily seen that matrices (6.4) and (6.5) from the Section above do commute. Indeed, one can show that matrices describing rings of all kinds commute with each other, i.e., form a commutative algebra.

Rings belong to the class of circulant matrices that were introduced already in Chapter 4. A circulant matrix is of the form

$$\mathbf{C} = \begin{pmatrix} c_1 & c_N & \cdots & c_3 & c_2 \\ c_2 & c_1 & c_N & & \\ \vdots & c_2 & c_1 & \ddots & \vdots \\ c_{N-1} & & \ddots & \ddots & c_N \\ c_N & c_{N-1} & \cdots & c_2 & c_1 \end{pmatrix}, \quad (6.9)$$

where the $c_k \in \mathbb{C}$, $k = 1, \dots, N$. The ring matrices (6.3), (6.4), and (6.5) can be constructed from this general form by choosing the c_k appropriately.

Circulant matrices form a commutative algebra [Gray, 2006; Golub and van Loan, 1996]. Any circulant matrix \mathbf{C} has the same set of eigenvectors \mathbf{v}_k according to (4.27),

$$\mathbf{v}_k = (1, \omega_k, \omega_k^2, \dots, \omega_k^{N-1}). \quad (6.10)$$

with $\omega_k = \exp(2\pi i k/N)$. Therefore, the matrix \mathbf{S} that contains these eigenvectors and diagonalizes \mathbf{C} as

$$\text{diag}(\gamma_k) = \mathbf{S}^* \mathbf{C} \mathbf{S} \quad (6.11)$$

is identical for any circulant matrix \mathbf{C} . Thus, any two circulant matrices commute.

Using the identical set of eigenvectors \mathbf{v}_k and the formula (4.26), which determines the corresponding eigenvalues of a circulant matrices, it is easy to calculate the pairs of

eigenvalues of two circulant matrices that belong to the same eigenvector. These pairs are used in the evaluation of the master stability function.

6.4. Nearest and next-nearest neighbors

Let me come back to the example of coupling to next and next-nearest neighbors. It is particularly interesting to investigate the effects of different delay times for both coupling matrices. This is motivated by the intuition that the delay time for a physically longer connection is potentially larger. Investigations with different delay times have already been performed for identical coupling matrices for the Bernoulli map [Englert et al., 2010], the logistic map [Greenshields, 2010], but also in a laser model [Englert et al., 2011].

6.5. Master stability function for different delay times

The master stability function itself depends on the two time delays $\tau^{(1)}$ and $\tau^{(2)}$, because the synchronous dynamics

$$\dot{\mathbf{x}}_s = \mathbf{F}[\mathbf{x}_s(t)] + \sigma^{(1)}\mathbf{H}^{(1)}\mathbf{x}_s(t - \tau^{(1)}) + \sigma^{(2)}\mathbf{H}^{(2)}\mathbf{x}_j(t - \tau^{(2)}) \quad (6.12)$$

depends on these delay times, but also the corresponding variational equation

$$\delta\dot{\tilde{\mathbf{x}}} = D\mathbf{F}|_{\mathbf{x}_s(t)}\delta\tilde{\mathbf{x}}(t) + \sigma^{(1)}\gamma^{(1)}\mathbf{H}^{(1)}\delta\tilde{\mathbf{x}}(t - \tau^{(1)}) + \sigma^{(2)}\gamma^{(2)}\mathbf{H}^{(2)}\delta\tilde{\mathbf{x}}(t - \tau^{(2)}), \quad (6.13)$$

from which the master stability function is calculated. The coupling schemes are kept identical $\mathbf{H}^{(1)} = \mathbf{H}^{(2)} = \mathbf{H}$ as in Chapter 2. The coupling strengths are chosen as $\sigma^{(1)} = \sigma^{(2)} = \sigma/2$.

6.6. The influence of the delay times

Figure 6.1 shows the master stability function arising from Eq. (6.13) in dependence on the parameters $\text{Re}\gamma^{(1)}$ and $\text{Re}\gamma^{(2)}$ for different values of the delay time for the longer-range couplings $\mathbf{G}^{(1)}$, $\tau^{(1)}$, while the other delay time – corresponding to the shorter-range coupling $\mathbf{G}^{(2)}$ – is fixed at $\tau^{(2)} = 1000$. Figures 6.1(a-f) correspond to $\tau^{(1)} = 250, 500, 750, 1000, 1500$, and 2000 , respectively. The other parameters

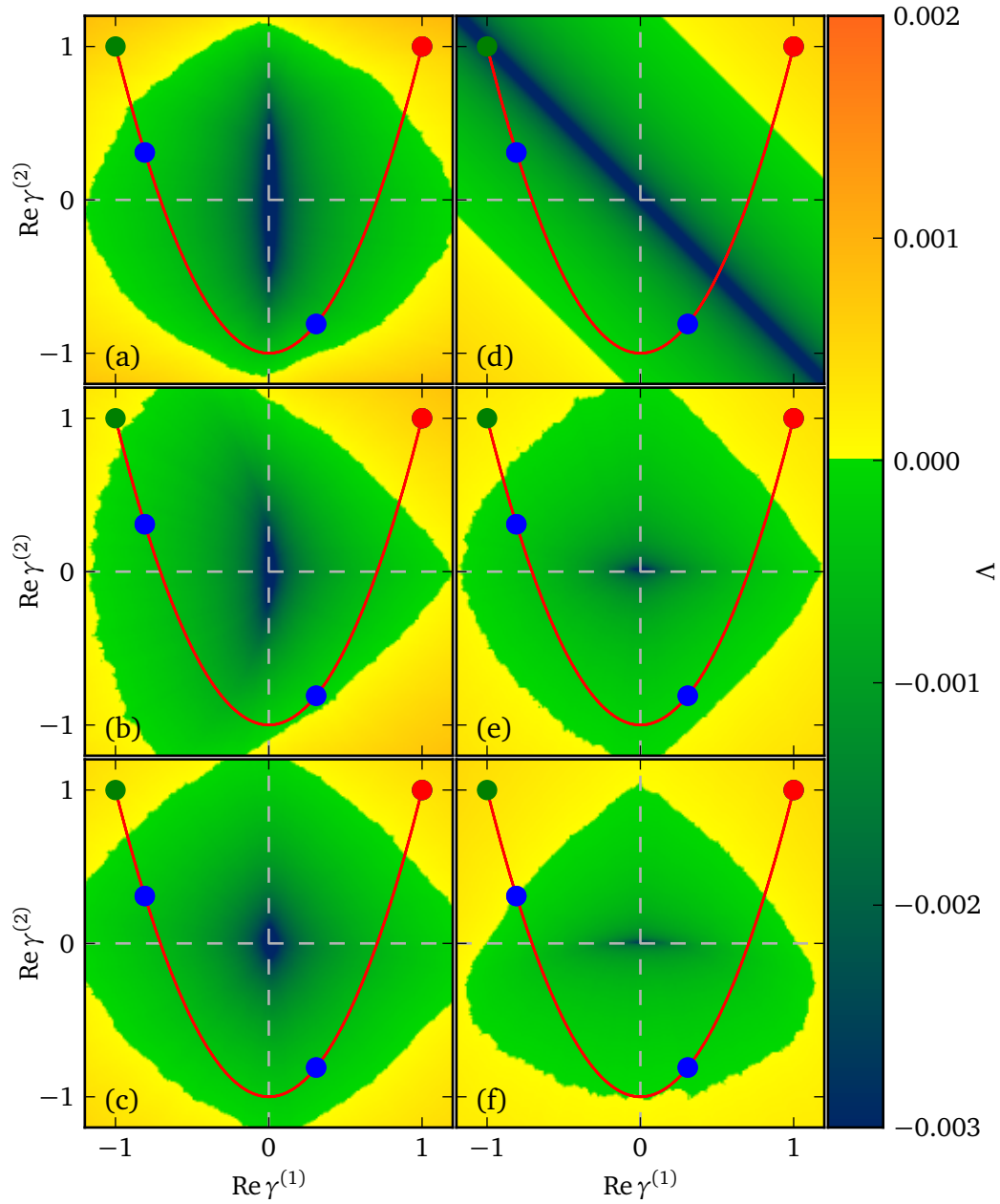


Figure 6.1.: Master stability function in dependence on the parameters $\text{Re } \gamma^{(1)}$ and $\text{Re } \gamma^{(2)}$ of two coupling matrices for different values of the delay time $\tau^{(1)}$ and fixed $\text{Im } \gamma^{(1)} = \text{Im } \gamma^{(2)} = 0$. (a-f): $\tau^{(1)} = 250, 500, 750, 1000, 1500$, and 2000 , respectively. $\sigma^{(1)} = \sigma^{(2)} = \sigma/2$ with $\sigma = 0.12$, $\tau^{(2)} = 1000$ and other parameters in the LFF regime in Tab. 2.2. Red dot: longitudinal eigenvalue pair $(1, 1)$, red line: general location of eigenvalue pairs of matrices (6.4) and (6.5), green and blue dots: transversal eigenvalue pairs of matrices (6.4) and (6.5) for $N = 2$ and $N = 5$, respectively.

are chosen to operate in the regime of low-frequency fluctuations (LFF) according to Tab. 2.2.

From the different panels in Fig. 6.1 it can be seen that choosing different delay times has no positive influence on the size of the stable region of the master stability function. The region is largest for identical time delays $\tau^{(1)} = \tau^{(2)} = 1000$. In this case it is also symmetric with respect to exchange of $\text{Re}\gamma^{(1)}$ and $\text{Re}\gamma^{(2)}$, which is due to the identical coupling terms in the synchronous dynamics (6.12). For other choices of the delay time $\tau^{(1)}$, i.e., non-unity ratios of $\tau^{(1)}$ and $\tau^{(2)}$, the stable region is smaller in comparison.

Also plotted in Fig. 6.1 are the locations of the eigenvalue pairs of the example matrices (6.4) and (6.5). The eigenspectra of these matrices follow Eqs. (6.6) and (6.7), respectively. For any number of nodes N , the eigenvalue pairs lie always on the red line that is depicted in Fig. 6.1. This line would be densely filled with eigenvalue pairs in the limit $N \rightarrow \infty$. The longitudinal eigenvalue pair $(1, 1)$ that is always present is shown as a red dot. The master stability function evaluated at this point is the longitudinal Lyapunov exponent, which determines whether the dynamics is chaotic. As can be seen, the color code at this point changes depending on $\tau^{(1)}$, i.e., the longitudinal Lyapunov exponent differs slightly. Nonetheless, the dynamics is chaotic for all choices of $\tau^{(1)}$.

The green and blue dots show the transverse eigenvalue pairs for $N = 2$ and $N = 5$, respectively, as examples. For $\tau^{(1)} = 1000$ the network with $N = 2$ can synchronize in a stable manner, which is not the case for any other choice of the delay time $\tau^{(1)}$. Concerning the example $N = 5$, it can synchronize for all choices of $\tau^{(1)}$ shown here. Note that for $\tau^{(1)} = 2000$ shown in Fig. 6.1(f), one transverse eigenvalue is just at the border of the stable region of the master stability function. For any higher value of N some of the transverse eigenvalue pairs will be outside the green – stable – region. For the other choices of the delay time $\tau^{(1)}$, the threshold for the number of nodes that can synchronize in this setup differs and has to be calculated considering the point where the red line crosses from the stable green to the unstable yellow region.

6.7. Conclusion

In conclusion, in this example of coupled lasers, different delay times do not enhance or improve synchronization in a significant way. This may be different for other models and also for smaller delay times in the Lang-Kobayashi model used here. As shown in Chapter 3, the shape of the master stability is no longer circular for a single small

delay. The effect of multiple small delays on synchronizability would be an interesting continuation of this investigations.

Overall, the use of multiple coupling matrices enables the use of multiple delays for all links in a single topology, but also the use of topologies where some links have different delays than others. The different coupling matrices that this yields have to obey the condition of being commutative.

7. Control of synchronization in oscillator networks

The results of the previous Chapters in this part of the thesis, in particular the stability analysis introduced in Chapter 3, hold for any type of system governing the local dynamics of the network's nodes, which can include fixed-point, periodic, or chaotic dynamics. The master stability function evaluated in terms of the largest Lyapunov exponent has proven to be a general and powerful method for determining stability of synchronization.

For periodic and fixed-point dynamics, instead of using Lyapunov exponents, stability can be described by Floquet exponents and eigenvalues of the Jacobian, respectively. This eases the numerical treatment, as analytic expressions can be derived in some cases.

In this Chapter, I use the generic Stuart-Landau model for periodic dynamics describing a wide range of systems near a Hopf bifurcation. This model allows for an analytical treatment, including the calculation of the Floquet exponents.

I develop analytical tools for determining stability of synchronization and derive analytical conditions for controlling the different states of synchrony [Choe et al., 2010, 2011] in networks of Stuart-Landau oscillators. I identify the phase of the complex coupling constant as a crucial control parameter and demonstrate that by adjusting this phase one can deliberately switch between synchronization and desynchronization.

7.1. The Stuart-Landau oscillator

The Stuart-Landau oscillator is a generic oscillator model, which arises naturally as an expansion in center-manifold coordinates around a Hopf bifurcation. A Hopf bifurcation occurs in a variety of systems, e.g. in semiconductor lasers [Tronciu et al., 2000] or in models for neuronal dynamics like the FitzHugh-Nagumo [FitzHugh, 1961; Nagumo

et al., 1962] or the Morris-Lecar model [Tsumoto et al., 2006]. In the type-II excitable FitzHugh-Nagumo model, for example, a Hopf bifurcation lies between the excitable and the oscillatory regime. The Stuart-Landau model is given as follows: In the center manifold, the dynamics of a complex variable $z \in \mathbb{C}$ is governed by the differential equation

$$f(z) = [\lambda + i\omega \mp (1 + i\gamma)|z|^2] z. \quad (7.1)$$

Here, the $-$ and $+$ signs describe a supercritical or a subcritical Hopf bifurcation, respectively. λ acts as a bifurcation parameter as illustrated in Fig. 7.1:

Subcritical Hopf bifurcation: The system shows a stable focus for $\lambda < 0$, surrounded by an unstable limit cycle with radius $\sqrt{-\lambda}$. Passing $\lambda = 0$, the limit cycle disappears and the focus becomes unstable.

Supercritical Hopf bifurcation: For $\lambda < 0$, only a stable focus exists. At $\lambda = 0$, a stable limit cycle with radius $\sqrt{\lambda}$ is born while the focus loses stability.

The time evolution $\dot{z}(t) = f[z(t)]$ of the Stuart-Landau oscillator can be rewritten in amplitude $r(t)$ and phase $\varphi(t)$ of the complex variable $z(t) = r(t)e^{i\varphi(t)}$:

$$\begin{aligned} \dot{r} &= (\lambda \mp r^2)r, \\ \dot{\varphi} &= \omega \mp \gamma r^2. \end{aligned} \quad (7.2)$$

From these equations the existence of the fixed points and periodic orbits described above can already be seen. Equation (7.2) also reveals that the parameters ω and γ determine the period of the limit cycle in both cases, which is given by $T = 2\pi/(\omega - \gamma\lambda)$. In particular, the choice of γ influences the period's dependence on the radius, which is determined by λ .

In this work, I focus on the supercritical case ($-$) and the parameter λ chosen as $\lambda = 0.1$, such that already the uncoupled system operates on a stable limit cycle. In the next Section, I show the dynamical equations of N such Stuart-Landau oscillators coupled in a network.

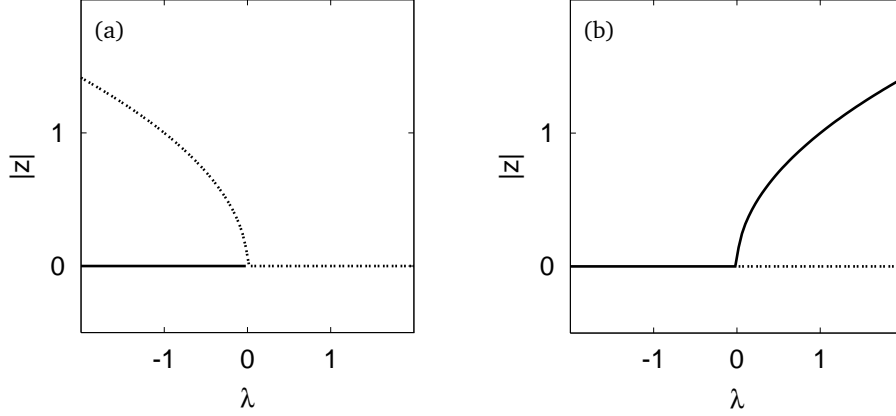


Figure 7.1.: (a) Subcritical and (b) supercritical Hopf bifurcation: Radius of oscillations and stability in dependence on the bifurcation parameter λ . Solid and dashed lines denote stable and unstable states, respectively.

7.2. Oscillator networks

Consider N oscillatory nodes in a network, where each node ($j = 1, \dots, N$) is modeled by the same local dynamics, given by the Stuart-Landau oscillator (7.1):

$$\dot{z}_j = f[z_j(t)] + \sigma \sum_{n=1}^N G_{jn} [z_n(t - \tau) - z_j(t)], \quad (7.3)$$

with time delay τ and complex coupling strength $\sigma = Ke^{i\beta} \in \mathbb{C}$. The topology of the network is determined by the real-valued coupling matrix $\mathbf{G} = \{G_{jn}\}$.

The complex coupling strength. Such complex couplings have been shown to be important in overcoming the odd-number limitation of time-delayed feedback control [Fiedler et al., 2007] and in anticipating chaos synchronization [Pyragas and Pyragiene, 2008].

The phase β of the complex coupling strength can also be understood as a mixing strength between real and imaginary part of the z_j : Let $z_j = x_j + iy_j$; then Eq. (7.3) can

also be rewritten in the form

$$\begin{pmatrix} \dot{x}_j \\ \dot{y}_j \end{pmatrix} = \begin{pmatrix} \operatorname{Re}[f(x_j + iy_j)] \\ \operatorname{Im}[f(x_j + iy_j)] \end{pmatrix} + K \begin{pmatrix} \cos(\beta) & \sin(\beta) \\ -\sin(\beta) & \cos(\beta) \end{pmatrix} \sum_{n=1}^N G_{jn} \begin{pmatrix} x_n(t - \tau) - x_j(t) \\ y_n(t - \tau) - y_j(t) \end{pmatrix}. \quad (7.4)$$

In other words, seeing x and y as two variables instead of real and imaginary part of z , the phase β acts as the angle in the rotational matrix in the above equation, $\beta = 0$ results in an identity matrix. This rotational matrix is a special case of non-diagonal coupling. Already for the stabilization of fixed points in the Hopf normal form it has been shown that the introduction of such a coupling phase can enhance or impair the domain of stability [Hövel and Schöll, 2005; Dahms et al., 2007]. This has later been applied to a laser model where the phase is an important parameter in the external feedback loop [Dahms et al., 2008]; see also Sec. 2.4.

The coupling matrix. The coupling matrix is introduced in the same way as for laser networks; its entries may be real numbers. Nonzero diagonal elements, for instance, correspond to networks with delayed self-feedback. In the following, I consider only unity row sum $\sum_n G_{jn} = 1$ such that each node is subject to the same input in the case of complete synchronization. This generalizes the common assumption of zero row sum in the master stability function approach [Pecora and Carroll, 1998] as in the laser networks in Chapter 3. Note that a constant but non-unity row sum can be dealt with by adjusting the overall coupling strength K .

7.2.1. Synchronous oscillator dynamics

In order to study stability, one has to describe first the synchronous dynamics. Let me first write Eq. (7.3) in amplitude and phase variables $r_j = |z_j|$ and $\varphi_j = \arg(z_j)$:

$$\begin{aligned} \dot{r}_j &= \left[\lambda - r_j^2(t) \right] r_j(t) \\ &\quad + K \sum_{n=1}^N G_{jn} \left\{ r_n(t - \tau) \cos [\beta + \varphi_n(t - \tau) - \varphi_j(t)] - r_j(t) \cos \beta \right\}, \\ \dot{\varphi}_j &= \omega - \gamma r_j^2(t) \\ &\quad + K \sum_{n=1}^N G_{jn} \left\{ \frac{r_n(t - \tau)}{r_j(t)} \sin [\beta + \varphi_n(t - \tau) - \varphi_j(t)] - \sin \beta \right\}. \end{aligned} \quad (7.5)$$

Two kinds of synchronous solutions can be found from this equation:

In-phase (or zero-lag) synchronization: All oscillators share a common radius r_0 and a common phase, oscillating with a common frequency Ω :

$$\begin{aligned} r_j(t) &= r_0, \\ \varphi_j(t) &= \Omega t, \quad j = 1, \dots, N. \end{aligned} \quad (7.6)$$

Cluster and splay states: All oscillators share a common amplitude r_0 and frequency Ω , but there are constant differences in their phase variables:

$$\begin{aligned} r_j(t) &= r_0, \\ \varphi_j(t) &= \Omega t + j\Delta\phi_m, \quad j = 1, \dots, N, \end{aligned} \quad (7.7)$$

with

$$\Delta\phi_m = 2\pi m/N. \quad (7.8)$$

The integer $m = 0, \dots, N-1$ determines the specific state: The cluster number d_c , which determines how many clusters of oscillators exist, is given by the least common multiple (lcm) of m and N divided by m :

$$d_c = \frac{\text{lcm}(m, N)}{m} \quad (7.9)$$

for $m = 1, \dots, N-1$. $d_c = N$ corresponds to a splay state [Zillmer et al., 2007]. $m = 0$ resembles in-phase synchronization ($d_c = 1$), although Eq. (7.9) cannot be used in this case.

Note that in general more complex cluster states may exist as solutions of the dynamical system, for instance, states with non-uniform phase differences or different number of nodes in each cluster. The analysis shown in this Chapter uses states of the form (7.7) with constant phase differences according to Eq. (7.8).

Fig. 7.2 shows the possible scenarios for the simple example of 4 nodes coupled in a uni-directional ring. I will focus on in-phase synchronization according to Eq. (7.6) in this Chapter and extend the theory to cluster and splay states in Chapter 10.

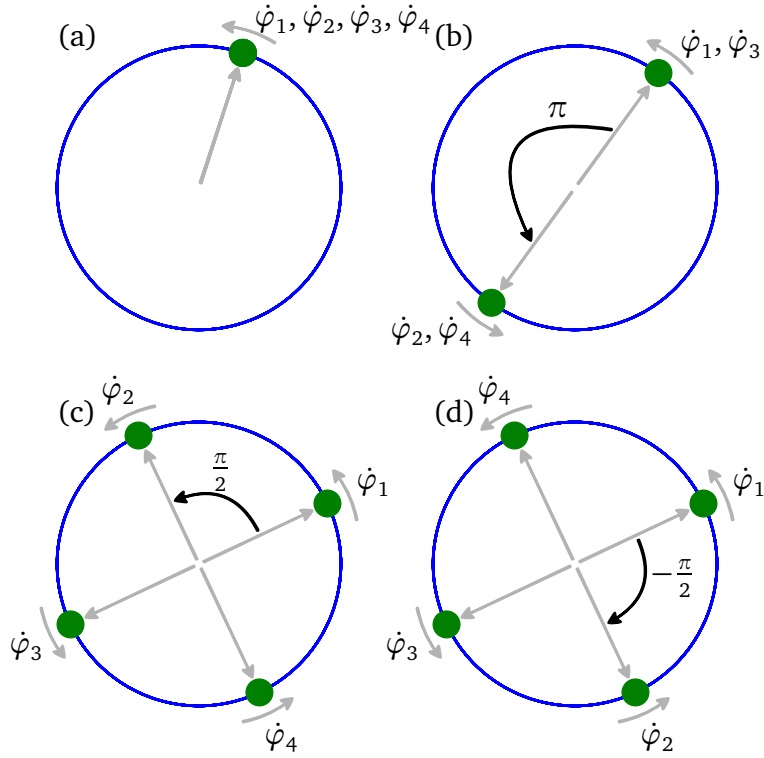


Figure 7.2.: Schematic view of (a) in-phase, (b) two-cluster, and (c)-(d) splay states in a network with 4 oscillators. The phase differences are $\Delta\phi_0 = 0$, $\Delta\phi_2 = \pi$, $\Delta\phi_1 = \pi/2$, and $\Delta\phi_3 = 3\pi/2$ in panels (a), (b), (c), and (d), respectively, according to Eqs. (7.8) and (7.9).

7.3. Stability of in-phase synchronization

Looking at Eq. (7.6), which describes in-phase dynamics, the common radius r_0 and frequency Ω are yet to be determined. Given that such a common frequency Ω exists, I can write

$$\varphi_j(t) - \varphi_n(t - \tau) = \Omega\tau \quad (7.10)$$

for any pair of nodes (j, n) . Using this and Eq. (7.6), we obtain the common radius and frequency by solving Eq. (7.5) for r_0^2 and Ω :

$$\begin{aligned} r_0^2 &= +\{\lambda + K [\cos(\beta - \Omega\tau) - \cos\beta]\}, \\ \Omega &= \omega - \gamma r_0^2 + K [\sin(\beta - \Omega\tau) - \sin\beta], \end{aligned} \quad (7.11)$$

This is a set of transcendental equations for r_0 and Ω . It cannot be solved analytically. Numerical solution yields a multi-leaved structure as shown in Figs. 7.3 and 7.4 in dependence on the time delay τ for different coupling parameters. Namely, the amplitude of the coupling strength was chosen as $K = 0.3$ in Fig. 7.3, while it is $K = 0.7$ in Fig. 7.4. The phase of the coupling strength was fixed at $\beta = 0$.

Panels (a) and (b) show the collective frequency Ω and the squared collective radius r_0^2 , respectively, in both Figures. The collective frequency Ω is distributed around the intrinsic frequency $\omega = 1$, where multiple solutions are obtained with increasing time delay τ . This behavior becomes more pronounced for higher K (Fig. 7.4). The collective amplitude also shows this multivalued behavior. That is, for a given value of the time delay τ and the coupling strength's amplitude K , one obtains different possible solutions for the common amplitude r_0 and frequency Ω . The degree of this multistability increases with higher values of the time delay τ . Spurious solutions with $r_0^2 < 0$ – indicated by red color – can be observed. These would result in nonreal radii r_0 which correspond to amplitude death, i.e., no oscillations occur in this range.

As most of our calculations regarding stability of synchronization are based on calculating Floquet exponents – as opposed to running direct simulations – it is crucial to ensure that only stability of physical solutions $r_0^2 \geq 0$, i.e., blue colored solutions in Figs. 7.3 and 7.4, is calculated. I will come back to this later in the next Section.

7.3.1. Obtaining the master stability function

Stability analysis is carried out by forming variational equations from the equations describing the network dynamics. These variational equations can be diagonalized in a fashion similar to Chapter 3, which decouples the calculation of the Floquet exponents from the network topology.

As it turns out, forming variational equations from the synchronous network dynamics becomes most simple when using the ansatz $r_j(t) = r_0[1 + \delta r_j(t)]$, $\varphi_j(t) = \Omega t + \delta \varphi_j(t)$.

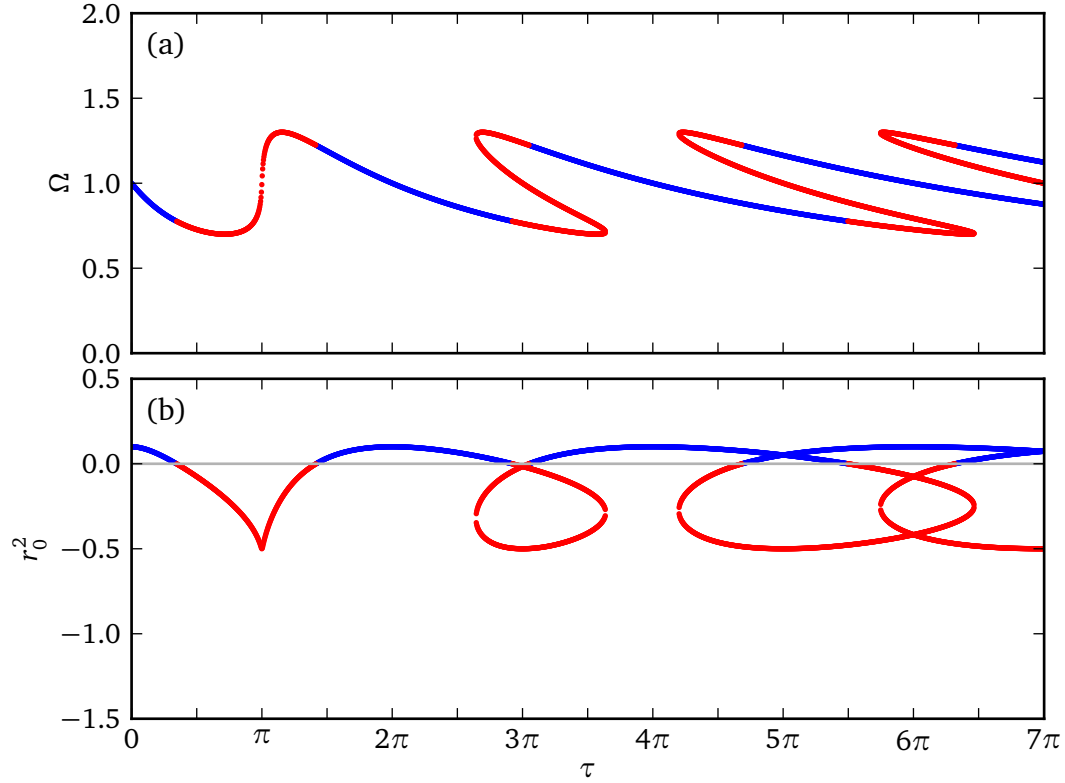


Figure 7.3.: (a) Collective frequency Ω and (b) squared amplitude r_0^2 of in-phase oscillation vs. time delay τ for coupling strength $K = 0.3$ and phase $\beta = 0$. Blue and red curves correspond to physical and unphysical solutions, i.e. $r_0^2 \geq 0$ and < 0 , respectively. Parameters: $\lambda = 0.1$, $\omega = 1$, $\gamma = 0$.

Expanding Eq. (7.5) to linear order in the small deviations δr_j and $\delta \varphi_j$, I obtain the variational equation

$$\begin{pmatrix} \delta \dot{r}_j \\ \delta \dot{\varphi}_j \end{pmatrix} = \begin{pmatrix} -2r_0^2 & 0 \\ -2\gamma r_0^2 & 0 \end{pmatrix} \begin{pmatrix} \delta r_j \\ \delta \varphi_j \end{pmatrix} - K \begin{pmatrix} \cos \Delta & -\sin \Delta \\ \sin \Delta & \cos \Delta \end{pmatrix} \begin{pmatrix} \delta r_j \\ \delta \varphi_j \end{pmatrix} + K \sum_n G_{jn} \begin{pmatrix} \cos \Delta & -\sin \Delta \\ \sin \Delta & \cos \Delta \end{pmatrix} \begin{pmatrix} \delta r_n(t - \tau) \\ \delta \varphi_n(t - \tau) \end{pmatrix}, \quad (7.12)$$

where I abbreviate $\Delta = \beta - \Omega\tau$.

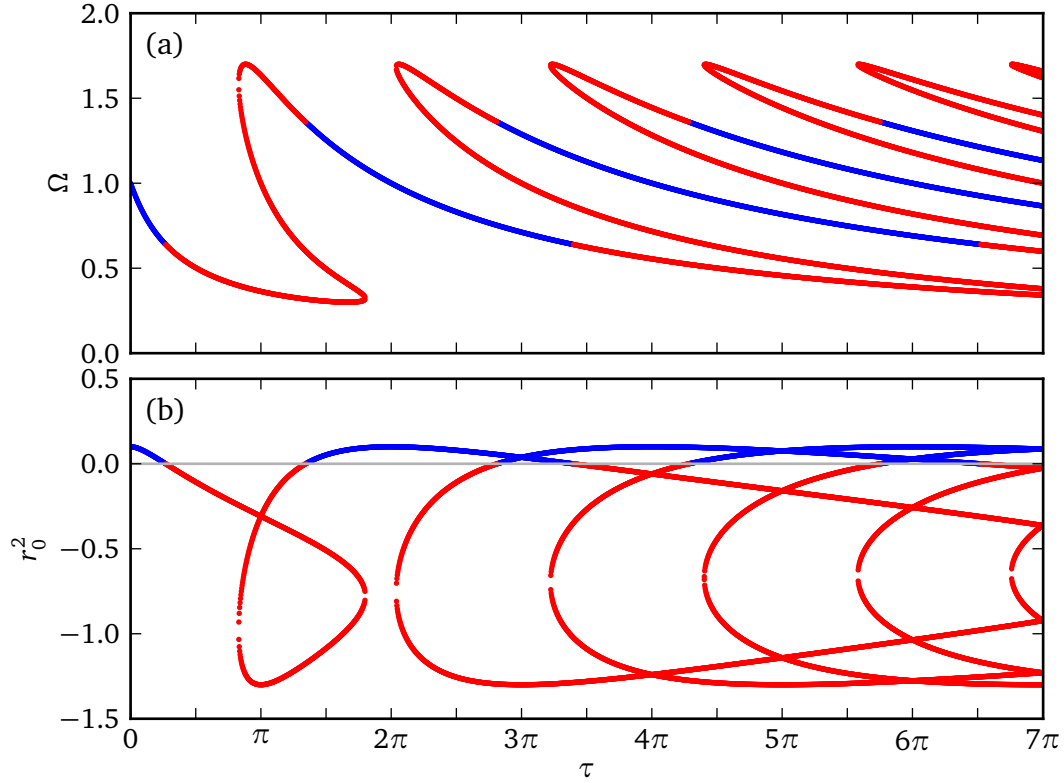


Figure 7.4.: (a) Collective frequency Ω and (b) squared amplitude r_0^2 of in-phase oscillation vs. time delay τ for coupling strength $K = 0.7$ and phase $\beta = 0$. Blue and red curves correspond to physical and unphysical solutions, i.e., $r_0^2 \geq 0$ and < 0 , respectively. Parameters: $\lambda = 0.1$, $\omega = 1$, $\gamma = 0$.

Using the variational vector $\xi_j = \begin{pmatrix} \delta r_j \\ \delta \varphi_j \end{pmatrix}$, the Jacobian of the Stuart-Landau local dynamics $\mathbf{J}_0 = \begin{pmatrix} -2r_0^2 & 0 \\ -2\gamma r_0^2 & 0 \end{pmatrix}$, and the rotational matrix $\mathbf{R} = \begin{pmatrix} \cos \Delta & -\sin \Delta \\ \sin \Delta & \cos \Delta \end{pmatrix}$, Equation (7.12) is rewritten as

$$\dot{\xi}_j = \mathbf{J}_0 \xi_j - K \mathbf{R} \xi_j + K \sum_n G_{jn} \mathbf{R} \xi_n(t - \tau), \quad j = 1, \dots, N. \quad (7.13)$$

The rotational matrix \mathbf{R} plays the role of the coupling scheme \mathbf{H} (cf. Chapter 2). In networks with multiple-variable nodes it determines which of the variables are involved in

the coupling. Here, where we have only one complex variable describing the dynamics of each node, the coupling phase yields a 2×2 coupling scheme in the notation of phases φ_j and amplitudes r_j .

In a similar fashion as in Chapter 3, Eq. (7.13) can be rewritten with one state vector $\xi = (\xi_1, \dots, \xi_N)$ including the dynamics of all nodes:

$$\dot{\xi} = (\mathbf{I}_N \otimes \mathbf{J}_0)\xi - K(\mathbf{I}_N \otimes \mathbf{R})\xi + K(\mathbf{G} \otimes \mathbf{R})\xi(t - \tau). \quad (7.14)$$

If the coupling matrix \mathbf{G} is diagonalizable, a block-diagonal form of this variational equation can be obtained:

$$\dot{\zeta}_k(t) = \mathbf{J}_0 \zeta_k(t) - K\mathbf{R} [\zeta_k(t) - v_k \zeta_k(t - \tau)], \quad k = 1, \dots, N, \quad (7.15)$$

where v_k is the k th eigenvalue of \mathbf{G} . One eigenvalue is always one, $v_1 = 1$, following from the unity row sum condition. The variational equation corresponding to this eigenvalue describes variations inside the synchronization manifold while all other eigenvalues correspond to transverse directions.

Floquet exponents In contrast to Chapter 3, where the master stability function was calculated in terms of Lyapunov exponents, the periodic behavior of the Stuart-Landau oscillator allows for the use of Floquet exponents. Usually, solving a given Floquet problem involves numerically integrating an evolution matrix and is therefore as expensive as calculating Lyapunov exponents [Just, 1999]. I will show, however, that the Floquet problem simplifies to an eigenvalue problem here, since the coefficient matrices \mathbf{J}_0 and \mathbf{R} in Eq. (7.15) do not depend on time.

Consider an n -dimensional system of differential equations

$$\dot{\mathbf{x}}(t) = \mathbf{h}[\mathbf{x}(t)], \quad (7.16)$$

which exhibits a periodic solution $\xi(t) = \xi(t + T)$ with period T . Stability of this periodic solution is determined by considering trajectories in the vicinity of this solution:

$$\mathbf{x}(t) = \xi(t) + \delta\mathbf{x}(t). \quad (7.17)$$

Then, a Taylor expansion in $\mathbf{x}(t)$ reveals that, in linear order, the deviations $\delta\mathbf{x}$ are described by

$$\delta\dot{\mathbf{x}}(t) = D\mathbf{h}[\xi(t)]\delta\mathbf{x}(t). \quad (7.18)$$

Solving this Floquet problem usually complicates to a numerical problem. However, if we assume the Jacobian to be time-independent – $D\mathbf{h}[\xi(t)] = D\mathbf{h}$ – we can use a simple exponential ansatz $\delta\mathbf{x}(t) = \exp(\Lambda t)\mathbf{x}(t)$. Equation (7.18) then simplifies to

$$\Lambda\delta\mathbf{x}(t) = D\mathbf{h}\delta\mathbf{x}(t), \quad (7.19)$$

which is equivalent to the eigenvalue problem

$$0 = \det(D\mathbf{h} - \Lambda\mathbf{I}_n). \quad (7.20)$$

That is, the Floquet exponents that describe the evolution of the deviations $\delta\mathbf{x}$ according to Eq. (7.18) are calculated as eigenvalues of the Jacobian $D\mathbf{h}$. Stability of the orbit ξ is then given by the real parts of the eigenvalue spectrum $\Lambda_1, \dots, \Lambda_n$. The imaginary parts describe a possible torsion of the orbit and are not important for stability concerns. Note that due to the translational invariance of a periodic orbit, one of these eigenvalues – or Floquet exponents – will always be zero. This has to be kept in mind since this value does not play a role in determining stability of synchronization.

Applying this scheme to Eq. (7.15) yields

$$0 = \det \left[\mathbf{J}_0 - \Lambda\mathbf{I}_2 + K \left(-1 + v_k e^{-\Lambda\tau} \right) \mathbf{R} \right], \quad (7.21)$$

where the exponential term $\exp(-\Lambda\tau)$ results from the delayed term $\zeta_k(t - \tau)$. Equation (7.21) is of course equivalent to

$$\begin{aligned} 0 &= \begin{vmatrix} -2r_0^2 + KQ_k(\Lambda)\cos\Delta - \Lambda & -KQ_k(\Lambda)\sin\Delta \\ -2\gamma r_0^2 + KQ_k(\Lambda)\sin\Delta & KQ_k(\Lambda)\cos\Delta - \Lambda \end{vmatrix} \\ &= KQ_k(\Lambda) \left[(-2r_0^2 - 2\Lambda)\cos\Delta - 2\gamma r_0^2\sin\Delta + KQ_k(\Lambda) \right] + 2r_0^2\Lambda - \Lambda^2, \end{aligned} \quad (7.22)$$

where $Q_k(\Lambda) = -1 + v_k e^{-\Lambda\tau}$ and in particular $Q_1(\Lambda) = e^{-\Lambda\tau} - 1$ since $v_1 = 1$.

Equation (7.22) is a transcendental equation for the eigenvalues Λ and can in general not be solved analytically. In the following, I will show results from numerically solving the equation for different parameters in different projections of the parameter plane. Note that the plane of the coupling parameters alone is 3-dimensional, consisting of the coupling strength's amplitude K and phase β and the time delay τ . I will therefore fix the model parameters as $\lambda = 0.1$, $\omega = 1$, and $\gamma = 0$ and show the dependence of synchronizability on the coupling parameters only.

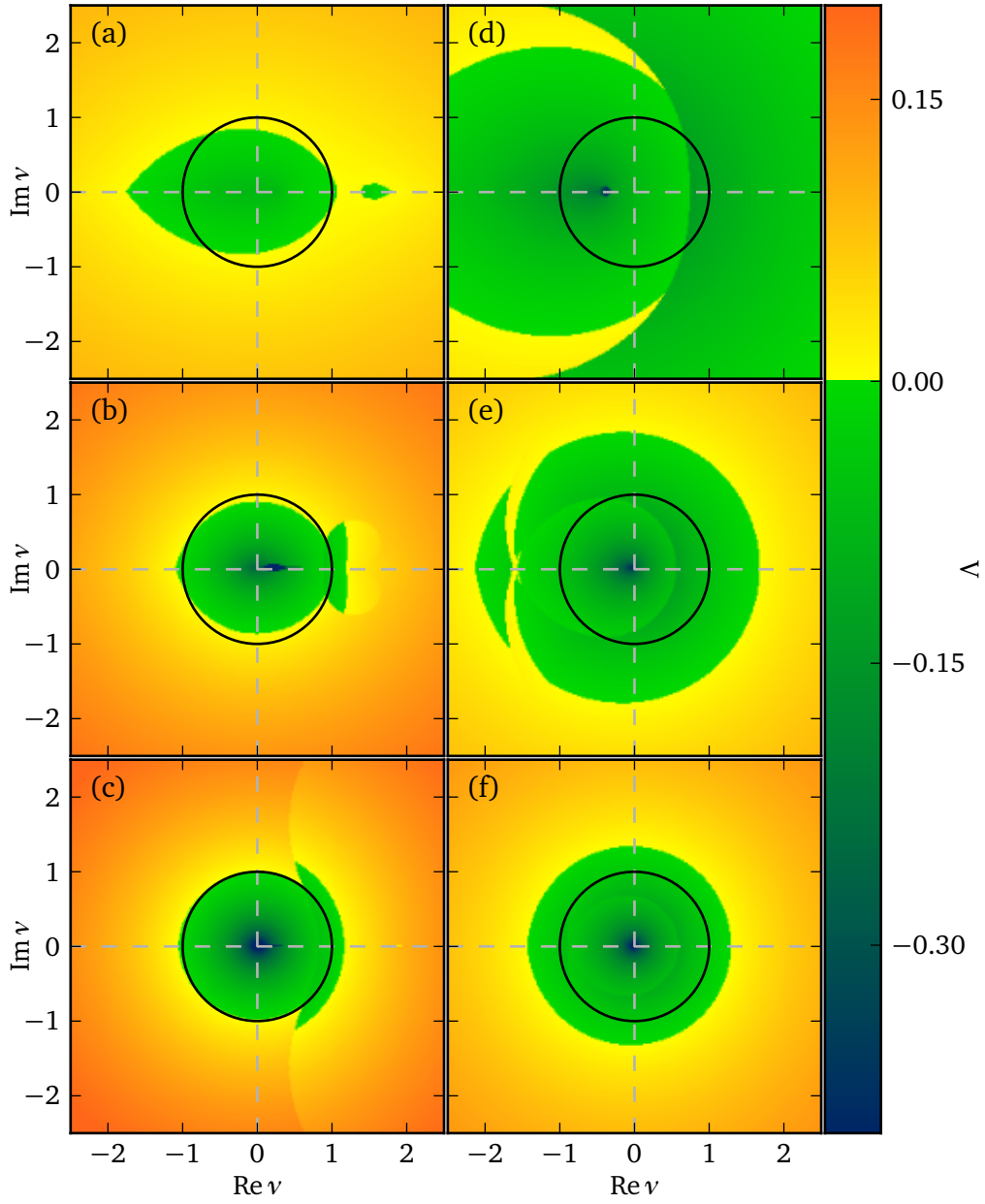


Figure 7.5.: Master stability function for in-phase synchronization of Stuart-Landau oscillators in the $(\text{Re } \nu, \text{Im } \nu)$ -plane for $\beta = 0$ and different coupling strengths K and delay times τ . The color code corresponds to the largest real part of the Floquet exponents for a given value of the parameter ν . All eigenvalues of the coupling matrix \mathbf{G} of a unidirectional ring lie on the black circle. Parameters: (a) $K = 0.08$, $\tau = 3\pi/2$, (b) $K = 0.3$, $\tau = 3\pi/2$, (c) $K = 0.7$, $\tau = 3\pi/2$, (d) $K = 0.08$, $\tau = 2\pi$, (e) $K = 0.3$, $\tau = 2\pi$, (f) $K = 0.7$, $\tau = 2\pi$; others as in Fig. 7.3.

Figure 7.5 depicts the master stability function, i.e., the largest real part of the Floquet exponents, calculated from Eq. (7.21) for different coupling parameters. The coupling strength is chosen as $K = 0.08, 0.3$, and 0.7 in panels (a,d), (b,e), and (c,f), respectively. The coupling phase is chosen as $\beta = 0$ and the time delay is $\tau = 3\pi/2$ in panels (a-c) and 2π in panels (d-e). Note that for a unidirectionally coupled ring all eigenvalues, i.e., $v_k = \exp(2\pi i k/N)$ with $k = 1, \dots, N$ (see Sec. 4.5.1), are located on the black circle. Hence, for the choice of parameters in panels (c-f) all eigenvalues lie in the region of negative maximum real part of the Floquet exponent. The unidirectional ring shows stable in-phase synchronization for these parameters. For the parameters in panels (a-b) in-phase synchronization of the unidirectional ring is unstable for $N > 2$. Furthermore, it can be shown using Gerschgorin's disk theorem (see Sec. 7.3.3 [Gerschgorin, 1931; Earl and Strogatz, 2003]) that the eigenvalues are located on or inside this circle $S(0, 1)$ centered at 0 with radius 1 for any network topology with unity row sum. As a special case, the same holds for the circle $S(G_{jj}, 1 - G_{jj})$ centered at G_{jj} if self-feedback (constant G_{jj} , $j = 1 \dots, N$) is added while keeping the unity row sum condition. This circle is contained in $S(0, 1)$ which describes the more general case with arbitrary diagonal elements. Note that the master stability function is symmetric with respect to a change of sign of $\text{Im } v$.

In order to further illustrate the dependence on the coupling strength K , Fig. 7.6 shows the master stability function in the $(\text{Re } v, K)$ plane for fixed delay times $\tau = 3\pi/2$ and 2π in panels (a) and (b), respectively. The imaginary part $\text{Im } v$ is chosen to be zero. It can be seen that the master stability function shows stability inside the interval $\text{Re } v \in [-1, 1]$ regardless of the coupling strength K . This implies that any undirected network topology ($\text{Im } v = 0$) with a unity row sum shows stable synchronization for any coupling strength and these two fixed delay times.

Until now, the influence of the coupling phase β was not discussed yet. I will show this dependence for some exemplary values of the other coupling parameters. Figure 7.7 shows the master stability function in the $(\text{Re } v, \beta)$ plane for the same sets of parameters as in Fig. 7.5 in panels (a-f). On one hand, for each set of parameters there are ranges for the coupling phase β where the master stability function shows instability in the interval $\text{Re } v \in [-1, 1]$. In fact, in some regions, not even solutions for the common frequency and amplitude exist (white color). On the other hand, for every panel, i.e., every set of parameters, there is a range where the interval $\text{Re } v \in [-1, 1]$ shows stable synchronization, which corresponds to stable synchronization of any network with row sum 1. For some regions, the size of the interval even exceeds the interval $\text{Re } v \in [-1, 1]$ considerably. In the following Section I will show how these optimal values of the coupling phase β can be determined using an analytic equation.

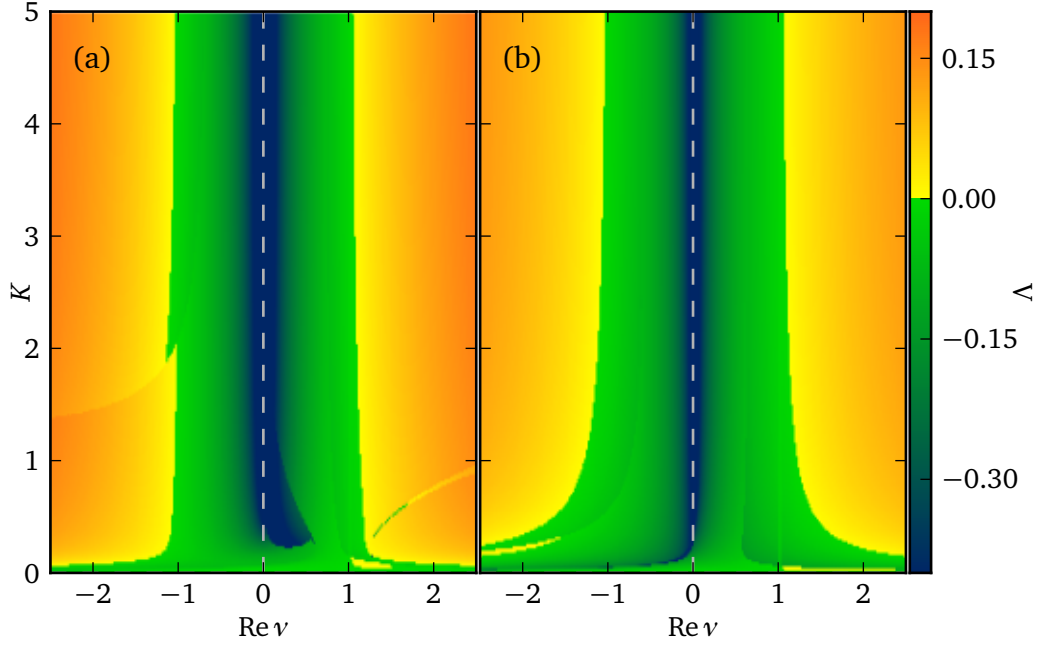


Figure 7.6.: Master stability function for in-phase synchronization of Stuart-Landau oscillators in the $(\text{Re } \nu, K)$ plane for fixed $\text{Im } \nu = 0$. (a) $\tau = 3\pi/2$, (b) $\tau = 2\pi$. Other parameters as in Fig. 7.5.

7.3.2. Control of in-phase synchronization

I have shown that for zero coupling phase ($\beta = 0$) stability of in-phase synchronization strongly depends on the choice of the coupling parameters K and τ . To overcome this dependence, the coupling phase can be used to achieve stability of synchronization in the whole plane of parameters K and τ . Desynchronization, on the other hand, can as well be stabilized independently of K and τ by choosing a different coupling phase. As a result, switching between synchronization and desynchronization can be achieved by tuning this coupling phase.

As we will see, a choice of $\beta = \Omega\tau$ is the optimal value of the coupling phase to control in-phase synchronization. Note that the equations (7.11) determining the collective amplitude and frequency do depend on the choice of β . One can expect a different picture than that shown in Figs. 7.3 and 7.4 obtained for $\beta = 0$. It is easily seen that inserting $\beta = \Omega\tau$ instead of $\beta = 0$ leaves the collective frequency unchanged because of the asymmetry of the sine function. Using the symmetry of the cosine on the other

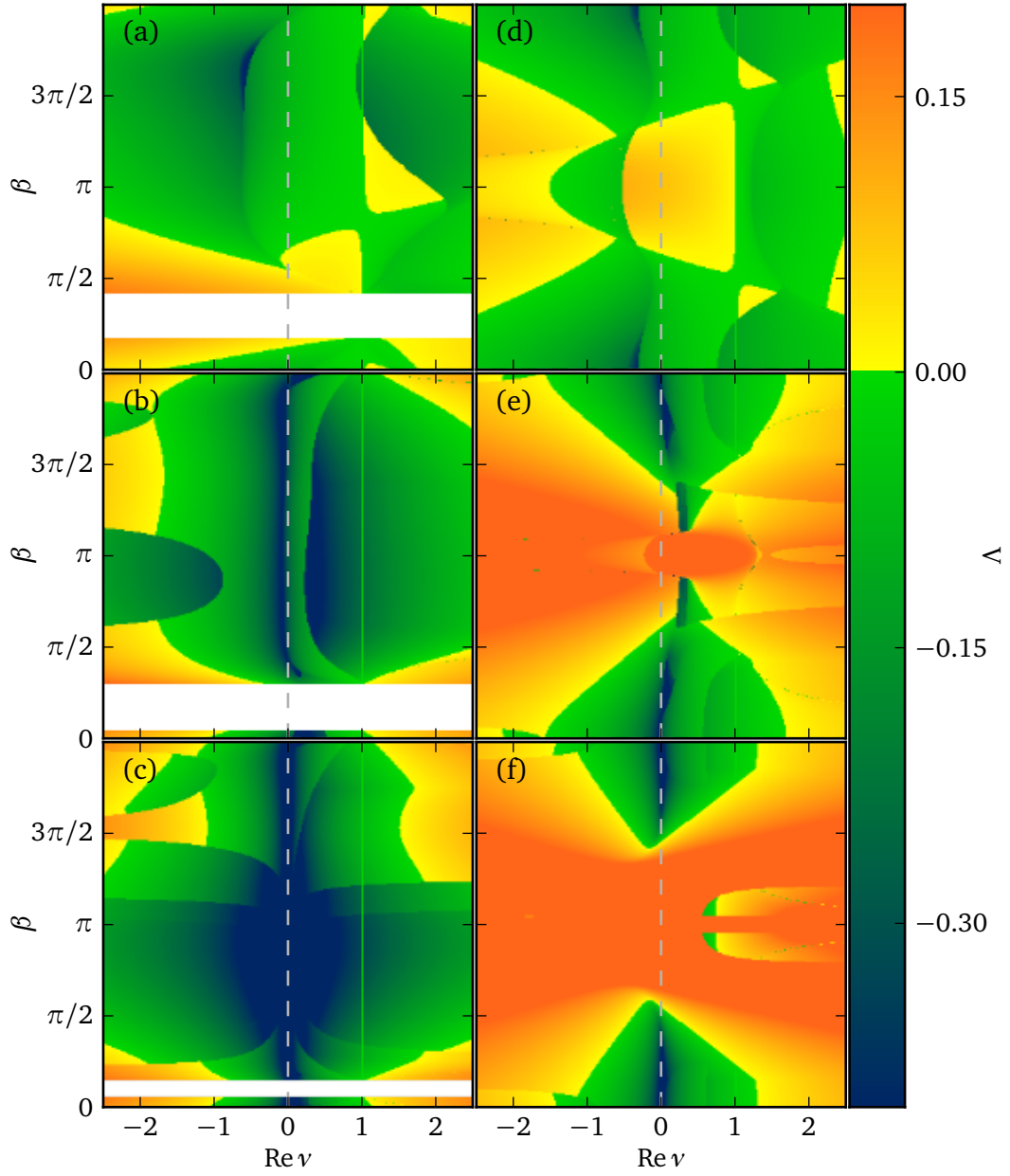


Figure 7.7.: Master stability function for in-phase synchronization of Stuart-Landau oscillators in the $(\text{Re } \nu, \beta)$ plane for fixed $\text{Im } \nu = 0$. Other parameters as in the respective panels of Fig. 7.5.

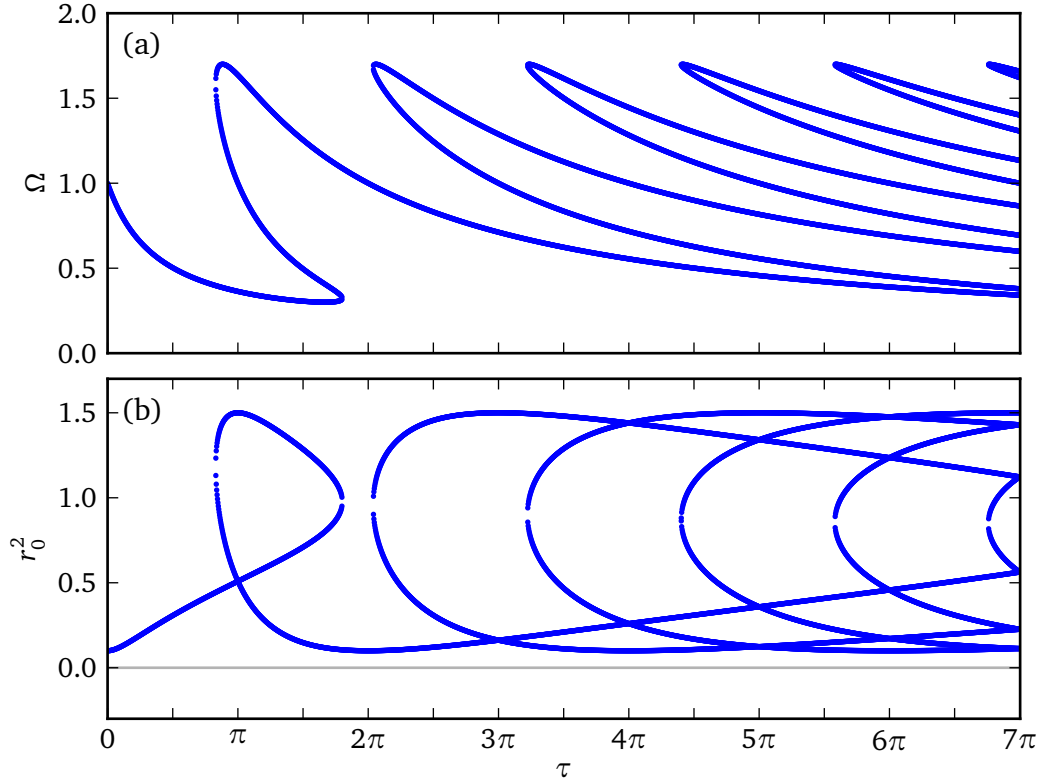


Figure 7.8.: (a) Collective frequency Ω and (b) squared amplitude r_0^2 of in-phase oscillation vs. time delay τ for coupling strength $K = 0.7$ and phase $\beta = \Omega\tau$. Parameters: $\lambda = 0.1$, $\omega = 1$, $\gamma = 0$.

hand, shows that the squared collective amplitude r_0^2 is mirrored around the value of λ . This result is also shown in Fig. 7.8, which uses the same parameters as Fig. 7.4, but a phase of $\beta = \Omega\tau$ instead of $\beta = 0$. As a first result, this means that this choice of the coupling phase does not show any unphysical solutions any more, i.e., no solutions with $r_0^2 < 0$.

Let me now investigate stability of these solutions. Inserting the value $\beta = \Omega\tau$ into Eq. (7.22), that equation factorizes and yields

$$\begin{cases} \Lambda = K(-1 + v_k e^{-\Lambda\tau}) - 2r_0^2, \\ \Lambda = K(-1 + v_k e^{-\Lambda\tau}), \end{cases} \quad (7.23)$$

For concerns of stability, only the largest Floquet exponent is of interest. As shown

above, I find that r_0^2 is always positive for this choice of the coupling phase. Thus the largest Floquet exponents can be obtained from

$$\Lambda = K(-1 + v_k e^{-\Lambda\tau}). \quad (7.24)$$

In order to draw a general conclusion from Eq. (7.24), I will make use of a theorem by Gerschgorin [1931]. The theorem reads as follows.

7.3.3. Gerschgorin's circle theorem

Let \mathbf{A} be a – potentially complex – $N \times N$ matrix with entries a_{ij} . For every row $i = 1, \dots, N$, let

$$R_i = \sum_{j \neq i} |a_{ij}| \quad (7.25)$$

be the sum of the absolute values of the non-diagonal entries in this i th row. Let $S(a_{ii}, R_i)$ be the circle centered at a_{ii} with radius R_i . I refer to such a circle as Gerschgorin circle.

Theorem: Every eigenvalue of the matrix \mathbf{A} lies within at least one of the Gerschgorin circles $S(a_{ii}, R_i)$ ($i = 1, \dots, N$).

Application of Gerschgorin's circle theorem to Eq. (7.24) allows the eigenvalues of any network to be written as

$$v_k = a_0 + (1 - a_0)\rho_k e^{i\theta_k}, \quad (7.26)$$

where $a_0 = 0$ and $\in [0, 1]$ for a network without and with self-feedback, respectively, and $\rho_k \in [0, 1]$, $\theta_k \in [0, 2\pi)$. Self-feedback in this context means a constant diagonal element in each row of the matrix. For the network without self-feedback, Equation (7.24) becomes

$$\Lambda = K(-1 + \rho_k e^{-\Lambda\tau + i\theta_k}), \quad (7.27)$$

while for networks with self-feedback I obtain

$$\Lambda = K[-1 + a_0 e^{-\Lambda\tau} + (1 - a_0)\rho_k e^{-\Lambda\tau + i\theta_k}]. \quad (7.28)$$

Following the method similar to [D'Huys et al., 2008], one can prove that solutions of the above two equations remain always in the left half plane of the complex Λ plane:

It is obvious that $\text{Re}(\Lambda) \leq 0$ for zero delay ($\tau = 0$). The growth rate of Λ depends continuously on the delay time τ . If a state loses stability, the value of τ must correspond to a purely imaginary value $\Lambda = iq$ with $q \in \mathbb{R}$. Since the above expressions for Floquet exponents do not admit such solutions, all of the real parts of Floquet exponents must be negative for any τ . Self-feedback facilitates the stability of synchronization since $a_0 > 0$.

7.3.4. Control of desynchronization

In the same way that $\beta = \Omega\tau$ enhances synchronization, I can show that a choice of $\beta = \Omega\tau + \pi \pmod{2\pi}$ always leads to either desynchronization or amplitude death, i.e., no oscillations.

With this choice, the matrix \mathbf{R} becomes $-\mathbf{I}_2$, which results again in a factorization of Eq. (7.22). The Floquet exponents then follow

$$\begin{cases} \Lambda = K(1 - v_k e^{-\Lambda\tau}) - 2r_0^2, \\ \Lambda = K(1 - v_k e^{-\Lambda\tau}), \end{cases} \quad (7.29)$$

where $k = 1, \dots, N$. Note that, unlike the case of $\beta = \Omega\tau$, there might exist regions with $r_0^2 < 0$ for $\beta = \Omega\tau + \pi$. Nevertheless, it is sufficient to consider the second equation

$$\Lambda = K(1 - v_k e^{-\Lambda\tau}), \quad (7.30)$$

because one can show that all of the solutions of Eq. (7.30) lie in the right-half plane of the complex Λ -plane. In fact, according to Gerschgorin's theorem, Equation (7.30) can be rewritten for the network without self-feedback as

$$\Lambda = K(1 - \rho_k e^{-\Lambda\tau + i\theta_k}) \quad (7.31)$$

and now it is possible to prove that any solution of Eq. (7.31) has positive real part. Having shown that all solutions of this second equation have positive real part, the location of the solutions of the first equation in (7.29) cannot change stability. Adding self-delayed feedback strengthens the desynchronization since $a_0 = 1$. Note that the term *desynchronization* here refers to any state that differs from the in-phase synchronized dynamics. The exact realization of a desynchronized state depends on many factors.

In Chapter 10 I will show that certain network topologies allow for an ordered structure of non-in-phase states. These states are called cluster states. It will be seen that the

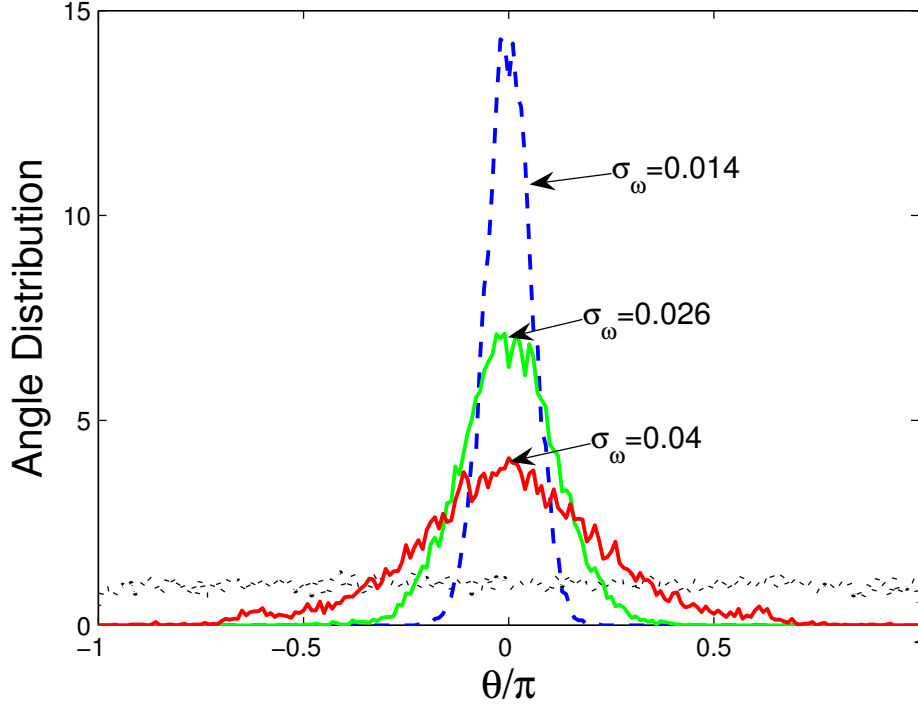


Figure 7.9.: Distribution of the relative phases $\theta = \varphi_i - \Theta$ around the order parameter (7.32) for 200 slightly nonidentical elements with different standard deviations σ_ω of the frequencies ω for $\beta = \Omega\tau$. Dotted (black) curve: $\beta = \Omega\tau + \pi$ (desynchronization). Other coupling parameters $\tau = 0.52\pi$, $K = 0.08$.

value of $\beta = \Omega\tau$ is always able to desynchronize the in-phase synchronization, but will eventually stabilize a two-cluster state in permitting topologies. More cluster states can be stabilized choosing an appropriate value of the coupling phase.

7.4. Robustness against parameter mismatch

All analytic results obtained in this Chapter rely on identical oscillators and identical delay times in the network. I ran simulations on a globally coupled network of $N = 200$ oscillators with slightly different frequencies ω_i for each oscillator $i = 1, \dots, N$ following a

Gaussian distribution with mean ω and standard deviation σ_ω . Figure 7.9 shows angular deviations from the Kuramoto order parameter [Kuramoto, 1984]

$$Re^{i\Theta} = \frac{1}{N} \sum_{k=1}^N e^{i\varphi_k}, \quad (7.32)$$

where the phases φ_k of the oscillators are obtained using the relation $\exp(i\varphi_k) = z_k/|z_k|$. Using the value of $\beta = \Omega\tau$, which is the optimal value of the coupling phase to stabilize synchronization, the width of the angular distribution broadens with increasing variance of the frequency distribution, but the mean value is still significantly pronounced. Using the value of $\beta = \Omega\tau + \pi$ for desynchronization, there is no peak left, i.e., no coherence is left in the network. The corresponding black line is obtained regardless of the width of the frequency distribution.

7.5. Conclusion

Using the Stuart-Landau model for periodic dynamics on the nodes in a network, the analysis of stability of synchronization reduces to analytic equations for the Floquet exponents. In general, these equations can only be solved numerically due to the delay influence. Notable results can, however, be obtained rigorously. The coupling phase is identified as a crucial parameter influencing stability of synchronization. Deriving an analytic condition, I show that stability of synchronization is achieved independently of the coupling strength and the delay time for optimal values of the coupling phase. Concerning possible applications, I have shown that the results are robust against noise and parameter mismatch.

I will come back to networks of Stuart-Landau oscillators in Chapter 10, where I will show that cluster and splay states can be treated in the same way for certain network topologies. This will also allow the calculation of optimal values for the coupling phase in order to stabilize a desired state of synchronization.

Part II.

Cluster and group synchronization

8. Stability of cluster and group synchronization

So far only stability of isochronous synchronization was considered. In general more complicated synchronization patterns may be observed. Cluster synchronization will be investigated in this Chapter [Dahms et al., 2011]. In a state of cluster synchronization, certain clusters inside the network show isochronous synchronization, but not the entire network. Group synchronization is a generalization of cluster synchronization where the local dynamics can be different in each cluster.

Sorrentino and Ott [2007] have shown that it is possible to treat non-isochronous synchronization with a master stability approach. In their work they considered two groups of nodes governed by different local dynamics $\mathbf{F}(\mathbf{x}_i)$ and $\mathbf{G}(\mathbf{y}_j)$, where \mathbf{x}_i (respectively, \mathbf{y}_j) describe the dynamics of the N_x (N_y) elements $i = 1, \dots, N_x$ ($j = 1, \dots, N_y$) of the first (second) group.

After introducing the notion of cluster and group dynamics in Sec. 8.1, I derive the master stability function in Sec. 8.2 and show the restrictions that arise on the topology in Sec. 8.3. In Sections 8.4 and 8.5 I investigate the symmetries that group and cluster synchronization implies on the spectrum of the coupling matrix and on the master stability function, respectively. Finally, in Sections 8.6-8.9, I show exemplary results obtained for networks of delay-coupled lasers.

8.1. The network dynamics

In a network consisting of N identical nodes, I refer to cluster synchronization as a state where clusters of nodes exist that show isochronous synchronization internally, but synchronization among these cluster is not existent or of non-isochronous type, e.g., there may be a phase lag between clusters [Choe et al., 2010, 2011].

Group synchronization describes a similar state of synchrony, but the type of nodes – determined by the local dynamics function – differs from cluster to cluster, which

I refer to as groups in this case. As the description of cluster synchronization is a special case of group synchronization, I use the more general notion of groups in the following.

Assume the number of groups to be M with $k = 1, \dots, M$ numbering the individual groups. The dynamical variables of the nodes in each group are then given by $\mathbf{x}_i^{(k)} \in \mathbb{R}^{d_k}$ with $i = 1, \dots, N_k$, where N_k denotes the number of nodes in the k th group. The dimension d_k of the $\mathbf{x}_i^{(k)}$ themselves is given by the particular node model, e.g., the complex Hopf normal-form oscillator (that will be used in Chapter 10), the two-dimensional FitzHugh-Nagumo model [Lehnert et al., 2011], or the three-dimensional Lang-Kobayashi equations that I use in this Chapter and that I already used in Part I of the thesis.

In general the dimension of the nodes $\mathbf{x}_i^{(k)}$ may be different for each group k . Consequently, also the local dynamics $\mathbf{F}^{(k)}(\mathbf{x}_i^{(k)})$ can be different for each group, but has to be identical for all nodes $i = 1, \dots, N_k$ in a given group k . For example, consider a network of neurons, where one group contains inhibitory neurons and another group contains excitatory ones. The local dynamics will be different for each group and depending on the model used to describe both types of neurons, also the dimension of the nodes' equations may be different.

Let $\sigma^{(kn)}$ be the coupling strength for the coupling from the n th to the k th group. In the same sense, let $\mathbf{A}^{(kn)}$ be an $N_k \times N_n$ coupling matrix, such that its entries $\{A_{ij}^{(kn)}\}$ represent the coupling of system j (which is in the n th group) to system i (which is in the k th group). Without loss of generality I assume the row sums of the coupling matrices $\mathbf{A}^{(kn)}$ to be only either one or zero:

- (i) If there is no coupling from the n th group to the k th group, the coupling matrix $\mathbf{A}^{(kn)}$ is the zero matrix, hence its row sum is zero:

$$a^{(kn)} := \sum_{j=1}^{N_n} A_{ij}^{(kn)} = 0, \quad i = 1, \dots, N_k. \quad (8.1)$$

- (ii) If there is coupling from group n to group k , then I assume the row of the corresponding coupling matrix to be unity:

$$a^{(kn)} = \sum_{j=1}^{N_n} A_{ij}^{(kn)} = 1, \quad i = 1, \dots, N_k. \quad (8.2)$$

Note that (ii) is equivalent to the condition of a unity row sum deployed in Chapter 3 for complete isochronous synchronization. Any constant row sum can be rescaled here to allow for coupling matrices with constant but non-unity row sum, as will be shown in the following.

A certain coupling strength $\sigma^{(kn)}$ may also be scaled to compensate for a corresponding coupling matrix $\mathbf{A}^{(kn)}$ that has a row sum not equal to one [see Sorrentino and Ott, 2007, Sec. II]. As an example, let $a^{(kn)} = \sum_{j=1}^{N_n} A_{ij}^{(kn)}$ be the constant row sum of the coupling matrix $\mathbf{A}^{(kn)}$. Then, to comply with Eq. (8.2), both $\mathbf{A}^{(kn)}$ and $\sigma^{(kn)}$ can be rescaled as $\mathbf{A}^{(kn)} \rightarrow (1/a^{(kn)})\mathbf{A}^{(kn)}$ and $\sigma^{(kn)} \rightarrow a^{(kn)}\sigma^{(kn)}$.

The coupling schemes $\mathbf{H}^{(kn)}$ are introduced as in the standard master stability approach (see Chapter 3). These coupling schemes are $d_k \times d_n$ -dimensional, given that d_k and d_n are the dimensions of the k th and n th group, respectively.

Note that Sorrentino and Ott used – potentially nonlinear – coupling functions $\mathbf{H}^{(kn)} : \mathbb{R}^{d_n} \rightarrow \mathbb{R}^{d_k}$ instead of matrices for $\mathbf{H}^{(kn)}$. Since I consider only linear coupling functions – which apply to the coupling scenarios used in all networks considered in this thesis – the restriction to matrices is reasonable here.

Finally, I allow the coupling delays $\tau^{(kn)}$ to be different for any pair (k, n) of groups being connected. Applying the local dynamics and the coupling contributions, the dynamics of any single node in the network can be described by the differential equation

$$\dot{\mathbf{x}}_i^{(k)} = \mathbf{F}^{(k)}[\mathbf{x}_i^{(k)}(t)] + \sum_{n=1}^M \sigma^{(kn)} \sum_{j=1}^{N_n} A_{ij}^{(kn)} \mathbf{H}^{(kn)} \mathbf{x}_j^{(n)}(t - \tau^{(kn)}). \quad (8.3)$$

The synchronized manifold for group synchronization is given by

$$\dot{\mathbf{x}}_s^{(k)} = \mathbf{F}^{(k)}[\mathbf{x}_s^{(k)}(t)] + \sum_{n=1}^M \sigma^{(kn)} a^{(kn)} \mathbf{H}^{(kn)} \mathbf{x}_s^{(n)}(t - \tau^{(kn)}), \quad (8.4)$$

which can easily be seen by inserting $\mathbf{x}_i^{(k)} = \mathbf{x}_j^{(k)}$ into Eq. (8.3) ($\forall i, j = 1, \dots, N_k, k = 1, \dots, M$).

Note that every group may exhibit different synchronous dynamics in this synchronization manifold which has dimension $\sum_{i=1}^M d_i$. Even when the functions $\mathbf{F}^{(k)}$, the coupling schemes $\mathbf{H}^{(kn)}$, and the coupling strengths $\sigma^{(kn)}$ are identical for every group and every coupling, respectively, different initial conditions potentially lead to different dynamics; this would correspond to the notion of cluster synchronization.

8.2. Stability of the synchronous state for group synchronization

In order to investigate stability of the synchronous state, a linearization around the synchronization manifold $\mathbf{x}_s^{(k)}$ ($k = 1, \dots, M$) yields

$$\delta \dot{\mathbf{x}}_i^{(k)} = \mathbf{DF}^{(k)}|_{\mathbf{x}_s^{(k)}} \delta \mathbf{x}_i^{(k)}(t) + \sum_{n=1}^M \sigma^{(kn)} \sum_{j=1}^{N_n} A_{ij}^{(kn)} \mathbf{H}^{(kn)} \delta \mathbf{x}_j^{(n)}(t - \tau^{(kn)}). \quad (8.5)$$

The master stability function for isochronous synchronization shown in Chapter 3 utilizes a transformation in the space of the network's dimension. In this transformed space there exist N vectors that still allow to represent all N linearly independent solutions. The diagonalizability of the coupling matrix ensured that its eigensystem was able to span this N -dimensional space.

The idea is very similar in the case of group synchronization. While it is not possible to perform a straight-forward diagonalization, the idea is to find a transformation in which the variational equations decouple in a way that they become independent of the particular coupling matrices, but at the same time the transformation must yield a set of vectors which span the same space of dimension $\sum_{k=1}^M N_k$.

Assume that for each group $k = 1, \dots, M$ every of the N_k solutions of Eq. (8.5) can be written in the form

$$\delta \mathbf{x}_i^{(k)} = c_i^{(k)} \delta \bar{\mathbf{x}}^{(k)}, \quad (8.6)$$

where $\{c_i^{(k)}\}$ are appropriately chosen time-independent scalars. I show that the space of the vectors formed from the possible combinations of the

$$c_{i_1}^{(1)}, \dots, c_{i_M}^{(M)} (i_1 = 1, \dots, N_1; \dots; i_M = 1, \dots, N_M) \quad (8.7)$$

has dimension $\sum_{k=1}^M N_k$, which means that the form (8.6) yields all solutions of Eq. (8.5) as linear combinations. Using the form (8.6), Equation (8.5) becomes

$$c_i^{(k)} \delta \dot{\bar{\mathbf{x}}}^{(k)} = c_i^{(k)} \mathbf{DF}^{(k)}|_{\mathbf{x}_s^{(k)}} \delta \bar{\mathbf{x}}^{(k)}(t) + \sum_{n=1}^M \left(\sum_{j=1}^{N_n} A_{ij}^{(kn)} c_j^{(n)} \right) \sigma^{(kn)} \mathbf{H}^{(kn)} \delta \bar{\mathbf{x}}^{(n)}(t - \tau^{(kn)}). \quad (8.8)$$

This equation has to be satisfied for each group $k = 1, \dots, M$ and for each node $i = 1, \dots, N_k$ therein. Given these conditions the following can be observed:

- (i) For a given k , no general conclusion can be drawn if the first sum $\sum_{n=1}^M$ contains more than one summand, i.e., more than one of the $\mathbf{A}^{(kn)}$ ($n = 1, \dots, M$) is not zero.
- (ii) If the sum $\sum_{n=1}^M$ contains exactly one element for a given k , i.e., exactly one of the $\mathbf{A}^{(kn)}$ ($n = 1, \dots, M$) is non-zero, the relation

$$\frac{1}{c_i^{(k)}} \sum_{j=1}^{N_n} A_{ij}^{(kn)} c_j^{(n)} = C^{(k)} \quad (8.9)$$

can be derived, which yields $C^{(k)}$ as a factor that is independent of $i = 1, \dots, N_k$.

This can be seen by dividing Eq. (8.8) by $c_i^{(k)}$:

$$\delta \dot{\bar{\mathbf{x}}}^{(k)} = \mathbf{DF}^{(k)}|_{\mathbf{x}_s^{(k)}} \delta \bar{\mathbf{x}}^{(k)}(t) + \frac{1}{c_i^{(k)}} \sum_{n=1}^M \left(\sum_{j=1}^{N_n} A_{ij}^{(kn)} c_j^{(n)} \right) \sigma^{(kn)} \mathbf{H}^{(kn)} \delta \bar{\mathbf{x}}^{(n)}(t - \tau^{(kn)}). \quad (8.10)$$

Assuming that the k th group gets input from exactly one other group n the sum over n vanishes and the coefficients in the coupling term can be substituted by $C^{(k)}$:

$$\delta \dot{\bar{\mathbf{x}}}^{(k)} = \mathbf{DF}^{(k)}|_{\mathbf{x}_s^{(k)}} \delta \bar{\mathbf{x}}^{(k)}(t) + \underbrace{\frac{1}{c_i^{(k)}} \sum_{j=1}^{N_n} A_{ij}^{(kn)} c_j^{(n)}}_{C^{(k)}} \sigma^{(kn)} \mathbf{H}^{(kn)} \delta \bar{\mathbf{x}}^{(n)}(t - \tau^{(kn)}). \quad (8.11)$$

I will elaborate on the restrictions this implies in Sec. 8.3. For a 2-cluster state, for example, this would lead to a bipartite network.

- (iii) If such a factor $C^{(k)}$ (see (ii)) can be derived for every $k = 1, \dots, M$, i.e., for every row of the $M \times M$ block matrix $\mathbf{Q} = [\mathbf{A}^{(kn)}; k, n = 1, \dots, M]$ contains exactly one non-zero block, Equation (8.8) can be written as

$$\delta \dot{\bar{\mathbf{x}}}^{(k)} = \mathbf{DF}^{(k)}|_{\mathbf{x}_s^{(k)}} \delta \bar{\mathbf{x}}^{(k)}(t) + C^{(k)} \sigma^{(kn)} \mathbf{H}^{(kn)} \delta \bar{\mathbf{x}}^{(n)}(t - \tau^{(kn)}), \quad k = 1, \dots, M, \quad (8.12)$$

where the relation (8.9) was used. Equivalently, by defining the vectors $\mathbf{c}^{(k)} = (c_1^{(k)}, c_2^{(k)}, \dots, c_{N_k}^{(k)})$ for every $k = 1, \dots, M$, the relations (8.9) ($k = 1, \dots, M$) can

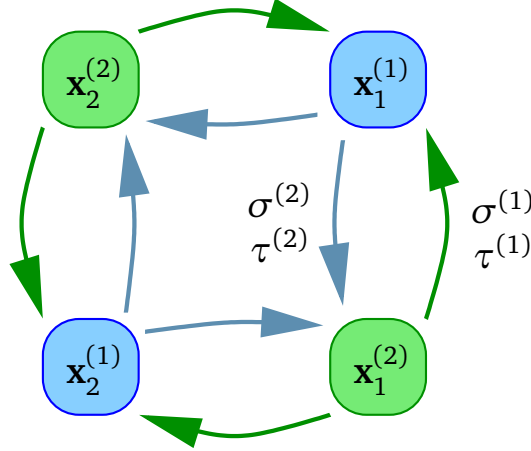


Figure 8.1.: Bidirectionally coupled ring of 4 lasers in 2 groups, where the elements of group (1) and (2) are colored in blue and green, respectively. $\sigma^{(1)}$ and $\sigma^{(2)}$ and $\tau^{(1)}$ and $\tau^{(2)}$ denote the coupling strengths and the time delays for couplings from group (2) to (1) and (1) to (2), respectively.

be written as

$$\mathbf{Q} \begin{pmatrix} \mathbf{c}^{(1)} \\ \mathbf{c}^{(2)} \\ \vdots \\ \mathbf{c}^{(M)} \end{pmatrix} = \begin{pmatrix} C^{(1)}\mathbf{c}^{(1)} \\ C^{(2)}\mathbf{c}^{(2)} \\ \vdots \\ C^{(M)}\mathbf{c}^{(M)} \end{pmatrix}. \quad (8.13)$$

Note that the k th group receives input from exactly one group, which is designated by the index n in Eq. (8.12). This is unique, since there is only one $\mathbf{A}^{(kn)} \neq \mathbf{0}$ in the k th row of \mathbf{Q} . In Sec. 8.3.1 I will show that any topology that falls under this condition can be rearranged to a unidirectional ring structure of the cluster, which will ease the notation greatly.

I now restrict myself to the case (iii), as this is the only case where stability of synchronization can be investigated using a master stability function, as will be shown in the following. Figure 8.1 shows a scheme of this topology for the case of two groups or clusters. As an additional constraint, I consider only cases where the non-zero blocks in the matrix \mathbf{Q} may never lie on the diagonal of this very matrix.

Setting

$$C^{(1)} = C^{(2)} = \dots = C^{(M)} = \gamma, \quad (8.14)$$

one special solution $\mathbf{c}_0^{(1)}, \dots, \mathbf{c}_0^{(M)}$ of Eq. (8.13) (and equivalently of Eq. (8.12)) is obtained as

$$\mathbf{Q} \begin{pmatrix} \mathbf{c}_0^{(1)} \\ \mathbf{c}_0^{(2)} \\ \vdots \\ \mathbf{c}_0^{(M)} \end{pmatrix} = \begin{pmatrix} \gamma \mathbf{c}_0^{(1)} \\ \gamma \mathbf{c}_0^{(2)} \\ \vdots \\ \gamma \mathbf{c}_0^{(M)} \end{pmatrix}. \quad (8.15)$$

It can be shown that by choosing $M - 1$ rescaling factors z_1, \dots, z_{M-1} , Equation (8.15) yields all solutions of Eq. (8.13), hence Eq. (8.12) can be written as

$$\delta \dot{\mathbf{x}}^{(k)} = \mathbf{D}\mathbf{F}^{(k)}|_{\mathbf{x}_s^{(k)}} \delta \bar{\mathbf{x}}^{(k)}(t) + \sigma^{(kn)} \gamma \mathbf{H}^{(kn)} \delta \bar{\mathbf{x}}^{(n)}(t - \tau^{(kn)}), \quad k = 1, \dots, M, \quad (8.16)$$

where γ is chosen from the set of eigenvalues of the matrix \mathbf{Q} . I will show this for an example in the following Section. That example will be a generic one onto which other cluster topologies can be mapped. I will also show counterexamples for matrices \mathbf{Q} that do not fulfill the condition (iii) above, i.e., matrices where no factor $C^{(k)}$ can be derived independently of the individual nodes.

In conclusion, Equation (8.16) qualifies as a master stability equation for group and cluster synchronization. Here, γ is chosen from the set of eigenvalues of the block matrix $\mathbf{Q} = [\mathbf{A}^{(kn)}; k, n = 1, \dots, M]$. In Sec. 8.6 I will show examples for the laser network. I will characterize the stability of cluster states in simple network motifs as well as in more complex topologies.

8.3. Allowed topologies

Here, I will discuss the possible topologies that are covered by block matrices with only one block in each row. First consider the example of two groups. A possible coupling matrix reads

$$\mathbf{Q} = \begin{pmatrix} 0 & \mathbf{A}^{(1)} \\ \mathbf{A}^{(2)} & 0 \end{pmatrix}. \quad (8.17)$$

Regardless of the particular entries of the matrices $\mathbf{A}^{(1)}$ and $\mathbf{A}^{(2)}$, this always describes a bipartite network. In a bipartite network, two kinds of nodes exist and no links may exist between the same kind of nodes. Going to a higher number of groups or cluster, i.e., more blocks in the coupling matrix, this leads to tripartite, quadripartite, i.e., in general multipartite networks.

8.3.1. Groups coupled in a unidirectional ring structure

Assume a network with M groups and a matrix \mathbf{Q} where the groups are coupled in a unidirectional ring structure. For convenience in the following calculations, I change the naming of the inter-group coupling matrices. For a unidirectional ring, only the lower off-diagonal element blocks $\mathbf{A}^{(kn)} = \mathbf{A}^{(k,k-1)}$ are nonzero. Thus I abbreviate $\mathbf{A}^{(k,k-1)}$ by $\mathbf{A}^{(k)}$. The coupling matrix \mathbf{Q} then reads

$$\mathbf{Q} = \begin{pmatrix} 0 & 0 & \cdots & 0 & \mathbf{A}^{(1)} \\ \mathbf{A}^{(2)} & 0 & 0 & \cdots & 0 \\ 0 & \mathbf{A}^{(3)} & 0 & \cdots & 0 \\ & & \vdots & & \\ 0 & \cdots & 0 & \mathbf{A}^{(M)} & 0 \end{pmatrix}. \quad (8.18)$$

The notation of the coupling strengths, coupling schemes, and delay times is changed in a similar fashion; I abbreviate $\sigma^{(k,k-1)}$ by $\sigma^{(k)}$, $\mathbf{H}^{(k,k-1)}$ by $\mathbf{H}^{(k)}$, and $\tau^{(k,k-1)}$ by $\tau^{(k)}$. Note that any of the matrices $\mathbf{A}^{(k)}$ ($k = 1, \dots, M$) may have different dimensions depending on the size of the groups.

Using this special form of \mathbf{Q} , Equation (8.13) reads

$$\begin{pmatrix} 0 & 0 & \cdots & 0 & \mathbf{A}^{(1)} \\ \mathbf{A}^{(2)} & 0 & 0 & \cdots & 0 \\ 0 & \mathbf{A}^{(3)} & 0 & \cdots & 0 \\ & & \vdots & & \\ 0 & \cdots & 0 & \mathbf{A}^{(M)} & 0 \end{pmatrix} \begin{pmatrix} \mathbf{c}^{(1)} \\ \mathbf{c}^{(2)} \\ \vdots \\ \mathbf{c}^{(M)} \end{pmatrix} = \begin{pmatrix} C^{(1)}\mathbf{c}^{(1)} \\ C^{(2)}\mathbf{c}^{(2)} \\ \vdots \\ C^{(M)}\mathbf{c}^{(M)} \end{pmatrix} \quad (8.19)$$

and equivalently Eq. (8.15) becomes

$$\begin{pmatrix} 0 & 0 & \cdots & 0 & \mathbf{A}^{(1)} \\ \mathbf{A}^{(2)} & 0 & 0 & \cdots & 0 \\ 0 & \mathbf{A}^{(3)} & 0 & \cdots & 0 \\ & & \vdots & & \\ 0 & \cdots & 0 & \mathbf{A}^{(M)} & 0 \end{pmatrix} \begin{pmatrix} \mathbf{c}_0^{(1)} \\ \mathbf{c}_0^{(2)} \\ \vdots \\ \mathbf{c}_0^{(M)} \end{pmatrix} = \begin{pmatrix} \gamma \mathbf{c}_0^{(1)} \\ \gamma \mathbf{c}_0^{(2)} \\ \vdots \\ \gamma \mathbf{c}_0^{(M)} \end{pmatrix}, \quad (8.20)$$

which is equivalent to

$$\mathbf{A}^{(k)} \mathbf{c}_0^{(k-1)} = \gamma \mathbf{c}_0^{(k)}, \quad k = 1, \dots, M, \quad (8.21)$$

where $k - 1$ is $k - 1 \bmod M$, also in what follows. Introducing $M - 1$ rescaling factors z_1, \dots, z_{M-1} , this can be rewritten as

$$\begin{aligned} \mathbf{A}^{(k)} z_k \mathbf{c}_0^{(k-1)} &= \gamma z_k \mathbf{c}_0^{(k)}, & k = 1, \dots, M-1, \\ \mathbf{A}^{(M)} \mathbf{c}_0^{(M-1)} &= \gamma \mathbf{c}_0^{(M)}. \end{aligned} \quad (8.22)$$

Note that this is equivalent to the even simpler form

$$\mathbf{A}^{(k)} z_k \mathbf{c}_0^{(k-1)} = \gamma z_k \mathbf{c}_0^{(k)}, \quad k = 1, \dots, M, \quad (8.23)$$

when introducing a fixed $z_M = 1$, which I use in the following to simplify the notation. Substituting $\mathbf{c}^{(k)} = z_{k+1} \mathbf{c}_0^{(k)}$ ($k = 1, \dots, M$), Eq. (8.23) becomes

$$\mathbf{A}^{(k)} \mathbf{c}^{(k-1)} = \gamma \frac{z_k}{z_{k+1}} \mathbf{c}^{(k)}, \quad k = 1, \dots, M. \quad (8.24)$$

Setting

$$C^{(k)} = \gamma \frac{z_k}{z_{k+1}}, \quad k = 1, \dots, M, \quad (8.25)$$

it is easily seen that Eq. (8.24) yields all possible solutions of Eq. (8.19) assuming that z_1, \dots, z_{M-1} are free parameters and $z_M = 1$.

The particular choice of the z_1, \dots, z_{M-1} is not important for the stability of synchronization, as it only rescales the magnitude of the transformed vectors $\tilde{\mathbf{x}}^{(k)}$. The master stability function is calculated in terms of Lyapunov exponents, which measure the growth or shrinkage relative to an initial magnitude and thus do not depend on the factors z_1, \dots, z_{M-1} . Therefore, setting $\delta \tilde{\mathbf{x}}^{(k)} = z_{k+1} \delta \tilde{\mathbf{x}}^{(k)}$ for $k = 1, \dots, M$ into Eq. (8.12) yields

$$\delta \dot{\tilde{\mathbf{x}}}^{(k)} = \mathbf{D}\mathbf{F}^{(k)}|_{\tilde{\mathbf{x}}_s^{(k)}} \delta \tilde{\mathbf{x}}^{(k)}(t) + \sigma^{(k)} \gamma \mathbf{H}^{(k)} \delta \tilde{\mathbf{x}}^{(k-1)}(t - \tau^{(k)}), \quad k = 1, \dots, M. \quad (8.26)$$

In conclusion, Equation (8.26) qualifies as a master stability equation for this network topology.

8.3.2. The ring is generic

This unidirectional ring cluster structure is generic in the sense that any topology that fulfills the conditions

- (i) Each row in the coupling matrix \mathbf{Q} contains exactly one non-zero block,
 - (ii) Each column of the coupling matrix \mathbf{Q} contains exactly one non-zero block,
 - (iii) None of the non-zero blocks lies on the diagonal of the coupling matrix \mathbf{Q} ,
- can be transformed to a unidirectional ring structure by renumbering the clusters.

Condition (i) has to be fulfilled in order to treat synchronization with the master stability function. Violating this condition, one cannot arrive at a valid master stability equation to calculate stability from. This can be seen by considering an example of three groups coupled with a matrix \mathbf{Q} like

$$\mathbf{Q} = \begin{pmatrix} 0 & \mathbf{A} & \mathbf{B} \\ \mathbf{C} & 0 & 0 \\ 0 & \mathbf{D} & 0 \end{pmatrix}. \quad (8.27)$$

Inserting this matrix into Eq. (8.8) yields for the first group

$$\begin{aligned} c_i^{(1)} \delta \dot{\mathbf{x}}^{(1)} &= c_i^{(1)} \mathbf{D}\mathbf{F}^{(1)}|_{\mathbf{x}_s^{(1)}} \delta \bar{\mathbf{x}}^{(1)}(t) \\ &+ \left(\sum_{j=1}^{N_2} A_{ij} c_i^{(2)} \right) \sigma^{(1,2)} \mathbf{H}^{(1,2)} \delta \bar{\mathbf{x}}^{(2)}(t - \tau^{(1,2)}) \\ &+ \left(\sum_{j=1}^{N_3} B_{ij} c_i^{(3)} \right) \sigma^{(1,3)} \mathbf{H}^{(1,3)} \delta \bar{\mathbf{x}}^{(3)}(t - \tau^{(1,3)}). \end{aligned} \quad (8.28)$$

From here, it can easily be seen that no relation similar to Eq. (8.9) can be derived, since the two summands arising due to the coupling cannot be reduced into one.

Condition (ii) means that one group cannot be the input of more than one other group. This is indeed a restriction and not necessary for the master stability function for group synchronization to work. I will show an example where this condition is not met in Sec. 8.3.3.

Condition (iii) is trivial when condition (ii) is already met. As condition (i) has to be fulfilled at the same time, a non-zero block on the diagonal of \mathbf{Q} means that the corresponding cluster is totally uncoupled from the rest of the network, since it is coupled only to itself. Thus it can be separated from that rest and separate master stability functions have to be obtained. If, on the other hand, condition (ii) is not fulfilled, condition (iii) is indeed a restriction of the possible matrices similar to condition (ii).

8.3.3. Two groups having the same input

Consider an example of three groups:

$$\mathbf{Q} = \begin{pmatrix} 0 & \mathbf{A} & 0 \\ \mathbf{B} & 0 & 0 \\ 0 & \mathbf{C} & 0 \end{pmatrix}. \quad (8.29)$$

Using this in Eq. (8.13) yields

$$\begin{pmatrix} 0 & \mathbf{A} & 0 \\ \mathbf{B} & 0 & 0 \\ 0 & \mathbf{C} & 0 \end{pmatrix} \begin{pmatrix} \mathbf{c}^{(1)} \\ \mathbf{c}^{(2)} \\ \mathbf{c}^{(3)} \end{pmatrix} = \begin{pmatrix} C^{(1)}\mathbf{c}^{(1)} \\ C^{(2)}\mathbf{c}^{(2)} \\ C^{(3)}\mathbf{c}^{(3)} \end{pmatrix}, \quad (8.30)$$

and equivalently for Eq. (8.15):

$$\begin{pmatrix} 0 & \mathbf{A} & 0 \\ \mathbf{B} & 0 & 0 \\ 0 & \mathbf{C} & 0 \end{pmatrix} \begin{pmatrix} \mathbf{c}_0^{(1)} \\ \mathbf{c}_0^{(2)} \\ \mathbf{c}_0^{(3)} \end{pmatrix} = \begin{pmatrix} \gamma \mathbf{c}_0^{(1)} \\ \gamma \mathbf{c}_0^{(2)} \\ \gamma \mathbf{c}_0^{(3)} \end{pmatrix}. \quad (8.31)$$

Introducing two rescaling factors z_1 and z_2 this can be rewritten as

$$\begin{pmatrix} 0 & \mathbf{A} & 0 \\ \mathbf{B} & 0 & 0 \\ 0 & \mathbf{C} & 0 \end{pmatrix} \begin{pmatrix} z_2 \mathbf{c}_0^{(1)} \\ z_1 \mathbf{c}_0^{(2)} \\ \mathbf{c}_0^{(3)} \end{pmatrix} = \begin{pmatrix} \gamma \frac{z_1}{z_2} \mathbf{c}_0^{(1)} \\ \gamma \frac{z_2}{z_1} \mathbf{c}_0^{(2)} \\ \gamma z_1 \mathbf{c}_0^{(3)} \end{pmatrix}. \quad (8.32)$$

Using $\mathbf{c}^{(1)} = z_2 \mathbf{c}_0^{(1)}$, $\mathbf{c}^{(2)} = z_1 \mathbf{c}_0^{(2)}$, $\mathbf{c}^{(3)} = \mathbf{c}_0^{(3)}$, $C^{(1)} = \gamma z_1/z_2$, $C^{(2)} = \gamma z_2/z_1$, $C^{(3)} = \gamma z_1$ it can easily be seen that all solutions of Eq. (8.30) can be found with a proper choice of the parameters z_1 and z_2 . Additionally, using the substitutions $\delta \tilde{\mathbf{x}}^{(1)} = z_2 \delta \tilde{\mathbf{x}}^{(1)}$ and $\delta \tilde{\mathbf{x}}^{(2)} = z_1 \delta \tilde{\mathbf{x}}^{(2)}$, it can be seen that Eq. (8.16) is satisfied for this particular choice of \mathbf{Q} with $\delta \tilde{\mathbf{x}}^{(1)}$, $\delta \tilde{\mathbf{x}}^{(2)}$, and $\delta \tilde{\mathbf{x}}^{(3)}$. In conclusion, Eq. (8.16) qualifies as a master stability equation for this network topology.

In conclusion, the three conditions from Sec. 8.3.2 cover a wide range of possible topologies, with exceptions as shown here exemplarily. Nonetheless, the structures that are covered by those condition are general enough to investigate the properties of the corresponding coupling matrices. As I will show, the eigenvalue spectrum has a characteristic symmetry that is also present in the underlying master stability function. As a result, the extent of γ 's parameter space in which $\Lambda(\gamma)$ has to be calculated becomes restricted which lowers the numerical costs.

8.4. The spectrum of the coupling matrix

In this Section, I investigate the spectrum of the coupling matrix $\mathbf{Q} = [\mathbf{q}_{k,n}; k, n = 1, \dots, M]$ with $\mathbf{q}_{k,k-1} = \mathbf{A}^{(k)}$ and zeros otherwise. \mathbf{Q} has at least n_0 eigenvalues zero, where

$$n_0 = \sum_k |N_k - N_{k-1}| \quad (8.33)$$

arises solely due to the block structure of \mathbf{Q} : If all $\mathbf{A}^{(k)}$ have maximum rank equal to $\min(N_k, N_{k-1})$, there are exactly these n_0 zeros. In general, the exact number of zeros is given by $\sum_k (N_k - \text{rank} \mathbf{A}^{(k)})$, which may be larger than n_0 due to the particular structure of the matrices $\mathbf{A}^{(k)}$.

Consider the matrix \mathbf{Q}^M , which is of block diagonal structure

$$(\mathbf{Q}^M)_{kk} = \mathbf{A}^{(k)} \mathbf{A}^{(k-1)} \dots \mathbf{A}^{(1)} \mathbf{A}^{(M)} \mathbf{A}^{(M-1)} \dots \mathbf{A}^{(k+1)} \quad (8.34)$$

and zeros otherwise. Note that each block is a product of all $\mathbf{A}^{(k)}$, only the order differs.

Assume that the groups are arranged such that $N_1 \leq N_j$ ($j = 2, \dots, M$), which can always be achieved by an index shift, and that every $\mathbf{A}^{(k)}$ has maximum rank equal to $\min(N_k, N_{k-1})^1$. Then of the blocks in \mathbf{Q}^M , $(\mathbf{Q}^M)_{11}$ has lowest rank, since it is an $N_1 \times N_1$ matrix. The non-zero eigenvalues of a matrix product are invariant against exchange of the factors, their number (including degeneracy) equals the rank of the product with lowest rank, i.e., $(\mathbf{Q}^M)_{11}$ in our case. See Appendix A for the details regarding this invariance. As a consequence, the non-zero eigenvalues of \mathbf{Q}^M are given by the non-zero eigenvalues of $(\mathbf{Q}^M)_{11}$; $\{\lambda_1, \dots, \lambda_{N_1}\}$. As there are M blocks yielding these very eigenvalues, each of them is M -fold degenerate. In particular, since the row sum of \mathbf{Q}^M is unity, there is an M -fold unity eigenvalue.

The non-zero eigenvalues of \mathbf{Q} are then given by the M th roots of the non-zero eigenvalues of \mathbf{Q}^M , and the whole spectrum $\Gamma = \{\gamma_j\}_{j=1, \dots, \sum N_k}$ of \mathbf{Q} reads

$$\Gamma = \underbrace{\{0, \dots, 0\}}_{n_0} \cup \bigcup_{k=1}^M \left\{ \sqrt[M]{|\lambda_1|} e^{[\arg(\lambda_1) + 2\pi k]i/M}, \dots, \sqrt[M]{|\lambda_M|} e^{[\arg(\lambda_M) + 2\pi k]i/M} \right\}. \quad (8.35)$$

¹The latter assumption simplifies the argument regarding the zero eigenvalues, but the final result is valid for arbitrary ranks of the block matrices

Note, in particular, that the unity eigenvalue $\lambda = 1$ of \mathbf{Q}^M corresponds to the M longitudinal eigenvalues $\gamma_k = \exp(2\pi i k/M)$ of \mathbf{Q} , which are related to directions longitudinal to the group synchronization manifold. Their existence can already be seen solely by looking at \mathbf{Q} itself, because the eigenvectors

$$\mathbf{v}_k = \begin{pmatrix} \exp(-2\pi i k/M) \\ \vdots \\ \exp(-2\pi i k/M) \\ \exp(-4\pi i k/M) \\ \vdots \\ \exp(-4\pi i k/M) \\ \vdots \\ \exp(-2\pi i k) \\ \vdots \\ \exp(-2\pi i k) \end{pmatrix} \begin{matrix} \left. \vphantom{\exp(-2\pi i k/M)} \right\} N_1 \\ \left. \vphantom{\exp(-4\pi i k/M)} \right\} N_2 \\ \left. \vphantom{\exp(-2\pi i k)} \right\} N_M \end{matrix}, \quad (8.36)$$

that correspond to the longitudinal eigenvalues $\gamma_k = \exp(2\pi i k/M)$, do not depend on the inner structure of the blocks $\mathbf{A}^{(k)}$.

Let me assume that the master stability function is invariant with respect to rotations $\gamma \rightarrow \exp(2\pi i/M)\gamma$, which I will show in the next Section, see Fig. 8.2. Also note that each of the multiple roots of $\lambda_1, \dots, \lambda_M$ is obtained as a rotation by multiples of $2\pi/M$ with respect to the roots $\{\sqrt[M]{|\lambda_1|} \exp[i \arg(\lambda_1)/M], \dots, \sqrt[M]{|\lambda_M|} \exp[i \arg(\lambda_M)/M]\}$. As a consequence, we can restrict ourselves to evaluating the master stability function at the location of the eigenvalues

$$\begin{aligned} & \{\sqrt[M]{|\lambda_1|} \exp[i \arg(\lambda_1)/M], \dots \\ & \dots, \sqrt[M]{|\lambda_M|} \exp[i \arg(\lambda_M)/M], 0\}, \end{aligned} \quad (8.37)$$

which lie all inside the sector $\arg(\gamma) \in [0, 2\pi/M)$. Note that the zero eigenvalue is only added here if $n_0 > 0$, i.e., if at least one block $\mathbf{A}^{(k)}$ differs from the others in size. The location of the longitudinal eigenvalues, which are the M th roots of unity, are shown as stars in Fig. 8.2, which illustrates this symmetry.

8.5. The symmetry of the master stability function

Looking closely at the master stability equation (8.26), one can observe another symmetry. The equation is invariant with respect to the transformation $\delta \tilde{\mathbf{x}}^{(k)} \rightarrow \exp(2k\pi i/M) \delta \tilde{\mathbf{x}}^{(k)}$:

$$e^{\frac{2k\pi i}{M}} \delta \dot{\tilde{\mathbf{x}}}^{(k)} = D\mathbf{F}^{(k)}(\mathbf{x}_s^{(k)}) e^{\frac{2k\pi i}{M}} \delta \tilde{\mathbf{x}}^{(k)} + \sigma^{(k)} \gamma \mathbf{H}^{(k)} e^{\frac{2(k-1)\pi i}{M}} \delta \tilde{\mathbf{x}}^{(k-1)}(t - \tau^{(k)}) \quad (8.38)$$

$$\Leftrightarrow \delta \dot{\tilde{\mathbf{x}}}^{(k)} = D\mathbf{F}^{(k)}(\mathbf{x}_s^{(k)}) \delta \tilde{\mathbf{x}}^{(k)} + \sigma^{(k)} \gamma \mathbf{H}^{(k)} e^{\frac{-2\pi i}{M}} \delta \tilde{\mathbf{x}}^{(k-1)}(t - \tau^{(k)}) \quad (8.39)$$

With the transformation $\gamma \rightarrow \exp(-2\pi i/M) \gamma$ the original equation is regained, meaning that the master stability equation is invariant with respect to rotations of $2\pi/M$.

Combining both results – the master stability function and the spectrum of \mathbf{Q} are invariant against rotations of $2\pi/M$ – I conclude that it is sufficient to evaluate the master stability function in a sector given by $\arg(\gamma) \in [0, 2\pi/M)$. Let me stress that this symmetry holds even when considering nonidentical groups. This includes nonidentical local dynamics but also nonidentical coupling parameters – strength and delay time – between the clusters.

In the following, I demonstrate this symmetry and calculate the master stability function in terms of the largest Lyapunov exponent for the example of delay-coupled laser networks.

8.6. Cluster synchronization in laser networks

The results obtained here will be restricted to cluster synchronization where I use identical local dynamics $\mathbf{F}^{(k)}(\mathbf{x}^{(k)}) = \mathbf{F}(\mathbf{x}^{(k)})$ for each cluster $k = 1, \dots, M$. Also the coupling schemes will be identical for each coupling:

$$\mathbf{H}^{(k)} = \mathbf{H} = \begin{pmatrix} 0 & 0 & 0 \\ 0 & 1 & 0 \\ 0 & 0 & 1 \end{pmatrix}. \quad (8.40)$$

I will, however, allow for different coupling strengths $\sigma^{(k)}$ between the clusters (see Sec. 8.8), where $\sigma^{(k)}$ denotes the coupling strength for the coupling from the $(k-1)$ th

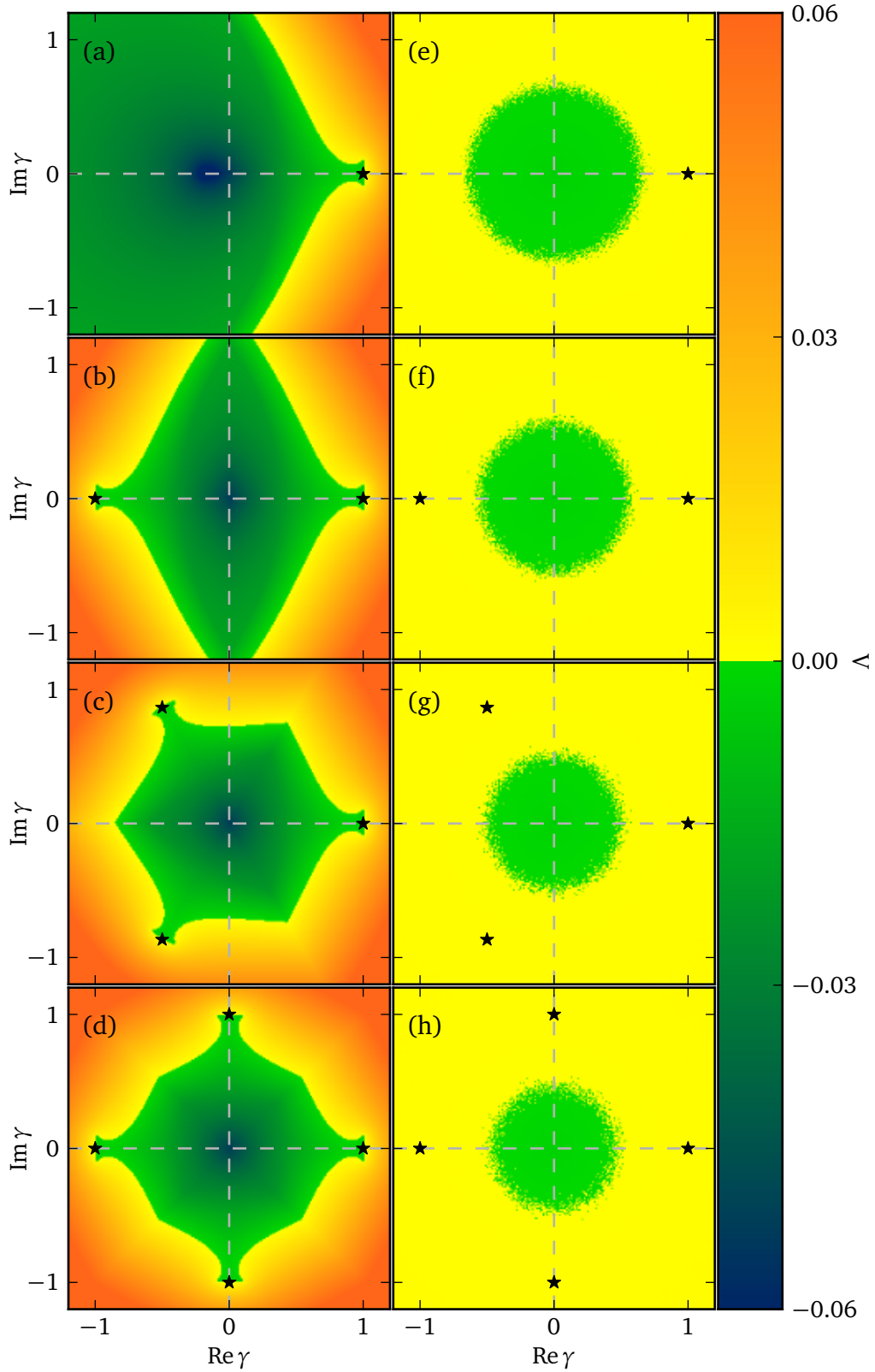


Figure 8.2.: Master stability function in terms of the largest Lyapunov exponent Λ from Eq. (8.26) for $M = 1, 2, 3$, and 4 groups of delay-coupled lasers (2.17) in panels (a,e), (b,f), (c,g), and (d,h), respectively. Black stars mark the position of longitudinal eigenvalues. (a-d): $\tau^{(k)} = \tau = 1$, (e-h): $\tau^{(k)} = \tau = 1000$. $\sigma^{(k)} = \sigma = 0.12$. Other parameters chosen in the LFF regime according to Tab. 2.2.

to the k th group. The cluster synchronization manifold and thus the master stability equation (8.26) are $3M$ -dimensional.

Figure 8.2 shows the master stability function for one, two, three, and four clusters in panel (a), (b), (c), and (d), respectively. The parameters are chosen in the regime of low-frequency fluctuations (LFF, see Tab. 2.2). Also the coupling strengths are kept identical in this example: $\sigma^{(k)} = \sigma = 0.12$. The black stars mark the position of the longitudinal eigenvalues of \mathbf{Q} ; $\gamma_k = \exp(2\pi i k/M)$. There is a symmetry in the master stability function with respect to rotations of $2\pi/M$ observable in Fig. 8.2. This symmetry is a result of the invariance of the master stability equation (8.26) discussed in Sec. 8.5.

For large delay, as shown in the right part of the Figure, the master stability function has a circular shape for one group (panel (e)). This is a universal feature of networks where the coupling delay is large compared to the time scale of the local dynamics, as discussed in Chapter 3; see also the publication by Flunkert et al. [2010]. Due to the rotational symmetry discussed before, the circular shape cannot change when increasing the number of groups, hence the shape of the master stability function is independent of the number of groups when large delay is present in the network (see Fig. 8.2(f-h)), but one can observe that the disc of stability is shrinking with increasing number of clusters.

8.7. The relation of the number of clusters and the delay time

This shrinking of the master stability function with increasing number of clusters can be explained as follows: The dimension of the synchronization manifold (8.4) is proportional to the number of groups. Since the blocks of the matrix \mathbf{Q} are arranged in a unidirectional ring, the dynamics inside the synchronization manifold takes place inside such a unidirectional ring. Hence, the time that it takes for a signal to travel through this ring scales linearly with the number of groups M .

This signal traveling-time can be seen as an effective time delay governing the degree of chaos, i.e., the longitudinal Lyapunov exponent. As I have discussed in Chapter 3, a larger longitudinal Lyapunov exponent due to a longer delay time yields a smaller radius of the stable region [Flunkert et al., 2010].

Against the background of the results obtained for the master stability function, I will discuss several example topologies in the following. I will start with one of the simplest

motifs that allows for a 2-cluster state and will then also cover more complex network topologies.

8.8. Application: two-cluster states in laser networks

As a first example I will consider a network of 4 lasers in a bidirectionally coupled ring, where each two opposite lasers belong to the same group, which lets the network have two groups. Figure 8.1 depicts the scenario schematically.

In the notation derived above, a bidirectionally coupled ring of two groups yields the block matrix $\mathbf{Q} = \{\mathbf{A}^{(k)}\}$ denoting the inter-group connections as

$$\mathbf{Q} = \begin{pmatrix} 0 & \mathbf{A}^{(1)} \\ \mathbf{A}^{(2)} & 0 \end{pmatrix}. \quad (8.41)$$

The dynamics of the network follows Eq. (8.3), where here the number of groups is $M = 2$ and the number of elements in groups is $N_1 = N_2 = 2$:

$$\begin{aligned} \dot{\mathbf{x}}_i^{(1)} &= \mathbf{F}[\mathbf{x}_i^{(1)}(t)] + \sigma^{(1)} \sum_{j=1}^2 A_{ij}^{(1)} \mathbf{H}^{(1)} \mathbf{x}_j^{(2)}(t - \tau^{(1)}), \\ \dot{\mathbf{x}}_i^{(2)} &= \mathbf{F}[\mathbf{x}_i^{(2)}(t)] + \sigma^{(2)} \sum_{j=1}^2 A_{ij}^{(2)} \mathbf{H}^{(2)} \mathbf{x}_j^{(1)}(t - \tau^{(2)}). \end{aligned} \quad (8.42)$$

The synchronization manifold is given according to Eq. (8.4):

$$\begin{aligned} \dot{\mathbf{x}}_s^{(1)} &= \mathbf{F}[\mathbf{x}_s^{(1)}(t)] + \sigma^{(1)} \mathbf{H}^{(1)} \mathbf{x}_s^{(2)}(t - \tau^{(1)}), \\ \dot{\mathbf{x}}_s^{(2)} &= \mathbf{F}[\mathbf{x}_s^{(2)}(t)] + \sigma^{(2)} \mathbf{H}^{(2)} \mathbf{x}_s^{(1)}(t - \tau^{(2)}) \end{aligned} \quad (8.43)$$

using Eq. (8.41). Following Eq. (8.16) the master stability equation reads

$$\begin{aligned} \delta \dot{\mathbf{x}}^{(1)} &= \mathbf{DF}^{(1)}|_{\mathbf{x}_s^{(1)}} \delta \bar{\mathbf{x}}^{(1)}(t) + \sigma^{(1)} \gamma \mathbf{H}^{(1)} \delta \bar{\mathbf{x}}^{(2)}(t - \tau^{(1)}), \\ \delta \dot{\mathbf{x}}^{(2)} &= \mathbf{DF}^{(2)}|_{\mathbf{x}_s^{(2)}} \delta \bar{\mathbf{x}}^{(2)}(t) + \sigma^{(2)} \gamma \mathbf{H}^{(2)} \delta \bar{\mathbf{x}}^{(1)}(t - \tau^{(2)}). \end{aligned} \quad (8.44)$$

8.8.1. Stability of the 2-cluster state

As I have already shown in Chapter 4, isochronous synchronization is unstable for bidirectionally coupled rings of any size. Therefore, no isochronous synchronization will take place within the synchronization manifold described by Eq. (8.43). I will now show under which circumstances the 2-cluster state described by Eqs. (8.43) is stable. Note that the parameter space is four-dimensional, as one can vary the time delays $\tau^{(1)}$ and $\tau^{(2)}$ as well as the coupling strengths $\sigma^{(1)}$ and $\sigma^{(2)}$.

For the coupling from group 2 to group 1 I will, however, keep the coupling strengths and the time delays fixed at the values formerly used for the investigations of the isochronous synchronization manifold. As the coupling strength was $\sigma = 0.12$ and the delay time $\tau = 1000$, this yields $\tau^{(2)} = 1000$ and $\sigma^{(2)} = 0.12$. Still the parameter space for the master stability function includes the delay and coupling strength in the other direction:

$$\Lambda = \Lambda(\gamma, \sigma^{(1)}, \tau^{(1)}) \quad (8.45)$$

The eigenvalues γ_k are calculated from the matrix

$$\mathbf{Q} = \frac{1}{2} \begin{pmatrix} 0 & 0 & 1 & 1 \\ 0 & 0 & 1 & 1 \\ 1 & 1 & 0 & 0 \\ 1 & 1 & 0 & 0 \end{pmatrix}, \quad (8.46)$$

which has unity row sum and does not include any information about the nonidenticality of the parameters for each coupling directions. Its eigenvalues are given by

$$\begin{aligned} \gamma_1 &= 1, \\ \gamma_2 &= -1, \\ \gamma_3 &= 0, \\ \gamma_4 &= 0 \end{aligned} \quad (8.47)$$

with the corresponding eigenvectors

$$\mathbf{v}_1 = \begin{pmatrix} 1 \\ 1 \\ 1 \\ 1 \end{pmatrix}, \mathbf{v}_2 = \begin{pmatrix} -1 \\ -1 \\ 1 \\ 1 \end{pmatrix}, \mathbf{v}_3 = \begin{pmatrix} 0 \\ 0 \\ -1 \\ 1 \end{pmatrix}, \mathbf{v}_4 = \begin{pmatrix} -1 \\ 1 \\ 0 \\ 0 \end{pmatrix}. \quad (8.48)$$

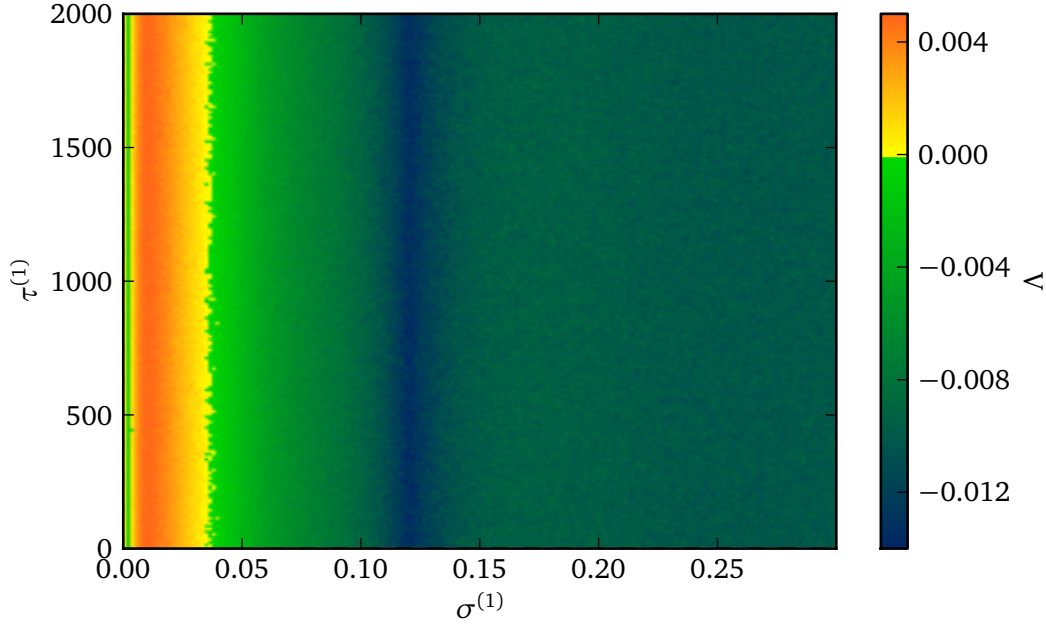


Figure 8.3.: Master stability function evaluated at $\gamma = 0$, which corresponds to stability of cluster synchronization in the bidirectionally coupled ring with $N = 4$, in dependence of the coupling strength $\sigma^{(1)}$ and coupling delay $\tau^{(1)}$. Other parameters are chosen in the LFF regime according to Tab. 2.2.

Remember that the theory employed here only considers the stability of synchronization inside each group but not between the group. It can be seen that the eigenvalues γ_1 and γ_2 correspond to directions inside this generalized synchronization manifold since the first two and the last two entries in the corresponding eigenvectors \mathbf{v}_1 and \mathbf{v}_2 are not linearly independent. This is a special case of the general properties derived in Sec. 8.4.

As a consequence only the two-fold degenerate eigenvalue $\gamma_3 = \gamma_4 = 0$ describes the dynamics transversal to synchronization manifold. This allows the master stability function to be exhaustive when evaluated only at $\gamma = 0$. Figure 8.3 shows the master stability function at $\gamma = 0$ in terms of the largest Lyapunov exponent λ in dependence on the coupling strength $\sigma^{(1)}$ and the delay time $\tau^{(1)}$ for fixed $\sigma^{(2)} = 0.12$ and $\tau^{(2)} = 1000$ corresponding to the regime of low-frequency fluctuations (LFF) according to Tab. 2.2.

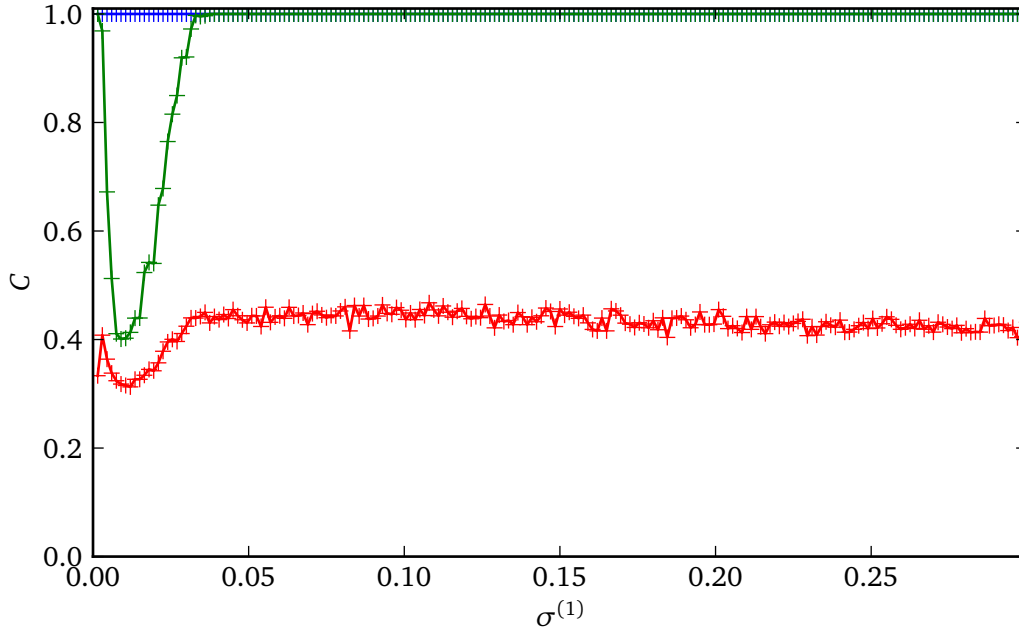


Figure 8.4.: Cross correlations in a bidirectionally coupled ring of 4 nodes in dependence on the coupling strength $\sigma^{(1)}$ for fixed $\tau^{(1)} = 1000$. Blue: correlation in cluster (1), green: correlation in cluster (2), red: correlation of the whole network. Other parameters are chosen in the LFF regime according to Tab. 2.2.

It can be seen that the difference in time delay does not yield any significant effects. This will be further investigated using the time series of simulations further below. Varying the coupling strength $\sigma^{(1)}$, there is a critical value for which synchronization becomes unstable. By running direct simulations of this very bidirectional ring, the predictions of the master stability function are matched. In Fig. 8.4 I show the cross correlations in the network in dependence on the parameter $\sigma^{(1)}$ for fixed $\tau^{(1)} = 1000$ and the other parameters as before. The red curve depicts the mean correlations of the intensities in the entire network, while the blue and green curves show the mean correlation in cluster (1) and cluster (2), respectively. Again, it can be seen that the coupling strength $\sigma^{(1)}$, shows a threshold, below which the cluster state becomes unstable as the correlation inside cluster (2) gets lost. The dynamical scenario that emerges when changing the coupling strength in one group below this threshold is depicted schematically in Fig. 8.5. Note that in Fig. 8.4 it can be observed that the correlation increases for very small values of $\sigma^{(1)}$. One may get the impression that synchronization is enhanced

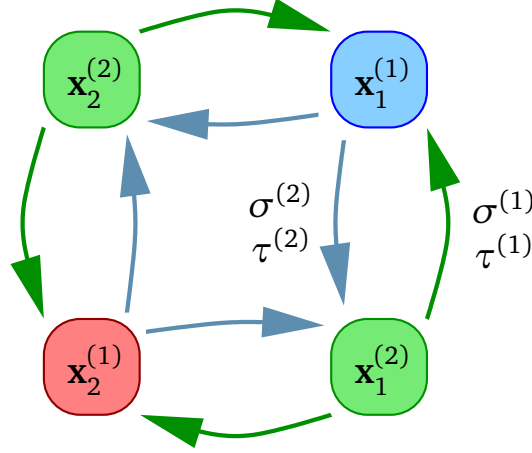


Figure 8.5.: Scheme of the partial synchronization that arises in the bidirectional ring of 4 lasers for low correlation inside group (1) according to Fig. 8.4. Elements of group (1) are colored in blue and red, elements of group (2) are green. $\sigma^{(1)}$ and $\sigma^{(2)}$ and $\tau^{(1)}$ and $\tau^{(2)}$ denote the coupling strengths and the time delays for couplings from group (2) to (1) and (1) to (2), respectively.

again, but this is only due to cluster (2) going to fixed point dynamics for very small $\sigma^{(1)}$.

8.9. Bipartite random networks

While the previous Section focused on the effects of the coupling parameters in a fixed example topology, the influence of the topology itself will be looked at here. The simplest example of a complex network that can show cluster synchronization and be treated with the master stability approach derived in this Chapter is a bipartite random network. This follows from the results of Chapter 5, where I have shown that there is a threshold in the link probability at which a phase transition from desynchronization to synchronization takes place.

The coupling matrix of a bipartite random network that is treatable with the master stability function derived in this Chapter is constructed as

$$\mathbf{Q} = \begin{pmatrix} 0 & \mathbf{A}^{(1)} \\ \mathbf{A}^{(2)} & 0 \end{pmatrix}, \quad (8.49)$$

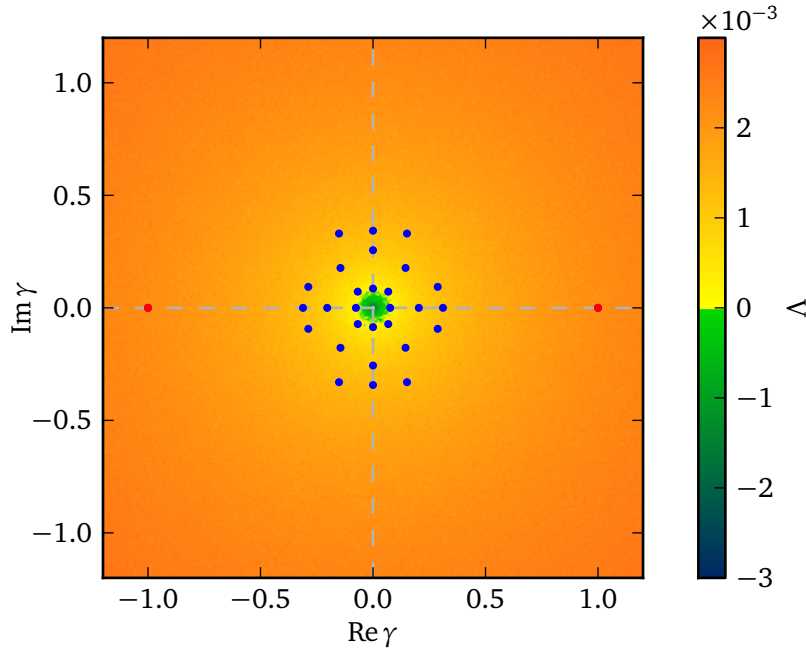


Figure 8.6.: Master stability function in terms of largest Lyapunov exponent Λ from Eq. (8.26) for $M = 2$ groups of delay-coupled lasers (2.17). Parameters: $\tau^{(k)} = \tau = 1000$, $\sigma^{(k)} = \sigma = 0.12$, $T = 200$, $p = 1$, $\alpha = 4$, according to the CC regime in Tab. 2.2. Blue dots indicate the location of the eigenvalues of a directed bipartite random graph of $N = 30$ nodes with link probability $p = 0.4$, red dots show the longitudinal values $\gamma = \pm 1$.

where $\mathbf{A}^{(1)}$ and $\mathbf{A}^{(2)}$ are directed Erdős-Rényi random graphs of the size $\frac{N}{2} \times \frac{N}{2}$ that are renormalized to unity row sum. The master stability function would also work for different sizes of both clusters, but I focus on the influence of the link probability p here and consider only equally sized clusters.

Figure 8.6 shows the eigenvalues of the matrix (8.49) for a link probability $p = 0.4$ for $N = 30$ lasers, i.e., 15 nodes in each cluster, against the master stability function in the coherence-collapse regime (CC, see Tab. 2.2) as before. It can be seen that this network does not show stable two-cluster synchronization. As with the isochronous synchronization, the eigenspectrum is distributed around zero, where the radius of this distribution increases when lowering the link probability p . Again, there is a phase transition to desynchronization for small p .

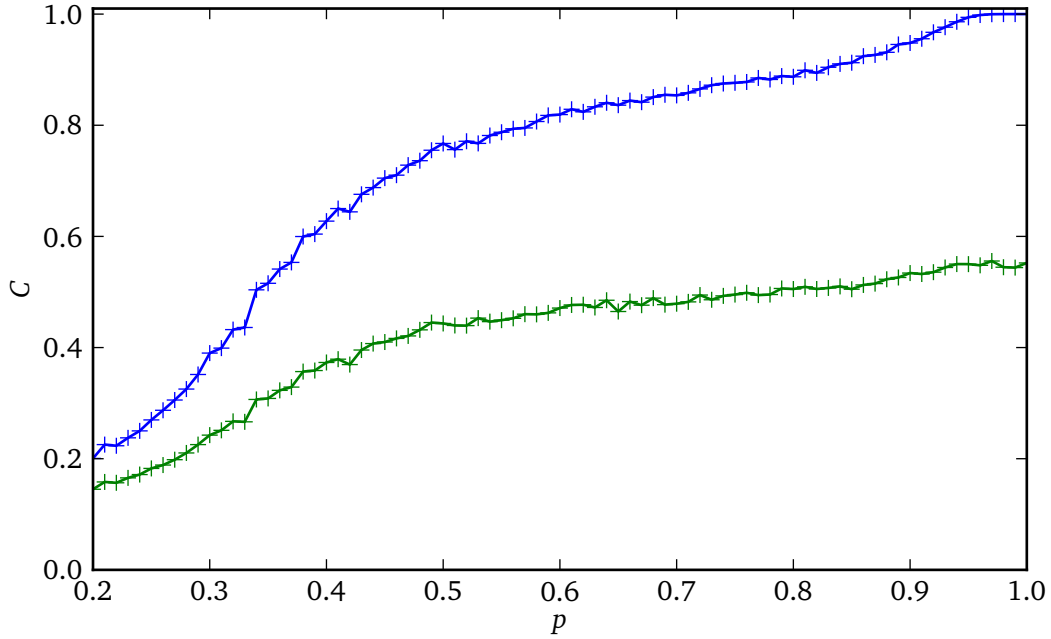


Figure 8.7.: Mean cross correlations in a bipartite random network of $N = 30$ lasers in dependence on the link probability p . Blue: correlation inside the clusters, green: correlation in the whole network. Parameters are chosen in the CC regime according to Tab. 2.2.

This behavior is illustrated in Fig. 8.7, which shows the average correlations in the bipartite random network of 30 lasers in dependence on the parameter p for the CC regime. The blue and green lines correspond to the average correlation inside the clusters and in the whole network, respectively. While the overall correlation is low for any value of p , the phase transition can be seen in the correlation for the clusters, which decreases at lower values of p . I chose the CC regime here as an example. In the LFF regime, synchronization will be stable for any value of p above the percolation threshold, as I have already shown for isochronous synchronization in Chapter 5.

8.10. Conclusion

In this Chapter, I introduced a technique to characterize cluster and group synchronization using an extension of the master stability function. The formalism is restricted to a class of coupling matrices that have a block structure with one block in each row of the coupling matrix, i.e., multipartite networks. While several matrices have this form or can be transformed to this form, the following Chapter partially overcomes this limitation by using multiple coupling matrices.

Using the example of the bidirectional ring I have shown how the master stability framework can be used to predict thresholds in the coupling strength, below which cluster synchronization breaks down. To illustrate the dependence on topology, I used a bipartite Erdős-Rényi random graph, where the results from Chapter 5 could be generalized to cluster synchronization.

9. Beyond the one-block restriction

In Chapter 8 I developed a master stability formalism to determine the stability of group and cluster synchronization. In order to utilize the master stability framework, one major restriction came up: Each group has to get input from one and only one other group. More complex topologies beyond multipartite structures like, for instance, lattices as described by Kestler et al. [2007, 2008] could not be dealt with. There sublattice synchronization as a special form of cluster synchronization was considered.

Following the spirit of Chapter 6, where I have shown that stability of isochronous synchronization in a network with multiple coupling matrices can be determined by a master stability function if these multiple coupling matrices commute pairwise with each other, I will develop this idea further and transfer it to the scope of group and cluster synchronization in this Chapter.

I will derive the master stability equation for group synchronization with multiple coupling matrices. Some restrictions – although not as tight as before – arise, which I will explain in detail.

9.1. The master stability function

The network dynamics for group synchronization with one coupling matrix could be written in the form (8.3), and the synchronization manifold and the master stability equation were given by Eqs. (8.4) and (8.16), respectively.

Generalizing this to two coupling matrices yields for the network dynamics of M clusters:

$$\begin{aligned} \dot{\mathbf{x}}_i^{(k)} = & \mathbf{F}^{(k)}[\mathbf{x}_i^{(k)}(t)] + \\ & \sum_{n=1}^M \left[\sigma_1^{(kn)} \sum_{j=1}^{N_n} A_{ij}^{(kn)} \mathbf{H}^{(kn)} \mathbf{x}_j^{(n)}(t - \tau^{(kn)}) + \sigma_2^{(kn)} \sum_{j=1}^{N_n} B_{ij}^{(kn)} \mathbf{H}^{(kn)} \mathbf{x}_j^{(n)}(t - \tau^{(kn)}) \right]. \end{aligned} \quad (9.1)$$

For the sake of simplicity and readability, I use identical coupling schemes and identical time delays for both coupling terms. Similarly to Chapter 6, the sum of $\sigma_1^{(kn)}$ and $\sigma_2^{(kn)}$ must yield the overall coupling strength $\sigma^{(kn)}$ from Chapter 8 in order to arrive at the same dynamical regime: $\sigma_1^{(kn)} + \sigma_2^{(kn)} = \sigma^{(kn)}$.

From the above, the synchronization manifold is obtained as

$$\dot{\mathbf{x}}_s^{(k)} = \mathbf{F}^{(k)}[\mathbf{x}_s^{(k)}(t)] + \sigma_1^{(kn)} \sum_{n=1}^M a^{(kn)} \mathbf{H}^{(kn)} \mathbf{x}_s^{(n)}(t - \tau^{(kn)}) + \sigma_2^{(kn)} \sum_{n=1}^M b^{(kn)} \mathbf{H}^{(kn)} \mathbf{x}_s^{(n)}(t - \tau^{(kn)}) \quad (9.2)$$

for $k = 1, \dots, M$, where $a^{(kn)}$ and $b^{(kn)}$ denote the row sums of the matrices $\mathbf{A}^{(kn)}$ and $\mathbf{B}^{(kn)}$. As in Chapter 8, for a given k , only one of the $\mathbf{A}^{(kn)}$ can be non-zero. This one non-zero matrix is assumed to have a unity row sum as before. The same holds for $\mathbf{B}^{(kn)}$, which is part of a second block matrix. Effectively, each of the sums in the above equation simplifies to one summand. The index n can be different for both contributions, though.

Finally, the master stability equation becomes

$$\delta \dot{\mathbf{x}}^{(k)} = \mathbf{DF}^{(k)}|_{\mathbf{x}_s^{(k)}} \delta \bar{\mathbf{x}}^{(k)}(t) + \sigma_1^{(kn)} \gamma^{(1)} \mathbf{H}^{(kn)} \delta \bar{\mathbf{x}}^{(n)}(t - \tau^{(kn)}) + \sigma_2^{(km)} \gamma^{(2)} \mathbf{H}^{(km)} \delta \bar{\mathbf{x}}^{(m)}(t - \tau^{(km)}), \quad (9.3)$$

for $k = 1, \dots, M$, where the indices n and m denote the location of the non-zero block in the matrices \mathbf{Q}_1 and \mathbf{Q}_2 , respectively. \mathbf{Q}_1 and \mathbf{Q}_2 are the matrices containing the blocks $\mathbf{A}^{(kn)}$ and $\mathbf{B}^{(kn)}$, respectively, following the notation of Sec. 8.2.

This is a very heavy-weight notation in the case of an arbitrary number of clusters M and arbitrary location of the non-zero blocks in both matrices \mathbf{Q}_1 and \mathbf{Q}_2 . For a specific application, however, this notation simplifies greatly. I will show examples in the following.

9.2. A minimal example for groups

Let me first consider the most simple example, namely only two groups. Synchronization in two groups has already been studied by Sorrentino and Ott [2007] when using a single coupling matrix of the form

$$\mathbf{Q}_1 = \begin{pmatrix} 0 & \mathbf{A}^{(1)} \\ \mathbf{A}^{(2)} & 0 \end{pmatrix}, \quad (9.4)$$

where the matrices $\mathbf{A}^{(1)}$ and $\mathbf{A}^{(2)}$ describe the coupling from the second to the first group and vice versa, respectively.

A generalization to more than two groups was given in Chapter 8, with the restriction that each row in the coupling matrix \mathbf{Q} had to have exactly one block, i.e., each group had to get input from exactly one other group. In the case of two groups, I will now elaborate what happens when introducing a second coupling matrix

$$\mathbf{Q}_2 = \begin{pmatrix} \mathbf{B}^{(1)} & 0 \\ 0 & \mathbf{B}^{(2)} \end{pmatrix}. \quad (9.5)$$

Both matrices have unity row sum and the dynamical equations of the network (cf. Eq. (9.1)) read

$$\begin{aligned} \dot{\mathbf{x}}_i^{(1)} &= \mathbf{F}[\mathbf{x}_i^{(1)}(t)] + \sigma_1^{(1)} \sum_{j=1}^{N_2} A_{ij}^{(1)} \mathbf{H}\mathbf{x}_j^{(2)}(t - \tau) + \sigma_2^{(1)} \sum_{j=1}^{N_1} B_{ij}^{(1)} \mathbf{H}\mathbf{x}_j^{(1)}(t - \tau), \\ \dot{\mathbf{x}}_i^{(2)} &= \mathbf{F}[\mathbf{x}_i^{(2)}(t)] + \sigma_1^{(2)} \sum_{j=1}^{N_1} A_{ij}^{(2)} \mathbf{H}\mathbf{x}_j^{(1)}(t - \tau) + \sigma_2^{(2)} \sum_{j=1}^{N_2} B_{ij}^{(2)} \mathbf{H}\mathbf{x}_j^{(2)}(t - \tau). \end{aligned}$$

Note that here I chose to use only one time delay τ for simplicity. For the same reason, the local dynamics \mathbf{F} and the coupling scheme \mathbf{H} are identical for both groups in this example. The synchronization manifold is given as

$$\begin{aligned} \dot{\mathbf{x}}_s^{(1)} &= \mathbf{F}[\mathbf{x}_s^{(1)}(t)] + \sigma_1^{(1)} \mathbf{H}\mathbf{x}_s^{(2)}(t - \tau) + \sigma_2^{(1)} \mathbf{H}\mathbf{x}_s^{(1)}(t - \tau), \\ \dot{\mathbf{x}}_s^{(2)} &= \mathbf{F}[\mathbf{x}_s^{(2)}(t)] + \sigma_1^{(2)} \mathbf{H}\mathbf{x}_s^{(1)}(t - \tau) + \sigma_2^{(2)} \mathbf{H}\mathbf{x}_s^{(2)}(t - \tau), \end{aligned} \quad (9.6)$$

from which these master stability equations arise as variational equations:

$$\begin{aligned} \delta \dot{\bar{\mathbf{x}}}^{(1)} &= \mathbf{DF}|_{\mathbf{x}_s^{(1)}} \delta \bar{\mathbf{x}}^{(1)}(t) + \sigma_1^{(1)} \gamma^{(1)} \mathbf{H} \delta \bar{\mathbf{x}}^{(2)}(t - \tau) + \sigma_2^{(1)} \gamma^{(2)} \mathbf{H} \delta \bar{\mathbf{x}}^{(1)}(t - \tau), \\ \delta \dot{\bar{\mathbf{x}}}^{(2)} &= \mathbf{DF}|_{\mathbf{x}_s^{(2)}} \delta \bar{\mathbf{x}}^{(2)}(t) + \sigma_1^{(2)} \gamma^{(1)} \mathbf{H} \delta \bar{\mathbf{x}}^{(1)}(t - \tau) + \sigma_2^{(2)} \gamma^{(2)} \mathbf{H} \delta \bar{\mathbf{x}}^{(2)}(t - \tau). \end{aligned} \quad (9.7)$$

Figure 9.1 shows the master stability function for the structure given by these matrices \mathbf{Q}_1 and \mathbf{Q}_2 and for laser parameters in the regime of low-frequency fluctuations (LFF, see Tab. 2.2). The eigenvalue pairs depicted by the blue dots correspond to a particular topology that will be discussed in the following Section.

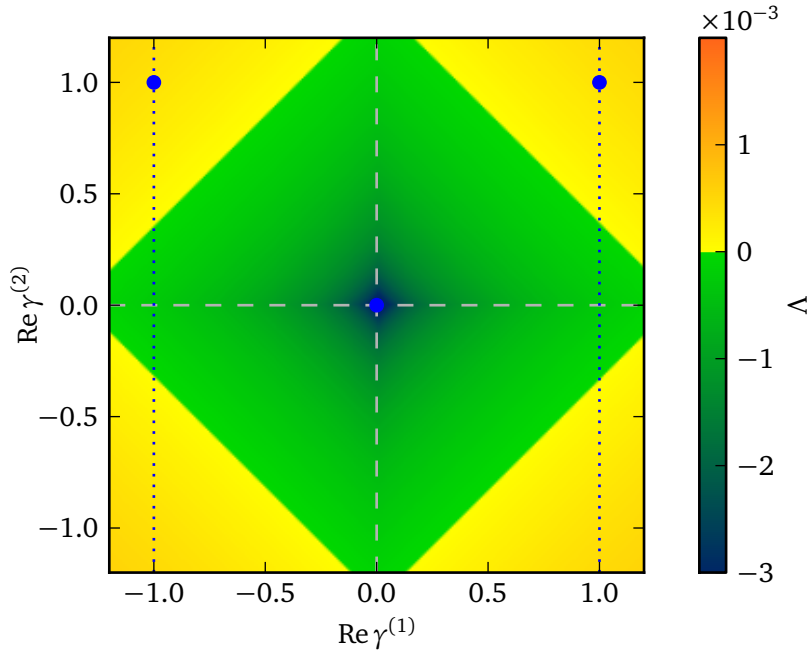


Figure 9.1.: Master stability function for two coupling matrices using the structures \mathbf{Q}_1 as in Eq. (9.4) and \mathbf{Q}_2 as in Eq. (9.5) with coupling strengths $\sigma_1^{(1)} = \sigma_2^{(1)} = \sigma_1^{(2)} = \sigma_2^{(2)} = \sigma/2$. Parameters chosen in the LFF regime according to Tab. 2.2. The pairs $(\text{Re } \gamma^{(1)}, \text{Re } \gamma^{(2)})$ plotted as blue dots correspond to eigenvalues of the matrices (9.4) and (9.5) using Eq. (9.11), i.e., an all-to-all network.

In order for the master stability function to yield valid results for a given topology, the matrices \mathbf{Q}_1 and \mathbf{Q}_2 have to commute. Using the forms (9.4) and (9.5), the relation $[\mathbf{Q}_1, \mathbf{Q}_2] = 0$ is equivalent to

$$\begin{cases} \mathbf{A}^{(1)}\mathbf{B}^{(2)} = \mathbf{B}^{(1)}\mathbf{A}^{(1)} \\ \mathbf{A}^{(2)}\mathbf{B}^{(1)} = \mathbf{B}^{(2)}\mathbf{A}^{(2)}. \end{cases} \quad (9.8)$$

These conditions are fulfilled for certain classes of matrices only. Deriving a more specific condition for the $\mathbf{A}^{(1)}$, $\mathbf{A}^{(2)}$, $\mathbf{B}^{(1)}$, and $\mathbf{B}^{(2)}$ is not possible, because Eq. (9.8) is not only a condition for matrices to commute, but the mixed products introduce tighter conditions. I will show examples in the following that use matrices which fulfill these conditions.

9.2.1. Cluster states in an all-to-all network?

Looking at Eqs. (9.4) and (9.5), the most simple example that can be considered is an all-to-all – or globally coupled – network. Such a network including self-couplings has the renormalized coupling matrix

$$\mathbf{G} = \frac{1}{N} \begin{pmatrix} 1 & 1 & \cdots & 1 \\ 1 & 1 & \cdots & 1 \\ \vdots & \vdots & \ddots & \vdots \\ 1 & 1 & \cdots & 1 \end{pmatrix} \quad (9.9)$$

The question may arise whether cluster states may exist and be stable in this network. I have shown that such a topology shows stable isochronous synchronization with Lang-Kobayashi laser nodes in Chapter 4. If a cluster state exists, this would mean multistability between these states.

The existence of a two-cluster state can be investigated using the matrices \mathbf{Q}_1 and \mathbf{Q}_2 according to Eqs. (9.4) and (9.5), respectively, with

$$\mathbf{G} = \frac{1}{2} (\mathbf{Q}_1 + \mathbf{Q}_2), \quad (9.10)$$

where each of the matrices \mathbf{Q}_1 and \mathbf{Q}_2 has unity row sum, and coupling strengths $\sigma_1^{(1)} = \sigma_2^{(1)} = \sigma_1^{(2)} = \sigma_2^{(2)} = \sigma/2$. Splitting \mathbf{G} without additional renormalization of the row sums can then only be achieved by splitting into two clusters of the same size $N/2$. An even number of nodes N is thus a necessary condition. The matrices \mathbf{A}_1 , \mathbf{A}_2 , \mathbf{B}_1 , and \mathbf{B}_2 in Eqs. (9.4) and (9.5) then all are identical $N/2 \times N/2$ matrices:

$$\mathbf{A}^{(1)} = \mathbf{A}^{(2)} = \mathbf{B}^{(1)} = \mathbf{B}^{(2)} = \frac{2}{N} \begin{pmatrix} 1 & 1 & \cdots & 1 \\ 1 & 1 & \cdots & 1 \\ \vdots & \vdots & \ddots & \vdots \\ 1 & 1 & \cdots & 1 \end{pmatrix} \quad (9.11)$$

Matrices \mathbf{Q}_1 and \mathbf{Q}_2 have unity row sum and do commute in this case, since the relations (9.8) hold trivially for identical matrices. The eigenvalue pairs $(\gamma^{(1)}, \gamma^{(2)})$ in this example are obtained using a straight calculation of the eigenvectors corresponding to the eigenvalues. Note that for general and especially for non-circulant matrices, a joint diagonalization algorithm, for instance by [Cardoso and Souloumiac \[1996\]](#), can be used. The results are plotted in Fig. 9.1 for $N = 30$. There are two pairs of eigenvalues

corresponding to dynamics longitudinal to the synchronization manifold: $(\gamma^{(1)}, \gamma^{(2)}) = (1, 1)$ and $(-1, 1)$. The other $N - 2$ pairs are degenerate at $(0, 0)$.

The Figure suggests that a two-cluster state should indeed exist in an all-to-all network. Given that the isochronous synchronization is also stable in this model (cf. Sec. 4.5.3), this would indicate multistability between these states. Keeping in mind that in an all-to-all network the coupling matrix is invariant against permutations of any two nodes, the degree of multistability would be even higher, as different realizations of the two-cluster state select different nodes being a member of one or the other cluster.

We will see in the following that the 2-cluster state exists only “formally” and the dynamics in this state are identical to a state of isochronous synchronization.

9.2.2. A sufficient condition for the existence of a cluster state

The synchronous dynamics in the 2-cluster state is governed by Eq. (9.6). This equation for the synchronized dynamics in cluster (1) and cluster (2) can as well be seen as governing the dynamics of two nodes $\mathbf{x}_s^{(1)}$ and $\mathbf{x}_s^{(2)}$ with a coupling matrix

$$\hat{\mathbf{G}} = \begin{pmatrix} \sigma_2^{(1)} & \sigma_1^{(1)} \\ \sigma_1^{(2)} & \sigma_2^{(2)} \end{pmatrix}. \quad (9.12)$$

In the all-to-all network I used $\sigma_1^{(1)} = \sigma_2^{(1)} = \sigma_1^{(2)} = \sigma_2^{(2)} = \sigma/2$, which yields

$$\hat{\mathbf{G}} = \frac{\sigma}{2} \begin{pmatrix} 1 & 1 \\ 1 & 1 \end{pmatrix}. \quad (9.13)$$

This now is again just the coupling matrix of an all-to-all network with feedback and unity row sum. I have shown in Sec. 4.5.3 that isochronous synchronization is always stable in such a network for the Lang-Kobayashi model. Translating this back to the synchronous dynamics in the two cluster considered here, both clusters will synchronize and the whole network will end up in a state of isochronous synchronization. In other words, the master stability function that is calculated from Eq. (9.7) determines the stability of a two-cluster state with identical dynamics in both clusters in this case. In conclusion, there is no two-cluster state – in its real sense – in the all-to-all network.

Using Eq. (9.12), it is possible to formulate a condition that determines in what kind of cluster topologies the existence of a “real” two-cluster state – stable or not – is possible:

The dynamics of the synchronized solution is governed by the coupling strengths $\sigma_1^{(1)}$, $\sigma_2^{(1)}$, $\sigma_1^{(2)}$, and $\sigma_2^{(2)}$. Thus, Equation (9.12) describes the synchronous dynamics. With the all-to-all to all example it is easily seen that using identical coupling strengths in Eq. (9.12), this resembles Eq. (9.13). Separating the coupling strength from Eq. (9.12), i.e., using unity row sum in $\hat{\mathbf{G}}$ and using the relations $\sigma_1^{(1)} + \sigma_2^{(1)} = \sigma$ and $\sigma_1^{(2)} + \sigma_2^{(2)} = \sigma$, Equation (9.12) corresponds to motif no. 5 from Tab. 4.1 in Chapter 4. The existence of a two-cluster state is thus equivalent to the instability of that motif, which has been covered in Sec. 4.2.1 in detail.

In general, if the coupling matrix (9.12) yields unstable isochronous synchronization, a two-cluster state does exist in the network built by \mathbf{Q}_1 and \mathbf{Q}_2 . In the laser model, the stability of the isochronous synchronization generally forbids the existence of any other state, thus the other direction is also valid: If the coupling matrix (9.12) yields stable isochronous synchronization, a two-cluster state does not exist in the network built by \mathbf{Q}_1 and \mathbf{Q}_2 . In general, several states may coexist, and thus only the former formulation is valid.

Using equal coupling strengths for each cluster, i.e., $\sigma_1^{(1)} = \sigma_1^{(2)}$ and $\sigma_2^{(1)} = \sigma_2^{(2)}$ and the condition that both coupling strength have to sum up to the overall coupling strength σ , it is possible to compare Eq. (9.12) to Eq. (4.1) and use the results from Sec. 4.2.1. Then, instability of the isochronous synchronization is obtained if either

$$\begin{aligned} \sigma_1^{(1)}/\sigma = \sigma_1^{(2)}/\sigma &> 0.825 \quad \text{or} \\ \sigma_1^{(1)}/\sigma = \sigma_1^{(2)}/\sigma &< 0.175 \end{aligned} \tag{9.14}$$

is fulfilled and only in this case a 2-cluster can exist as a solution of the dynamics.

Note that this consideration does only determine the existence of a two-cluster state. Stability is then to be investigated using the master stability function on the whole network including the matrices \mathbf{Q}_1 and \mathbf{Q}_2 . In the following Section, I will use an example that exhibits a “real” two-cluster state and calculate the stability of this state.

9.3. Towards hierarchical networks

A hierarchical network usually consists of topological clusters that are densely coupled inside, while links to other such topological clusters are sparse. The hierarchy is then

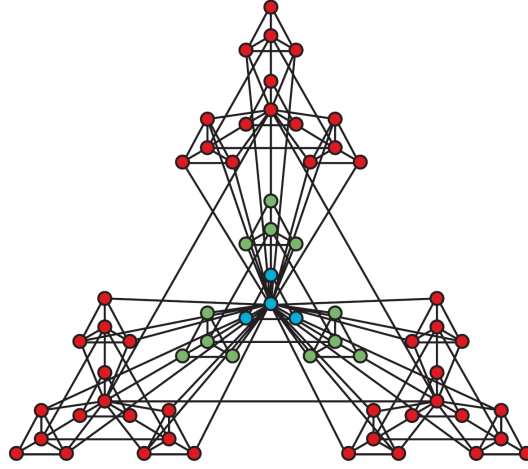


Figure 9.2.: Scheme of a hierarchical structure [reproduced from [Barabási and Oltvai, 2004](#)].

built by larger topological clusters that contain the smaller ones [[Zhou et al., 2006](#); [Zhou and Kurths, 2006](#)]. This procedure can be continued over many levels of hierarchy. See Fig. 9.2 for a schematic view of such a structure. It is important to distinguish these topological clusters from the dynamical cluster states that are investigated in this part of the thesis.

The most simple hierarchical structure consists of just two topological clusters. Figure 9.3 illustrates this in a schematic sketch of a graph of 30 nodes with two topological clusters. Blue color corresponds to links inside one cluster while red color denotes links that across both clusters. In this Section I will show that each cluster can show isochronous synchronization in its own under certain conditions. In this sense, the notation of topological cluster and dynamic cluster merges at this point since the dynamic clusters will be identical to the topological clusters.

The graph in Fig. 9.3 is modeled by the coupling matrixes

$$\mathbf{Q}_1 = \begin{pmatrix} 0 & \mathbf{1}_{N/2} \\ \mathbf{1}_{N/2} & 0 \end{pmatrix} \quad (9.15)$$

and

$$\mathbf{Q}_2 = \begin{pmatrix} \mathbf{B} & 0 \\ 0 & \mathbf{B} \end{pmatrix}, \quad (9.16)$$

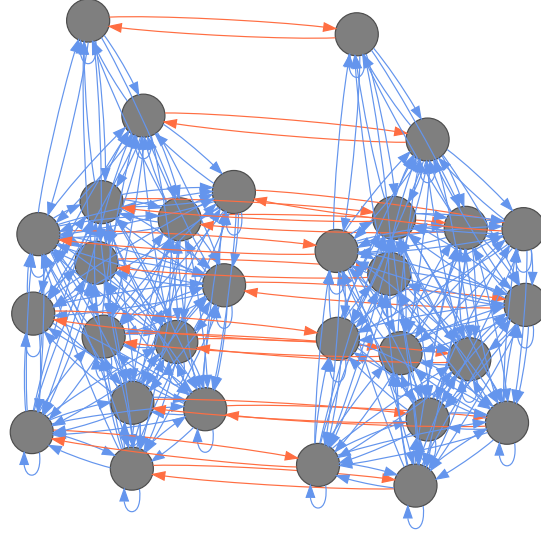


Figure 9.3.: Schematic view of a simple hierarchical network structure according to Eqs. (9.15) and (9.16) with 30 nodes. The two topological clusters are separated for illustration. Blue and red arrows correspond to links inside and between the clusters, respectively.

where $\mathbf{1}_{N/2}$ is the identity matrix and \mathbf{B} is an undirected $N/2 \times N/2$ Erdős-Rényi random graph with a certain link probability p . The undirectedness is necessary to obtain a real-valued eigenvalue spectrum. Then it is sufficient to calculate the master stability function in the $(\text{Re } \gamma^{(1)}, \text{Re } \gamma^{(2)})$ plane.

In order to operate in a “real” two-cluster state I choose the coupling strength for the two matrices \mathbf{Q}_1 and \mathbf{Q}_2 to be different. The coupling strengths $\sigma_1^{(1)}$ and $\sigma_1^{(2)}$ corresponding to the coupling matrix \mathbf{Q}_1 are chosen as $\sigma_1^{(1)} = \sigma_1^{(2)} = 0.05\sigma$, where $\sigma = 0.12$ is the overall coupling strength corresponding to the regime of low-frequency fluctuations (LFF, see Tab. 2.2). The coupling strengths corresponding to \mathbf{Q}_2 are chosen as $\sigma_2^{(1)} = \sigma_2^{(2)} = 0.95\sigma$. For a high link probability p in the random matrix \mathbf{B} , the matrix \mathbf{Q}_2 contains comparatively more links than \mathbf{Q}_1 , which has only one link per row. It is therefore a reasonable choice that \mathbf{Q}_1 has a significantly smaller row sum.

Figure 9.4 shows the master stability function for this choice of the coupling strengths.

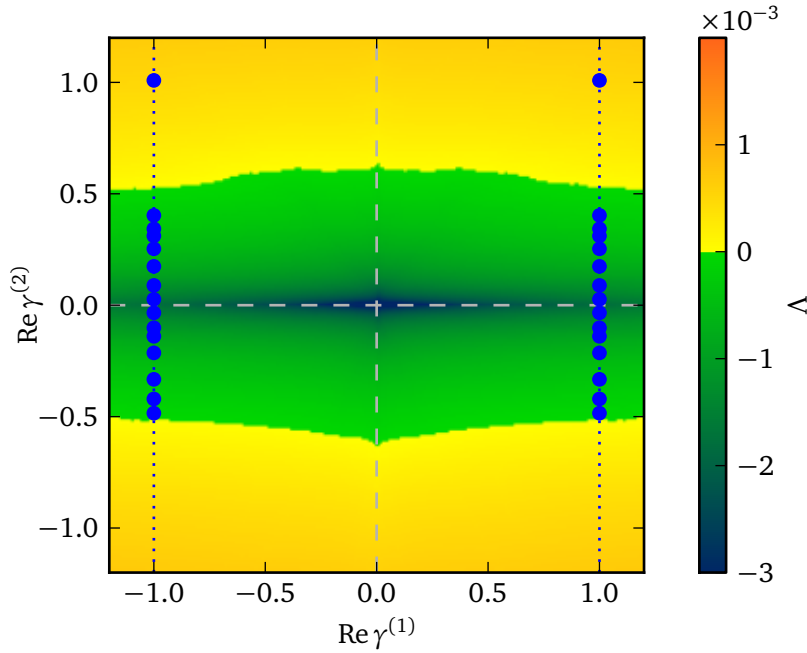


Figure 9.4.: Master stability function for two commuting matrices with the structures \mathbf{Q}_1 as in Eq. (9.4) and \mathbf{Q}_2 as in Eq. (9.5) with coupling strengths $\sigma_1 = 0.05\sigma$ and $\sigma_2 = 0.95\sigma$. The pairs $(\text{Re } \gamma^{(1)}, \text{Re } \gamma^{(2)})$ plotted as blue dots correspond to eigenvalues of the hierarchical example with matrices (9.15) and (9.16) using a link probability $p = 0.5$ in the Erdős-Rényi graph (9.16).

Plotted as blue dots are the eigenvalue pairs $(\gamma^{(1)}, \gamma^{(2)})$ of the hierarchical example given by Eqs. (9.15) and (9.16) using a link probability of $p = 0.5$ in the random matrix \mathbf{B} for $N = 30$. It can be seen that this network shows stable synchronization in this 2-cluster state. That is, each topological cluster shows synchronization inside itself. The eigenvalues will always be lined up on the dotted vertical lines, which are given by the \mathbf{Q}_1 being constructed from identity-matrix blocks.

The link probability $p = 0.5$ is just at the threshold to stable synchronization. Using lower values, some eigenvalues will cross the boundary of the stable region of the master stability function, leading to desynchronization.

Since the eigenvalues are always aligned along the lines $\text{Re } \gamma^{(1)} = \pm 1$ in this example, the stability for other choices of the coupling strength can easily be obtained by evaluating the master stability function at a fixed value of $\text{Re } \gamma^{(1)} = 1$. The other value $\text{Re } \gamma^{(1)} =$

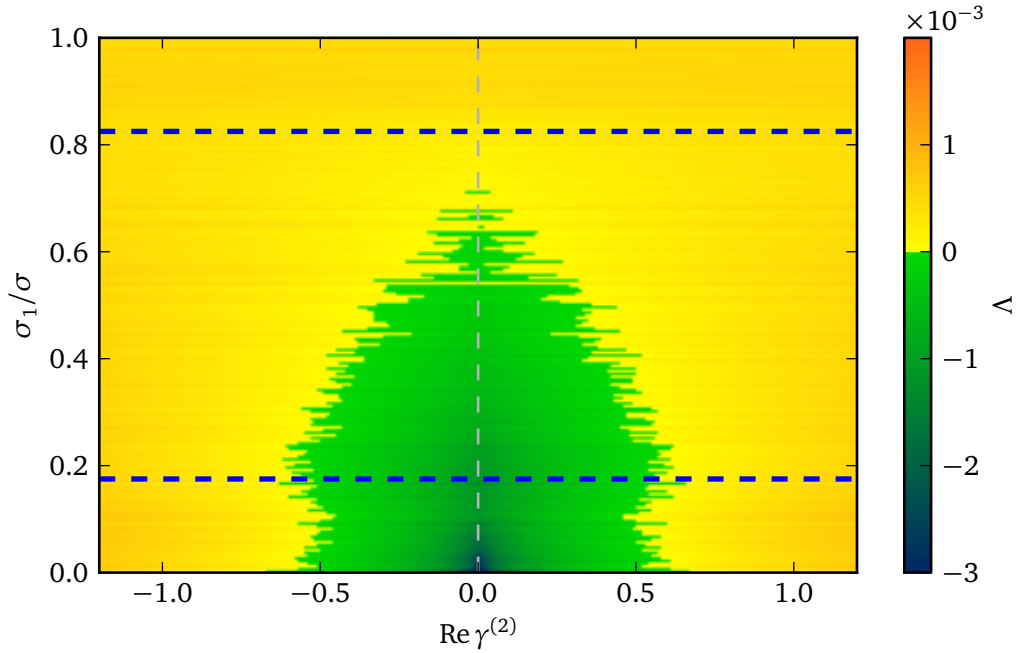


Figure 9.5.: Master stability function for two commuting matrices with the structures \mathbf{Q}_1 as in Eq. (9.4) and \mathbf{Q}_2 as in Eq. (9.5) in the $(\text{Re } \gamma^{(2)}, \sigma_1/\sigma)$ plane. The parameter $\text{Re } \gamma^{(2)}$ is fixed as unity and the coupling strength σ_2 arises as $\sigma - \sigma_1$. The dashed blue lines form the boundary of the parameter range where no 2-cluster exists. Parameters chosen in the LFF regime according to Tab. 2.2.

−1 yields identical results and must therefore not be considered, which is a results from the symmetry discussed in Sec. 8.5 and observable in Fig. 9.4.

Figure 9.5 shows the master stability function in the $(\text{Re } \gamma^{(2)}, \sigma_1/\sigma)$ plane, where $\sigma_1 := \sigma_1^{(1)} = \sigma_1^{(2)}$. The other coupling strength is set using the relation $\sigma_2 := \sigma_2^{(1)} = \sigma_2^{(2)} = \sigma - \sigma_1$, where the overall coupling strength is chosen as $\sigma = 0.12$ corresponding to the LFF regime in Tab. 2.2. This relation ensures that the overall coupling strength leads to an operation in this LFF regime. The dashed blue lines correspond to conditions (9.14), thus enclose the region where no 2-cluster state can exist. The stability of the 2-cluster state is therefore only meaningful below the lower and above the upper dashed blue line. The 2-cluster state is almost equally stable everywhere in the lower range of $\sigma_1/\sigma < 0.175$, which corresponds to a high coupling strength inside the clusters, but a low coupling strength between clusters. The upper range of $\sigma_1/\sigma > 0.825$, which corresponds to low coupling strength inside the clusters, but high coupling strength be-

tween them, also allows for the existence of the 2-cluster state, but this state cannot be stable for any topology here. In conclusion, the coupling strength has to be comparatively higher inside the clusters to exhibit both the 2-cluster state as solution and stability of this state at the same time.

9.4. More than two clusters

For two clusters, the only possible structure of \mathbf{Q}_1 and \mathbf{Q}_2 is given by Eqs. (9.4) and (9.5). The size of each cluster may of course differ in general, but a more interesting generalization is to go to three clusters. Then, assuming that one coupling matrix is given by

$$\mathbf{Q}_1 = \begin{pmatrix} 0 & 0 & \mathbf{A}^{(1)} \\ \mathbf{A}^{(2)} & 0 & 0 \\ 0 & \mathbf{A}^{(3)} & 0 \end{pmatrix}, \quad (9.17)$$

a possible second coupling matrix \mathbf{Q}_2 may exist in several forms.

Both matrices must commute; one necessary condition is that the cluster structures themselves do commute. In other words, let the *structure matrix* $\tilde{\mathbf{Q}}_1$ be the 3×3 matrix that is derived by substituting each non-zero block in \mathbf{Q}_1 by a scalar 1:

$$\tilde{\mathbf{Q}}_1 = \begin{pmatrix} 0 & 0 & 1 \\ 1 & 0 & 0 \\ 0 & 1 & 0 \end{pmatrix}. \quad (9.18)$$

In general, the structure matrix of an M -cluster state is an $M \times M$ matrix. Using this formalism, a possible additional coupling matrix \mathbf{Q}_2 can be found by first searching for structure matrices $\tilde{\mathbf{Q}}_2$ that commute with $\tilde{\mathbf{Q}}_1$.

Take, for example, the structure

$$\tilde{\mathbf{Q}}_2 = \begin{pmatrix} 0 & 1 & 0 \\ 0 & 0 & 1 \\ 1 & 0 & 0 \end{pmatrix}; \quad (9.19)$$

the commutator $[\tilde{\mathbf{Q}}_1, \tilde{\mathbf{Q}}_2]$ vanishes. But also

$$\tilde{\mathbf{Q}}_2 = \begin{pmatrix} 1 & 0 & 0 \\ 0 & 1 & 0 \\ 0 & 0 & 1 \end{pmatrix} \quad (9.20)$$

is a valid structure for a second coupling matrix, since it – being an identity matrix – commutes trivially with $\tilde{\mathbf{Q}}_1$.

Let us focus on the structure (9.19) together with the primary coupling matrix (9.17). The coupling matrix that emerges from (9.19) reads, in general,

$$\mathbf{Q}_2 = \begin{pmatrix} 0 & \mathbf{B}^{(1)} & 0 \\ 0 & 0 & \mathbf{B}^{(2)} \\ \mathbf{B}^{(3)} & 0 & 0 \end{pmatrix}, \quad (9.21)$$

and the commutator condition $[\mathbf{Q}_1, \mathbf{Q}_2] = 0$ is equivalent to

$$\begin{cases} \mathbf{A}^{(1)}\mathbf{B}^{(3)} = \mathbf{B}^{(1)}\mathbf{A}^{(2)} \\ \mathbf{A}^{(2)}\mathbf{B}^{(1)} = \mathbf{B}^{(2)}\mathbf{A}^{(3)} \\ \mathbf{A}^{(3)}\mathbf{B}^{(2)} = \mathbf{B}^{(3)}\mathbf{A}^{(1)}. \end{cases} \quad (9.22)$$

One problem that arises is that the structures used here do not allow for a real-valued eigenvalue spectrum of \mathbf{Q}_1 and \mathbf{Q}_2 . As I have shown in Chapter 8, the structure of \mathbf{Q}_1 itself leads to the existence of eigenvalues that are the – complex-valued – third roots of \mathbf{Q}_1^3 .

Having a complex eigenvalue spectrum of both matrices \mathbf{Q}_1 and \mathbf{Q}_2 , the pairs of eigenvalues would have to be checked against the master stability function in a 4-dimensional space:

$$\Lambda = \Lambda(\text{Re } \gamma^{(1)}, \text{Im } \gamma^{(1)}, \text{Re } \gamma^{(2)}, \text{Im } \gamma^{(2)}). \quad (9.23)$$

This 4-dimensional space is hard to visualize on 2-dimensional paper. One solution would be to study the different 2-dimensional projections that arise from this 4-dimensional space. In applications, however, the coupling matrices may show certain specialties or symmetries that would allow to consider these projections for fixed values of some of the parameters. Compare, for example, the hierarchical example of Sec. 9.3 which resulted in a unity eigenvalue for one of the matrices and thus a reduction to the investigation of the eigenvalues of the second matrix.

9.5. Conclusion

Being able to use multiple coupling matrices in the framework of cluster synchronization is a valuable generalization of the work shown in Chapter 8. Stability of cluster

states can be characterized in more general network topologies, include a very simple hierarchical example.

Applying the method, one has to carefully check that the state under investigation is indeed a cluster state by performing a stability analysis for the network motif describing the underlying synchronization manifold itself. Also, it is still unclear to which extent the condition on commuting matrices restricts a general application here.

10. Controlling cluster synchronization: an analytic approach

In this Chapter I will get back to the networks of Stuart-Landau oscillators [Choe et al., 2010, 2011]. In Chapter 7 I studied the stability of isochronous – or in-phase – synchronization in these networks. But already there I introduced the possible existence of cluster and splay states in networks of Stuart-Landau oscillators described by Eq. (7.3) from Chapter 7,

$$\dot{z}_j = f[z_j(t)] + \sigma \sum_{n=1}^N G_{jn} [z_n(t - \tau) - z_j(t)]. \quad (10.1)$$

The function $f(z)$ is given by the Stuart-Landau model (see Eq. (7.1)) as

$$f(z) = [\lambda + i\omega - (1 + i\gamma)|z|^2] z. \quad (10.2)$$

Again, the coupling is described by a coupling matrix $\{G_{ij}\}_{i=1,\dots,N}$, a complex coupling strength $\sigma = Ke^{i\beta}$ and a delay time τ .

Already shown in Chapter 7, the dynamics in cluster and splay states can be expressed using phase differences to each others. Considering the simplest example of an equal phase difference between neighboring clusters, the dynamical variables can be written as

$$\begin{aligned} r_j(t) &= r_0, \\ \varphi_j(t) &= \Omega t + j\Delta\phi_m, \quad j = 1, \dots, N, \end{aligned} \quad (10.3)$$

with

$$\Delta\phi_m = 2\pi m/N. \quad (10.4)$$

This of course assumes common amplitudes r_0 and frequencies Ω for all nodes. The integer $m = 0, \dots, N - 1$ determines the specific state: The cluster number d_c , which

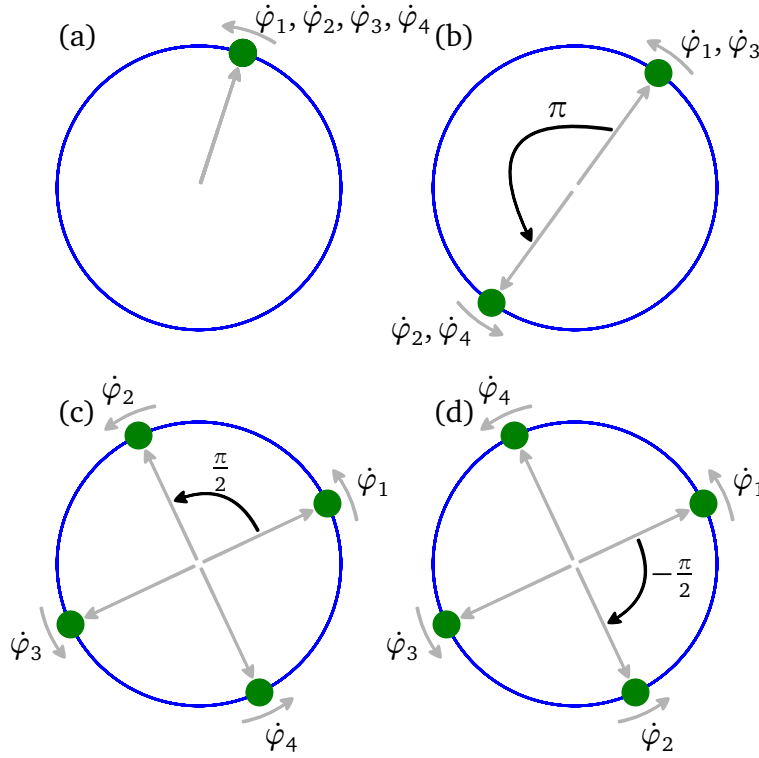


Figure 10.1.: Schematic view of (a) in-phase, (b) two-cluster, and (c)-(d) splay states in a network with 4 oscillators. The phase differences are $\Delta\phi_0 = 0$, $\Delta\phi_2 = \pi$, $\Delta\phi_1 = \pi/2$, and $\Delta\phi_3 = 3\pi/2$ in panels (a), (b), (c), and (d), respectively, according to Eqs. (7.8) and (7.9).

determines how many clusters of oscillators exist, is given by the least common multiple (lcm) of m and N divided by m :

$$d_c = \frac{\text{lcm}(m, N)}{m} \quad (10.5)$$

for $m = 1 \dots N - 1$. $d_c = N$ corresponds to a splay state [Zillmer et al., 2007]. $m = 0$ resembles in-phase synchronization ($d_c = 1$), although Eq. (10.5) cannot be used in this case.

Figure 10.1 shows again the possible scenarios for the simple example of 4 nodes coupled in a unidirectional ring (see also Fig. 7.2). After I have fully described the stability

of the in-phase synchronization (a) in Chapter 7, I will show how this can be extended to the cluster (b) and splay states (c,d) in certain special topologies.

In Sec. 10.1 I will show a general notation for cluster and splay states in networks of Stuart-Landau oscillators with which variational equations can be derived. A stability analysis using a master stability function works only if these variational equations uncouple by a diagonalization. For a unidirectional ring topology I will show this in Sec. 10.1.2. In this topology, several cluster states may coexist depending on the parameters and the number of nodes. Similar to the case of in-phase synchronization I will derive conditions for the coupling phase under which the stability of a desired cluster state is extended to the whole plane of the parameters K and τ while the other cluster states are suppressed. This allows for easy selection of a desired state of synchronization. The analytic part of this Chapter will close with Sec. 10.3 including remarks on possible generalizations beyond the unidirectional ring.

In Sec. 10.4 I will introduce an order parameter that is based on the common Kuramoto order parameter [Kuramoto, 1984]. This makes the numerical characterization of the dynamics more accessible, but more importantly it opens up the control of synchronization by an adaptive scheme which can be used to select cluster states without prior knowledge of the system's parameters [Selivanov et al., 2011].

10.1. Cluster and splay states

10.1.1. Synchronous states

Using the notation of amplitudes r_j and phases φ_j of the complex variables z_j in analogy to Eq. (7.5) from Chapter 7, common amplitude and frequency Ω can be obtained for a cluster state obeying $r_j(t) = r_0$ and $\varphi_j(t) = \Omega t + \Delta\theta_j$. The latter assumes that every oscillator has the same frequency Ω but each has a different phase offset $\Delta\theta_j$. Inserting these assumptions into Eq. (7.5) yields

$$\begin{aligned} r_0^2 &= \lambda - K \cos \beta + K \sum_{n=1}^N G_{jn} \cos \Phi_n^j, \\ \Omega &= \omega - \gamma r_0^2 - K \sin \beta + K \sum_{n=1}^N G_{jn} \sin \Phi_n^j, \end{aligned} \quad (10.6)$$

where $\Phi_n^j = \beta - \Omega\tau + \Delta\theta_n - \Delta\theta_j$.

Note that in the special case of zero-lag – or in-phase – synchronization, i.e., $\Delta\theta_j = 0$, the expressions $\sum_n G_{jn} \cos \Phi_n^j = \cos(\varphi - \Omega\tau)$ and $\sum_n G_{jn} \sin \Phi_n^j = \sin(\varphi - \Omega\tau)$ hold so that Eq. (10.6) is reduced to Eq. (7.11).

Using these results for the common frequency Ω and the common amplitude r_0 of all oscillators, variational equations can be formed using the same ansatz $r_j(t) = r_0[1 + \delta r_j(t)]$ and $\varphi_j(t) = \Omega t + \delta\varphi_j(t)$ as before. Using Eq. (7.5), the linear order of δr_j and $\delta\varphi_j$ follows

$$\begin{pmatrix} \delta \dot{r}_j \\ \delta \dot{\varphi}_j \end{pmatrix} = \begin{pmatrix} -2r_0^2 & 0 \\ -2\gamma r_0^2 & 0 \end{pmatrix} \begin{pmatrix} \delta r_j \\ \delta \varphi_j \end{pmatrix} - K \begin{pmatrix} \sum_n G_{jn} \cos \Phi_n^j & -\sum_n G_{jn} \sin \Phi_n^j \\ \sum_n G_{jn} \sin \Phi_n^j & \sum_n G_{jn} \cos \Phi_n^j \end{pmatrix} \begin{pmatrix} \delta r_j \\ \delta \varphi_j \end{pmatrix} + K \sum_n G_{jn} \begin{pmatrix} \cos \Phi_n^j & -\sin \Phi_n^j \\ \sin \Phi_n^j & \cos \Phi_n^j \end{pmatrix} \begin{pmatrix} \delta r_n(t-\tau) \\ \delta \varphi_n(t-\tau) \end{pmatrix}, \quad (10.7)$$

where $\Phi_n^j = \beta - \Omega\tau + \Delta\theta_n - \Delta\theta_j$. This can be described equivalently in the form of a vector equation as

$$\dot{\xi}_j = \mathbf{J}_0 \xi_j - K \Psi \xi_j + K \sum_n G_{jn} \mathbf{R}_{nj} \xi_n(t-\tau), \quad (10.8)$$

where $\xi_j = (\delta r_j, \delta \varphi_j)$. The matrix

$$\mathbf{J}_0 = \begin{pmatrix} 2r_0^2 & 0 \\ 2\gamma r_0^2 & 0 \end{pmatrix} \quad (10.9)$$

describes the Jacobian of the local dynamics, the matrix

$$\Psi = \begin{pmatrix} \sum_n G_{jn} \cos \Phi_n^j & -\sum_n G_{jn} \sin \Phi_n^j \\ \sum_n G_{jn} \sin \Phi_n^j & \sum_n G_{jn} \cos \Phi_n^j \end{pmatrix} \quad (10.10)$$

includes contributions from the coupling matrix and from the phase differences between the individual oscillators, and the matrix

$$\mathbf{R}_{nj} = \begin{pmatrix} \cos \Phi_n^j & -\sin \Phi_n^j \\ \sin \Phi_n^j & \cos \Phi_n^j \end{pmatrix} \quad (10.11)$$

includes only these differences and is thus independent from the topology.

In order to determine stability by a master stability function, Eq. (10.8) has to be transformed into a form in which the individual equation for the ξ_j decouple. In Chapter 7 this was done by first rewriting the form of Eq. (10.8) in matrix form using $\xi = (\xi_1, \dots, \xi_N)$ and the notation of the direct product (cf. Eq. (7.14)) and diagonalizing that equation.

In the general case of arbitrary coupling matrices \mathbf{G} and arbitrary phase differences $\theta_j - \theta_n$ between two nodes j and n , Equation (10.8) cannot be represented in such a form, because the matrix \mathbf{R}_{nj} depends on the index n . This implies that it is – in general delay-coupled networks – impossible to decouple the above variational equations in a master stability framework.

In some specific networks, however, the difficulty of applying the master stability function approach to the cluster and splay synchronization can be eliminated: The ring structure with uni- or bidirectional coupling and the star-coupling structure are the typical examples in which the Floquet exponents for cluster and splay synchronization can be treated analytically. Also, it is evident that the matrix \mathbf{R} in the case of zero-lag synchronization is independent of n , which yields the variational equation

$$\dot{\xi} = \mathbf{I}_N \otimes (\mathbf{J}_0 - K\mathbf{R}_0)\xi + K(\mathbf{G} \otimes \mathbf{R}_0)\xi(t - \tau), \quad (10.12)$$

which resembles Eq. (7.14) with

$$\mathbf{R}_0 = \begin{pmatrix} \cos \Delta & -\sin \Delta \\ \sin \Delta & \cos \Delta \end{pmatrix}$$

and $\Delta = \beta - \Omega\tau$. As shown in Chapter 7 this permits decomposition into a diagonal form.

In the following, I will consider the unidirectional ring structure as a special case where a diagonalization of the variational equations is also possible. In consequence, stability of cluster synchronization can be determined using a master stability function.

10.1.2. The unidirectionally coupled ring

A unidirectional ring is described by a coupling matrix

$$\mathbf{G} = \begin{pmatrix} 0 & 1 & 0 & \cdots \\ 0 & 0 & 1 & \cdots \\ \vdots & \vdots & \vdots & \ddots \\ 1 & 0 & 0 & \cdots \end{pmatrix}; \quad (10.13)$$

see also Chapter 4 where I discussed synchronization of laser network with this structure.

This network allows for N different splay and cluster states $\varphi_j(t) = \Omega t + \Delta\theta_j = \Omega t + j\Delta\phi_m$ with $\Delta\phi_m = 2m\pi/N$, $m = 1, \dots, N$. As discussed at the beginning of the Chapter, $m = 0$ corresponds to in-phase synchronization, $m = N$ is the splay state, and any value in between describes a d_c -cluster state with $d_c = \text{lcm}(m, N)/m$ clusters. This description yields

$$\Phi_n^j = \beta - \Omega\tau + (n - j)\Delta\phi_m. \quad (10.14)$$

Because the coupling matrix of the unidirectional ring has nonzero entries only at $G_{j, j+1 \bmod N}$, $j = 1, \dots, N$, only the j -independent $\Phi_{j+1}^j = \beta - \Omega\tau + \Delta\phi_m$ lead to contributions in the variational equation (10.8) and I abbreviate these as $\Phi_{j+1}^j = \Phi_1$. $j + 1$ has to be understood as $j + 1 \bmod N$ in what follows.

This brings up two important points that are due to using the unidirectional ring: First, only the matrix $\mathbf{R}_{j+1, j}$ (Eq. (10.11)) contributes to the variational equation. Since $\mathbf{R}_{j+1, j}$ includes the $\Phi_{j+1}^j \equiv \Phi_1$, I abbreviate $\mathbf{R}_{j+1, j}$ by \mathbf{R}_1 . Second, the matrix Ψ (see Eq. (10.10)) becomes identical to the matrix \mathbf{R}_1 .

As a consequence, Equation (10.8) can be represented in matrix form as follows:

$$\dot{\xi} = \mathbf{I}_N \otimes (\mathbf{J}_0 - K\mathbf{R}_1)\xi + K(\mathbf{G} \otimes \mathbf{R}_1)\xi(t - \tau), \quad (10.15)$$

where

$$\mathbf{R}_1 = \begin{pmatrix} \cos \Phi_1 & -\sin \Phi_1 \\ \sin \Phi_1 & \cos \Phi_1 \end{pmatrix}, \quad (10.16)$$

and $\Phi_1 = \beta - \Omega\tau + \Delta\phi_m$. Remember that the phase difference $\Delta\phi_m = 2m\pi/N$ is determined by the particular cluster state under investigation.

Diagonalizing Eq. (10.15) with respect to the coupling matrix \mathbf{G} yields a set of decoupled variational equations:

$$\dot{\zeta}_k(t) = (\mathbf{J}_0 - K\mathbf{R}_1)\zeta_k(t) + K\nu_k\mathbf{R}_1\zeta_k(t - \tau), \quad k = 1, \dots, N, \quad (10.17)$$

where $\nu_k = e^{2ik\pi/N}$, $k = 1, \dots, N$ are the eigenvalues of the coupling matrix \mathbf{G} of the unidirectional ring, which I already used in Sec. 4.5.1.

I already used the time-independence of the Jacobian \mathbf{J}_0 before. In this case, the Floquet exponents that arise from the variational equation above can be calculated as eigenvalues from characteristic equation

$$0 = \det [\mathbf{J}_0 - \Lambda \mathbf{I}_2 + KQ_k(\Lambda)\mathbf{R}_1], \quad (10.18)$$

in which I abbreviated the term that arises from the delay as $Q_k(\Lambda) = -1 + e^{-\Lambda\tau + 2ik\pi/N}$. Equation (10.18) is equivalent to

$$0 = \begin{vmatrix} -2r_0^2 + KQ_k(\Lambda)\cos\Phi_1 - \Lambda & -KQ_k(\Lambda)\sin\Phi_1 \\ -2\gamma r_0^2 + KQ_k(\Lambda)\sin\Phi_1 & KQ_k(\Lambda)\cos\Phi_1 - \Lambda \end{vmatrix}. \quad (10.19)$$

Note that for stable synchronization in the given cluster state in this unidirectional ring, Equation (10.19) has to yield a negative Λ for any transversal eigenvalue ν_k , $k = 1, \dots, N-1$, of the coupling matrix. The eigenvalue $\nu_{N-1} = 1$ corresponds to dynamics inside the synchronization manifold. This eigenvalue will always yield the Goldstone mode $\Lambda(\nu_{N-1} = 1) = 0$ for periodic dynamics. In conclusion, Equation (10.19) has to be evaluated for every $k = 1, \dots, N-1$. Additionally, the parameter Φ_1 includes the phase difference $\Delta\varphi_m$ determined by the particular cluster state. Thus, for every of the N different states $m = 1, \dots, N$, the result for the Floquet exponents determined by Eq. (10.19) will be different. As I will show there are even parameter regions, where multiple cluster or splay states are stable at the same time.

Figure 10.2 shows the stability regions for the four possible states of synchronization in a unidirectional ring of $N = 4$ nodes in dependence on the coupling parameters K and τ . The coupling phase is fixed at $\beta = 0$. The color in panels (a), (b), (c), and (d) indicates stability, i.e., negative real part of the Floquet exponent Λ for all $k = 1, \dots, N-1$, for the in-phase synchronization ($m = 0$), splay state ($m = 1$), 2-cluster state ($m = 2$), and another splay state ($m = 3$). White regions correspond to positive Floquet exponents indicating instability.

Figure 10.3(a) illustrates the multistability by showing the stability boundaries of these different dynamical scenarios in the (K, τ) -plane for unidirectional coupling of $N = 4$

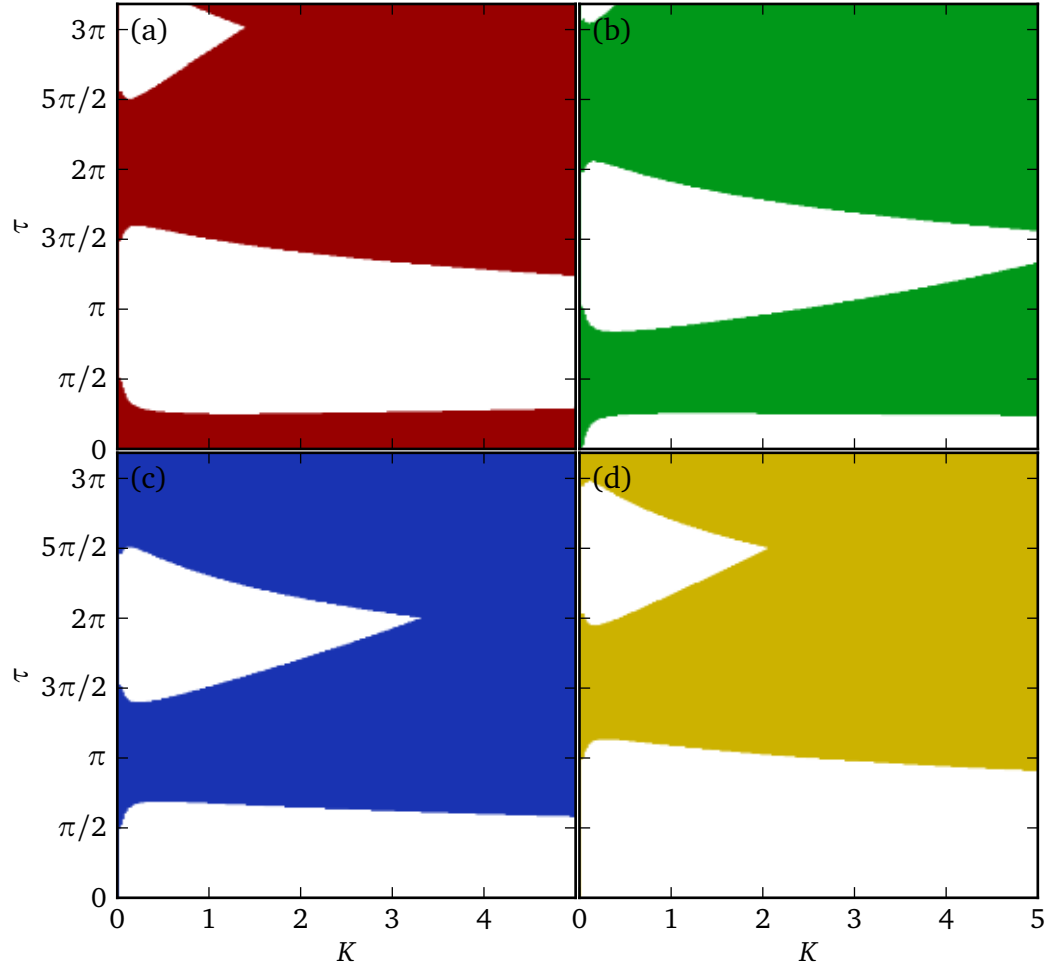


Figure 10.2.: Stability diagram of a unidirectional ring of $N = 4$ oscillators in the (K, τ) -plane ($\beta = 0$). Panels (a), (b), (c), and (d) show the domain of stability for in-phase ($m = 0$), splay state ($m = 1$), 2-cluster state ($m = 2$), and splay state ($m = 3$), respectively. White regions denote instability of the corresponding state.

oscillators altogether in one picture. Here, the color code indicates regions of different multistability of in-phase ($m = 0$), 2-cluster ($m = 2$), and splay states ($m = 1, m = 3$): Black (blue), dark gray (red), light gray (green), and yellow (white) color corresponds to regions where one, two, three, or four of these dynamical states are stable, respectively.

In the following Section I will show how the coupling phase β can be used to suppress this multistability and lead to the control and selection of a desired state of synchronization.

10.2. Controlling and selecting cluster and splay states

Already in the case of isochronous synchronization, an optimal choice for the coupling phase β existed which enables stable synchronization in the entire plane of the other coupling parameters K and τ .

Such an analytic condition can also be found in the case of cluster and splay states. If $\Phi_1 = 0$, i.e., $\beta = \Omega\tau - \Delta\phi_m + 2l\pi$, $l = 0, \pm 1, \pm 2, \dots$, Eq. (10.19) for the Floquet exponents factorizes and the exponents are given by

$$\Lambda = KQ_k(\Lambda) - 2r_0^2, \quad (10.20)$$

$$\Lambda = KQ_k(\Lambda). \quad (10.21)$$

Taking into account that I obtain $r_0^2 > 0$ at $\beta = \Omega\tau - \Delta\phi_m$, one can see that the dominant Floquet exponents are governed by the latter of the two, i.e.,

$$\Lambda = K(-1 + e^{-\Lambda\tau + 2ik\pi/N}). \quad (10.22)$$

Using a similar argument as in Sec. 7.3.2, it is obvious that the solutions of Eq. (10.22) have negative real part for any $K > 0$ and any τ . This means that the unidirectional ring configuration of Stuart-Landau oscillators exhibits stable in-phase synchronization, splay states or clustering according to the choice of the control parameter β as $\beta = \Omega_0\tau$, $\Omega_1\tau - 2\pi/N$ and $\Omega_m\tau - 2\pi m/N$ ($m > 1, N > 2$), respectively. This stability persists for any value of the coupling strength K and the time delay τ . Note that for every cluster state determined by the index m , a different value of the common frequency Ω_m is obtained.

To illustrate this further and demonstrate the robustness of the stability results for slightly nonidentical oscillators, I choose a set of control parameters $K = 3$ and $\tau = 3\pi$,

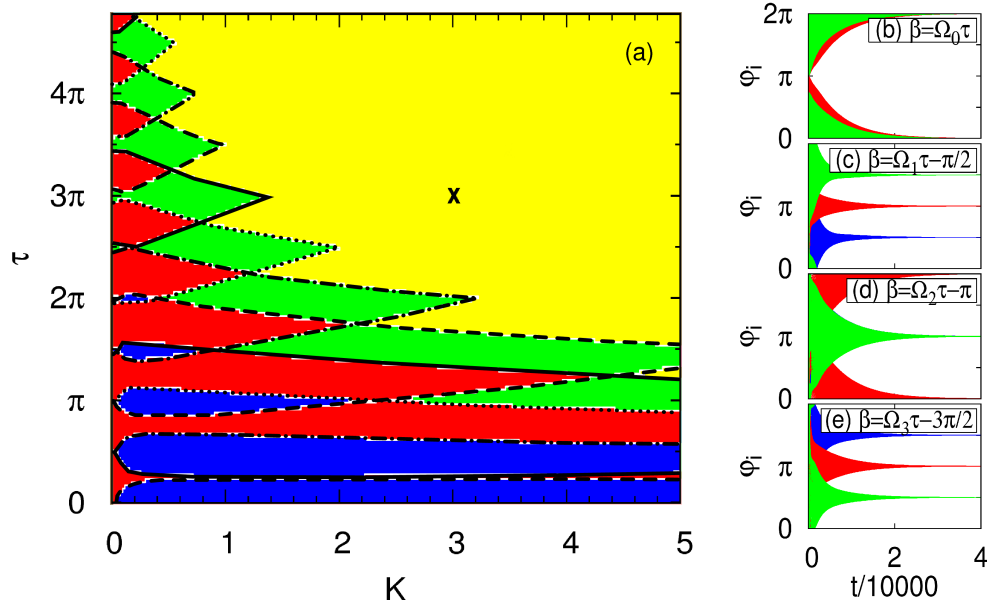


Figure 10.3.: (a) Stability diagram of a unidirectional ring of $N = 4$ oscillators in the (K, τ) -plane ($\beta = 0$). Solid, dash-dotted, dashed, and dotted boundaries correspond to a stability change of in-phase ($m = 0$), 2-cluster ($m = 2$), splay states with $m = 1$, and $m = 3$, respectively. The blue, red, green, and yellow regions denote multistability of one, two, three, and four of the above states. (b)-(e) Time series of the phase differences for a unidirectional ring of four slightly nonidentical oscillators: (b) $\beta = \Omega_0 \tau$, (c) $\Omega_1 \tau - \pi/2$, (d) $\Omega_2 \tau - \pi$, (e) $\Omega_3 \tau - 3\pi/2$, with $\Omega_0 = 1$, $\Omega_1 = 0.83903$, $\Omega_2 = 1$, and $\Omega_3 = 1.16097$. Black (blue), dark gray (red), and light gray (green) lines denote the differences $\phi_2 - \phi_1$, $\phi_3 - \phi_1$, and $\phi_4 - \phi_1$, respectively (in (b),(d) black (blue) is hidden behind light gray (green)). Parameters: $\lambda = 0.1$, $\gamma = 0$, $K = 3$, $\tau = 3\pi$, $\omega_1 = 0.99757$, $\omega_2 = 0.99098$, $\omega_3 = 1.01518$ and $\omega_4 = 0.99496$ [Choe et al., 2010].

denoted by the black cross in Fig. 10.3(a), for which multistability of all four possible synchronization states is found for the coupling phase $\beta = 0$. Figures 10.3(b)-(e) show time series from numerical simulations of four Stuart-Landau oscillators in a unidirectional ring configuration with slightly different frequencies ω . For each choice of β in panel (b) - (e) the solutions Ω_m were obtained by solving Eqs. (10.6) such that the solution of Ω_m closest to unity was chosen. The differences of the phases φ_i ($i = 2, 3, 4$) relative to the first oscillator phase φ_1 are plotted. After transients (note that the transient oscillations are not resolved on the time scale chosen), the oscillators behave exactly as predicted by the theory, i.e., they lock into in-phase synchronization for $\beta = \omega\tau$ (b), into a splay state for $\beta = \omega\tau - \pi/2$ (c), into a 2-cluster state for $\beta = \omega\tau - \pi$, where $\varphi_1 = \varphi_3$ and $\varphi_2 = \varphi_4$ (d), and again into a splay state, albeit with inverted ordering of the phases, for $\beta = \omega\tau - 3\pi/2$ (e).

Having demonstrated the value of our theory on the example of the unidirectional ring, the question regarding the possible network topologies that permit a treatment with this theory is still unanswered. In the following I make an attempt into this direction by discussing the possible topologies that allow for a common amplitude and frequency for all oscillators.

10.3. Topologies allowing for cluster states

In the following, I extend the control of in-phase, cluster, and splay states from unidirectional rings to more general network topologies. To this end I elaborate conditions on the coupling matrix $\mathbf{G} = \{G_{jn}\}$ for which in-phase, cluster, and splay states with a common amplitude $r_j \equiv r_{0,m}$ and phases $\varphi_j = \Omega_m t + j\Delta\phi_m = \Omega_m t + j2\pi m/N$ can be found. These conditions hold for general networks (with unity row sum $\sum_{n=1}^N G_{jn} = 1$) in the case of in-phase states. For cluster and splay states, networks satisfying these conditions include, for instance, configurations with a circulant coupling matrix [Golub and van Loan, 1996], where G_{jn} depends only on $(n - j) \bmod N$, e.g., uni- and bidirectional rings; see also Sec. 4.5.4.

Starting from the system's equations (10.1) and (10.2) I can split the complex equation (10.1) into two real equations (for amplitude r_j and phase φ_j) as follows

$$\dot{r}_j = \left(\lambda + r_j^2 \right) r_j + K \sum_{n=1}^N G_{jn} \left[r_n(t - \tau) \cos(\beta + \varphi_n(t - \tau) - \varphi_j) - r_j \cos \beta \right] \quad (10.23)$$

$$\dot{\varphi}_j = \omega - \gamma r_j^2 + K \sum_{n=1}^N G_{jn} \left[\frac{r_n(t - \tau)}{r_j} \sin(\beta + \varphi_n(t - \tau) - \varphi_j) - \sin \beta \right]. \quad (10.24)$$

Since I investigate in-phase, cluster, and splay states, I assume a common amplitude $r_j \equiv r_{0,m}$ and phases given by $\varphi_j(t) = \Omega_m t + j\Delta\phi_m = \Omega_m t + j2\pi m/N$. Using this notation I obtain for the amplitude equation with $\varphi_n(t - \tau) - \varphi_j = \varphi_1(t - \tau) - \varphi_1 + (n - j)\Delta\phi_m$:

$$r_{0,m}^2 = \lambda - K \cos \beta + K \sum_{n=1}^N G_{jn} \cos(\beta + \varphi_1(t - \tau) - \varphi_1 + (n - j)\Delta\phi_m). \quad (10.25)$$

This can be rewritten using the trigonometric identity $\cos(a + b) = \cos(a)\cos(b) - \sin(a)\sin(b)$ with $a = \beta + \varphi_1(t - \tau) - \varphi_1$ and $b = (n - j)\Delta\phi_m$ as follows

$$\begin{aligned} r_{0,m}^2 &= \lambda - K \cos \beta + K \cos(\beta + \varphi_1(t - \tau) - \varphi_1) \sum_{n=1}^N G_{jn} \cos((n - j)\Delta\phi_m) \\ &\quad - K \sin(\beta + \varphi_1(t - \tau) - \varphi_1) \sum_{n=1}^N G_{jn} \sin((n - j)\Delta\phi_m). \end{aligned} \quad (10.26)$$

The last equation is identical for all $j = 1, \dots, N$, keeping in mind $\Delta\phi_m = 2\pi m/N$, if the following conditions hold, independently of j :

$$\sum_{n=1}^N G_{jn} \cos\left((n - j)\frac{2\pi m}{N}\right) = \text{const.} \quad \text{and} \quad \sum_{n=1}^N G_{jn} \sin\left((n - j)\frac{2\pi m}{N}\right) = \text{const.} \quad (10.27)$$

I stress that the same conditions can be derived from the phase equation (10.24).

For in-phase states ($m = 0$), these conditions hold for any coupling matrix \mathbf{G} with unity row sum since the arguments of the cosine and sine function vanish due to $\Delta\phi_0 = 0$. In case of cluster states ($m \neq 0$), for example for circulant matrices \mathbf{G} , i.e., if $G_{jn} = g[(n - j) \bmod N]$ is a function of $(n - j) \bmod N$ only, the conditions are met due to the

periodicity of the cosine and sine functions and the cyclic properties of such matrices. This can be seen by inserting this matrix structure into the expressions in Eq. (10.27) for the j th row:

$$\sum_{n=1}^N g[(n-j) \bmod N] \cos \left[\frac{(n-j)2\pi m}{N} \right], \sum_{n=1}^N g[(n-j) \bmod N] \sin \left[\frac{(n-j)2\pi m}{N} \right]. \quad (10.28)$$

Evaluating the same conditions for the $(j+1)$ th row yields

$$\sum_{n=2}^{N+1} g[(n-j) \bmod N] \cos \left[\frac{(n-j)2\pi m}{N} \right], \sum_{n=2}^{N+1} g[(n-j) \bmod N] \sin \left[\frac{(n-j)2\pi m}{N} \right]. \quad (10.29)$$

Using the cyclic properties of the circulant matrix, it can easily be seen that this summation in Eq. (10.29) is equivalent to the one in Eq. (10.28). Hence, irrespectively of index j , both equations are equivalent. This shows that conditions (10.27) hold for circulant matrices.

An example for $N = 3$ which satisfies conditions (10.27) for any m is provided by the circulant matrix

$$\mathbf{G} = \begin{pmatrix} 2 & 1 & 3 \\ 3 & 2 & 1 \\ 1 & 3 & 2 \end{pmatrix}. \quad (10.30)$$

In summary, Eqs. (10.27) provides conditions on the topology of the network for which the amplitude and phase of all elements are determined by the same equations, i.e., independent of the index j , even for cluster states (non-in-phase, $m \neq 0$). I stress that our theory holds as well for any coupling matrix that can be transformed to a circulant matrix by renumbering of the nodes. Also note that for certain values of m this independence of j is also given in a wider class of coupling matrices than circulant matrices. Consider for example, $N = 4$ and $m = 2$. Then the matrix

$$\mathbf{G} = \begin{pmatrix} 1 & 1 & 0 & 0 \\ 0 & 1 & 1 & 0 \\ 1 & 0 & 0 & 1 \\ 0 & 0 & 1 & 1 \end{pmatrix} \quad (10.31)$$

satisfies conditions (10.27). For a large number of coupling schemes treated in the literature, condition (10.27) holds. For example, let us consider networks of all-to-all coupling, unidirectional ring, bidirectional ring and star-coupling. For these configurations, Eqs. (10.6) yield a common amplitude and frequency, irrespectively of index j , as follows:

All-to-all coupling: $G_{ij} = 1$ for $i \neq j$, $G_{ii} = 0$

$$\begin{aligned} r_{0,m}^2 &= \lambda - K \cos \beta + K \sum_{l=1}^{N-1} \cos [\beta - \Omega_m \tau + l \Delta \phi_m], \\ \Omega_m &= \omega - \gamma r_{0,m}^2 - K \sin \beta + K \sum_{l=1}^{N-1} \sin [\beta - \Omega_m \tau + l \Delta \phi_m] \end{aligned} \quad (10.32)$$

Unidirectional ring: $G_{ij} = \delta_{j,i+1 \bmod N}$

$$\begin{aligned} r_{0,m}^2 &= \lambda - K \cos \beta + K \cos [\beta - \Omega_m \tau + \Delta \phi_m], \\ \Omega_m &= \omega - \gamma r_{0,m}^2 - K \sin \beta + K \sin [\beta - \Omega_m \tau + \Delta \phi_m] \end{aligned} \quad (10.33)$$

Bidirectional ring: $G_{ij} = G_{ji} = \delta_{j,i+1 \bmod N}$

$$\begin{aligned} r_{0,m}^2 &= \lambda + K [-2 \cos \beta + \cos (\beta - \Omega_m \tau + \Delta \phi_m) + \cos (\beta - \Omega_m \tau - \Delta \phi_m)], \\ \Omega_m &= \omega - \gamma r_{0,m}^2 K [-2 \sin \beta + \sin (\beta - \Omega_m \tau + \Delta \phi_m) + \sin (\beta - \Omega_m \tau - \Delta \phi_m)] \end{aligned}$$

Star coupling: $G_{1i} = 1$, $G_{i1} = N - 1$ for $i = 2, \dots, N$, all other $G_{ij} = 0$

This network does not fall into the class of circulant matrices, but admits synchrony in the following generalized sense:

$$\varphi_1(t) = \Omega t, \quad \varphi_l(t) = \Omega t + m\pi, \quad (10.34)$$

where index $j = 1$ corresponds to the hub and $l = 2, \dots, N$ denote the elements connected to the hub. Odd m refer to the drumhead clustering, i.e., the hub and the outer elements are in anti-phase, and even m correspond to in-phase synchrony. Synchronous amplitude and frequency for the outer elements $l = 2, \dots, N$ in the drumhead mode (odd m) are given by

$$\begin{aligned} r_{0,m}^2 &= \lambda - K [\cos (\beta - \Omega_m \tau) + \cos \beta], \\ \Omega_m &= \omega - \gamma r_{0,m}^2 - K [\sin (\beta - \Omega_m \tau) + \sin \beta]. \end{aligned} \quad (10.35)$$

Note that in these example the index m denotes the solutions for a particular cluster state determined by the phase difference $\Delta\phi_m = 2\pi m/N$. In Eq. (10.6) I omitted this index for readability reasons.

For all these network topologies the dynamics in cluster and splay states is given by the above equations. Using these solutions, stability conditions have to be derived which yield the same form as Eqs. (10.15), (10.18) as in Section 10.1.2 in order that in-phase, cluster, and splay states can be controlled in a similar way by changing the coupling phase.

10.4. A generalized order parameter for cluster states

So far, stability of synchronization was only treated from the point of view of linear stability analysis: From the dynamical equations a synchronized solution can be found. The stability of this very solution can then be found by using the variational equations for small perturbations from the synchronization manifold and is expressed in terms of Floquet or Lyapunov exponents.

Several reasons introduce the need to go away from this pure stability analysis. Studying the robustness of synchronization against noise or parameter mismatch between nodes are the most prominent. Comparing theoretical results to experimental data also gets easier when having a quantity at hand that can be derived from both sources of data. I will introduce such a quantity in this Section.

This generalized order parameter is also a crucial ingredient for a recent work by [Selivanov et al. \[2011\]](#), where we aim at adaptive control of cluster synchronization without prior knowledge of the system or coupling parameters. In the *speed gradient method* used as adaptation scheme there, it is necessary to have a dynamically evolving quantity that is minimized in the desired dynamical state [[Fradkov, 2007](#)]. As it turns out, a function based on the generalized order parameter introduced is most appropriate to adaptively control the cluster and splay states in networks of Stuart-Landau oscillators.

10.4.1. The Kuramoto order parameter

A very simple measure to quantify the coherence in networks in order to verify existence of isochronous synchronization was proposed by [Kuramoto \[1984\]](#) for networks of

phase oscillators. Consider an ensemble of N oscillators with phases φ_k ($k = 1, \dots, N$). The order parameter

$$R = \frac{1}{N} \left| \sum_{k=1}^N e^{i\varphi_k} \right| \quad (10.36)$$

is bounded between zero and unity due to the nature of the complex exponential function. If the network is in a state of complete synchronization, i.e., $\varphi_k = \varphi_m \forall k, m = 1, \dots, N$, the order parameter becomes $R = 1$. If, on the other hand, the nodes are completely desynchronized with their phases distributed randomly in $[0, 2\pi)$, the order parameter approaches $R = 0$.

Although the Kuramoto order parameter was initially used to quantify order in ensembles of phase oscillators, it can be used unmodified for Stuart-Landau oscillators, if only the coherence of the phases is considered. Disregarding the amplitude is valid for the following reasons: I have shown that in Eqs. (10.6) that a synchronized solution shows identical amplitudes and phases for all oscillators. If, on the other hand, the network desynchronizes, this will happen in both amplitude and phase variables simultaneously. Note that, in principal, also phase synchronized solutions may exist, where only the phases are in synchrony, but not the amplitudes. The Kuramoto order parameter would also be unity for these states, but I only consider completely synchronized states. The order parameter can then be calculated from the complex oscillator variables using the relation $\exp(i\varphi_k) = z_k/|z_k|$, $k = 1, \dots, N$.

10.4.2. Identifying a two-cluster state

Let us now consider a two-cluster state. In the sense of this Chapter, this means that half of the nodes is in one cluster while the other half is in another cluster. Both clusters have a phase shift of π between them. Obviously, the contributions of both clusters compensate in Eq. (10.36), thus the order parameter is zero. I propose a generalization of Eq. (10.36):

$$R_2 = \frac{1}{N} \left| \sum_{k=1}^N e^{2i\varphi_k} \right|. \quad (10.37)$$

This order parameter will approach unity in a two-cluster state. It will, however, also be $R_2 = 1$ in an in-phase state. Therefore, in order to distinguish the two-cluster state from the in-phase state, the difference

$$r_2 = R_2 - R \quad (10.38)$$

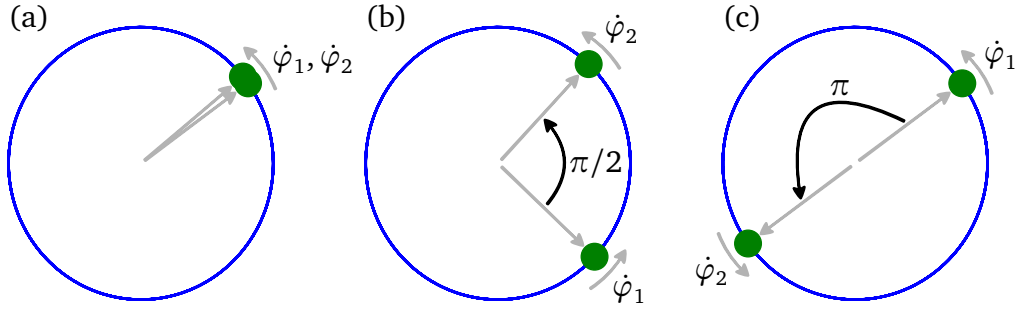


Figure 10.4.: Snapshot of the dynamics of two oscillators with different phase differences in between them. (a) $\varphi_2 - \varphi_1 = 0$, (b) $\varphi_2 - \varphi_1 = \pi/2$, and (c) $\varphi_2 - \varphi_1 = \pi$.

has to be considered. r_2 is zero for an in-phase state, but unity for the two-cluster state. Desynchronization also yields $r_2 < 1$. Note that r_2 may in principal – as opposed to R and R_2 – take on any values from the interval $[-1, 1]$.

Consider, for example, the case of just two nodes as depicted in Fig. 10.4. In this case, Equation (10.38) simplifies to

$$\begin{aligned} r_2 &= \frac{1}{2} |e^{2i\varphi_1} + e^{2i\varphi_2}| - \frac{1}{2} |e^{i\varphi_1} + e^{i\varphi_2}| \\ &= |\cos(\varphi_2 - \varphi_1)| - |\cos[(\varphi_2 - \varphi_1)/2]|. \end{aligned} \quad (10.39)$$

This result is plotted in Fig. 10.5 in red color in dependence of the phase difference of $\varphi_2 - \varphi_1$ between both oscillators. Also plotted are the individual terms R_2 (green) and R (blue). The dashed lines indicate phase differences of 0, $\pi/2$, and π , corresponding to Fig. 10.4(a), (b), and (c), respectively.

From Fig. 10.5, it can clearly be seen that the parameter R can well determine the in-phase state (a), while r_2 has its maximum only in the two-cluster state (c). Although the in-phase state (a) yields a local maximum in the order parameter r_2 , this local maximum is well distinguished from its global maximum at $\varphi_2 - \varphi_1 = \pi$.

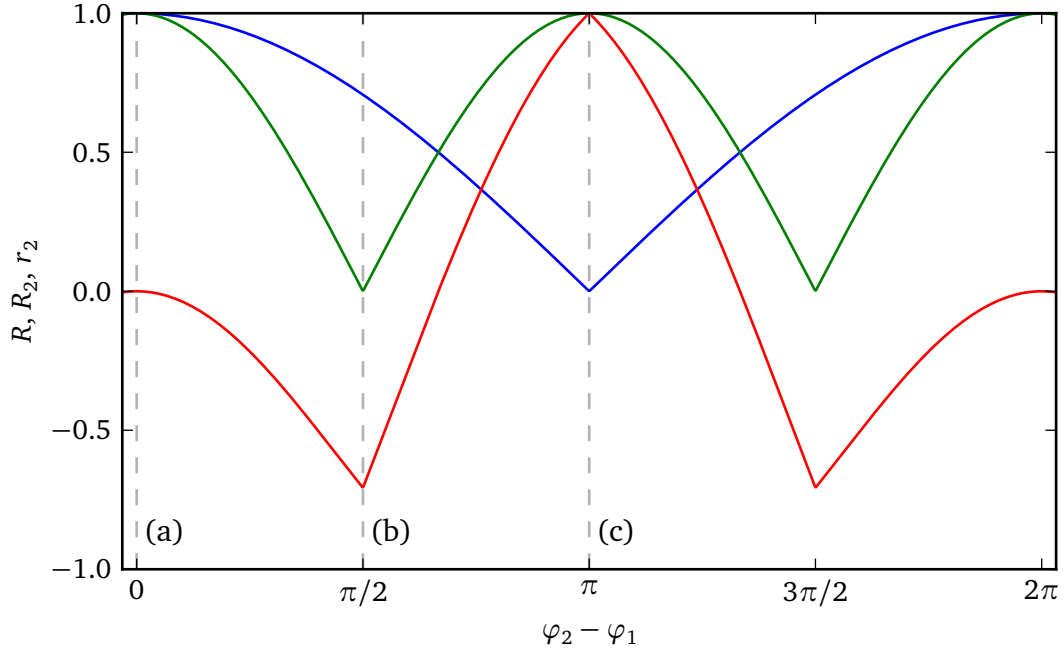


Figure 10.5.: Order parameters R (blue), R_2 (green), and r_2 (red) in dependence of the phase difference $\varphi_2 - \varphi_1$ for two oscillators. Dashed lines correspond to phase differences of 0, $\pi/2$, and π , corresponding to Fig. 10.4(a), (b), and (c), respectively.

10.4.3. Higher-order cluster states

These findings can be generalized to higher cluster states with c clusters and also to the play state ($c = N$). For these cases, I propose to use

$$R_c = \frac{1}{N} \left| \sum_{k=1}^N e^{ci\varphi_k} \right|. \quad (10.40)$$

Note that again, a given order parameter R_c becomes unity for the cluster with cluster number c , but also for certain cluster states with cluster number smaller than c . I simply subtract the order parameters for these lower order cluster states

$$r_c = R_c - \sum_{n|c} r_n, \quad (10.41)$$

where the notation $n|c$ means that n is a positive divisor of c , but $n \neq c$. This sum then includes all lower order cluster states, for which considering solely R_c would yield a

unity result.

10.4.4. Example: Ring of 4 oscillators

I will consider an example of four coupled oscillators here. This allows for a convenient comparison with the results from the linear stability analysis performed in Sections 10.1 and 10.2. Figures 10.6, 10.7, 10.8, and 10.9 show the order parameters R , r_2 , and r_4 in dependence on the coupling parameters K and τ for different initial conditions. Also the frequencies of the four oscillators were chosen slightly nonidentical as $\omega_1 = 0.99757$, $\omega_2 = 0.99098$, $\omega_3 = 1.01518$ and $\omega_4 = 0.99496$ for these numerical studies. These frequency correspond to the ones used in Figs. 10.3(b-e). As shown in Fig. 10.3(a), there is multistability among the four possible states of synchronization, thus one expects different synchronous dynamics for different initial conditions chosen for the simulations that I ran to compute the order parameters. In Fig. 10.6, the initial phase differences were chosen as $\varphi_{k+1 \bmod 4} - \varphi_k = 0$, $k = 1, \dots, 4$, while I set $\varphi_{k+1 \bmod 4} - \varphi_k = 2\pi/2$, $2\pi/4$, and $-2\pi/4$ in Figs. 10.7, 10.8, and 10.9, respectively. These choices correspond to the in-phase state, the cluster state, and the two different splay states possible in the unidirectional ring of four elements.

In these pictures the control phase is chosen as $\beta = 0$ similar to Fig. 10.3. This allows for easy comparison of both the results from calculating Floquet exponents and running direct simulations of the network as done here. For in-phase synchronization, the order parameter R has to be looked at, while for the cluster and splay states, r_2 and r_4 are the relevant parameters, respectively. As a consequence, if the numerical simulations match the analytic predictions perfectly, Figs. 10.6(a), 10.7(b), 10.8(c), and 10.9(c) should resemble panels (a), (c), (b), and (d) of Fig. 10.2.

This is not exactly the case, however. Even for initial conditions in the desired state, other states are more attractive for the dynamics for certain parameters. See, for example, the upper right of Fig. 10.6, where the simulation reaches a 2-cluster or a splay state despite the in-phase state being stable. This is caused by the nonidentical frequencies of the oscillators. Also for very small values of the coupling strength K , synchronization is not perfect in all cases as measured by the order parameters. For these small coupling strengths, the coupling cannot compensate for the differences in frequencies between the four oscillators. In all of the examples, however, states that are not stable according to the predictions from the master stability function are never reached in the simulations. This proves once more the validity of the master stability function.

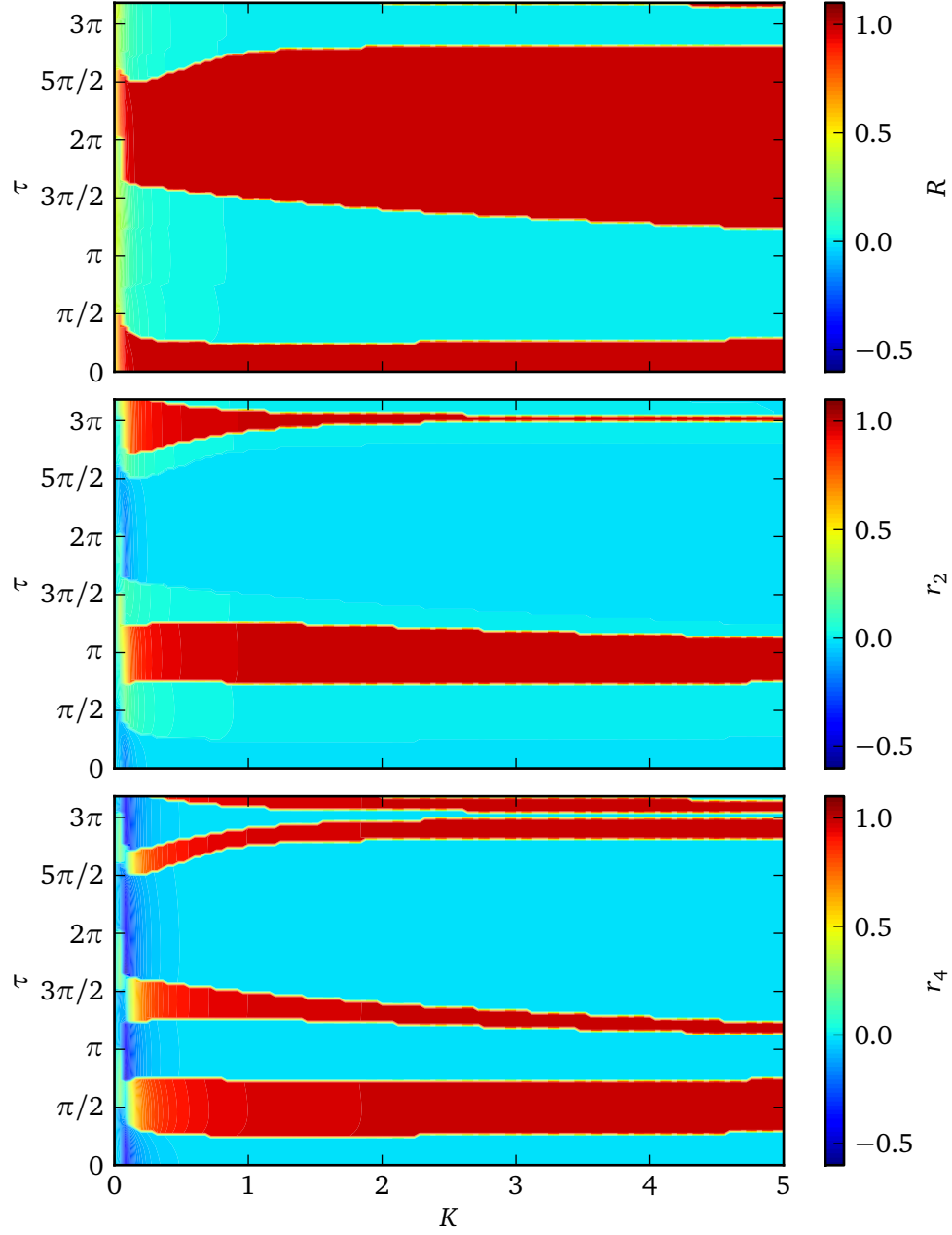


Figure 10.6.: Order parameters R , r_2 , and r_4 for the unidirectionally coupled ring of 4 Stuart-Landau oscillators. Initial conditions are chosen as $r_k = \sqrt{\lambda}$, $\varphi_{k+1 \bmod 4} - \varphi_k = 0$, $k = 1, \dots, 4$, i.e. in an in-phase state.

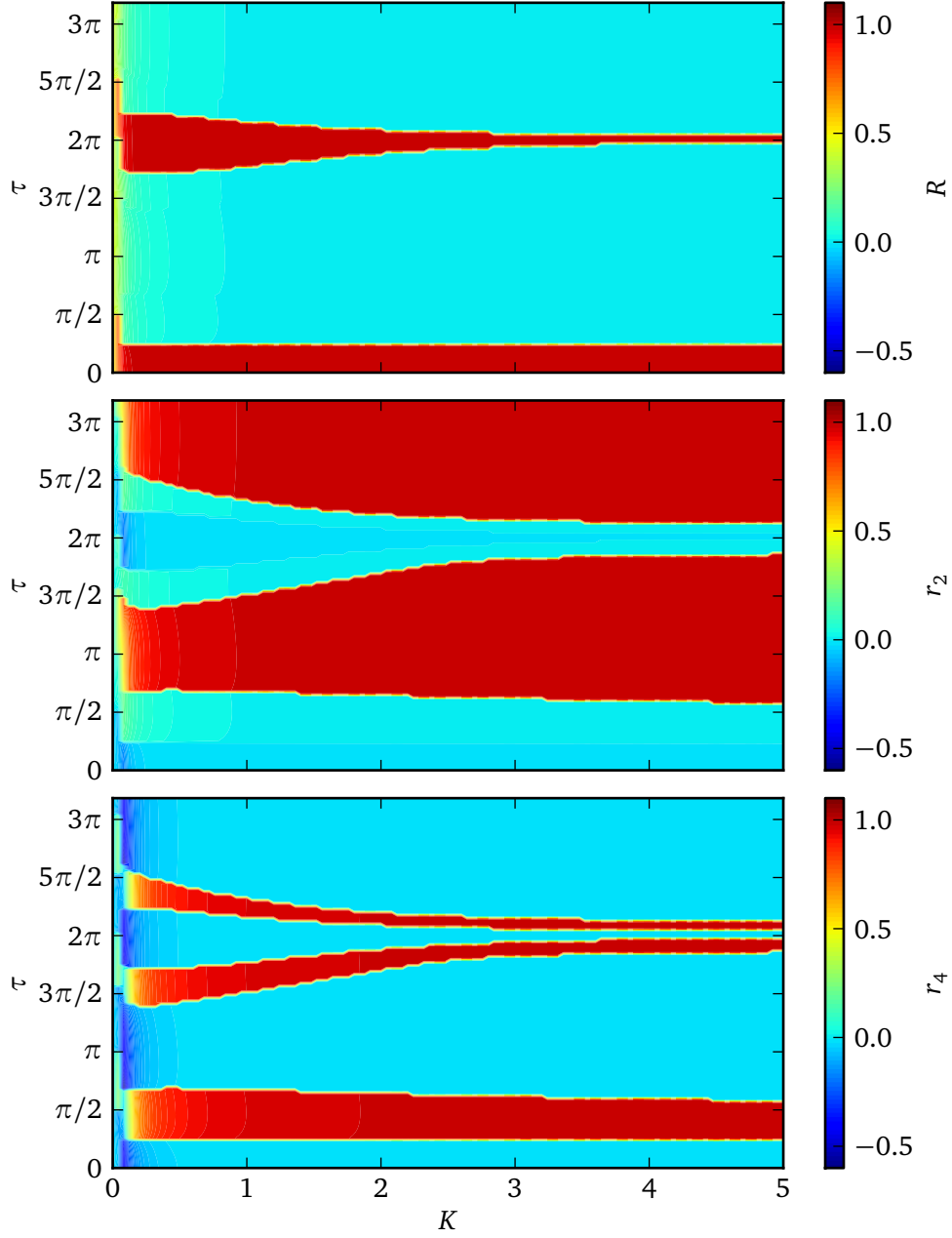


Figure 10.7.: Order parameters R , r_2 , and r_4 for the unidirectionally coupled ring of 4 Stuart-Landau oscillators. Initial conditions are chosen as $r_k = \sqrt{\lambda}$, $\varphi_{k+1 \bmod 4} - \varphi_k = 2\pi/2$, $k = 1, \dots, 4$, i.e., in the 2-cluster state.

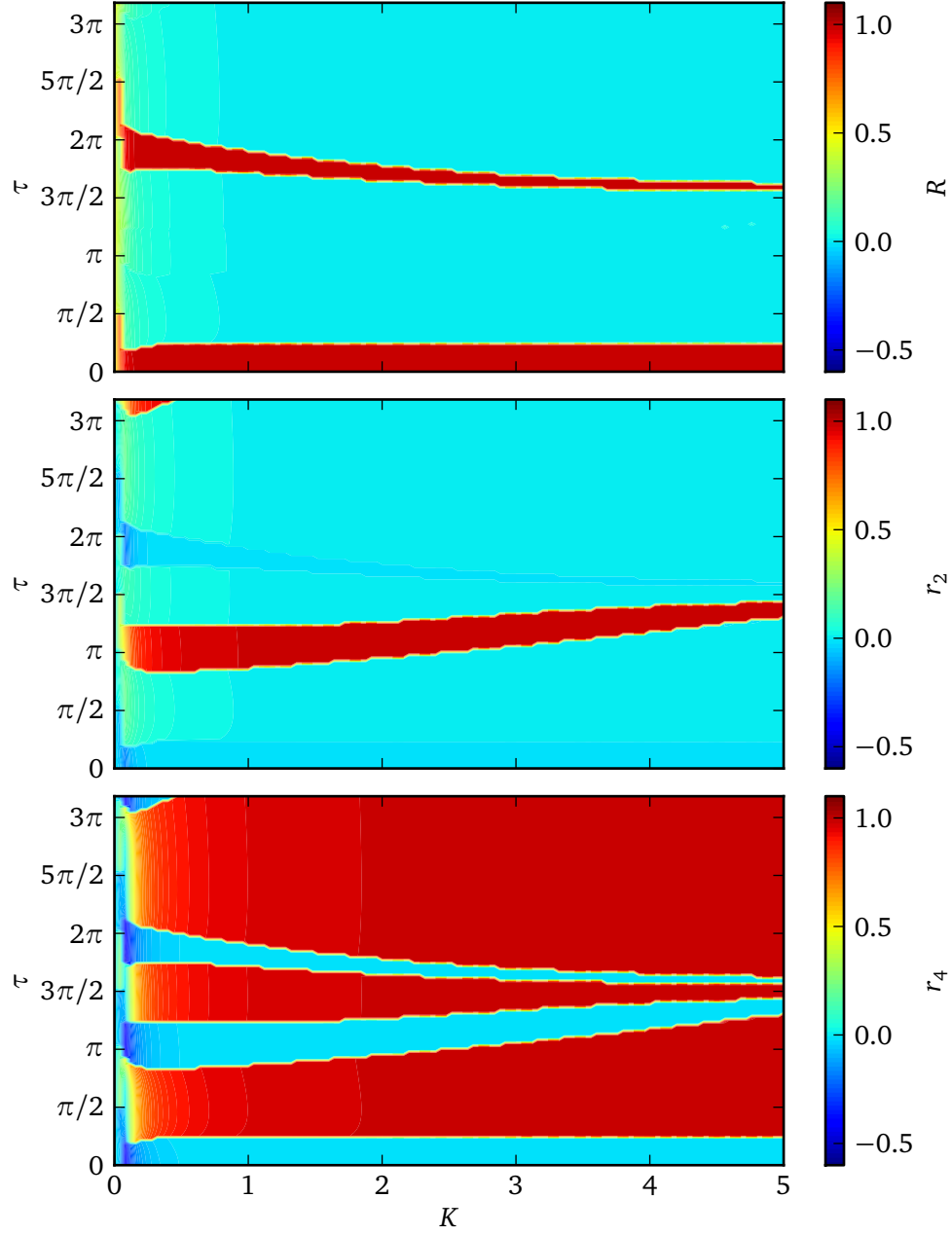


Figure 10.8.: Order parameters R , r_2 , and r_4 for the unidirectionally coupled ring of 4 Stuart-Landau oscillators. Initial conditions are chosen as $r_k = \sqrt{\lambda}$, $\varphi_{k+1 \bmod 4} - \varphi_k = 2\pi/4$, $k = 1, \dots, 4$, i.e., in a splay state.

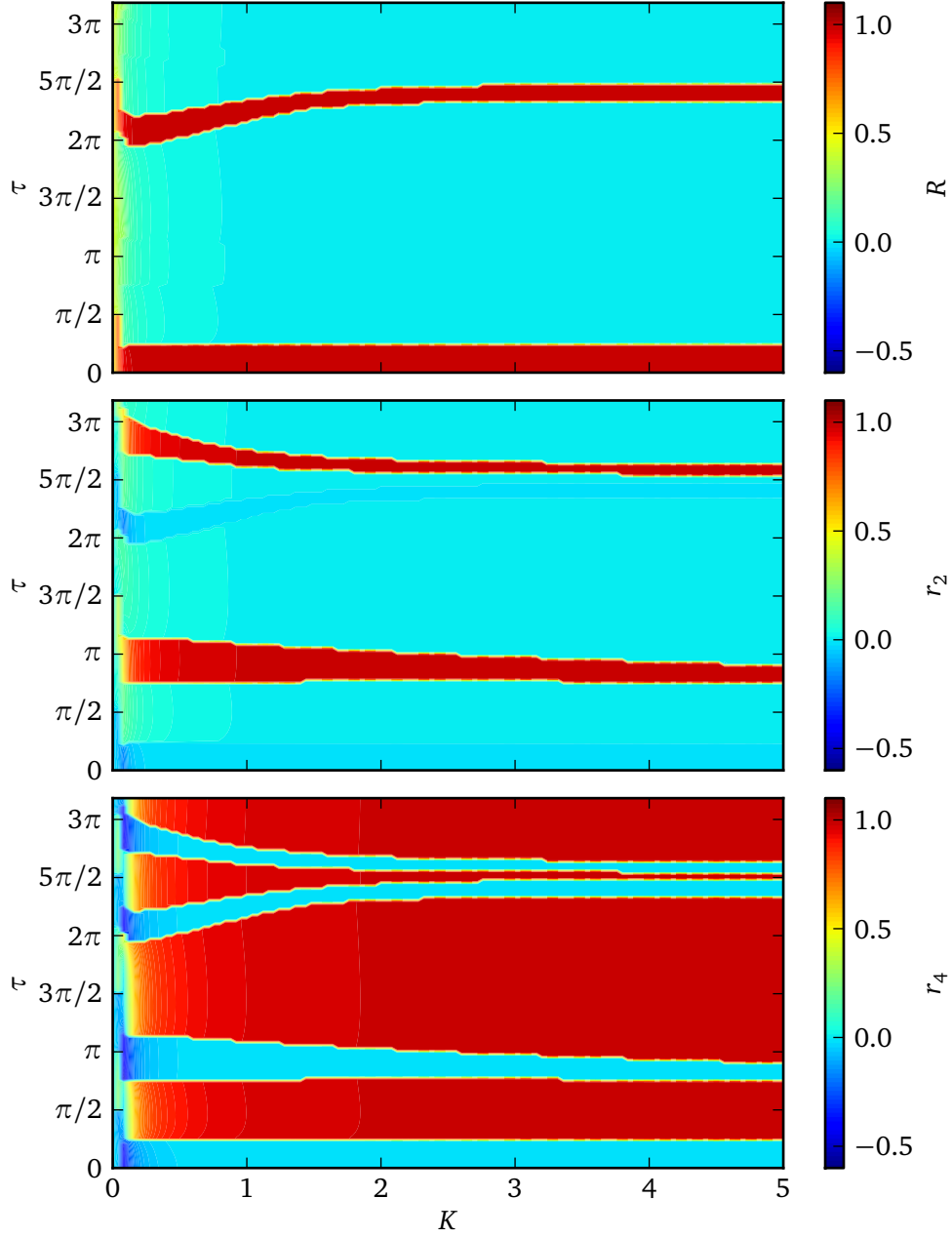


Figure 10.9.: Order parameters R , r_2 , and r_4 for the unidirectionally coupled ring of 4 Stuart-Landau oscillators. Initial conditions are chosen as $r_k = \sqrt{\lambda}$, $\varphi_{k+1 \bmod 4} - \varphi_k = -2\pi/4$, $k = 1, \dots, 4$, i.e., in a splay state.

In Fig. 10.8 and 10.9, the order parameter r_4 may give the impression that the respective splay state is reached for parameters outside the stable region (see Fig. 10.2). The order parameter r_4 cannot distinguish between the two splay states with $m = 1$ and $m = 3$. For example, in Fig. 10.8, which has initial conditions corresponding to the splay state with $m = 1$, the system may evolve into the splay state with $m = 3$ where the $m = 1$ state is unstable. In the Figure which shows the order parameter r_4 , these two states cannot be distinguished.

In the above examples I chose $\beta = 0$. In Sec. 10.2 I have shown that an appropriate choice of β leads to stability of a single state in the whole (K, τ) plane. Considering in-phase synchronization as an example, I ran simulations in the unidirectional ring using $\beta = \Omega\tau$, which corresponds to the predicted optimal value to stabilize in-phase synchronization. The numerical results shown in Fig. 10.10 confirm this. The order parameter R is almost unity throughout the (K, τ) plane, while the other two parameters are always nearly zero. Only for small values of the coupling strength the order parameter R is significantly smaller than unity, which is due to the nonidentical frequencies used in the simulations. I conclude that the in-phase state is stable regardless of the choice of K and τ for sufficiently large K . Using identical frequencies, stability would already be obtained for infinitesimally small coupling strength K .

10.5. Outlook: Nonidentical oscillators

The master stability function allows to characterize the stability of the different states only for identical frequencies of the oscillators. Although I have shown that slightly nonidentical frequencies still lead to a near perfect agreement with the master stability predictions, it is unclear to which extent the parameters of the nodes may differ.

Recently, a theory by Ott and Antonsen [2008] has had much impact on the network and synchronization community. In that work, Ott and Antonsen studied networks of globally coupled phase oscillators of the form

$$\frac{d\theta_i(t)}{dt} = \omega_i + \frac{K}{N} \sum_{j=1}^N \sin [\theta_j(t) - \theta_i(t)], \quad (10.42)$$

where the frequencies ω_i of the oscillators are chosen from a distribution $g(\omega)$, K is the coupling strength, and N is the number of nodes. In the limit of $N \rightarrow \infty$, the state of the network at any time t can be described by a continuous function

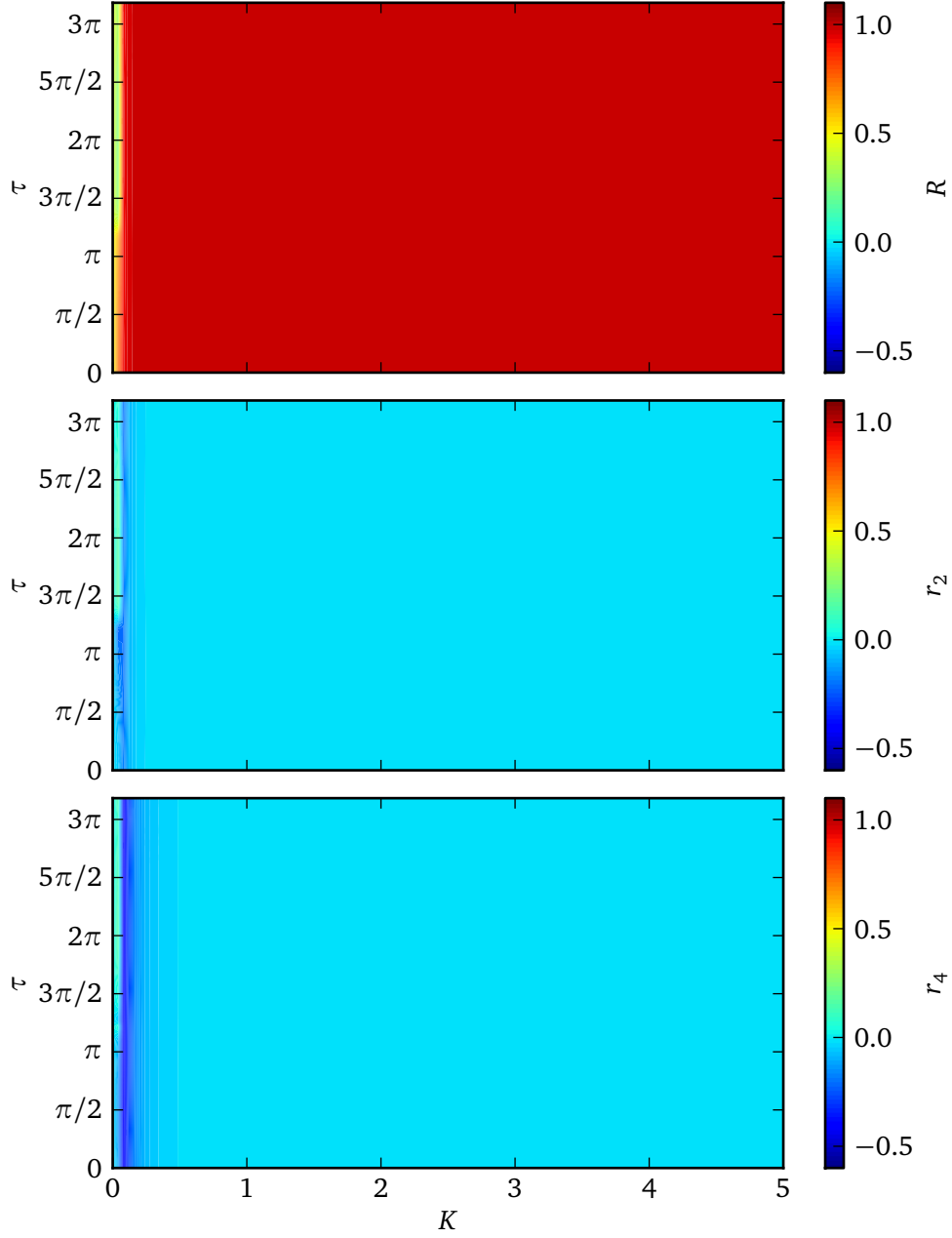


Figure 10.10.: Order parameters R , r_2 , and r_4 for a unidirectionally coupled ring of 4 Stuart-Landau oscillators with a coupling phase $\beta = \Omega\tau$. Initial conditions are chosen as $r_k = \sqrt{\lambda}$, $\varphi_{k+1 \bmod 4} - \varphi_k = 0$, $k = 1, \dots, 4$, i.e., in an in-phase state.

$f(\omega, \theta, t)$ as a distribution over the frequencies and the phases of the individual oscillators.

[Ott and Antonsen](#) have shown that rewriting the original equations yields

$$\begin{aligned} 0 &= \frac{\partial f}{\partial t} + \frac{\partial}{\partial \theta} \left\{ \left[\omega + \frac{K}{2i}(re^{-i\theta} - r^*e^{i\theta}) \right] f(\omega, \theta, t) \right\}, \\ r &= \int_0^{2\pi} d\theta \int_{-\infty}^{\infty} d\omega f(\omega, \theta, t) e^{i\theta}, \end{aligned} \quad (10.43)$$

where r is equivalent to the Kuramoto order parameter [[Kuramoto, 1984](#)]. Under certain assumptions regarding the evolution of the dynamics – which turned out to be valid [[Ott and Antonsen, 2009](#)] – they showed that the long term evolution can be reduced to the evolution of the order parameter when assuming a Lorentzian shape of the frequency distribution $g(\omega)$. The order parameter $r = \rho e^{i\phi}$ then evolves as

$$\begin{aligned} \frac{d\rho}{dt} &= -\left(1 - \frac{K}{2}\right)\rho + \frac{K}{2}\rho^3, \\ \frac{d\phi}{dt} &= 0. \end{aligned} \quad (10.44)$$

The solutions of these equation proved a heuristic prediction for the dependence of the order parameter on the coupling strength K by [Kuramoto \[1984\]](#). It has later been shown that the strength of the theory is not restricted to Lorentzian distributions of the frequencies [[Ott and Antonsen, 2009](#)].

When omitting the amplitude from the Stuart-Landau oscillator, it becomes very similar to the Kuramoto phase oscillator (Eq. (10.42)), which can already be seen by comparing Eq. (10.42) to the phase equation of the coupled Stuart-Landau oscillators, Equation (7.5). In particular, the coupling phase β is included in a very simple manner. There have been applications of the Ott-Antonsen theory to systems with delay [[Lee et al., 2009](#)] and the effect of the coupling phase in these setups would be an interesting subject of further investigations based on the results obtained and presented in this thesis.

10.6. Conclusion

In conclusion, I have shown that by tuning the complex coupling strength in delay-coupled networks of Stuart-Landau oscillators one can easily control the stability of different synchronous periodic states. I have specified analytic conditions for the coupling phase, under which stability of a desired state is established. Using the example of unidirectional rings, I have shown that either in-phase, cluster or splay states can be selected. The coupling phase is a parameter which is readily accessible, e.g., in optical experiments [[Schöll and Schuster, 2008](#); [Flunkert and Schöll, 2011a](#)], which makes these results interesting for applications.

I have given an outlook on the possible topologies beyond the unidirectional ring by deriving conditions on the coupling matrices. Finally, our results are robust even for slightly nonidentical elements of the network. As another outlook, the theory by [Ott and Antonsen \[2008\]](#) may provide a valuable tool to characterize synchronization for nonidentical oscillators. Furthermore, I introduced an order parameter to characterize the existence of cluster and splay states, which has proven to be especially useful in adaptive control of synchronization [[Selivanov et al., 2011](#)].

11. Conclusion

11.1. Summary

In this thesis I studied patterns of synchronization in laser networks. The dynamics of the networks' nodes was modeled by the Lang-Kobayashi model. Additionally, I investigated the Stuart-Landau oscillator as a model for periodic node dynamics.

In part I I focused on isochronous – or zero-lag – synchronization and employed the master stability function formalism to determine synchronization. The coupling-induced dynamics leads to a master stability function which is no longer independent of the coupling parameters as in the original work by [Pecora and Carroll \[1998\]](#).

In laser networks, depending on the dynamical regime the lasers operate in, the shape and size of the stable region of master stability region differs substantially. I have demonstrated a rotational symmetry in the case of large delay times, which reduces the analysis for a given network topologies to determining the extent of the eigenvalue distribution. Note that this is closely connected to the terminology of the eigenvalue gap [[Englert et al., 2011](#)]. That is, knowledge of the gap between the longitudinal and the transversal eigenvalue with largest absolute value suffices for the characterization of stability of synchronization. Using multiple coupling matrices, I have shown how topologies that include heterogeneous delay times can be treated with the master stability analysis.

Concerning the application of the results of the master stability function to particular network topologies, I have shown results for small network motifs, regular networks, but also complex random networks modeled by the Erdős-Rényi model. For motifs, I have shown that most configurations can only show stable synchronization with additional self-feedback loops. The results obtained for networks could be used to understand the stability of synchronization in more complex network by considering the subgraphs that exist in these complex topologies. I have shown this using the example of the Erdős-Rényi random model.

I have complemented the numerical results obtained for the chaotic laser networks with studies on networks of Stuart-Landau oscillators. The periodic dynamics in this network allow for the characterization of stability using analytic equations for the Floquet exponents. Most notably, I have shown the derivation of analytic conditions for the coupling phase, for which synchronization can be stabilized or destabilized deliberately.

In Part II of the thesis I generalized the concepts and methods from Part I to cluster and group synchronization. I have discussed a master stability function which is able to characterize stability of cluster states. This formalism is only valid for a restricted class of networks, namely multipartite networks. This structure also allows to obtain symmetries in the eigenvalue spectrum and in the master stability function itself. The restriction to multipartite networks can, however, be overcome by using multiple coupling matrices. I have demonstrated these results using bipartite random networks, but also simple hierarchical structures.

Concerning cluster states in networks of Stuart-Landau oscillators, I obtained analytic results in the stability analysis in analogy to in-phase synchronization for certain network topologies. I derived rigorous conditions under which multistability of several cluster states is suppressed and a single cluster state is selected.

11.2. Outlook

The most interesting extension to this work would be the discussion of heterogeneous delay times or system parameters. I have introduced multiple coupling matrices in order to deal with multiple delays in a network. In the light of applications, where fully heterogeneous delay times may occur in a network, this method is very restrictive and a suitable theory remains to be found. In general, parameter mismatch in the system or the coupling remains unfeasible with the master stability function and appropriate extension are missing.

Another promising extension of the work in this thesis leads into the direction of hierarchical network structures, where higher levels of hierarchy could possibly be obtained using many coupling matrices at the same time.

Concerning networks with periodic local dynamics, I have discussed stability of cluster states in unidirectional rings of Stuart-Landau oscillators in detail. These states do, however, also exist in other regular networks. It is still unclear how the particular topology affects the stability of these solutions. Finally, using the theory by [Ott and Antonsen](#)

could possibly yield valuable result regarding nonidentical nodes in the networks of Stuart-Landau oscillators.

A. Invariance of eigenvalues in matrix products

Let \mathbf{A} and \mathbf{B} be $m \times n$ and $n \times m$ matrices, respectively. I show that the eigenvalues of the product \mathbf{AB} are identical to those of \mathbf{BA} except for a potentially different number of zero eigenvalues. Or, more precisely:

$$\lambda^n \chi_{\mathbf{AB}}(\lambda) = \lambda^m \chi_{\mathbf{BA}}(\lambda), \quad (\text{A.1})$$

where $\chi_{\mathbf{M}}(\lambda) = \det(\lambda \mathbf{I}_m - \mathbf{M})$ denotes the characteristic polynomial of an $m \times m$ matrix \mathbf{M} . Consider the following matrix equations:

$$\begin{pmatrix} \lambda \mathbf{I}_m & -\mathbf{A} \\ 0 & \mathbf{I}_n \end{pmatrix} \begin{pmatrix} \mathbf{I}_m & \mathbf{A} \\ \mathbf{B} & \lambda \mathbf{I}_n \end{pmatrix} = \begin{pmatrix} \lambda \mathbf{I}_m - \mathbf{AB} & 0 \\ \mathbf{B} & \lambda \mathbf{I}_n \end{pmatrix}, \quad (\text{A.2})$$

$$\begin{pmatrix} \lambda \mathbf{I}_m & 0 \\ -\mathbf{B} & \mathbf{I}_n \end{pmatrix} \begin{pmatrix} \mathbf{I}_m & \mathbf{A} \\ \mathbf{B} & \lambda \mathbf{I}_n \end{pmatrix} = \begin{pmatrix} \lambda \mathbf{I}_m & \lambda \mathbf{A} \\ 0 & \lambda \mathbf{I}_n - \mathbf{BA} \end{pmatrix}, \quad (\text{A.3})$$

which are true as can be easily seen by calculating the matrix products. Then calculating the determinant in both equations and using the property of the determinant $\det(\mathbf{FG}) = \det(\mathbf{F})\det(\mathbf{G})$ yields

$$\lambda^n \det(\lambda \mathbf{I}_m - \mathbf{AB}) = \lambda^m \det \begin{pmatrix} \mathbf{I}_m & \mathbf{A} \\ \mathbf{B} & \lambda \mathbf{I}_n \end{pmatrix} = \lambda^m \det(\lambda \mathbf{I}_n - \mathbf{BA}), \quad (\text{A.4})$$

which proves Eq. (A.1).

A.1. Implications

If $m = n$, the product \mathbf{AB} will have exactly the same spectrum as \mathbf{BA} . If however, m is larger than n , the spectrum of \mathbf{AB} will have $m - n$ more zeros than that of \mathbf{BA} since Eq. (A.1) is equivalent to

$$\chi_{\mathbf{AB}}(\lambda) = \lambda^{m-n} \chi_{\mathbf{BA}}(\lambda). \quad (\text{A.5})$$

Bibliography

- AGRAWAL, G. P. (1988), *Spectral hole-burning and gain saturation in semiconductor lasers: Strong-signal theory*, J. Appl. Phys. **63**, 1232. (Cited on page 48.)
- AHLBORN, A. AND PARLITZ, U. (2006), *Laser stabilization with multiple-delay feedback control*, Opt. Lett. **31**, 465. (Cited on page 40.)
- ALBERT, R. AND BARABÁSI, A.-L. (2002), *Statistical mechanics of complex networks*, Rev. Mod. Phys. **74**, 47. (Cited on pages 18, 25, 35, 37, 38, 101, 103, 107 and 108.)
- ALSING, P. M., KOVANIS, V., GAVRIELIDES, A., AND ERNEUX, T. (1996), *Lang and Kobayashi phase equation*, Phys. Rev. A **53**, 4429. (Cited on page 43.)
- AMANN, A., POKROVSKIY, A., OSBORNE, S., AND O'BRIEN, S. (2008), *Complex networks based on discrete-mode lasers*, in *International Workshop on Multi-Rate Processes and Hysteresis, Cork 2008*, J. Phys.: Conf. Ser., volume 138, page 012001, IOP Publishing. (Cited on page 28.)
- ARGYRIS, A., HAMACHER, M., CHLOUVERAKIS, K. E., BOGRIS, A., AND SYVRIDIS, D. (2008), *Photonic Integrated Device for Chaos Applications in Communications*, Phys. Rev. Lett. **100**, 194101. (Cited on page 68.)
- ARGYRIS, A., SYVRIDIS, D., LARGER, L., ANNOVAZZI-LODI, V., COLET, P., FISCHER, I., GARCÍA-OJALVO, J., MIRASSO, C. R., PESQUERA, L., AND SHORE, K. A. (2005), *Chaos-based communications at high bit rates using commercial fibre-optic links*, Nature **438**, 343. (Cited on pages 26 and 46.)
- AUST, R., HÖVEL, P., HIZANIDIS, J., AND SCHÖLL, E. (2010), *Delay control of coherence resonance in type-I excitable dynamics*, Eur. Phys. J. ST **187**, 77. (Cited on page 36.)
- AVIAD, Y., REIDLER, I., KINZEL, W., KANTER, I., AND ROSENBLUH, M. (2008), *Phase synchronization in mutually coupled chaotic diode lasers*, Phys. Rev. E **78**, 025204. (Cited on page 28.)

- BALANOV, A. G., JANSON, N. B., POSTNOV, D. E., AND SOSNOVTSEVA, O. V. (2009), *Synchronization: From Simple to Complex*, Springer, Berlin. (Cited on page 25.)
- BARABÁSI, A.-L. (2002), *Linked: The New Science of Networks*, Perseus Publishing, ISBN 0-7382-0667-9. (Cited on pages 25, 37 and 38.)
- BARABÁSI, A.-L. AND BONABEAU, E. (2003), *Scale-free networks*, Sci. Am. **288**, 50. (Cited on pages 25, 101 and 118.)
- BARABÁSI, A.-L. AND OLTVAI, Z. N. (2004), *Network biology: understanding the cell's functional organization*, Nat. Rev. Genet. **5**, 101. (Cited on pages 21 and 176.)
- BARAHONA, M. AND PECORA, L. M. (2002), *Synchronization in Small-World Systems*, Phys. Rev. Lett. **89**, 054101. (Cited on page 25.)
- BAUER, S., BROX, O., KREISSL, J., SARTORIUS, B., RADZIUNAS, M., SIEBER, J., WÜNSCHE, H. J., AND HENNEBERGER, F. (2004), *Nonlinear dynamics of semiconductor lasers with active optical feedback*, Phys. Rev. E **69**, 016206. (Cited on page 40.)
- BERMAN, A. AND PLEMMONS, R. J. (1979), *Nonnegative matrices in the mathematical sciences*, Computer Science and Applied Mathematics, Academic Press, New York, ISBN 0-12-092260-8. (Cited on page 57.)
- BLYUSS, K. B., KYRYCHKO, Y. N., HÖVEL, P., AND SCHÖLL, E. (2008), *Control of unstable steady states in neutral time-delayed systems*, Eur. Phys. J. B **65**, 571. (Cited on page 41.)
- BOCCALETTI, S., KURTHS, J., OSIPOV, G., VALLADARES, D. L., AND ZHOU, C. S. (2002), *The synchronization of chaotic systems*, Phys. Rep. **366**, 1. (Cited on page 25.)
- BOCCALETTI, S., LATORA, V., MORENO, Y., CHAVEZ, M., AND HWANG, D. U. (2006), *Complex networks: Structure and dynamics*, Physics Reports **424**, 175, ISSN 0370-1573. (Cited on pages 25, 35, 37, 38 and 101.)
- BOLLOBÁS, B. (2001), *Random graphs*, Cambridge University Press, 2nd edition. (Cited on page 107.)
- BROWN, R. AND RULKOV, N. F. (1997), *Designing a Coupling That Guarantees Synchronization between Identical Chaotic Systems*, Phys. Rev. Lett. **78**, 4189. (Cited on page 25.)
- CALLAN, K. E., ILLING, L., GAO, Z., GAUTHIER, D. J., AND SCHÖLL, E. (2010), *Broadband chaos generated by an opto-electronic oscillator*, Phys. Rev. Lett. **104**, 113901. (Cited on page 41.)

- CARDOSO, J.-F. AND SOULOUMIAC, A. (1996), *Jacobi angles for simultaneous diagonalization*, SIAM J. Mat. Anal. Appl. **17**, 161. (Cited on pages 117 and 173.)
- CHAVEZ, M., HWANG, D. U., AMANN, A., AND BOCCALETTI, S. (2006), *Synchronizing weighted complex networks*, Chaos **16**, 015106. (Cited on pages 25 and 39.)
- CHAVEZ, M., HWANG, D. U., AMANN, A., HENTSCHEL, H. G. E., AND BOCCALETTI, S. (2005), *Synchronization is Enhanced in Weighted Complex Networks*, Phys. Rev. Lett. **94**, 218701. (Cited on pages 25 and 39.)
- CHOE, C. U., DAHMS, T., HÖVEL, P., AND SCHÖLL, E. (2010), *Controlling synchrony by delay coupling in networks: from in-phase to splay and cluster states*, Phys. Rev. E **81**, 025205(R). (Cited on pages 22, 35, 123, 145, 183 and 192.)
- CHOE, C. U., DAHMS, T., HÖVEL, P., AND SCHÖLL, E. (2011), *Control of synchrony by delay coupling in complex networks*, in *Proceedings of the Eighth AIMS International Conference on Dynamical Systems, Differential Equations and Applications*. In print. (Cited on pages 35, 123, 145 and 183.)
- CHUNG, F. AND LU, L. (2001), *The Diameter of Sparse Random Graphs*, Adv. Appl. Math. **26**, 257, ISSN 0196-8858. (Cited on page 107.)
- DAHLEM, M. A., SCHNEIDER, F. M., AND SCHÖLL, E. (2008), *Failure of feedback as a putative common mechanism of spreading depolarizations in migraine and stroke*, Chaos **18**, 026110. (Cited on page 40.)
- DAHMS, T., FLUNKERT, V., HENNEBERGER, F., HÖVEL, P., SCHIKORA, S., SCHÖLL, E., AND WÜNSCHE, H. J. (2010), *Noninvasive optical control of complex semiconductor laser dynamics*, Eur. Phys. J. ST **191**, 71. (Cited on pages 27, 40 and 45.)
- DAHMS, T., HÖVEL, P., AND SCHÖLL, E. (2007), *Control of unstable steady states by extended time-delayed feedback*, Phys. Rev. E **76**, 056201. (Cited on page 126.)
- DAHMS, T., HÖVEL, P., AND SCHÖLL, E. (2008), *Stabilizing continuous-wave output in semiconductor lasers by time-delayed feedback*, Phys. Rev. E **78**, 056213. (Cited on pages 27, 40 and 126.)
- DAHMS, T., LEHNERT, J., AND SCHÖLL, E. (2011), *Cluster and group synchronization in delay-coupled laser networks*, in preparation . (Cited on page 145.)
- DHAMALA, M., JIRSA, V. K., AND DING, M. (2004), *Enhancement of Neural Synchrony by Time Delay*, Phys. Rev. Lett. **92**, 074104. (Cited on page 36.)

- D'HUYS, O., FISCHER, I., DANCKAERT, J., AND VICENTE, R. (2011), *Role of delay for the symmetry in the dynamics of networks*, Phys. Rev. E **83**, 046223. (Cited on pages 26 and 27.)
- D'HUYS, O., VICENTE, R., ERNEUX, T., DANCKAERT, J., AND FISCHER, I. (2008), *Synchronization properties of network motifs: Influence of coupling delay and symmetry*, Chaos **18**, 037116. (Cited on pages 25, 26 and 139.)
- DITZINGER, T., NING, C. Z., AND HU, G. (1994), *Resonancelike responses of autonomous nonlinear systems to white noise*, Phys. Rev. E **50**, 3508. (Cited on page 36.)
- EARL, M. G. AND STROGATZ, S. H. (2003), *Synchronization in oscillator networks with delayed coupling: A stability criterion*, Phys. Rev. E **67**, 036204. (Cited on pages 25 and 135.)
- ENGLERT, A., HEILIGENTHAL, S., KINZEL, W., AND KANTER, I. (2011), *Synchronization of chaotic networks with time-delayed couplings: An analytic study*, Phys. Rev. E **83**, 046222. (Cited on pages 26, 66, 67, 115, 119 and 211.)
- ENGLERT, A., KINZEL, W., AVIAD, Y., BUTKOVSKI, M., REIDLER, I., ZIGZAG, M., KANTER, I., AND ROSENBLUH, M. (2010), *Zero lag synchronization of chaotic systems with time delayed couplings*, Phys. Rev. Lett. **104**, 114102. (Cited on pages 26 and 119.)
- ERDŐS, P. AND RÉNYI, A. (1959), *On random graphs*, Publ. Math. Debrecen **6**, 290. (Cited on pages 25, 75, 101 and 118.)
- ERDŐS, P. AND RÉNYI, A. (1960), *On the evolution of random graphs*, Publ. Math. Inst. Hung. Acad. Sci **5**, 17. (Cited on pages 25, 75, 101, 102 and 118.)
- ERZGRÄBER, H. AND KRAUSKOPF, B. (2007), *Dynamics of a filtered-feedback laser: influence of the filter width*, Opt. Lett. **32**, 2441. (Cited on page 27.)
- ERZGRÄBER, H., KRAUSKOPF, B., AND LENSTRA, D. (2007a), *Bifurcation Analysis of a Semiconductor Laser with Filtered Optical Feedback*, SIAM J. Appl. Dyn. Syst. **6**, 1. (Cited on page 27.)
- ERZGRÄBER, H., KRAUSKOPF, B., LENSTRA, D., FISCHER, A. P. A., AND VEMURI, G. (2006), *Frequency versus relaxation oscillations in a semiconductor laser with coherent filtered optical feedback*, Phys. Rev. E **73**, 055201(R). (Cited on page 27.)
- ERZGRÄBER, H., LENSTRA, D., KRAUSKOPF, B., FISCHER, A. P. A., AND VEMURI, G. (2007b), *Feedback phase sensitivity of a semiconductor laser subject to filtered optical feedback: Experiment and theory*, Phys. Rev. E **76**, 026212. (Cited on page 27.)

- ERZGRÄBER, H., LENSTRA, D., KRAUSKOPF, B., WILLE, E., PEIL, M., FISCHER, I., AND EL-SÄSSER, W. (2005), *Mutually delay-coupled semiconductor lasers: Mode bifurcation scenarios*, Opt. Commun. **255**, 286. (Cited on page 26.)
- FARMER, J. D. (1982), *Chaotic attractors of an infinite-dimensional dynamical system*, Physica D **4**, 366. (Cited on pages 53 and 54.)
- FIEDLER, B., FLUNKERT, V., GEORGI, M., HÖVEL, P., AND SCHÖLL, E. (2007), *Refuting the odd number limitation of time-delayed feedback control*, Phys. Rev. Lett. **98**, 114101. (Cited on pages 27 and 125.)
- FIEDLER, B., YANCHUK, S., FLUNKERT, V., HÖVEL, P., WÜNSCHE, H. J., AND SCHÖLL, E. (2008), *Delay stabilization of rotating waves near fold bifurcation and application to all-optical control of a semiconductor laser*, Phys. Rev. E **77**, 066207. (Cited on page 40.)
- FISCHER, A., ANDERSEN, O., YOUSEFI, M., STOLTE, S., AND LENSTRA, D. (2000a), *Experimental and theoretical study of filtered optical feedback in a semiconductor laser*, IEEE J. Quantum Electron. **36**, 375. (Cited on page 40.)
- FISCHER, I., HESS, O., EL-SÄSSER, W., AND GÖBEL, E. O. (1994), *High-dimensional chaotic dynamics of an external-cavity semiconductor-laser*, Phys. Rev. Lett. **73**, 2188. (Cited on page 27.)
- FISCHER, I., LIU, Y., AND DAVIS, P. (2000b), *Synchronization of chaotic semiconductor laser dynamics on subnanosecond time scales and its potential for chaos communication*, Phys. Rev. A **62**, 011801. (Cited on pages 26 and 46.)
- FISCHER, I., VICENTE, R., BULDÚ, J. M., PEIL, M., MIRASSO, C. R., TORRENT, M. C., AND GARCÍA-OJALVO, J. (2006), *Zero-Lag Long-Range Synchronization via Dynamical Relaying*, Phys. Rev. Lett. **97**, 123902. (Cited on page 27.)
- FITZHUGH, R. (1961), *Impulses and physiological states in theoretical models of nerve membrane*, Biophys. J. **1**, 445. (Cited on pages 35 and 123.)
- FLUNKERT, V. (2007), *Control of noise induced oscillations in semiconductor lasers*, Master's thesis, TU Berlin. (Cited on page 43.)
- FLUNKERT, V. (2010), *Delayed complex systems and applications to lasers*, Ph.D. thesis, TU-Berlin. (Cited on pages 27, 43 and 115.)
- FLUNKERT, V. (2011), *Delay-Coupled Complex Systems*, Springer Theses, Springer, Heidelberg, ISBN 978-3-642-20249-0. (to be published in June 2011). (Cited on pages 27, 43 and 115.)

- FLUNKERT, V., D'HUYS, O., DANCKAERT, J., FISCHER, I., AND SCHÖLL, E. (2009), *Bubbling in delay-coupled lasers*, Phys. Rev. E **79**, 065201 (R). (Cited on pages 26, 27, 59, 80 and 81.)
- FLUNKERT, V. AND SCHÖLL, E. (2007), *Suppressing noise-induced intensity pulsations in semiconductor lasers by means of time-delayed feedback*, Phys. Rev. E **76**, 066202. (Cited on page 40.)
- FLUNKERT, V. AND SCHÖLL, E. (2011a), *Synchronization of all-optically coupled lasers: Role of the coupling phases*. In preparation. (Cited on pages 27, 56 and 209.)
- FLUNKERT, V. AND SCHÖLL, E. (2011b), *Towards easier realization of time-delayed feedback control of odd-number orbits*, Phys. Rev. E In print. (Cited on pages 27 and 40.)
- FLUNKERT, V., YANCHUK, S., DAHMS, T., AND SCHÖLL, E. (2010), *Synchronizing distant nodes: a universal classification of networks*, Phys. Rev. Lett. **105**, 254101. (Cited on pages 66, 67 and 160.)
- FRADKOV, A. L. (2007), *Cybernetical Physics: From Control of Chaos to Quantum Control*, Springer, Heidelberg, Germany. (Cited on page 197.)
- FUJISAKA, H. AND YAMADA, T. (1983), *Stability Theory of Synchronized Motion in Coupled-Oscillator Systems*, Prog. Theor. Phys. **69**, 32. (Cited on page 26.)
- FUJISAKA, H. AND YAMADA, T. (1986), *Stability Theory of Synchronized Motion in Coupled-Oscillator Systems. IV*, Prog. Theor. Phys. **75**, 1087. (Cited on page 26.)
- GERSCHGORIN, S. A. (1931), *Über die Abgrenzung der Eigenwerte einer Matrix*, Izv. Akad. Nauk. SSSR **7**, 749. (Cited on pages 57, 135 and 139.)
- GOLUB, G. H. AND VAN LOAN, C. F. (1996), *Matrix computations*, The Johns Hopkins University Press, Baltimore. (Cited on pages 118 and 193.)
- GRASSBERGER, P. AND PROCACCIA, I. (1984), *Dimensions and entropies of strange attractors from a fluctuating dynamics approach*, Physica D **13**, 34, ISSN 0167-2789. (Cited on page 54.)
- GRAY, R. M. (2006), *Toeplitz And Circulant Matrices: A Review*, in *Foundations and Trends® in Communications and Information Theory*, volume 2, pages 155–239, Now Publishers Inc., Hanover, MA, USA, ISBN 1933019239. (Cited on pages 96 and 118.)
- GREEN, K. AND KRAUSKOPF, B. (2006), *Mode structure of a semiconductor laser subject to filtered optical feedback*, Opt. Commun. **258**, 243. (Cited on page 27.)

- GREENSHIELDS, C. (2010), *Master stability function for systems with two coupling delays*. Private communication. (Cited on page 119.)
- GROSS, N., KINZEL, W., KANTER, I., ROSENBLUH, M., AND KHAYKOVICH, L. (2006), *Synchronization of mutually versus unidirectionally coupled chaotic semiconductor lasers*, Opt. Commun. **267**, 464, ISSN 0030-4018. (Cited on page 26.)
- HADELER, K. P. (2008), *Neutral delay equations from and for population dynamics*, Proc. 8th Coll. QTDE, Electron. J. Qual. Theory Differ. Equ. **11**, 1. (Cited on page 41.)
- HAUSCHILD, B., JANSON, N. B., BALANOV, A. G., AND SCHÖLL, E. (2006), *Noise-induced cooperative dynamics and its control in coupled neuron models*, Phys. Rev. E **74**, 051906. (Cited on page 82.)
- HEIL, T., FISCHER, I., AND ELSÄSSER, W. (1998), *Coexistence of low-frequency fluctuations and stable emission on a single high-gain mode in semiconductor lasers with external optical feedback*, Phys. Rev. A **58**, 2672. (Cited on page 27.)
- HEIL, T., FISCHER, I., AND ELSÄSSER, W. (2000), *Stabilization of feedback-induced instabilities in semiconductor lasers*, J. Opt. B: Quantum Semiclass. Opt. **2**, 413. (Cited on page 27.)
- HEIL, T., FISCHER, I., ELSÄSSER, W., KRAUSKOPF, B., GREEN, K., AND GAVRIELIDES, A. (2003), *Delay dynamics of semiconductor lasers with short external cavities: Bifurcation scenarios and mechanisms*, Phys. Rev. E **67**, 066214. (Cited on page 27.)
- HEIL, T., FISCHER, I., ELSÄSSER, W., MULET, J., AND MIRASSO, C. R. (2001), *Chaos Synchronization and Spontaneous Symmetry-Breaking in Symmetrically Delay-Coupled Semiconductor Lasers*, Phys. Rev. Lett. **86**, 795. (Cited on page 26.)
- HEIL, T., MULET, J., FISCHER, I., MIRASSO, C. R., PEIL, M., COLET, P., AND ELSÄSSER, W. (2002), *ON/OFF phase shift keying for chaos-encrypted communication using external-cavity semiconductor lasers*, IEEE J. Quantum Electron. **38**, 1162, ISSN 0018-9197. (Cited on pages 26 and 46.)
- HEILGENTHAL, S., DAHMS, T., YANCHUK, S., JÜNGLING, T., FLUNKERT, V., KANTER, I., SCHÖLL, E., AND KINZEL, W. (2011), *Strong and weak chaos in nonlinear networks with time-delayed couplings*, in preparation. (Cited on page 68.)
- HICKE, K., D'HUYS, O., FLUNKERT, V., SCHÖLL, E., DANCKAERT, J., AND FISCHER, I. (2011), *Mismatch and synchronization: Influence of asymmetries in systems of two delay-coupled lasers*, Phys. Rev. E **83**, 056211. (Cited on pages 27 and 41.)

- HINDMARSH, J. L. AND ROSE, R. M. (1982), *A model of the nerve impulse using two first-order differential equations*, *Nature* **296**, 162. (Cited on page 35.)
- HIZANIDIS, J., AUST, R., AND SCHÖLL, E. (2008), *Delay-induced multistability near a global bifurcation*, *Int. J. Bifur. Chaos* **18**, 1759. (Cited on page 36.)
- HOHL, A. AND GAVRIELIDES, A. (1999), *Bifurcation cascade in a semiconductor laser subject to optical feedback*, *Phys. Rev. Lett.* **82**, 1148. (Cited on pages 46 and 49.)
- HORN, R. A. AND JOHNSON, C. R. (1985), *Matrix Analysis*, Cambridge University Press, ISBN 978-0-521-38632-6. (Cited on page 39.)
- HÖVEL, P. (2010), *Control of Complex Nonlinear Systems with Delay*, Springer Theses, Springer, Heidelberg. (Cited on pages 27 and 37.)
- HÖVEL, P., DAHLEM, M. A., AND SCHÖLL, E. (2010), *Control of synchronization in coupled neural systems by time-delayed feedback*, *Int. J. Bifur. Chaos* **20**, 813. (Cited on page 82.)
- HÖVEL, P. AND SCHÖLL, E. (2005), *Control of unstable steady states by time-delayed feedback methods*, *Phys. Rev. E* **72**, 046203. (Cited on page 126.)
- HÖVEL, P., SHAH, S. A., DAHLEM, M. A., AND SCHÖLL, E. (2009), *Feedback-dependent control of stochastic synchronization in coupled neural systems*, *Proc. 4th International Scientific Conference on Physics and Control (PhysCon 09)*, ed. L. Fortuna and M. Frasca, IPACS Open Access Library <http://lib.physcon.ru> (e-Library of the International Physics and Control Society). (Cited on page 37.)
- HU, G., DITZINGER, T., NING, C. Z., AND HAKEN, H. (1993), *Stochastic Resonance without External Periodic Force*, *Phys. Rev. Lett.* **71**, 807. (Cited on page 36.)
- HWANG, D. U., CHAVEZ, M., AMANN, A., AND BOCCALETTI, S. (2005), *Synchronization in Complex Networks with Age Ordering*, *Phys. Rev. Lett.* **94**, 138701. (Cited on page 25.)
- ILLING, L. AND GAUTHIER, D. J. (2006), *Ultra-high-frequency chaos in a time-delay electronic device with band-limited feedback*, *Chaos* **16**, 033119. (Cited on page 41.)
- JUST, W. (1999), *Zur Analyse zeitverzögerter Rückkopplungskontrolle*. Technical Report, MPI SF Göttingen. (Cited on page 132.)
- JUST, W., PELSTER, A., SCHANZ, M., AND SCHÖLL, E. (2010), *Delayed Complex Systems*, Theme Issue of *Phil. Trans. R. Soc. A* **368**, ISSN 1364-503X. Pp.301-513. (Cited on pages 27 and 41.)

- KANE, D. M. AND SHORE, K. A. (Editors) (2005), *Unlocking Dynamical Diversity: Optical Feedback Effects on Semiconductor Lasers*, Wiley VCH, Weinheim. (Cited on page 44.)
- KANTER, I., KOPELOWITZ, E., KESTLER, J., AND KINZEL, W. (2008a), *Chaos synchronization with dynamic filters: Two-way is better than one-way*, Europhys. Lett. **83**, 50005. (Cited on page 26.)
- KANTER, I., KOPELOWITZ, E., AND KINZEL, W. (2008b), *Public channel cryptography: chaos synchronization and Hilbert's tenth problem*, Phys. Rev. Lett. **101**, 84102. (Cited on page 26.)
- KANTER, I., KOPELOWITZ, E., VARDI, R., ZIGZAG, M., KINZEL, W., ABELES, M., AND COHEN, D. (2011a), *Nonlocal mechanism for cluster synchronization in neural circuits*, Europhys. Lett. **93**, 66001. (Cited on page 28.)
- KANTER, I., ZIGZAG, M., ENGLERT, A., GEISSLER, F., AND KINZEL, W. (2011b), *Synchronization of unidirectional time delay chaotic networks and the greatest common divisor*, Europhys. Lett. **93**, 60003. (Cited on page 28.)
- KAPLAN, J. L. AND YORKE, J. A. (1979), *Chaotic behavior of multidimensional difference equations*, in H. O. Peitgen and H. O. Walther (Editors), *Functional differential equations and approximations of fixed points. Lecture notes in mathematics Vol. 730*, Springer, Berlin. (Cited on page 54.)
- KESTLER, J., KINZEL, W., AND KANTER, I. (2007), *Sublattice synchronization of chaotic networks with delayed couplings*, Phys. Rev. E **76**, 035202. (Cited on pages 28 and 169.)
- KESTLER, J., KOPELOWITZ, E., KANTER, I., AND KINZEL, W. (2008), *Patterns of chaos synchronization*, Phys. Rev. E **77**, 046209. (Cited on pages 28 and 169.)
- KINZEL, W., ENGLERT, A., AND KANTER, I. (2010), *On chaos synchronization and secure communication*, Phil. Trans. R. Soc. A **368**, 379. (Cited on pages 26 and 46.)
- KINZEL, W., ENGLERT, A., REENTS, G., ZIGZAG, M., AND KANTER, I. (2009), *Synchronization of networks of chaotic units with time-delayed couplings*, Phys. Rev. E **79**, 056207. (Cited on page 26.)
- KINZEL, W. AND KANTER, I. (2008), *Secure Communication with Chaos Synchronization*, in E. Schöll and H. G. Schuster (Editors), *Handbook of Chaos Control*, Wiley-VCH, Weinheim. Second completely revised and enlarged edition. (Cited on pages 26 and 46.)
- KIRKLAND, S. (2005), *Girth and subdominant eigenvalues for stochastic matrices*, Electronic Journal of Linear Algebra **12**, 25. (Cited on page 57.)

- KLEIN, E., GROSS, N., KOPELOWITZ, E., ROSENBLUH, M., KHAYKOVICH, L., KINZEL, W., AND KANTER, I. (2006a), *Public-channel cryptography based on mutual chaos pass filters*, Phys. Rev. E **74**, 046201. (Cited on page 26.)
- KLEIN, E., GROSS, N., ROSENBLUH, M., KINZEL, W., KHAYKOVICH, L., AND KANTER, I. (2006b), *Stable isochronal synchronization of mutually coupled chaotic lasers*, Phys. Rev. E **73**, 066214. (Cited on page 26.)
- KLEIN, E., MISLOVATY, R., KANTER, I., AND KINZEL, W. (2005), *Public-channel cryptography using chaos synchronization*, Phys. Rev. E **72**, 016214. (Cited on page 26.)
- KOCAREV, L. AND PARLITZ, U. (1995), *General Approach for Chaotic Synchronization with Applications to Communication*, Phys. Rev. Lett. **74**, 5028. (Cited on page 25.)
- KRAUSKOPF, B., VAN TARTWIJK, G. H. M., AND GRAY, G. R. (2000), *Symmetry properties of lasers subject to optical feedback*, Opt. Commun. **177**, 347. (Cited on page 27.)
- KURAMOTO, Y. (1984), *Chemical Oscillations, Waves and Turbulence*, Springer-Verlag, Berlin. (Cited on pages 142, 185, 197 and 208.)
- KYRYCHKO, Y. N., BLYUSS, K. B., HOGAN, S. J., AND SCHÖLL, E. (2009), *Control of spatio-temporal patterns in the Gray-Scott model*, Chaos **19**, 043126. (Cited on page 41.)
- LANG, R. AND KOBAYASHI, K. (1980), *External optical feedback effects on semiconductor injection laser properties*, IEEE J. Quantum Electron. **16**, 347. (Cited on pages 28, 35, 40 and 43.)
- LEE, W. S., OTT, E., AND ANTONSEN, T. M. (2009), *Large Coupled Oscillator Systems with Heterogeneous Interaction Delays*, Phys. Rev. Lett. **103**, 044101. (Cited on page 208.)
- LEHNERT, J. (2010), *Dynamics of Neural Networks with Delay*, Master's thesis, Technische Universität Berlin. (Cited on page 38.)
- LEHNERT, J., DAHMS, T., HÖVEL, P., AND SCHÖLL, E. (2011), *Loss of synchronization in complex neural networks with delay*, submitted . (Cited on pages 25, 26, 36, 38, 101 and 146.)
- LIU, Y. AND OHTSUBO, J. (1997), *Dynamics and Chaos Stabilization of Semiconductor Lasers with Optical Feedback from an Interferometer*, IEEE J. Quantum Electron. **33**, 1163. (Cited on page 40.)
- LORENZ, E. N. (1963), *Deterministic nonperiodic flow*, J. Atmos. Sci. **20**, 130. (Cited on pages 35 and 54.)

- LÜDGE, K. (2011), *Nonlinear Laser Dynamics- From Quantum Dots to Cryptography*, WILEY-VCH, Weinheim, ISBN 978-3-527-41100-9. (Cited on page 43.)
- MANDRE, S. K., FISCHER, I., AND ELSÄSSER, W. (2003), *Control of the spatiotemporal emission of a broad-area semiconductor laser by spatially filtered feedback*, Opt. Lett. **28**, 1135. (Cited on page 27.)
- MILO, R., SHEN-ORR, S., ITZKOVITZ, S., KASHTAN, N., CHKLOVSKII, D., AND ALON, U. (2002), *Network motifs: simple building blocks of complex networks*, Science **298**, 824. (Cited on pages 16, 73 and 74.)
- MOSEKILDE, E., MAISTRENKO, Y., AND POSTNOV, D. (2002), *Chaotic Synchronization: Applications to Living Systems*, World Scientific, Singapore. (Cited on page 25.)
- MULET, J., MIRASSO, C. R., HEIL, T., AND FISCHER, I. (2004), *Synchronization scenario of two distant mutually coupled semiconductor lasers*, J. Opt. B **6**, 97. (Cited on page 26.)
- MURPHY, T. E., COHEN, A. B., RAVOORI, B., SCHMITT, K. R. B., SETTY, A. V., SORRENTINO, F., WILLIAMS, C. R. S., OTT, E., AND ROY, R. (2009), *Chaotic Dynamics and Synchronization of Delayed-Feedback Nonlinear Oscillators*, Phil. Trans. R. Soc. A Submitted. (Cited on pages 26 and 41.)
- MURPHY, T. E., COHEN, A. B., RAVOORI, B., SCHMITT, K. R. B., SETTY, A. V., SORRENTINO, F., WILLIAMS, C. R. S., OTT, E., AND ROY, R. (2010), *Complex dynamics and synchronization of delayed-feedback nonlinear oscillators*, Phil. Trans. R. Soc. A **368**, 343. (Cited on page 26.)
- NAGUMO, J., ARIMOTO, S., AND YOSHIZAWA, S. (1962), *An active pulse transmission line simulating nerve axon.*, Proc. IRE **50**, 2061. (Cited on pages 35 and 123.)
- NAKAJIMA, H. AND UEDA, Y. (1998), *Limitation of generalized delayed feedback control*, Physica D **111**, 143. (Cited on page 27.)
- NEWMAN, M. E. J. (2001a), *Scientific collaboration networks. I. Network construction and fundamental results*, Phys. Rev. E **64**, 016131. (Cited on page 25.)
- NEWMAN, M. E. J. (2001b), *Scientific collaboration networks. II. Shortest paths, weighted networks, and centrality*, Phys. Rev. E **64**, 016132. (Cited on page 25.)
- NEWMAN, M. E. J. (2003), *The Structure and Function of Complex Networks*, SIAM Review **45**, 167. (Cited on pages 18, 25, 35, 37, 38, 101, 103 and 106.)

- NEWMAN, M. E. J., BARABÁSI, A.-L., AND WATTS, D. J. (2006), *The Structure and Dynamics of Networks*, Princeton University Press, ISBN 0-691-11357-2. (Cited on pages 25, 37 and 38.)
- NISHIKAWA, T. AND MOTTER, A. E. (2006), *Synchronization is optimal in nondiagonalizable networks*, Phys. Rev. E **73**, 065106. (Cited on page 87.)
- OSBORNE, S., AMANN, A., BUCKLEY, K., RYAN, G., HEGARTY, S. P., HUYET, G., AND O'BRIEN, S. (2009), *Antiphase dynamics in a multimode semiconductor laser with optical injection*, Phys. Rev. A **79**, 023834. (Cited on page 28.)
- OTT, E. AND ANTONSEN, T. M. (2008), *Low dimensional behavior of large systems of globally coupled oscillators*, Chaos **18**, 037113. (Cited on pages 26, 206, 208, 209 and 212.)
- OTT, E. AND ANTONSEN, T. M. (2009), *Long time evolution of phase oscillator systems*, Chaos **19**, 023117. (Cited on page 208.)
- OTTO, C., GLOBISCH, B., LÜDGE, K., SCHÖLL, E., AND ERNEUX, T. (2012), *Complex Dynamics of Semiconductor Quantum Dot Lasers Subject to Delayed Optical Feedback*, Int. J. Bif. Chaos Submitted. (Cited on pages 27 and 40.)
- OTTO, C., LÜDGE, K., AND SCHÖLL, E. (2010), *Modeling quantum dot lasers with optical feedback: sensitivity of bifurcation scenarios*, phys. stat. sol. (b) **247**, 829. (Cited on pages 27 and 40.)
- PECORA, L. M. (1998), *Synchronization conditions and desynchronizing patterns in coupled limit-cycle and chaotic systems*, Phys. Rev. E **58**, 347. (Cited on page 26.)
- PECORA, L. M. AND BARAHONA, M. (2006), *Synchronization of Oscillators in Complex Networks*, in F. F. Orsucci and N. Sala (Editors), *New Research on Chaos and Complexity*, chapter 5, pages 65–96, Nova Science Publishers, ISBN 1-60021-275-1. (Cited on page 25.)
- PECORA, L. M. AND CARROLL, T. L. (1990), *Synchronization in chaotic systems*, Phys. Rev. Lett. **64**, 821. (Cited on page 25.)
- PECORA, L. M. AND CARROLL, T. L. (1998), *Master Stability Functions for Synchronized Coupled Systems*, Phys. Rev. Lett. **80**, 2109. (Cited on pages 5, 7, 26, 28, 37, 60, 62, 63, 64, 70, 126 and 211.)
- PECORA, L. M., CARROLL, T. L., JOHNSON, G. A., MAR, D. J., AND HEAGY, J. F. (1997), *Fundamentals of synchronization in chaotic systems, concepts, and applications*, Chaos **7**, 520. (Cited on pages 25 and 59.)

- PEIL, M., HEIL, T., FISCHER, I., AND ELSÄSSER, W. (2002), *Synchronization of Chaotic Semiconductor Laser Systems: A Vectorial Coupling-Dependent Scenario*, Phys. Rev. Lett. **88**, 174101. (Cited on page 26.)
- PEIL, M., LARGER, L., AND FISCHER, I. (2007), *Versatile and robust chaos synchronization phenomena imposed by delayed shared feedback coupling*, Phys. Rev. E rapid comm. **76**, 045201. (Cited on page 28.)
- PIKOVSKY, A. S., ROSENBLUM, M. G., AND KURTHS, J. (2001), *Synchronization, A Universal Concept in Nonlinear Sciences*, Cambridge University Press, Cambridge. (Cited on page 25.)
- POPOVYCH, O. V., HAUPTMANN, C., AND TASS, P. A. (2005a), *Demand-Controlled Desynchronization of Brain Rhythms by Means of Nonlinear Delayed Feedback*, Proc. IEEE Eng. Med. Biol. 27th annual conf. (Cited on page 40.)
- POPOVYCH, O. V., HAUPTMANN, C., AND TASS, P. A. (2005b), *Effective Desynchronization by Nonlinear Delayed Feedback*, Phys. Rev. Lett. **94**, 164102. (Cited on page 40.)
- POPOVYCH, O. V., HAUPTMANN, C., AND TASS, P. A. (2006), *Control of neuronal synchrony by nonlinear delayed feedback*, Biol. Cybern. **95**, 69. (Cited on page 40.)
- PYRAGAS, K. (1992), *Continuous control of chaos by self-controlling feedback*, Phys. Lett. A **170**, 421. (Cited on pages 27 and 40.)
- PYRAGAS, K. AND PYRAGIENE, T. (2008), *Coupling design for a long-term anticipating synchronization of chaos*, Phys. Rev. E **78**, 046217. (Cited on page 125.)
- RADZIUNAS, M., WÜNSCHE, H. J., KRAUSKOPF, B., AND WOLFRUM, M. (2006), *External cavity modes in Lang-Kobayashi and travelling wave models*, Proc. SPIE **6184**. (Cited on page 27.)
- REIDLER, I. AND KANTER, I. (2011), *Experimental synchronization of distant lasers*, Talk at the Workshop “Synchronization in Complex Networks”. (Cited on page 28.)
- RESTREPO, J. G., OTT, E., AND HUNT, B. R. (2006), *Emergence of Coherence in Complex Networks of Heterogeneous Dynamical Systems*, Phys. Rev. Lett. **96**, 254103. (Cited on pages 26 and 61.)
- ROGISTER, F., LOCQUET, A., PIEROUX, D., SCIAMANNA, M., DEPARIS, O., MEGRET, P., AND BLONDEL, M. (2001), *Secure communication scheme using chaotic laser diodes subject to incoherent optical feedback and incoherent optical injection*, Opt. Lett. **26**, 1486. (Cited on page 46.)

- ROGISTER, F., MÉGRET, P., DEPARIS, O., BLONDEL, M., AND ERNEUX, T. (1999), *Suppression of low-frequency fluctuations and stabilization of a semiconductor laser subjected to optical feedback from a double cavity: theoretical results*, Opt. Lett. **24**, 1218. (Cited on page 40.)
- ROSENBLUM, M. G., PIKOVSKY, A. S., AND KURTHS, J. (1996), *Phase Synchronization of Chaotic Oscillators*, Phys. Rev. Lett. **76**, 1804. (Cited on page 25.)
- ROSENBLUM, M. G., PIKOVSKY, A. S., KURTHS, J., SCHÄFER, C., AND TASS, P. A. (2001), *Phase synchronization: from theory to data analysis*, *Handbook of Biological Physics*, volume 4, chapter 9, pages 279–321, Elsevier Science, Amsterdam, 1st edition. (Cited on page 82.)
- RÖSSLER, O. E. (1976), *An equation for continuous chaos*, Phys. Lett. A **57**, 397. (Cited on pages 35 and 54.)
- ROTTSCHÄFER, V. AND KRAUSKOPF, B. (2005), *The ECM-backbone of the Lang-Kobayashi equations: a geometric picture*, Applied Nonlinear Mathematics Research Report, University of Bristol Preprint. (Cited on page 27.)
- ROTTSCHÄFER, V. AND KRAUSKOPF, B. (2007), *The ECM-backbone of the Lang-Kobayashi equations: A geometric picture*, Int. J. Bif. Chaos **17**, 1575. (Cited on page 27.)
- SCHIKORA, S., HÖVEL, P., WÜNSCHE, H. J., SCHÖLL, E., AND HENNEBERGER, F. (2006), *All-optical noninvasive control of unstable steady states in a semiconductor laser*, Phys. Rev. Lett. **97**, 213902. (Cited on pages 27 and 40.)
- SCHIKORA, S., WÜNSCHE, H. J., AND HENNEBERGER, F. (2008), *All-optical noninvasive chaos control of a semiconductor laser*, Phys. Rev. E **78**, 025202. (Cited on page 27.)
- SCHIKORA, S., WÜNSCHE, H. J., AND HENNEBERGER, F. (2011), *Odd-number theorem: Optical feedback control at a subcritical Hopf bifurcation in a semiconductor laser*, Phys. Rev. E **83**, 026203. (Cited on page 27.)
- SCHNEIDER, F. M., SCHÖLL, E., AND DAHLEM, M. A. (2009), *Controlling the onset of traveling pulses in excitable media by nonlocal spatial coupling and time delayed feedback*, Chaos **19**, 015110. (Cited on page 40.)
- SCHÖLL, E., HÖVEL, P., FLUNKERT, V., AND DAHLEM, M. A. (2010), *Time-delayed feedback control: from simple models to lasers and neural systems*, in F. M. Atay (Editor), *Complex time-delay systems: theory and applications*, pages 85–150, Springer, Berlin. (Cited on page 27.)

- SCHÖLL, E. AND SCHUSTER, H. G. (Editors) (2008), *Handbook of Chaos Control*, Wiley-VCH, Weinheim. Second completely revised and enlarged edition. (Cited on pages 27, 41 and 209.)
- SELIVANOV, A., LEHNERT, J., DAHMS, T., HÖVEL, P., FRADKOV, A. L., AND SCHÖLL, E. (2011), *Adaptive synchronization for delay-coupled networks of Stuart-Landau oscillators*, in preparation . (Cited on pages 185, 197 and 209.)
- SETHIA, G. C., SEN, A., AND ATAY, F. M. (2008), *Clustered Chimera States in Delay-Coupled Oscillator Systems*, Phys. Rev. Lett. **100**, 144102. (Cited on page 25.)
- SIEBER, J., GONZALEZ-BUELGA, A., NEILD, S., WAGG, D., AND KRAUSKOPF, B. (2008), *Experimental Continuation of Periodic Orbits through a Fold*, Phys. Rev. Lett. **100**, 244101. (Cited on page 41.)
- SIMMENDINGER, C. AND HESS, O. (1996), *Controlling delay-induced chaotic behavior of a semiconductor laser with optical feedback*, Phys. Lett. A **216**, 97. (Cited on page 40.)
- SIMMENDINGER, C., MÜNKEL, M., AND HESS, O. (1999), *Controlling complex temporal and spatio-temporal dynamics in semiconductor lasers*, Chaos, Solitons and Fractals **10**, 851. (Cited on page 40.)
- SORRENTINO, F. AND OTT, E. (2007), *Network synchronization of groups*, Phys. Rev. E **76**, 056114. (Cited on pages 5, 7, 28, 145, 147 and 170.)
- SORRENTINO, F. AND OTT, E. (2008), *Adaptive Synchronization of Dynamics on Evolving Complex Networks*, Phys. Rev. Lett. **100**, 114101. (Cited on page 25.)
- SPROTT, J. C. (2003), *Chaos and Time-Series Analysis*, Oxford University Press. (Cited on page 54.)
- STROGATZ, S. H. AND STEWART, I. (1993), *Coupled Oscillators and Biological Synchronization*, Sci. Am. **269**, 102. (Cited on page 25.)
- TAGER, A. A. AND ELENKRIG, B. B. (1993), *Stability regimes and high-frequency modulation of laser diodes with short external cavity*, IEEE J. Quantum Electron. **29**, 2886. (Cited on page 44.)
- TRONCIU, V. Z., WÜNSCHE, H. J., SIEBER, J., SCHNEIDER, K., AND HENNEBERGER, F. (2000), *Dynamics of single mode semiconductor lasers with passive dispersive reflectors*, Opt. Commun. **182**, 221. (Cited on page 123.)

- TRONCIU, V. Z., WÜNSCHE, H. J., WOLFRUM, M., AND RADZIUNAS, M. (2006), *Semiconductor Laser under Resonant Feedback from a Fabry-Perot: Stability of Continuous-Wave Operation*, Phys. Rev. E **73**, 046205. (Cited on pages 27, 40, 43 and 45.)
- TSUMOTO, K., KITAYAMA, K., YOSHINAGA, T., AIHARA, K., AND KAWAKAMI, H. (2006), *Bifurcations in Morris-Lecar neuron model*, Neurocomputing **69**, 293, ISSN 0925-2312. (Cited on page 124.)
- USHAKOV, O., BAUER, S., BROX, O., WÜNSCHE, H. J., AND HENNEBERGER, F. (2004), *Self-Organization in Semiconductor Lasers with Ultrashort Optical Feedback*, Phys. Rev. Lett. **92**, 043902. (Cited on page 40.)
- VAN TARTWIJK, G. H. M. AND AGRAWAL, G. P. (1998), *Laser instabilities: a modern perspective*, Prog. Quantum Electronics **22**, 43. (Cited on page 46.)
- VENKATARAMANI, S. C., HUNT, B. R., AND OTT, E. (1996a), *Bubbling transition*, Phys. Rev. E **54**, 1346. (Cited on page 27.)
- VENKATARAMANI, S. C., HUNT, B. R., OTT, E., GAUTHIER, D. J., AND BIENFANG, J. C. (1996b), *Transitions to Bubbling of Chaotic Systems*, Phys. Rev. Lett. **77**, 5361. (Cited on page 27.)
- VICENTE, R., GOLLO, L. L., MIRASSO, C. R., FISCHER, I., AND GORDON, P. (2008), *Dynamical relaying can yield zero time lag neuronal synchrony despite long conduction delays*, Proc. Natl. Acad. Sci. **105**, 17157. (Cited on page 27.)
- VICENTE, R., GOLLO, L. L., MIRASSO, C. R., FISCHER, I., AND PIPA, G. (2009), *Far in space and yet in synchrony: neuronal mechanisms for zero-lag long-range synchronization*. To be published. (Cited on page 26.)
- VICENTE, R., MIRASSO, C. R., AND FISCHER, I. (2007), *Simultaneous bidirectional message transmission in a chaos-bases communication scheme*, Opt. Lett. **32**, 403. (Cited on pages 26 and 46.)
- WATTS, D. J. AND STROGATZ, S. H. (1998), *Collective dynamics of 'small-world' networks*, Nature **393**, 440. (Cited on pages 25, 101 and 118.)
- WÜNSCHE, H. J., BAUER, S., KREISSL, J., USHAKOV, O., KORNEYEV, N., HENNEBERGER, F., WILLE, E., ERZGRÄBER, H., PEIL, M., ELSÄSSER, W., AND FISCHER, I. (2005), *Synchronization of Delay-Coupled Oscillators: A Study of Semiconductor Lasers*, Phys. Rev. Lett. **94**, 163901. (Cited on page 26.)

- WÜNSCHE, H. J., SCHIKORA, S., AND HENNEBERGER, F. (2008), *Noninvasive Control of Semiconductor Lasers by Delayed Optical Feedback*, in E. Schöll and H. G. Schuster (Editors), *Handbook of Chaos Control*, Wiley-VCH, Weinheim. Second completely revised and enlarged edition. (Cited on page 27.)
- YAMADA, T. AND FUJISAKA, H. (1983), *Stability Theory of Synchronized Motion in Coupled-Oscillator Systems. II*, Prog. Theor. Phys. **70**, 1240. (Cited on page 26.)
- YAMADA, T. AND FUJISAKA, H. (1984), *Stability Theory of Synchronized Motion in Coupled-Oscillator Systems. III*, Prog. Theor. Phys. **72**, 885. (Cited on page 26.)
- YANG, T. (2004), *A Survey of Chaotic Secure Communication Systems*, International Journal of Computational Cognition **2**, 81. (Cited on pages 26 and 46.)
- ZHOU, C. AND KURTHS, J. (2006), *Hierarchical synchronization in complex networks with heterogeneous degrees*, Chaos **16**, 015104. (Cited on page 176.)
- ZHOU, C., ZEMANOVA, L., ZAMORA, G., HILGETAG, C. C., AND KURTHS, J. (2006), *Hierarchical Organization Unveiled by Functional Connectivity in Complex Brain Networks*, Phys. Rev. Lett. **97**, 238103. (Cited on page 176.)
- ZIEHE, A., LASKOV, P., NOLTE, G., AND MÜLLER, K.-R. (2004), *A Fast Algorithm for Joint Diagonalization with Non-orthogonal Transformations and its Application to Blind Source Separation*, J. Mach. Learn. Res. **5**, 777, ISSN 1532-4435. (Cited on page 117.)
- ZIGZAG, M., BUTKOVSKI, M., ENGLERT, A., KINZEL, W., AND KANTER, I. (2008), *Emergence of zero-lag synchronization in generic mutually coupled chaotic systems* ArXiv:0811.4066v1. (Cited on page 26.)
- ZIGZAG, M., BUTKOVSKI, M., ENGLERT, A., KINZEL, W., AND KANTER, I. (2009), *Zero-lag synchronization of chaotic units with time-delayed couplings*, Europhys. Lett. **85**, 60005. (Cited on page 26.)
- ZILLMER, R., LIVI, R., POLITI, A., AND TORCINI, A. (2007), *Stability of the splay state in pulse-coupled networks*, Phys. Rev. E **76**, 046102. (Cited on pages 127 and 184.)

Acknowledgments

First of all, I would like to thank Prof. Eckehard Schöll for giving me the opportunity to do research in the field of nonlinear dynamics with a focus on delay in his group. I also thank him for his supervision, valuable help, and support by suggestions and questions regarding my research.

Furthermore, I want to thank all the current, former, and visiting members of the Schöll group for the wonderful working atmosphere but also for creative discussions and exchange of ideas. Special thanks go to Dr. Philipp Hövel, Dr. Valentin Flunkert, Judith Lehnert, Andrew Keane, Colin Greenshields, Martin Heinrich, Dr. Markus Dahlem, Christian Otto, Roland Aust, Niels Majer, and Dr. Kathy Lüdge. I am very much indebted to Dr. Chol-Ung Choe for a very fruitful collaboration that led to the results presented in Chapters 7 and 10.

I thank Prof. Wolfgang Kinzel for preparing the second assessment of this thesis, but also for the valuable exchange of ideas in the frame of a very promising collaboration that has just started during the past months.

I am grateful for interesting discussions with Dr. Andreas Amann, Dr. Hans-Jürgen Wünsche, Prof. Ido Kanter, Sven Heiligenthal, and Steffen Zeeb.

I thank my family, especially my girlfriend Daniela and my sons Emil and Matteo, for the constant support and understanding during my work on this thesis.

This work was supported by Deutsche Forschungsgemeinschaft in the framework of the Collaborative Research Center 555 *Complex Nonlinear Processes*. Final stages of the thesis, in particular the results presented in Chapters 6 and 9, were supported in the framework of the Collaborative Research Center 910 *Control of self-organizing nonlinear systems: Theoretical methods and concepts of application*.

Index

- adjacency matrix, 37, 38, 74, 75, 102
- all-to-all network, 93, 107, 113, 173, 196
- average degree, 104, 107
- betweenness, 105
- bidirectional ring, 91, 116, 161, 196
- bipartite network, 149, 151, 165
- characteristic path length, 104
- circulant matrix, 96, 118, 195
- closeness, 105
- cluster, 41, 92, 127, 145, 169, 183
- cluster synchronization, 41, 92, 145, 169, 183
- clustering coefficient, 106
- coherence collapse, 46, 64, 75, 101, 166
- commuting matrices, 115, 169
- complex network, 101, 165
- constant row sum, 42, 64
- control of synchronization, 123, 185
- coupling matrix, 37, 38
- cross correlation, 80
- degree, 104
- degree distribution, 104
- delay, 26, 37, 40, 61
- desynchronization, 81, 112, 123, 140
- diameter, 105
- directed random network, 102, 111
- eigenvalue
 - longitudinal, 88, 121
 - transverse, 76, 189
- Erdős-Rényi network, 75, 101, 118, 166, 177
- feedback, 35, 39, 74, 88, 102
- Floquet exponents, 132, 189
- Gerschgorin circle theorem, 57, 135, 139
- globally coupled network, 93, 107, 113, 173, 196
- group, 35, 145, 169
- group synchronization, 35, 145, 169
- hierarchical network, 175
- in-phase synchronization, 82, 127, 184, 206
- invariant manifold, 56
- isochronous synchronization, 41, 59, 74, 115
- Kaplan-Yorke dimension, 54
- Lang-Kobayashi model, 35, 43
- laser dynamics, 43
- linear chain, 97
- longitudinal eigenvalue, 88, 121
- low-frequency fluctuations, 49, 64, 75
- Lyapunov exponent, 51, 61, 64

- manifold
 - invariant, 56
 - synchronization, 41, 59, 147
- master stability equation, 61, 151, 153, 170
- master stability function, 59, 115, 123, 145, 169, 185
- matrix
 - adjacency, 37, 38, 74, 75, 102
 - circulant, 96, 118, 195
 - commuting, 115, 169
 - coupling, 37, 38
 - weight, 39
- mean geodesic distance, 104
- mean synchronization error, 82
- multipartite network, 151, 169
- network, 35
 - all-to-all, 93, 107, 113, 173, 196
 - bipartite, 149, 151, 165
 - complex, 101, 165
 - directed random, 102, 111
 - Erdős-Rényi, 75, 101, 118, 166, 177
 - globally coupled, 93, 107, 113, 173, 196
 - hierarchical, 175
 - multipartite, 151, 169
 - random, 75, 101, 118, 166, 177
 - regular, 73, 88, 118
 - undirected, 103, 135
 - undirected random, 102, 108
- network motif, 74
- network motifs, 74
- network quantities, 103
 - average degree, 104, 107
 - betweenness, 105
 - characteristic path length, 104
 - closeness, 105
 - clustering coefficient, 106
 - degree distribution, 104
 - diameter, 105
 - node degree, 104
 - transitivity, 106
- network topology, 37
- node degree, 104
- order parameter, 141, 142, 197
- parameter mismatch, 41, 141, 197
- percolation, 106
- random network, 75, 101, 118, 166, 177
- regular network, 73, 88, 118
- ring
 - bidirectional, 91, 116, 161, 196
 - unidirectional, 88, 127, 135, 150, 152, 184
- row sum, 42, 60, 146
 - constant, 42, 64
 - unity, 57, 64, 102, 126, 147
- self-feedback, 35, 39, 74, 88, 102
- splay state, 127, 184, 188, 189, 200
- splay synchronization, 127, 184, 188, 189, 200
- stability of synchronization, 59, 115, 123, 145, 169, 183
- Stuart-Landau oscillator, 35, 123, 183
- subgraph, 107
- synchronization
 - cluster, 41, 92, 145, 169, 183
 - group, 35, 145, 169
 - in-phase, 82, 127, 184, 206
 - isochronous, 41, 59, 74, 115
 - splay, 127, 184, 188, 189, 200
 - zero-lag, 41
- synchronization manifold, 41, 59, 147
- time delay, 26, 37, 40, 61

topology, 37
transitivity, 106
transverse eigenvalue, 76, 189

undirected network, 103, 135
undirected random network, 102, 108
unidirectional ring, 88, 127, 135, 150,
152, 184
unity row sum, 57, 64, 102, 126, 147

weight matrix, 39
weighted motifs, 74

zero-lag synchronization, 41